

---

# Quantitative bacterial physiology during growth transitions and starvation

Severin Josef Schink

---



Munich 2017



---

# Quantitative bacterial physiology during growth transitions and starvation

Severin Josef Schink

---

Doctoral thesis  
presented to the Faculty of Physics  
of the Ludwig–Maximilians–Universität  
Munich

by  
Severin Josef Schink  
from Gräfelfing

Munich, 25.04.2017

Erstgutachter: Prof. Dr. Ulrich Gerland  
Zweitgutachter: Prof. Dr. Erwin Frey  
Tag der mündlichen Prüfung: 01.06.2017

# Contents

<b>Abstract</b>	<b>xiii</b>
<b>Zusammenfassung</b>	<b>xv</b>
<b>1 Bacterial physiology</b>	<b>1</b>
1.1 Introduction . . . . .	1
1.1.1 Wild type <i>E. coli</i> and pathogenicity . . . . .	1
1.1.2 Ecology . . . . .	1
1.1.3 Laboratory strain K-12 . . . . .	2
1.2 Life cycle of a bacterium . . . . .	3
1.3 Growth and growth laws . . . . .	3
1.3.1 Exponential growth . . . . .	3
1.3.2 Growth laws . . . . .	4
1.3.3 Growth dependency of the proteome . . . . .	7
1.4 Stationary phase and decline of viability . . . . .	10
1.4.1 RpoS: the primary stationary phase regulator . . . . .	10
1.4.2 Exponential decline of viability . . . . .	10
<b>2 The benefit of a proteome reserve</b>	<b>13</b>
2.1 Introduction . . . . .	13
2.2 The R-protein overcapacity . . . . .	13
2.3 A kinetic model for famine to feast upshifts . . . . .	14
2.4 R-proteins abundance determines transition kinetics to feast . . . . .	16
2.5 Fitness landscape for transitions from famine to feast . . . . .	18
2.5.1 Fitness landscape for different proteome reserves . . . . .	18
2.5.2 Fitness landscape for different upshifts . . . . .	20
2.6 Discussion . . . . .	22
<b>3 Growth transitions</b>	<b>25</b>
3.1 Introduction . . . . .	25
3.1.1 Carbon co-utilization upshift . . . . .	26
3.1.2 Carbon co-utilization downshift . . . . .	26
3.2 A flux-driven regulation (FDR) model . . . . .	27
3.2.1 Design principle . . . . .	27
3.2.2 Model components . . . . .	28
3.2.3 Analytical solution . . . . .	34
3.3 Comparison of the FDR model with data . . . . .	36
3.3.1 Upshifts without pre-expression . . . . .	36
3.3.2 Upshifts with pre-expression . . . . .	39

3.3.3	Upshifts with titratable pre-expression . . . . .	39
3.3.4	Diauxic shifts with co-utilized substrates . . . . .	40
3.3.5	Diauxic shifts with non co-utilized substrates . . . . .	41
3.4	Proteome sectors during growth transitions . . . . .	44
3.5	Adaptation strategy according to the FDR model . . . . .	46
3.6	Discussion . . . . .	49
<b>4</b>	<b>Death during carbon starvation</b>	<b>51</b>
4.1	Introduction . . . . .	51
4.2	Characterizing the starvation state . . . . .	52
4.2.1	Exponential decay of viability during starvation . . . . .	52
4.2.2	Carbon starvation is a static phase . . . . .	53
4.2.3	Cannibalisms during starvation . . . . .	55
4.3	Origin of the exponential decay of viability . . . . .	56
4.3.1	Maintenance rate . . . . .	57
4.3.2	Yield . . . . .	58
4.4	Perturbing the steady state state . . . . .	59
4.4.1	Titratable maintenance rate . . . . .	59
4.4.2	Inducing cell death . . . . .	60
4.5	Effect of genetic and environmental conditions on the death rate . . . . .	61
4.6	Discussion . . . . .	62
<b>5</b>	<b>Preventing systemic spread of pathogens</b>	<b>63</b>
5.1	Introduction . . . . .	63
5.2	Thrombus formation in the microvasculature . . . . .	64
5.2.1	The mouse cremaster muscle model . . . . .	64
5.2.2	Restricting dissemination of pathogens by thrombosis . . . . .	65
5.2.3	Accelerated thrombus formation in the inflamed microvasculature . . . . .	65
5.2.4	Immune cells drive platelet recruitment in the microvasculature . . . . .	66
5.3	<i>In vitro</i> analysis of the platelet capture . . . . .	68
5.3.1	Rheological perturbations inside a microfluidic device . . . . .	68
5.3.2	Rheological perturbations are essential for platelet recruitment . . . . .	68
5.4	Theoretical investigation of platelet capture . . . . .	69
5.4.1	Fluid flow . . . . .	69
5.4.2	Platelet motion . . . . .	71
5.4.3	Simulation results . . . . .	72
5.5	Biochemistry of platelet adhesion in the microvasculature . . . . .	72
5.6	Discussion . . . . .	75
	<b>Appendices</b>	<b>77</b>
<b>A</b>	<b>The benefit of a proteome reserve</b>	<b>79</b>
A.1	Theoretical analysis of the instantaneous model . . . . .	79
A.1.1	Kinetic modeling of the proteome composition . . . . .	79
A.1.2	Protein allocation . . . . .	80
A.1.3	R-proteins dynamics for constant $\sigma_R$ and $\chi_R$ with a generic initial state . . . . .	80
A.1.4	Upshifts and the R-sector offset . . . . .	81
A.2	Fitness landscape in upshifts to rich media . . . . .	82
A.2.1	Analysis of the fitness landscape . . . . .	83
A.2.2	Comparing different environments . . . . .	85

A.3	Supplementary Materials and Methods . . . . .	87
A.4	Supplementary Figures . . . . .	88
A.5	Supplementary Tables . . . . .	94
<b>B</b>	<b>Growth transitions</b>	<b>95</b>
B.1	Limits of the instantaneous model . . . . .	95
B.2	Parameters of the FDR model . . . . .	96
B.2.1	Conversion factor $\beta$ , substrate to carbon flux . . . . .	96
B.2.2	Conversion factors $\alpha$ and $\alpha_M$ , carbon flux to protein synthesis and biomass . . . . .	96
B.2.3	Constraining the microscopic parameters . . . . .	97
B.2.4	Growth rate composition formula for co-utilized substrates . . . . .	97
B.3	Analytical analysis of the FDR model . . . . .	98
B.3.1	Derivation of the central differential equation . . . . .	98
B.3.2	Solution of the central differential equation . . . . .	100
B.3.3	Continuity at the instant of shift . . . . .	103
B.3.4	Post-shift growth . . . . .	106
B.4	Adaptation strategy according to the FDR model . . . . .	111
B.4.1	A geometric view of adaptation kinetics . . . . .	111
B.4.2	First regime . . . . .	114
B.4.3	Second regime . . . . .	115
B.4.4	Impact of the two regimes on total recovery . . . . .	117
B.5	Supplementary Materials and Methods . . . . .	118
B.5.1	Growth medium . . . . .	118
B.5.2	Culture procedure . . . . .	118
B.5.3	Strains . . . . .	118
B.5.4	$\beta$ -galactosidase quantification . . . . .	118
B.5.5	Total RNA quantification . . . . .	119
B.5.6	Total protein quantification . . . . .	119
B.5.7	Dry mass quantification . . . . .	119
B.5.8	Growth transition mass spectrometry (MS) protocol . . . . .	119
B.5.9	Pulse-labeling MS Protocol . . . . .	120
B.5.10	Data analysis . . . . .	120
B.6	Supplementary Figures . . . . .	122
B.7	Supplementary Tables . . . . .	127
<b>C</b>	<b>Death during carbon starvation</b>	<b>131</b>
C.1	Supplementary Materials and Methods . . . . .	131
C.1.1	Culture medium . . . . .	131
C.1.2	Growth procedure . . . . .	131
C.1.3	Starvation . . . . .	132
C.1.4	Staining . . . . .	132
C.1.5	Strains . . . . .	132
C.2	Supplementary Figures . . . . .	133
<b>D</b>	<b>Preventing systemic spread of pathogens</b>	<b>135</b>
D.1	Supplementary Material and Methods . . . . .	135
D.1.1	Animals . . . . .	135
D.1.2	Reagents . . . . .	135
D.1.3	In vivo microscopy on the mouse cremaster muscle . . . . .	136
D.1.4	Microfluidic device . . . . .	137

D.1.5	Microfluidics experiments . . . . .	138
D.1.6	Fluid dynamics simulation . . . . .	138
D.1.7	Confocal microscopy . . . . .	138
D.1.8	Statistics . . . . .	139
D.2	Supplementary Figures . . . . .	140
	<b>Bibliography</b>	<b>141</b>
	<b>Acknowledgements</b>	<b>156</b>

# List of Figures

1.1	Scanning electron micrograph of <i>E. coli</i> .	2
1.2	The bacterial life cycle.	3
1.3	Growth law: Ribosome abundance	5
1.4	Growth law: Translational activity	5
1.5	Growth law: Catabolic proteins.	6
1.6	Proteome partitioning.	8
1.7	Composition of the proteome sectors.	9
2.1	Famine-to-feast transitions	14
2.2	A kinetic model for upshifts to feast.	15
2.3	Upshift kinetics in shifts to feast.	17
2.4	Fitness landscape for different proteome reserves.	19
2.5	Fitness landscape for different upshifts	21
3.1	Co-utilization upshift	27
3.2	Co-utilization downshift	28
3.3	Model of Flux-driven Regulation (FDR)	29
3.4	Regulatory functions.	33
3.5	Proteome remodeling	35
3.6	Upshifts from succinate	37
3.7	Upshifts from pyruvate	38
3.8	Upshift mannose adding OAA	39
3.9	Titrateable pre-expression	40
3.10	Diauxic shift with co-utilized carbon substrates	42
3.11	Glucose-lactose diauxie	43
3.12	Graphical synopsis of the proteome remodeling	44
3.13	Proteome remodeling during growth transitions	45
3.14	Protein degradation	46
3.15	Trajectories and time scales of growth transition	48
4.1	Exponential decay of viability during starvation.	52
4.2	Zoom into entry of exponential decay	53
4.3	Cryptic growth	54
4.4	Cell size during exponential growth and starvation	54
4.5	Gene expression during starvation	55
4.6	Long-term survival of adapted mutants	55
4.7	Cannibalism during starvation	56
4.8	Maintenance rate	58
4.9	Yield	59

4.10	Titrating the maintenance rate . . . . .	60
4.11	Inducing cell death . . . . .	60
4.12	Environmental and genetic dependence of the death rate . . . . .	61
5.1	Thrombus formation in the microvasculature. . . . .	65
5.2	Bacterial trapping inside a thrombus. . . . .	66
5.3	Spatiotemporal dynamics of microvascular thrombosis. . . . .	66
5.4	Role of leukocytes in microvascular thrombosis . . . . .	67
5.5	Microfluidic experiments on platelet capture. . . . .	69
5.6	fluid dynamics simulation of the platelet capture. . . . .	73
5.7	Biochemical interactions during microvascular thrombosis. . . . .	74
5.8	Graphical synopsis of the leukocytes-platelet cascade. . . . .	75
A.1	Upshifts to rich media . . . . .	88
A.2	RNA to protein mass ratio for different <i>E. coli</i> strains . . . . .	89
A.3	Relative fitness - 1 . . . . .	90
A.4	Relative fitness - 2 . . . . .	91
A.5	Relative fitness - 3 . . . . .	92
A.6	Relative fitness - 4 . . . . .	93
B.1	Limits of the instantaneous model . . . . .	96
B.2	Two carbon addition . . . . .	98
B.3	Upshift without pre-expression . . . . .	102
B.4	Upshift with pre-expression . . . . .	104
B.5	Downshift . . . . .	105
B.6	Adaptation strategy of the cell during upshifts (fast initial growth). . . . .	111
B.7	Adaptation strategy of the cell during upshifts (slow initial growth). . . . .	113
B.8	Relaxation times . . . . .	116
B.9	Dry mass and protein mass . . . . .	122
B.10	Serial dilution experiment . . . . .	123
B.11	Repeatability . . . . .	124
B.12	Titratable pre-expression pt. 2 . . . . .	125
C.1	Loss of membrane integrity after UV-sterilization . . . . .	133
C.2	Exponential decay in other environments and strains . . . . .	133
D.1	Thrombosis in arterioles. . . . .	140
D.2	Systemic inflammation. . . . .	140

# List of Tables

1.1	Proteome sectors defined by Hui et al. . . . .	8
A.1	Fit parameters of $\lambda_0$ . . . . .	94
B.1	Physiological parameters of wild type NCM3722 during steady state growth . . .	127
B.2	Physiological parameters of strains with titratable carbon uptake during steady state growth . . . . .	127
B.3	Parameters defining pu-dctA upshifts. . . . .	128
B.4	Parameters defining glucose-lactose diauxic shift. . . . .	128
B.5	Michaelis-Menten constants . . . . .	128
B.6	List of strains. . . . .	128
B.7	Co-utilization growth rates . . . . .	129
B.8	Proteome sectors during growth shifts . . . . .	129
B.9	Proteome groups during growth shifts . . . . .	130



# Abstract

Bacteria have been studied extensively for the last century, as they are easily cultivable and their relatively simple genetics, composition and regulation make them ideal candidates to study general biological questions in a minimally complex organism. While initial studies were mostly descriptive in nature, in recent decades studies on bacteria have become increasingly quantitative. To gain a deeper understanding of the underlying processes, researchers increasingly employ a combination of experiments and quantitative modeling, to elucidate bacterial properties such as its physiology, gene regulation or molecular mechanisms.

Almost all of these quantitative studies have focused on exponentially growing bacteria. This growth state is attained when bacteria are grown for many generations in a constant environment, such that they perfectly acclimatized and reach a reproducible steady state of constant growth, gene expression and compositions. While great progress was achieved studying exponentially growing bacteria, recent findings uncovered puzzling bacterial strategies, which have detrimental effects on growth and cannot be reconciled with the idea that bacteria are evolutionarily adapted to maximize exponential growth. Indeed, prolonged periods of undisturbed growth are rare in nature, and bacteria had to adapt to complex environmental changes and challenges. The understanding of growth physiology in these environments remains a grand challenge of quantitative biology and is necessary for a more complete understanding of bacterial physiology. This thesis takes on this challenge and focusses on growth transitions and starvation of *Escherichia coli*. In addition, this thesis studies the host's immune response to infections.

In the first part of this thesis we use a simple kinetic model in combination with experimental growth kinetics to identify a mechanistic link between proteome overcapacities and the ability of cells to quickly adapt when nutrient conditions improve. This transient benefit, however, comes at the expense of decreasing growth in prolonged favorable conditions. Within this constraining interplay, we find that *E. coli* implements a solution for this trade-off that is consistent with maximization of fitness during the feast period inside the mammalian gut, the main habitat of wild-type *E. coli*.

We further extend this theory in the second part to explicitly include regulation of growth-dependent proteins, with the aim to elucidate dynamic regulation strategies. Using only qualitative knowledge of the underlying regulatory processes and imposing the condition of flux balance, we derive a quantitative model of bacterial growth transitions independent of kinetic parameters. As validated by quantitative proteomics, the model predicts a global remodeling of the proteome that prevents channeling protein synthesis specifically into bottleneck proteins and thus slows recovery kinetics in response to nutrient shifts

In the third part of this thesis we study the survival of *E. coli* during carbon starvation, where *E. coli* shows an exponential decay of viability with the rate depending on environment and genetics. We identify the exponential decay to be a consequence of the energy required by cells for maintenance. During starvation, the only source of nutrients is their release into the environment during cell death and loss of membrane integrity. Such a biomass recycling process,

in which dying cells sustain the remaining viable cells, naturally leads to an exponential decay of viability. We identify this physiological state to be a well-controlled steady state, analogously to the steady-state exponential growth that revolutionized studies on growth in the mid last century, with broad implications for bacterial ecology, evolution and physiology.

The last part of this work deals with the mammalian organism fighting bacterial infections in the microvasculature. We find that at the first stage of defense, the mammalian organism employs thrombosis directed by immune cells. As a result of this "immunothrombosis", the infected part of the microvasculature is isolated from the blood system, so that the systemic dissemination of pathogens can be prevented. In addition, bacteria are trapped inside the thrombus, suggesting a strategy of the host's organism to capture and eliminate pathogens in targeted manner, which could be a major factor in the battle against infections.

# Zusammenfassung

Bakterien waren im vergangenen Jahrhundert Gegenstand einer Vielzahl an Studien. Ihre anspruchlose Kultivierung, einfachen Genetik, Zusammensetzung und Regulation machen sie zu idealen Kandidaten um grundlegende biologische Fragen zu untersuchen. Anfänglich lag der Fokus vieler Studien auf der bloßen Beschreibung von Phänomenen, in den letzten Jahrzehnten ist jedoch die quantitative Untersuchung modern geworden, wobei Wissenschaftler versuchen mit einer Kombination aus Theorie und Experimenten bakterielle Eigenschaften wie Physiologie, Genregulation oder molekulare Mechanismen auf einer grundlegenden Ebene zu verstehen.

Fast alle quantitativen Studien haben sich dabei auf exponentiell wachsende Bakterien beschränkt. Dieser Wachstumszustand wird erreicht wenn sich Bakterien für viele Generationen in einer gleichbleibenden Umgebung anpassen und dabei einen reproduzierbaren Zustand von konstanter Wachstumsrate, Genexpression und Zusammensetzung erreichen. Während großer Fortschritt bei dem Verständnis exponentiell wachsender Bakterien erreicht wurde, so bleiben einige Beobachtungen rätselhaft, da es scheint als würden Bakterien Strategien implementieren die sie sich nachteilig auf das exponentielle Wachstum auswirken. Solche Strategien sind nicht mit der Idee in Einklang zu bringen, dass die Zelle evolutionär auf maximales Wachstum ausgerichtet ist. In der Tat sind in der Natur lange, ungestörte Wachstumsphasen selten und Bakterien dadurch ständig neuen Änderungen und Herausforderungen ausgesetzt. Die Physiologie von Bakterien in solchen Umgebungen zu verstehen ist eine der großen Herausforderungen der quantitativen Biologie, und notwendig für ein vollständigeres Verständnis von bakterieller Physiologie. Diese Dissertation geht diese Herausforderung an und untersucht Wachstumsübergänge und Hungerphasen in *Escherichia coli*. Abschließend wird die Immunantwort von Säugetierwirten bei bakteriellen Infektionen behandelt.

Im ersten Teil dieser Dissertation benutzen wir ein einfaches kinetisches Model in Kombination mit experimenteller Wachstumskinetik um einen mechanistischen Zusammenhang zwischen Proteomeüberkapazitäten und der Anpassungsfähigkeit von Zellen bei Nährstoffverbesserung zu identifizieren. Der vorübergehende Vorteil kommt jedoch auf Kosten einer langfristigen Verlangsamung des Wachstums. Die Lösung dieses Trade-offs durch *E. coli* ist konsistent mit einer Maximierung der Fitness für die begrenzte Dauer der Nährstoffpräsenz im Säugetierdarm, dem Hauptlebensraum von Wildtyp *E. coli*.

Die Theorie zur Beschreibung der Wachstumsübergänge wird im zweiten Teil der Dissertation um die Regulierung von wachstumsabhängigen Proteinen erweitert, mit dem Ziel dynamische Regulationsstrategien zu ergründen. Mit Hilfe von qualitativen Wissens der zugrunde liegenden Regulationsmechanismen und der Annahme von Flussgleichgewicht der Metaboliten errechnen wir ein quantitatives Modell für Wachstumsübergänge das unabhängig von mikroskopischen Parametern ist. Wie von Proteomikexperimenten bestätigt, sagt das Modell eine globale Umgestaltung des Proteoms vorher, die verhindert dass die Proteinsynthese in einzelne Proteinengpässe geleitet wird und dadurch die Anpassungsgeschwindigkeit verringert.

Der dritte Teil der Arbeit widmet sich dem Überleben von *E. coli* bei Kohlenstoffmangel. Dort zeigt *E. coli* einen exponentiellen Zerfall der Lebensfähigkeit die von Umwelt und

Genetik abhängt. Wir verstehen den exponentiellen Zerfall als Konsequenz aus der notwendigen Energie zum Aufrechterhalten der Lebensfähigkeit. Während des Kohlenstoffmangels ist die einzige Nährstoffquelle durch den Tod und das Aufbrechen und von Zellen gegeben. Dieser Wiederverwertungsprozess bei dem tote Zellen lebende Zellen am Leben halten führt auf natürliche Weise zu einem exponentiellen Zerfall. Wir identifizieren diesen Zerfall als einen wohl definierten, stabilen Gleichgewichtszustand analog zu dem exponentiellen Wachstum, der in der Mitte des letzten Jahrhunderts die Studien zu wachsenden Zellen revolutioniert hat, und mit breiten Auswirkungen für bakterielle Ökologie, Evolution und Physiologie.

Der letzte Teil der Arbeit handelt vom Kampf des Säugetierorganismus gegen bakterielle Infektionen in der Mikrovaskulatur. Als erste Stufe der Immunverteidigung setzt der Organismus Thrombose ein, die durch Immunzellen gesteuert wird. Als Resultat dieser "Immunothrombose" wird das infizierte Teil der Mikrovaskulatur vom Blutsystem isoliert, so dass eine systemische Verbreitung der Erreger verhindert wird. Zusätzlich werden Bakterien in die Thromben eingebaut, was nahe legt dass es die Strategie des Wirtsorganismusses ist Bakterien gezielt einzufangen und zu eliminieren, und damit einen bedeutenden Teil zum Kampf gegen Infektionen beitragen könnte.

# Chapter 1

## Bacterial physiology

### 1.1 Introduction

In its life a bacterium undergoes many different states. They live and thrive, but also struggle and die in a fascinating variety of possible ways. These *states* of the cell's life, depend on the environment in which the cells are, with some environments supporting optimal, fast growth, others are more challenging and require a greater effort of the cell to grow, while again in other environments the lack of nutrition or even presence of stresses can kill the cells. The myriad of possible states poses a challenge for the bacteria, as they have to be adapted well for each one of these states of their life cycle, in order to perform well evolutionarily. But they also allow a great basis for studying bacteria, as many possible scenarios can be used to probe the cell's response to different environments.

#### 1.1.1 Wild type *E. coli* and pathogenicity

In this work *Escherichia coli* (*E. coli*) was studied, as it is easily cultured in laboratory conditions. *E. coli* is a Gram-negative, chemoorganoheterotrophic, facultatively anaerobic, rod-shaped bacterium of the genus *Escherichia* that is commonly found in the lower intestine of warm-blooded organisms (endotherms). Fig. 1.1 shows a scanning electron microscope image of *E. coli*. Most *E. coli* strains are non-pathogenic, but some serotypes can cause serious infections, such as food poisoning and pose a serious threat to human health. *E. coli* is a major cause of diarrheal diseases, peritonitis, colitis, bacteremia, infant mortality, and urinary tract infections that world-wide cost billions of dollars to treat and kill roughly 2 million humans each year [1–3]. Pathogenic strains can thrive in the mammalian gut microbiome, which is the main habitat for *E. coli* [4]. Fecal-oral transmission is the main route of transfection of pathogenic *E. coli*. The transfection route is typically indirect, with *E. coli* needing to survive in a variety of poor habitats, such as fecal matter, soil, waste or sea water or inorganic surfaces before being orally taken up by a new host. This makes the understanding of the survival of *E. coli* a medically important questions. Opportunistic *E. coli* infections are caused by normally harmless or beneficial strains when introduced to sick hosts or to parts of a host's body outside of the gut [3].

#### 1.1.2 Ecology

While much work is done on elucidating the molecular biology of *E. coli*, much less is known about its ecology, even if for proper understanding of molecular mechanisms, the evolutionary context is crucial. As mentioned above, *E. coli* thrives in the large intestines of mammals. After excretion of fecal matter, *E. coli* needs to survive in a multitude of abiotic environments to be

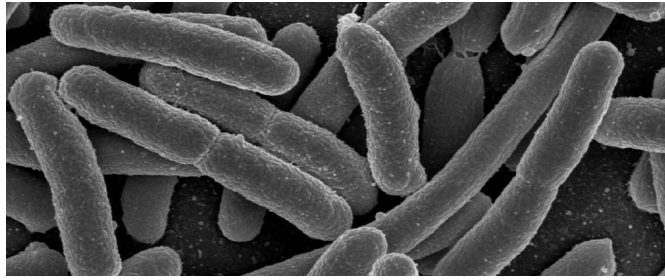


**Figure 1.1:** Scanning electron micrograph of *E. coli*, grown in culture and adhered to a cover slip [photo credit: Rocky Mountain Laboratories, NIAID, NIH]. Cells are rod-shaped, about 1  $\mu\text{m}$  in diameter and 1.5 to 4  $\mu\text{m}$  in length.

eventually be taken up orally by the new host. This biphasic lifestyle of host-independent and host-associated phases [5] has evolutionarily shaped *E. coli* [4].

### Host-associated – in the large intestine

A central question for correct interpretation of laboratory experiments on *E. coli* is about the growth of *E. coli* in the large intestine. How should the laboratory culture be chosen to reflect the environment *E. coli* evolutionarily adapted to? The entire fecal matter in the large intestine of a human doubles in mass about every 12 to 24 hours [6], estimated from first passage times through the human gut. In contrast, *E. coli* in cultured in the lab grows fast, reaching up to one doubling every 20 minutes [7], with typical doubling times studied in the lab being between 30 minutes and 2 hours. This discrepancy was resolved by in situ rRNA hybridization experiments in germ free mice [8, 9]. Experiments found that a small subpopulation of *E. coli* grows in the mucus layer of the large intestine at a high growth rate, between 30 and 80 minutes doubling time [9]. The larger population is located in the lumen is growth arrested and originated from the growing subpopulation in the large intestine [8]. Both populations combined lead to the average slow doubling of *E. coli* in the fecal matter.

The nutrient availability in the large intestine depends on the oral food uptake, and thus fluctuates. Nutrients are usually only available for a couple hours after food uptake by the host [10, 11]. This exerts an evolutionary pressure on the cells to not only adapt for fast growth, but also to be able to quickly adapt to improving or worsening nutrient conditions.

### Host independent – survival in open environments

After excretion of *E. coli* in fecal matter, the bacteria must survive in a multitude of environments, such as soil, manure and water, before taken up and colonizing a new host. Cells can survive from several days to even years [12–14], depending on how favorable the environment of the cell is. Negative impact on the viability were observed for high temperatures, oxygen content, pH or the availability of resources [4]. How these parameters impact the survival of *E. coli* remains unknown. Yet for successful propagation, *E. coli* must survive these harsh conditions.

#### 1.1.3 Laboratory strain K-12

Research on *E. coli* has led to many advances in a variety of fields, and it is widely regarded the most important model organism for biology [15, 16]. Central contributions for molecular biology, physiology and genetics include the elucidation of the genetic code [17], DNA replication [18], transcription [19], life cycle of lytic and lysogenic bacterial viruses [20, 21], gene regulation [22–24], or the discovery of restriction enzymes [25, 26].

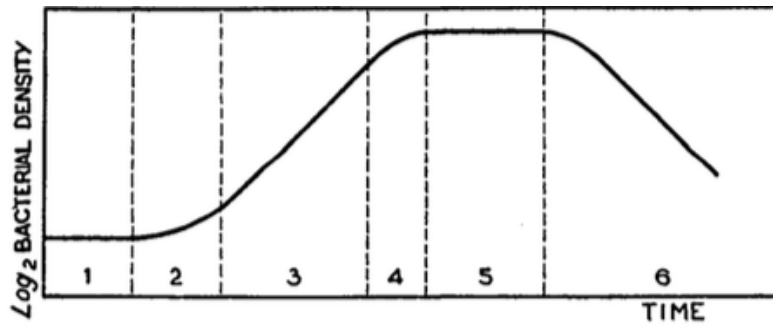


**Figure 1.2: The bacterial life cycle.** Jacques Monod [30] defined the different phases of the bacterial life cycle as 1. lag phase, 2. acceleration phase, 3. exponential phase, 4. retardation phase, 5. stationary phase and 6. phase of decline.

In this work we used *E. coli* K-12. The original K-12 strain was isolated “in the fall of 1922 from the stool of a convalescent diphtheria patient in Palo Alto, California, by [Dr.] Blair. [...] This culture [was] maintained in the department collection in stab cultures of nutrient agar, which [were] transferred from time to time.” [27]. Having started a new life in the lab, strain K-12 started mutating and adapting as it was continuously transferred from stab culture to stab culture. During the following decades, strain K-12 was “cured of the temperate bacteriophage lambda and F plasmid by means of ultraviolet light and acridine orange, respectively” [28] and stored at  $-80^{\circ}\text{C}$  to prevent further mutations.

One of the cured strain was named MG1655, which became the most popular *E. coli* strain after it was the first sequenced *E. coli* K-12 [28]. It possessed enough mutations to be incapable of colonizing the human intestine or survive outside the lab, thus allowing safe handling and low safety standards. Several of these mutations were reverted in Sydney Kustu’s lab [29], yielding strain NCM3722 that grows considerably faster than MG1655 (around 50%) and which was used in this study [7].

## 1.2 Life cycle of a bacterium

Whether *E. coli* grows in the wild or in the lab, cells undergo a life cycle, schematically shown in Fig. 1.2. Definitions of the phases are loose, with no consensus on naming or definitions. For example, while Monod [30] defines stationary phase to be a phase of constant viability after growth, the most common definition in the literature includes the entire life after growth to be stationary phase (i.e. including phase 6. phase of death). While the actual life cycle can show more complexity, the life cycle drawn by Jacques Monod [30] pinpoints to the fact that life for a bacterium is about more than just plain growth, but also about adaptation and survival.

Rather than trying to understand the ecology of bacterial growth with all of its complexity, research has moved towards controlled and well defined experimental procedures that allow to isolate and study phenomena in a reproducible way.

## 1.3 Growth and growth laws

### 1.3.1 Exponential growth

When cells are grown in constant environment for a prolonged period of time, they will eventually reach a state of balanced exponential growth. This steady state, or “balanced” growth [31] is maintained indefinitely, as long as the environment remains unchanged, and is a controlled

way to reach a reproducible state, in contrast to the "exponential phase" of the bacterial life cycle defined in the previous section, which lasts only until nutrient exhaustion. Experimentally this conditions can be achieved by growing cell in synthetic media. Providing the cell with a specific, sufficient set of nutrients at saturating concentrations ensures that during growth the environment does not change.

During balanced exponential growth any constituent of the cell accumulates exponentially within the culture at the same rate. In other words, if  $X(t)$  denotes the total abundance of a specific molecule or a class of molecules in a standard culture volume, e.g., 1 ml of culture, then  $X(t)$  increases as

$$\frac{dX}{dt} = \lambda^* X. \quad (1.1)$$

The steady state growth rate  $\lambda^*$  quantifies the ability of the bacteria to grow in the prescribed environment and can be quantified accurately, easily, and reproducibly [30]. Here and throughout this work, asterisks denote steady state values of the intensive variables. Growth rate  $\lambda^*$  depends on the medium in which cells grow, with different media supporting different growth rates.

### 1.3.2 Growth laws

Remarkably, despite the immense complexity of the underlying regulatory networks, the macromolecular composition of the bacterial cell is found to depend primarily on the growth rate of bacteria in steady state growth, largely independent of the specific nutrients in the growth medium [32–34].

#### Ribosome and associated proteins

One of the major macromolecular components of the cell is the protein synthesis machinery, i.e. ribosomes and their affiliated factors. To keep up with rates of protein synthesis required for growth, the cell modulates its ribosomal content [32, 33, 35–37]. The cellular ribosomal content can be quantified by the mass of ribosomal proteins  $M_{\text{Rb}}(t)$  per total protein mass  $M_{\text{P}}(t)$ . (Here and below, all extensive quantities such as  $M_{\text{Rb}}(t)$ ,  $M_{\text{P}}(t)$  are defined as mass per standard culture volume.) This ratio, denoted as  $\phi_{\text{Rb}}(t) \equiv M_{\text{Rb}}(t)/M_{\text{P}}(t)$ , is referred to as the ribosomal proteome fraction (or simply the ribosomal abundance). In steady exponential growth, there exists a linear relation between the ribosomal fraction and the growth rate [34, 35, 37–39]

$$\phi_{\text{Rb}}^* = \phi_{\text{Rb},0} + \frac{\lambda^*}{\gamma} \quad (1.2)$$

$\phi_{\text{Rb},0}$  is the vertical intercept, and  $\gamma$ , the inverse slope, has been identified molecularly with the maximal translation rate of the ribosome (up to a proportionality constant) [40]. Experimentally, it is convenient to measure the RNA-protein ratio  $r$ , defined as the mass of total RNA per total protein mass, rather than the ribosomal fraction itself. Since the RNA-protein ratio is a well-established proxy for the ribosomal content of a cell, with  $\phi_{\text{Rb}} \approx 0.46 r$  [34], the RNA-protein ratios shown in and are fitted to Eq. (1.2) to yield  $\phi_{\text{Rb},0} = (0.049 \pm 0.002)$  and  $\gamma = (10.9 \pm 0.4) / \text{h}$ . Experimental data is shown in Fig. 1.3.

Apart from ribosomes, *E. coli* requires a multitude of associated proteins, such as elongation factors, for protein synthesis. These proteins are largely co-expressed with ribosomes and can be grouped together with ribosomes as R-proteins [34]. The mass fraction of the R-proteins is about a factor of 1.6 bigger than just ribosomes,  $\phi_{\text{R}} = 1.6\phi_{\text{Rb}}$ . For reasons that will become

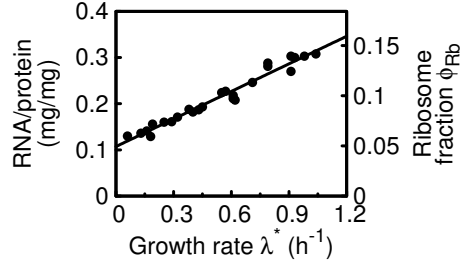


**Figure 1.3: Ribosome abundance.** Total RNA per total protein (left axis) is a proxy for the ribosome content (right axis), with the conversion factor being 0.46 mg RNA per mg ribosomal protein [34]. As a function of steady state growth rate  $\lambda^*$ , the ribosome content increases linearly.

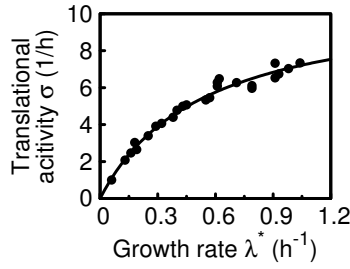


**Figure 1.4: Translational activity.** The translational activity,  $\sigma^*$ , describes the average translation rate and decreases for decreasing growth rate as a direct effect of the ribosome vertical intercept  $\phi_{\text{Rb},0}$ .

apparent in the following chapters, the entire R-sector will be used in Chapter 2, while Chapter 3 focusses on ribosomes only.

### Translational activity

We next introduce the macroscopic efficiency of protein synthesis, which we call “translational activity”  $\sigma$ , defined as

$$\sigma(t) \equiv \frac{J_{\text{R}}(t)}{M_{\text{Rb}}(t)}, \quad (1.3)$$

where  $J_{\text{R}} \equiv dM_{\text{P}}/dt$  is the rate of protein synthesis. The steady state translational activity  $\sigma$ , can be obtained from Eq. (1.2) as  $\sigma^* = \lambda^*/\phi_{\text{Rb}}^*$ , and is shown in Fig. 1.4.

This quantity is to be distinguished from the translation rate of single ribosomes [39, 40]: Translation rates of individual ribosomes can be heterogeneous, e.g. due to inactivity of a fraction of the ribosomes [37, 38]. The translational activity  $\sigma$  corresponds to an *average* translation rate<sup>1</sup>, assuming every ribosome contributes equally to protein synthesis, or as the fraction of actively translating ribosomes, assuming that all active ribosomes translates at a fixed rate. In reality, changes in  $\sigma(t)$  reflect changes in both, the translation rate and the fraction of active ribosomes, hence, the introduction of the term “translational activity” [41].

<sup>1</sup>Let the average mass of an amino acid be  $m_{\text{aa}}$  and the number of amino acid in proteins (in a standard culture volume) be  $N_{\text{P}}$ , then  $J_{\text{R}} = m_{\text{aa}} \cdot dN_{\text{P}}/dt$ . Further let the number of ribosomes (in the same culture volume) be  $N_{\text{Rb}}$ , then  $M_{\text{Rb}} = n_{\text{Rb}} m_{\text{aa}} N_{\text{Rb}}$ , where  $n_{\text{Rb}} = 7536$  is the number of amino acids in a ribosome. Together, Eq. (1.3) gives  $\sigma = (dN_{\text{P}}/dt)/(N_{\text{Rb}} \cdot n_{\text{Rb}})$ . Thus,  $\sigma$  is related to the average translation rate  $(dN_{\text{P}}/dt)/N_{\text{Rb}}$  (in number of aa per time) by the constant,  $n_{\text{Rb}}$ . In Ref. [40] it was shown that in a model with a constant active ribosomal fraction  $f_{\text{active}}$ , the inverse slope  $\gamma$  in Eq. (1.2) is given by the maximal elongation rate by the factor  $f_{\text{active}}/n_{\text{Rb}}$ .

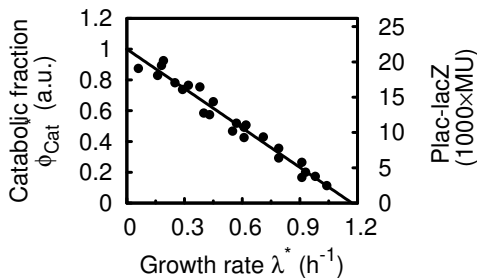


**Figure 1.5: Catabolic protein abundance.** Catabolic protein LacZ is used as a reporter for the expression of all cAMP-CRP controlled catabolic proteins, as established in [42]. The negative linear relation is a direct consequence of proteome partitioning [43].

For steady state growth, we can derive the dependence of the steady-state value of the translational activity,  $\sigma^*$ , on the steady state growth rate,  $\lambda^*$ . From Eq. (1.3) and the steady state relation  $J_R = \lambda^* M_P$  (due to the steady-state property 1.1), it follows that  $\sigma^* = \lambda^* / \phi_{Rb}^*$ . Further inserting the growth law Eq. (1.2), we obtain the following Michaelis-Menten form,

$$\sigma^* = \frac{\lambda^*}{\phi_{Rb}^*} = \frac{\lambda^*}{\phi_{Rb,0} + \lambda^* / \gamma}. \quad (1.4)$$

The translational activity  $\sigma(t)$  is in principle physically limited at  $\gamma$ , the maximal translation rate of the ribosome (up to a proportionality constant). During steady state growth, this limit is approached for fast growth, but only reached in the limit  $\lambda^* \rightarrow \infty$ . During growth transitions the translational activity can transiently increase above the steady state values, as outlined in the notes below. However the limit  $\gamma$  was not reached in any of the experiments investigated in this work.

### Catabolic proteins

The protein synthesis machinery needs to be supplied with the necessary building blocks for the assembly of proteins. Catabolism of carbon substrates provides the carbon skeleton of the building blocks and energy. Here we follow the approach from Ref. [42] and use LacZ as a reporter for the catabolic proteins, by deactivating the lac repressor LacI using isopropyl- $\beta$ -D-thiogalactopyranoside (IPTG), which results in the *lac* promoter being regulated only via the cyclic AMP (cAMP) pathway [42].

Activity of LacZ per mass, denoted as  $\phi_{lacZ}$ , follows the negative linear relation,

$$\phi_{lacZ}^* = \phi_{lacZ,max} \left( 1 - \frac{\lambda^*}{\lambda_C} \right), \quad (1.5)$$

with  $\lambda_C = (1.17 \pm 0.05) / \text{h}$  and  $\phi_{lacZ,max} = (21.8 \pm 0.5) \times 10^3 \text{ MU}$  see Fig. 1.5 Tables B.1 and B.2 for the data.

The regulation via the cyclic AMP (cAMP) pathway acts globally on all catabolic proteins [42], we thus assume LacZ activity reports the relative expression of all catabolic proteins  $Cat,j$ , with sufficiently similar  $\lambda_C$ , but different  $\phi_{Cat,j,max}$ . In general catabolic proteins may have a non-zero offset  $\phi_{Cat,j,0}$  (which is close to zero for lacZ [42]), which does not contribute to flux [43].

$$\phi_{lacZ}^* \propto \phi_{Cat,j,max} + \phi_{Cat,j,0}, \quad (1.6)$$

This relation was specifically confirmed for the Glycerol and Fucose promoters in Ref. [42], which yielded  $\lambda_C = (1.1 \pm 0.05) / \text{h}$  and  $\phi_{\text{Cat},j,0} \approx 0$  for both Glycerol and Fucose catabolic proteins. We thus generally write for all catabolic proteins  $\text{Cat},j$

$$\phi_{\text{Cat},j}^* = \phi_{\text{Cat},j,\text{max}} \left( 1 - \frac{\lambda^*}{\lambda_C} \right) + \phi_{\text{Cat},j,0}, \quad (1.7)$$

The negative correlation Eq. (1.5) occurs when growth is limited by the carbon source and was rationalized using proteome-partitioning arguments [42, 44]. If instead growth is limited by nutrients other than carbon, then the catabolic fraction  $\phi_{\text{Cat}}^*$  would decrease linearly with decreasing growth rate  $\lambda^*$ . This can be written analogously to Eq. (1.2) as

$$\phi_{\text{Cat}}^* = \frac{\lambda^*}{\nu}, \quad (1.8)$$

where  $\nu$ , the inverse slope, is interpreted as the efficiency of carbon uptake. Combining Eqs. (1.5) and (1.8), we can write

$$\nu = \frac{\lambda^*}{\phi_{\text{Cat}}^*(\lambda^*)} = \frac{\lambda^*}{\phi_{\text{Cat},\text{max}} (1 - \lambda^*/\lambda_C)}, \quad (1.9)$$

which gives the corresponding carbon uptake efficiency for cells growing in a medium supporting a given growth rate  $\lambda^*$ . It will further be convenient to define the maximum uptake rate,

$$\mu \equiv \nu \phi_{\text{C},\text{max}} = \frac{\lambda^*}{1 - \lambda^*/\lambda_C}, \quad (1.10)$$

which will play an important role in the kinetic theory described in Chapter 3. It provides a measure of the maximum possible uptake rate in a given medium (supporting a growth rate  $\lambda^*$ ) if catabolic proteins are turned on to the maximum.

Finally we note that the catabolic sector is composed of many proteins, each follows the the growth law of Eq. (1.5). Thus, the abundance of an individual protein  $\text{Cat},j$  is given by

$$\phi_{\text{Cat},j}^* = \phi_{\text{Cat},j,\text{max}} \left( 1 - \frac{\lambda^*}{\lambda_C} \right) + \phi_{\text{Cat},j,0}, \quad (1.11)$$

with the  $\phi_{\text{Cat},j,\text{max}}$  being the maximal expression for that protein.

### 1.3.3 Growth dependency of the proteome

*E. coli* expresses several hundreds of different proteins, about 80 % of these change their expression with growth rate [44]. Thus the remodeling of bacterial proteome goes well beyond ribosomes and catabolic proteins that were discussed above. Despite enormous complexity in the details of the underlying regulatory network, the proteome partitions into several coarse-grained sectors, with each sector's total mass abundance exhibiting positive or negative linear relations with the growth rate [44].

By applying growth limitations and recording the response of individual proteins (either increasing (up), decreasing (down) or remaining constant when growth rate is decreased by a growth limitation), all proteins can be classified to proteome sectors. For three growth limitations, carbon limitation, anabolic limitation and ribosome limitation, six sectors were identified in Ref. [44], see Table 1.1.

The catabolic proteins discussed in Section 1.3.2,  $\phi_{\text{Cat}}$ , are part of the C-sector  $\phi_C$ . The ribosomes discussed in Section 1.3.2,  $\phi_{\text{Rb}}$ , are a dominant part of the R-sector  $\phi_R$ . In addition

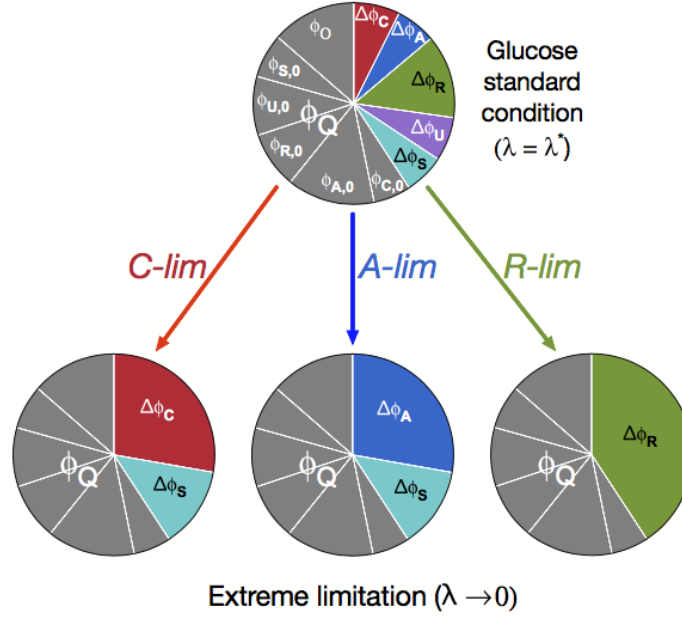


**Figure 1.6: Representation of the proteome responses in pie charts.** The size of each sector is can be represented by slice in a pie chart, with the proteome constraint, Eq. (1.12), meaning that all sectors sum up to a full pie (100%). In this representation by Hui et al. [44], the growth rate-independent component of the protein is represented as  $\phi_Q$  (the entire gray area), which is composed of the growth rate-independent components of the C-, A-, R-, U-, and S-sectors, and the O-sector. The growth rate-dependent part of a sector is labeled as  $\Delta\phi$ , distinguished by the different colors. The colored wedges in the top pie chart show the sizes of these sectors,  $\Delta\phi$ , under the glucose standard condition  $\lambda^* = 0.9/h$ .

**Table 1.1: Proteome sectors.** Upon limitation of carbon uptake, nitrogen uptake or protein synthesis (C-lim., A-lim. and R-lim) proteome composition is modulated. Proteins can be grouped by response of their expression change, yielding the sectors of this table [44].

Name	Symbol	Carbon lim.	Anabolic lim.	Ribosome lim.
C-sector	$\phi_C$	up	down	down
S-sector	$\phi_S$	up	up	down
R-sector	$\phi_R$	down	down	up
A-sector	$\phi_A$	down	up	down
U-sector	$\phi_U$	down	down	down
O-sector	$\phi_O$	constant	constant	constant

to these key proteins, both sectors contain other, co-regulated proteins, among others, ion transport, tricarboxylic acid cycle and locomotion in the C- sector and ribosome associated proteins in the R-sector [44].

The sum of all proteome sectors has to add up to unity

$$\phi_C + \phi_S + \phi_R + \phi_A + \phi_U + \phi_O = 1 \quad (1.12)$$

both during steady state growth and during growth transitions, and the division of the proteome to the individual sectors depends on the environmental conditions and can be understood using a flux balance model [44]. The environmental conditions set the efficiencies of the individual proteome sectors,  $\nu_R$ ,  $\nu_C$ ,  $\nu_A$  and  $\nu_S$ , to produce flux, and flux matching yields the steady

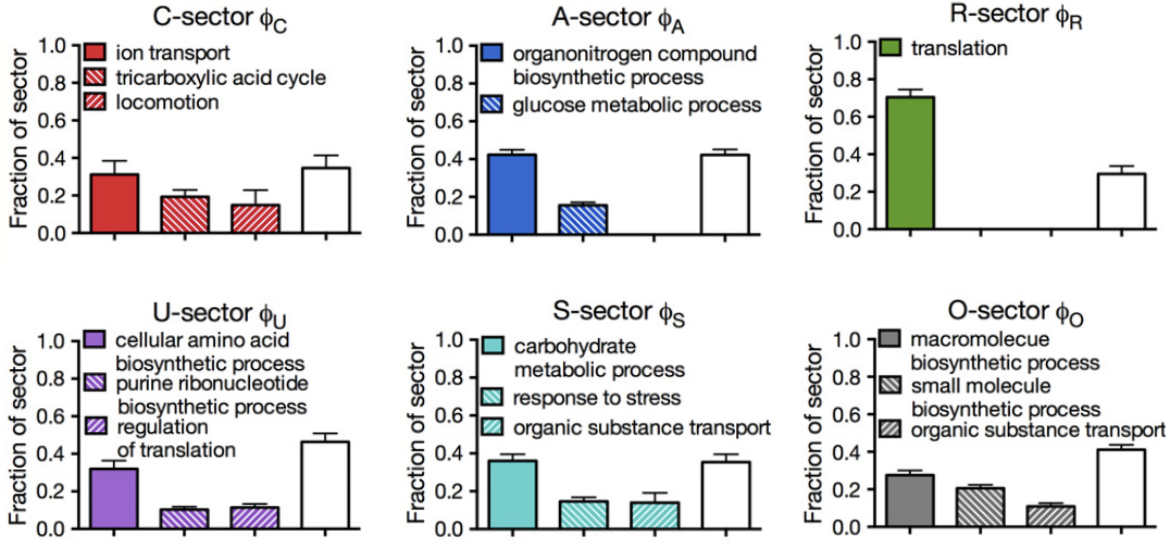


**Figure 1.7: Composition of proteome sectors.** Each bar graph shows the results of the abundance-based Gene Ontology analysis for each of the six sectors, as identified by Hui et al [44]. Each bar indicates the mass fraction the corresponding GO term accounts for within a sector. The empty bar in each graph indicates the remaining fraction of the sector not accounted for by the GO terms listed. Each bar height indicates the mean result and the standard deviation is shown as the error bar.

state proteome partitioning

$$\phi_C^* = \phi_{C,0} + (1 - f) \frac{\lambda^*}{\nu_C}, \quad (1.13)$$

$$\phi_S^* = \phi_{S,0} + f \left( \frac{\lambda^*}{\nu_C} + \frac{\lambda^*}{\nu_A} \right), \quad (1.14)$$

$$\phi_R^* = \phi_{R,0} + \frac{\lambda^*}{\nu_R}, \quad (1.15)$$

$$\phi_A^* = \phi_{A,0} + (1 - f) \frac{\lambda^*}{\nu_A}, \quad (1.16)$$

$$\phi_U^* = \phi_{U,0} + \frac{\lambda^*}{\nu_U}, \quad (1.17)$$

and the steady state growth rate  $\lambda^*$ . The constant factor  $f$  measures the size of the S-sector, which is co-regulated with C- and A-sector during C- and A-limitation, respectively. The proteome partitioning is often visualized in pie-charts, where the size of the slice represents the abundance of the sector, see Fig. 1.6. Each proteome sector has an offset  $\phi_{X,0}$  in addition to its growth dependent part. These offsets sum up to about half of the entire proteome. The origin of this non-zero offset is unclear, as it presents a overcapacity that effectively slows down growth. The composition of the proteome sectors is shown in Fig. 1.7.

In this work, we only apply C-limitation, thus we group all sectors increasing or decreasing in C-limitation together into  $\phi_{C\uparrow}^*$  and  $\phi_{C\downarrow}^*$

$$\phi_{C\uparrow}^* = \phi_C^* + \phi_S^*, \quad (1.18)$$

and

$$\phi_{C\downarrow}^* = \phi_R^* + \phi_A^* + \phi_U^*. \quad (1.19)$$

For consistency of the notation we introduce  $\phi_{C-}^* = \phi_O^*$ , which shows no response to C-limitation.

In steady state growth, the two reporters introduced in Section 1.3.2,  $\phi_{LacZ}^*$  and  $\phi_{Rb}^*$ , from Eqs. (1.2) and (1.5) are co-regulated with  $\phi_{C\uparrow}^*$  and  $\phi_{C\downarrow}^*$ . Since  $\phi_{LacZ}^*$  and  $\phi_{Rb}^*$ , and  $\phi_{C\uparrow}^*$  and  $\phi_{C\downarrow}^*$  depend linearly on growth rate, we can derive a linear relation between the reporters  $\phi_{LacZ}^*$  and  $\phi_{Rb}^*$  and the proteome sectors  $\phi_{C\uparrow}^*$  and  $\phi_{C\downarrow}^*$ ,

$$\phi_{C\downarrow}^* = a_{C\downarrow} + b_{C\downarrow}\phi_{Rb}^*, \quad (1.20)$$

and

$$\phi_{C\uparrow}^* = a_{C\uparrow} + b_{C\uparrow}\phi_{LacZ}^*. \quad (1.21)$$

The constants are chosen such they match the measured proteome sectors Eqs. (1.13) to (1.17) with the reporter sizes in Eqs. (1.2) and (1.5).

## 1.4 Stationary phase and decline of viability

When nutrients become limiting or environmental condition becomes toxic, growth stops and cells enter a "stationary phase". Microbes have developed a multitude of strategies to cope with starvation that help them to survive from days to years and millenniums. While microbes like *Bacillus subtilis*, a soil bacterium, can develop spores to survive, others like *Escherichia coli* are less fortunate. Without a sporulation program, a slow decay of viability of these microbes sets in soon after starvation [45–48]. In comparison to the well studied exponential phase, the stationary phase and decline of viability is "*far less studied [...], which leaves many questions regarding basic bacterial physiology unanswered*", as Bergkessel and coworkers noted in a recent review article [49]. The approaches that have been used to study bacterial cells in non-growing states are manifold, and the resulting findings are similarly diverse and often specific to the particular experimental choices.

### 1.4.1 RpoS: the primary stationary phase regulator

The central sigma factor RpoS is one of the best studied systems in stationary phase, and its effects are seen through many different experimental studies [50, 51]. RpoS is a subunit of RNA polymerase that acts as the master regulator of the general stress response in *E. coli*, directly controlling the expression of around 40 genes [50, 52]. RpoS controlled genes are often associated with stress response, such as DNA damage repair (*iraD* [53]), peroxide catalases (*ahpC*, *katE*, *katG* [54, 55] and several other small proteins [52]), protectants of osmotic stress (*otsBA* (synthesizes osmoprotectant trehalose) or lipoproteins *osmB* and *osmE* [52, 56]) and knock-out strains show increased mortality under stress conditions, such as oxidative stress or heat shock [50]. Expression of RpoS due to one kind of stress, in turn, leads to cross protection against other stresses, due to the global nature of the regulation [57].

Other genes regulated by RpoS control cell size (*ftsQAZ* and *bolA*), biofilm production (*Curli* [58]) or secondary metabolism [52]. Even RpoS-dependent programmed cell death was reported in the literature [59]. Mutations of the stationary phase regulator RpoS are commonly seen in evolution experiments [60, 61], yet counterintuitively, often these mutantion knock-out RpoS.

### 1.4.2 Exponential decline of viability

It appears to be commonly accepted that microbes die exponentially during stationary phase, even the bacterial life cycle drawn by Jacques Monod in 1949 and shown in Fig. 1.2, depicts the phase of decline of viability as an exponential function. On the other hand, the number of

experiments showing an exponentially decaying viability is relatively small [48, 62, 63], and the majority of reports shows more complex behavior [14, 46, 47, 60, 64–66]. It remains thus unclear under which circumstances cells die exponentially, and what this implies for the physiology of bacteria remains one of the major puzzles of microbiology. The simplicity of the exponential decay, however, is intriguing as it implies that the underlying processes are potentially simple and readily understandable, too. We will study the origin of the exponential decay in Chapter 4, in order to obtain a basic insight of bacterial physiology in starvation.



# Chapter 2

## The benefit of a proteome reserve

### 2.1 Introduction

The expression of useless proteins is a major burden for fast growing bacteria [34]. Paradoxically, recent characterization of the proteome of *E. coli* found many proteins expressed in excess of what appears to be optimal for exponential growth, as discussed Section 1.3.3. Here we quantitatively investigate the possibility that this overcapacity is a reserve kept by cells to quickly meet demand upon sudden changes in growth conditions. For cells exposed to repeated famine-and-feast cycles, we derive a simple relation between the duration of feast and the allocation of the ribosomal protein reserve to maximize the overall gain in biomass during the feast.

### 2.2 The R-protein overcapacity

Exponentially growing bacteria adapt their proteome composition to the medium they grow in [32, 34, 42, 44, 67–69], as discussed in Chapter 1. Recent research has established that the coarse-grained characteristics of proteome composition varies mostly with the growth rate of the culture according to the mode of growth limitation (e.g., carbon limitation vs antibiotic inhibition), and is insensitive to the details of the growth condition [34, 44]. A prominent example of the coarse-grained proteome sectors is the ribosome-affiliated “R-sector”, which includes ribosomes and the affiliated translation machinery, collectively referred to as R-proteins, discussed in Section 1.3.3, and which is responsible for protein synthesis. Its proteome fraction  $\phi_R$  is defined as the total mass of R-proteins  $M_R$  per total protein mass  $M$ , i.e.,  $\phi_R \equiv M_R/M$ .

For different nutrients giving different steady-state growth rates  $\lambda^*$ , the R-sector proteins occupy different shares of the proteome through the “growth laws” discussed in Section 1.3.3:

$$\phi_R^* = \phi_{R,0} + \frac{\lambda^*}{\nu_R}. \quad (2.1)$$

Here and below, steady state quantities are indicated by asterisks (or indices “i” or “f” if they correspond to initial or final steady states of a growth shift), to distinguish them from dynamic variables. The inverse slope  $\nu_R$  of this linear relationship, when converted to appropriate units, compares well with the maximum *in vitro* elongation rate by the ribosomes, and is referred to as the “translational capacity” of the cell [34]. In fact, if every ribosome were engaged in translation at the maximal rate, one would expect a protein synthesis flux  $\lambda^*M = \nu_R M_R$ . Thus  $\phi_{R,\min}^* = \lambda^*/\nu_R$  is the minimal ribosomal fraction needed to support exponential cell growth at a rate  $\lambda^*$ . Comparison of the growth law, Eq. (2.1), with this minimal demand shows that the R-sector proteins are expressed in excess by an amount  $\phi_{R,0}$ , i.e., an overcapacity, which equals the y-intercept of the growth law, Eq. (2.1). However, expressing proteins beyond the

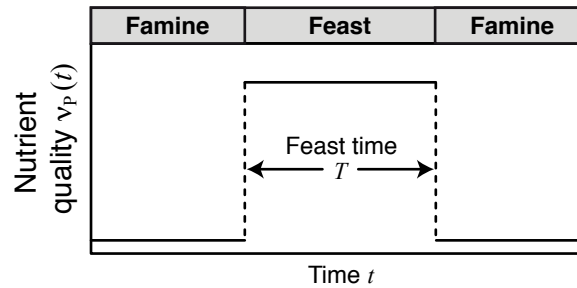


**Figure 2.1: Famine-to-feast transitions.** As rich nutrients are introduced into the environment, bacterial cells undergo a nutritional shift from a poor to rich medium, speeding up their growth; then, nutrients get depleted after a “feast time”  $T$ . If the feast time is short, repeated transitions between famine and feast will select for quickly adapting cells

minimal amount demanded for growth reduces the growth rate by a proportional amount, as has been validated quantitatively for specific over-expression systems [34]. Since  $\phi_{R,0}$  represents an amount of over-expressed R-proteins, it represents a negative effect on steady state growth.

This apparent sub-optimality in ribosomal protein allocation has been noted in the past [40, 70–73]. It was speculated that this ribosome overcapacity is an investment which becomes advantageous during growth upshift [70, 74]. Adaptation following abrupt changes in nutrient conditions, e.g., where a good nutrient source is added to the growth medium during exponential growth on a poor substrate, is conveniently studied in the laboratory [6, 67, 69, 75, 76] and occurs widely in natural ecological context [77]. In this chapter, we quantitatively connect the overcapacities in R-sector to the famine-to-feast transition encountered in natural environments such as the mammalian gut: Rich nutrients are provided for a limited period of time (“feast time”), e.g., a few hours following meals, and quickly exhausted outside of this time window; see Fig. 2.1. We develop a theory to capture the growth transition kinetics and predict the extent by which growth speeds up during upshift for different amount of R-sector overcapacity. The predicted adaptation dynamics is probed experimentally, and the predicted dependence on the pre-shift R-sector content is validated by varying pre-shift growth. Since the R-sector speeds up growth during transition while slowing down growth in the long run, we interpret them as a “reserve”, kept by the cell to meet increased demand more quickly in an improved environment. Our theory allows us to compute the optimal amount of this reserve, i.e. the amount maximizing the overall biomass accumulated throughout the course of the shift, for different duration of feast time and growth media.

### 2.3 A kinetic model for famine to feast upshifts

In this section we analyze a simple kinetic model to connect protein synthesis, and thus growth, to the abundance of ribosomal proteins during nutrient upshift. Cell growth originates from protein synthesis by the ribosomes and affiliated machinery (the R-proteins), and the total rate of protein synthesis  $dM/dt$  is proportional to the R-proteins mass  $M_R$  as

$$\frac{dM}{dt} = \sigma_R M_R \quad (2.2)$$

Here,  $\sigma_R$  is the “translational capacity”, which measures the average rate of protein synthesis per unit of R-protein mass (in contrast to the “translational activity”  $\sigma$  introduced in Chapter 1 which measures the average rate of protein synthesis per ribosome). Expressing  $dM/dt$  in terms of  $\phi_R \equiv M_R/M$ , Eq. (2.2) becomes,

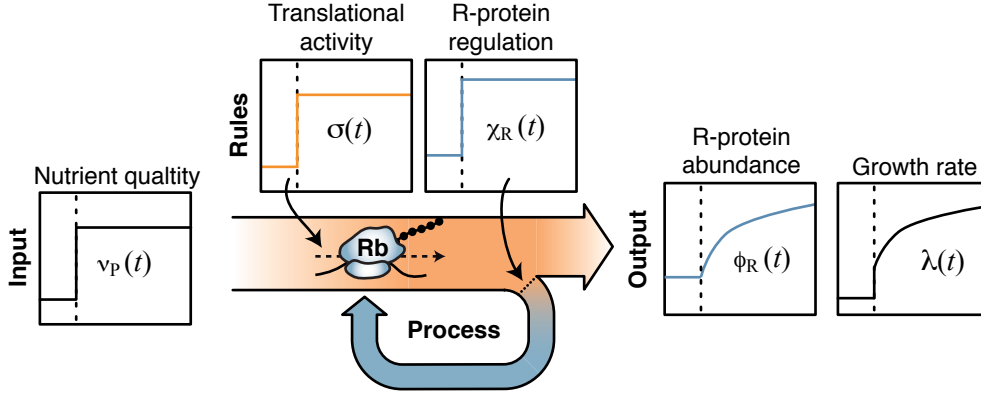


**Figure 2.2: A kinetic model for upshifts to feast.** As *input*, the model uses the nutrient quality  $\nu_P$ . Upon a switch of nutrient quality from poor to good, the *process* (protein synthesis and ribosome synthesis) adapts according to pre-defined *rules*: both the translational activity  $\sigma_R$  and the R-protein regulatory function  $\chi_R$  go from their initial to their final values in a step-function. The *output* of the model is the R-protein abundance  $\phi_R$  and the growth rate after a shift up. This model is agnostic to the molecular origins of the regulation, but rather sets the rules to follow closely the experimental observations [39, 78].

$$\frac{dM}{dt} = \sigma_R \phi_R M \quad (2.3)$$

In steady state, the mass fraction  $\phi_R^*$  is set by the growth law, Eq. (2.1). In changing environments, instead,  $\phi_R(t)$  varies with time due to modulation in the rate of R-sector protein synthesis,  $dM_R/dt$ , which is controlled by  $\chi_R$ , the fraction of total protein synthesis flux allocated to the R-proteins, i.e.,  $dM_R/dt = \chi_R dM/dt$ . When combined with Eq. (2.2), we have

$$\frac{dM_R}{dt} = \sigma_R \chi_R M_R \quad (2.4)$$

which is a closed equation for  $M_R$  subjected to the allocation  $\chi_R$ . The kinetics of  $\phi_R(t)$  can be obtained by combining Eqs. (2.3) and (2.4), yielding a logistic equation

$$\frac{d\phi_R}{dt} = \sigma \phi_R (\chi_R - \phi_R) \quad (2.5)$$

In balanced growth, where all cellular components increase at the same rate, we have  $\chi_R^* = \phi_R^*$ , with the latter given by the growth law Eq. (2.1). We focus here on the situation where cells experience a sudden shift from famine to feast, see Fig. 2.1. During the shift, cells transition between two different steady states: we will denote these states as “initial” and “final”, with the corresponding quantities indicated by the labels “i” and “f”, respectively. The cells are initially in balanced growth with growth rate  $\lambda_i$ , in a poor nutrient source. At the time of the upshift, rich nutrients are added and, as a consequence, both  $\sigma$  and  $\chi_R$  vary with time during growth transitions. A full treatment of the transition kinetics requires equations for  $\sigma(t)$  and  $\chi_R(t)$ , which will be discussed in the Chapter 3.

Instead, for transition from poor to rich nutrient quality, see Fig. 2.2 (*input*), it is known [39, 78] that the translational efficiency quickly increases from the initial value  $\sigma_i$  to its final steady state value in the feast condition,  $\sigma_f$ . Also, the fractional rate of ribosome accumulation,  $dM_R/dt/M_R = \sigma \chi_R$  as given by Eq. (2.4) is found [39, 78, 79] to increase immediately to the post-shift value, thus implying that the R-protein synthesis fraction  $\chi_R$  quickly shifts from  $\chi_R^i$  to  $\chi_R^f$ . We implement this knowledge as *rules*, see Fig. 2.2, that are agnostic of the underlying

mechanism. Concretely, we assume an instantaneous change of  $\sigma$  and  $\chi_R$  from their initial to final values (see Fig. 2.2),

$$\sigma_R(t) = \begin{cases} \sigma_{R,i}^*, & t < 0 \\ \sigma_{R,f}^*, & t \geq 0, \end{cases} \quad (2.6)$$

and

$$\chi_R(t) = \begin{cases} \chi_{R,i}^*, & t < 0 \\ \chi_{R,f}^*, & t \geq 0. \end{cases} \quad (2.7)$$

Under these conditions Eq. (2.5) can be solved analytically, and the R-sector protein fraction  $\phi_R(t)$  increases towards its final value as a logistic function (see Eq. (A.7) in Appendix A) and Fig. 2.2 (*output*). The instantaneous growth rate  $\lambda(t) \equiv d \log M / dt$ , is given via Eq. (2.2) by  $\lambda(t) = \sigma(t)\phi_R(t)$ . From the solution for  $\phi_R(t)$ ,  $\lambda(t)$  is predicted to switch from the pre-shift value,  $\lambda_i$  for  $t < 0$ , to the form

$$\lambda(t) = \lambda_0 + \frac{\lambda_f - \lambda_0}{1 + (\lambda_f/\lambda_0)/(e^{\lambda_f t} - 1)}, \quad t \geq 0 \quad (2.8)$$

This solution is the central output of the theory, see Fig. 2.2 (*output*). The relative increase in mass after a time  $t$  from the upshift is obtained by integrating Eq. (2.8) giving:

$$\frac{M(t)}{M(0)} = 1 + \frac{\lambda_0}{\lambda_f} (e^{\lambda_f t} - 1), \quad t \geq 0 \quad (2.9)$$

## 2.4 R-proteins abundance determines transition kinetics to feast

As depicted in Fig. 2.2 (*output*), Eq. (2.8) describes a transition kinetics featuring an instantaneous jump of the growth rate  $\lambda(t)$  from  $\lambda_i$  to a larger value  $\lambda_0$  at the instant of upshift, followed by a slow adaptation to the final growth rate  $\lambda_f$ . This jump, whose magnitude is given by the difference  $\Delta\lambda \equiv \lambda_0 - \lambda_i$ , characterizes the acceleration in transition kinetics from the simple adaptation of  $\lambda(t)$  from  $\lambda_i$  to  $\lambda_f$  according to a logistic equation. As explained in detail in Appendix A, the jump from  $\lambda_i$  to  $\lambda_0$  corresponds to a sudden increase in the efficiency of ribosome utilization (from  $\sigma_i$  to  $\sigma_f$ , Fig. 2.2 (*rules*, orange line)). The second, slower, phase reflects the progressive accumulation of ribosomes ( $\phi_R(t)$ , blue line in Fig. 2.2 (*output*), from  $\phi_R^i$  to  $\phi_R^f$ ), while keeping the translational efficiency at the post-shift value  $\sigma_R^f$  [39, 79]. Within the kinetic model, the value of  $\lambda_0$  depends on the pre-shift and post-shift R-sector protein fractions, as well as the final growth rate as

$$\lambda_0 = \phi_R^i \sigma_f = \phi_R^i \frac{\lambda_f}{\phi_R^f} \quad (2.10)$$

In particular, Eq. (2.10) shows that the parameter  $\lambda_0$ , which captures the acceleration in transition kinetics as explained above, is determined solely by steady state properties of the initial and final states. Equation (2.10) can be therefore directly tested by comparing the values of  $\lambda_0$ , extracted from upshift experiments to the known R-protein abundance as a function of the growth rate.

We performed a series of upshifts from defined medium (with pre-shift growth rate  $\lambda_i$  ranging between 0.06/h to 0.91/h; to rich medium (LB + glucose, 2.45/h). We show in Fig. 2.3 the growth kinetics for three representative experiments starting from medium with aspartate ( $\lambda_i = 0.06/h$ ), glycerol ( $\lambda_i = 0.68/h$ ) and glucose ( $\lambda_i = 0.91/h$ ). Before the nutrient shift, protein

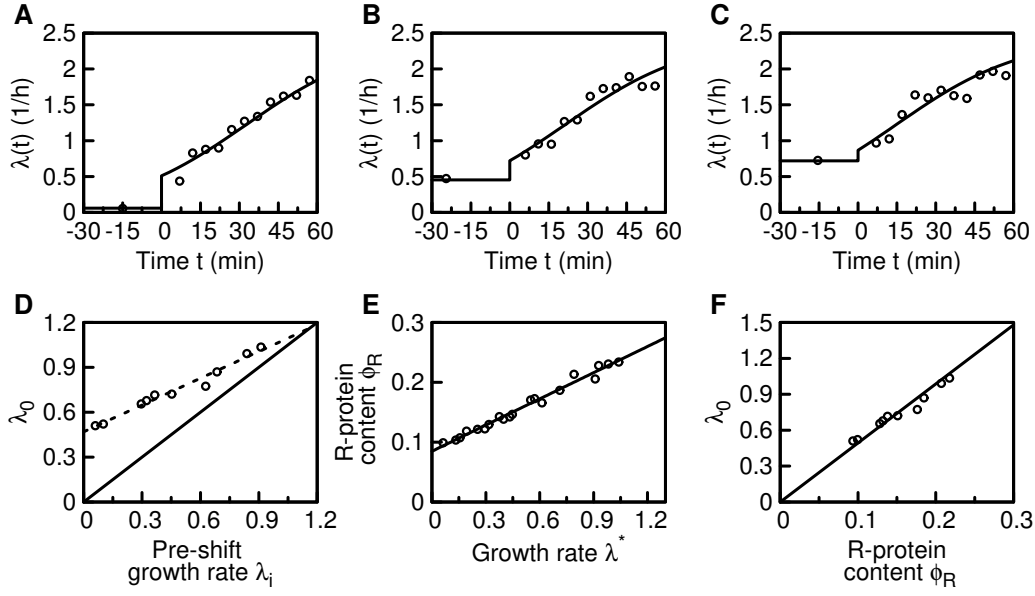


**Figure 2.3: The kinetics in upshifts to rich media depend on the pre-shift ribosomal content.** (A-C) Examples of shifts from poor to rich media. Cells in exponential phase in carbon minimal media: A: aspartate,  $\lambda_i = 0.06$ /h; B: mannose  $\lambda_i = 0.44$ /h, C glycerol,  $\lambda_i = 0.68$ /h undergo a nutrient shift to rich media (LB + glucose,  $\lambda_f = 2.45$ /h) at time  $t = 0$ . Solid lines is the solution of the instantaneous model, Eq. (2.8), using the saltatory increase of growth rate  $\lambda_0$  used as fitting parameter. (D) Experimental values of  $\lambda_0$  extracted from ten independent upshifts (three from panels A to C, seven are shown in Fig. A.1) from minimal media with different carbon sources to the same post-shift media, plotted against the pre-shift growth rate  $\lambda_i$ . For very poor pre-shift nutrients ( $\lambda_i \approx 0$ ),  $\lambda_0$  reaches 0.47/h (y-intercept of the dashed line). The solid line shows the diagonal  $\lambda_0 = \lambda_i$ , i.e. no saltatory increase, for reference. (E) R-protein content  $\phi_R$  follows a mostly linear relation with growth rate (grey line). The y-intercept is interpreted in this work as the ribosome reserve. (F) When plotted against each other,  $\lambda_0$  and  $\phi_R$  show a linear dependence. The solid line is the theoretical prediction from Eq. (2.10), computed using the experimentally measured  $\lambda_f = (2.45 \pm 0.05)$ /h and  $\phi_R^f = (49.0 \pm 1.3)\%$ .

mass (approximately proportional to the optical density of the sample, see Fig. B.9, accumulates exponentially at the pre-shift rates  $\lambda_i$  as indicated by the dashed lines Fig. 2.3. After the shift at time  $t$  (dotted line) the rates of mass accumulation increase as the cells adapt to the new growth medium. The growth curves for 7 other shifts are shown in Fig. A.1. We fitted the observed growth curves to Eq. (2.9), with  $\lambda_0$  being the only fitting parameter. The results are shown as lines with the values of  $\lambda_0$  listed in Table A.1. The instantaneous growth rate  $\lambda(t)$ , computed empirically as the discrete time derivative of  $\log M(t)$  for the shifts in Figs. A.1 and 2.3, are shown by the symbols in Figs. A.1 and 2.3, respectively. The data exhibit substantial scatter due to the derivatization; however, the general trends in the data are well captured by the lines, generated by Eq. (2.8), using the values of  $\lambda_0$  obtained from the growth curves.

Next we plotted the values of  $\lambda_0$  obtained for each shift (Table A.1) against the pre-shift growth rate  $\lambda_i$ , see Fig. 2.3D, it shows a linear relation ( $r^2 = 0.973$ ), intercepting for very poor pre-shift growth media close to 0.47/h. Since the difference  $\Delta\lambda = \lambda_0 - \lambda_i$  describes the acceleration in transition kinetics as described above we also show  $\lambda_0 = \lambda_i$  for comparison. The origin of the linear relationship between  $\lambda_0$  and  $\lambda_i$  lies in the growth law Eq. (1.2): According to Eq. (2.10), the model predicts that  $\lambda_0$  is directly proportional to the R-protein content before the shift, i.e.  $\lambda_0 \propto \phi_R^i$ , for shift going to the same post-shift medium. The ribosomal content  $\phi_R$  is itself a linear function of due to the growth law Eq. (1.2). Indeed, the empirical relation between  $\lambda_0$  and  $\phi_R^i$ , Fig. 2.3, are in excellent agreement with the prediction (black line) based on Eq. (2.10) using the measured measured  $\lambda_f$  and  $\phi_R^f$ , with a maximum deviation of less than

15%. This result thus confirms that the ribosome abundance in the pre-shift medium is the major factor determining the adaptation kinetics to rich medium.

We now focus on the role of the overcapacity  $\phi_{R,0}$  in the dynamics of cell growth during an upshift. Since  $\lambda_0$  depends on the R-sector protein abundance in the pre- and post-shift conditions according to Eq. (2.10), the overcapacity  $\phi_{R,0}$  directly affects the adaptation kinetics. At steady state, the R-protein levels are set by its growth law given by Eq. (1.2), which can be alternatively written as  $\phi_R^* = (\lambda^* + \lambda_R)$ , where we introduced the "R-sector offset"  $\lambda_R$ , with a value  $\lambda_R \approx 0.42/\text{h}$  for our strain (see Fig. 1.3). Specializing to the case of shift from the very slow to very fast growth, where  $\phi_R^i = \phi_R (\lambda_i \ll \lambda_R) \approx \lambda_R/\nu_R$  and  $\phi_R^f = \phi_R (\lambda_f \gg \lambda_R) \approx \lambda_f/\nu_R$ , Eq. (2.10) becomes

$$\lambda_0 \approx \lambda_R = \nu_R \phi_{R,0} \quad (2.11)$$

The value of  $\lambda_R \approx 0.42/\text{h}$  compares well to the empirical value of  $\lambda_0 = 0.47/\text{h}$  obtained when extrapolating  $\lambda_0$  to zero pre-shift growth rate, Fig. 2.3D.

This expression has an intuitive explanation: when shifting to rich media, the cell has an immediate boost in protein synthesis due to the "excess" ribosomes,  $\phi_{R,0}$ , being engaged in translation at the maximum activity,  $\nu_R$ . Thus, the ribosome overcapacity is quickly activated during these nutritional shifts, effectively acting as a reserve and playing a crucial role in speeding up the transition from famine to feast.

## 2.5 Fitness landscape for transitions from famine to feast

For *E. coli*, remarkably robust empirical laws relate the growth rate and the proteome composition [34, 43]. Such laws can be quantitatively captured by a simple model of proteome allocation [34], relating steady state growth rate and the abundance of the R-sector in terms of only a few parameters (see Section 1.3.2). By jointly using the adaptation kinetics and the protein allocation model, we can predict how strains with different overcapacities  $\phi_{R,0}$  (and thus different offsets  $\lambda_R$ ) perform when they experience a sudden increase in the nutrient quality from famine to feast.

First of all, the overcapacity  $\phi_{R,0}$  reduces the maximum possible growth rate during feast. According to the established proteome allocation model [34], the maximum size of the R-sector is limited to a ceiling of  $\phi_R^{\max} \approx 48\%$  of the proteome. This value is below 100% because of the expression of other housekeeping proteins. Because of Eq. (1.2), growth rate is maximal (e.g., when given the best possible nutrient) when  $\phi_R = \phi_R^{\max}$ , attaining a value  $\lambda_{\max}$  given by:

$$\lambda_{\max} \equiv \nu_R (\phi_R^{\max} - \phi_{R,0}) = \lambda_R^{\max} - \lambda_{R0} . \quad (2.12)$$

Here  $\lambda_R^{\max} \equiv \nu_R \phi_R^{\max} \approx 2.9/\text{h}$  is the maximal growth rate possible if there is no R-sector overcapacity (i.e.,  $\phi_{R,0} = 0$ ). Equation (2.12) shows that, while the R-sector overcapacity provides a boost to the adaptation kinetics (Eq. (2.11)), its protein cost reduces the steady state growth rates by reducing  $\lambda_{\max}$  by an amount given by the offset  $\lambda_{R0}$ .

### 2.5.1 Fitness landscape for different proteome reserves

Next we consider the situation in which cells with a specific value of  $\phi_{R,0}$  are shifted from a poor growth medium (barely growing, with  $\lambda_i \rightarrow 0$ ) to the best possible post-shift medium ( $\lambda_f = \lambda_{\max}$ ), with the latter lasting for a time  $T$  (the "feast time") after the shift as sketch in Fig. 2.1. We characterize the growth of these cells by computing the fitness  $W(T) \equiv M(T)/M(0)$ , defined as as the mass increase during the feast time  $T$ , as given by Eq. (2.9); see Section A.2

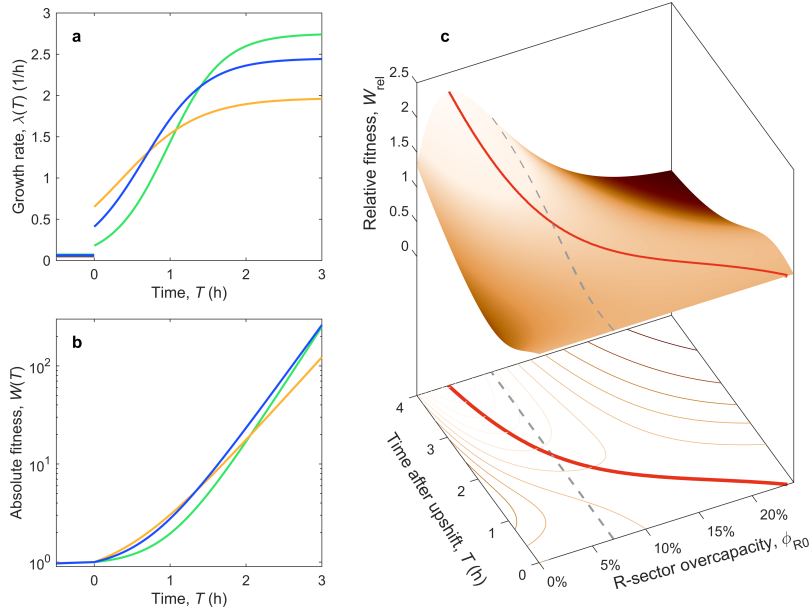


**Figure 2.4: Fitness landscape for different proteome reserves.** (A) Bacterial strains with different overcapacities  $\phi_{R,0}$  perform differently in upshifts from poor to rich media. Here we show three strains with different overcapacity (2% in green,  $\phi_{R,0}^{\text{WT}} = 7\%$  in blue, 15% in yellow) shifting from a poor nutrient source to a rich media. Strains with large overcapacities grow faster shortly after the upshift to rich media (at  $t = 0$ ), while strains with small overcapacities are advantaged in the long run. (B) Absolute fitness  $W(T) = M(T)/M(0)$ , Eq. (2.9), obtained by integrating the three instantaneous growth rates  $\lambda(T)$  shown in panel A. (C) Relative fitness landscape for slow ( $\lambda_i \rightarrow 0$ , corresponding to aspartate minimal media) to fast ( $\lambda_f \rightarrow \lambda_{\text{max}}$ , corresponding to rich media) growth transitions, as a function of the R-sector proteome overcapacity  $\phi_{R,0}$  and feast time (time after upshift)  $T$ . Relative fitness  $W_{\text{rel}}(\phi_{R,0}, T)$  is defined as the absolute fitness  $W$ , normalized by the average fitness of all other strains considered. Strains with large overcapacities ( $\gtrsim 10\%$ ) are heavily penalized for large feast times ( $T \gtrsim 3$  h). Strains with low overcapacities ( $\phi_{R,0} \lesssim 3\%$ , or  $\lambda_{R0} \lesssim 0.15/\text{h}$ ) are disadvantaged even many hours after the instant of the upshift, while the ones with large overcapacities are outpaced after a short amount of time. The dashed line indicates the overcapacity of the wild type strain, while the red line shows the optimal overcapacity  $\phi_{R,0}^{\text{opt}}(T)$  which maximizes  $W(\phi_{R,0}, T)$  for fixed  $T$ .

for analytical expressions of the fitness in terms of parameters of the steady state laws, Eqs. (1.2) and (2.12). We show in Fig. 2.4A & B the predicted upshift kinetics, for three different values of ribosome overcapacities: The value of our wild-type strain  $\phi_{R,0}^{\text{WT}} = 7\%$  (blue line), one below at  $\phi_{R,0} = 2\%$  (green line), and one above at  $\phi_{R,0} = 15\%$  (orange line). The strain with low overcapacity (in green) performs poorly compared to the other two strains if the feast time is short (for  $T < 3$  h, Fig. 2.4), since it is trapped in the slow recovery phase due to its small jump in growth rate,  $\lambda_0$  (Fig. 2.4A). Vice versa, the strain with large overcapacity (orange) initially performs well due to the large growth rate jump  $\lambda_0$  (Fig. 2.4A), but it is outperformed by the other strains in the long run (for  $T > 1.5$  h, Fig. 2.4B), since its final growth rate  $\lambda_f = \lambda_{\text{max}}$  is significantly reduced (Fig. 2.4A) due to its large ribosome overcapacity as given by Eq. (2.12). The wild type strain, with its intermediate value of  $\phi_{R,0}$ , performs well for the range of feast time shown: in fact, the corresponding fitness  $W(T)$  (blue line in Fig. 2.4B) is close to the orange line for short times (less than one hour) and to the green line for longer times (around three hours).

We show in Fig. 2.4C the “fitness landscape” for the same shift as in Fig. 2.4A & B, as a function of the feast time  $T$  and the overcapacity  $\phi_{R,0}$ . For the ease of display, we show a relative fitness  $W_{\text{rel}}(T, \phi_{R,0}) \equiv W^{\text{WT}}(T, \phi_{R,0})$  obtained by normalizing the fitness  $W(T, \phi_{R,0})$  by its average  $W(T)$  across different  $\phi_{R,0}$  at a given feast time. We also show as a red line the optimal overcapacity  $\phi_{R,0}^{\text{opt}}(T)$ , i.e. the overcapacity that maximizes the fitness  $W$  for the

corresponding feast time  $T$ . The overcapacity of the wild type strain is shown as dashed blue line for comparison. At time  $T = 0$ , all strains have the same fitness,  $W_{\text{rel}} = 1$ . For feast times less than one hour, the best performing strains have large overcapacity, with  $\phi_{\text{R},0}^{\text{opt}} > 10\%$ ; however, their corresponding fitness values  $W_{\text{rel}}^{\text{opt}}$  are not so significant, i.e., they are not so much better than other values of the overcapacity  $\phi_{\text{R},0}$ , because cellular growth is limited by the short time interval elapsed from the instant of the upshift. As time passes by, strains with smaller overcapacities outcompete the others; the strain with vanishing offset is optimal for steady state growth (recovered in the limit  $T \rightarrow \infty$ ). A very simple relation between  $\phi_{\text{R},0}^{\text{opt}}$  and the feast time  $T$  can be derived when  $T$  is a few fold larger than  $1/\lambda_{\text{max}}$  (corresponding approximately to  $T > 1$  h):

$$\nu_{\text{R}}\phi_{\text{R},0}^{\text{opt}} \equiv \lambda_{\text{R}}^{\text{opt}} \approx 1/T, \quad (2.13)$$

i.e., the optimal offset  $\lambda_{\text{R}}^{\text{opt}}$  is simply given by the reciprocal of the feast time  $T$ . A comparison of this relation with Eq. (2.11) shows that the optimal jump in growth rate at the from poor to rich media ( $\lambda_0 \approx \Delta\lambda$ ) is given by  $\lambda_0 \approx \Delta\lambda \approx 1/T$ . Based on Eq. (2.13), our wild-type strain performs optimally in upshifts to rich media characterized by a feast time  $T = 1/\lambda_{\text{R}0}^{\text{WT}}$  that is between 2 and 3 hours.

The fitness landscape shown in Fig. 2.4C is for shifts from very poor growth medium (i.e., famine, characterized by  $\lambda_i \rightarrow 0$ ) to very rich medium (i.e. feast,  $\lambda_f \rightarrow \lambda_{\text{max}}$ ). This analysis can be extended to pre-shift medium supporting generic pre-shift growth rates. To do so, we need to describe the growth rate of strains with arbitrary  $\phi_{\text{R},0}$  in different medium. We will characterize the quality of the medium by the growth rate it supports for the wild-type strain, denoted as  $\lambda_{\text{WT}}^*$ . It was shown by Scott et al. [34] that the expression of useless proteins reduced the steady state growth rate in a linear manner, with growth arrest occurring when the useless protein expressed reached  $\phi_{\text{R}}^{\text{max}}$ . Assuming that the ribosome overcapacity  $\phi_{\text{R},0}$  to exert the same effect on steady state growth rate as a generic useless protein, we expect the growth rate  $\lambda^*$  to be reduced by  $\phi_{\text{R},0}$  also in a linear way in the same nutrient condition. With respect to the growth rate of the wild type strain ( $\lambda_{\text{WT}}^*$ ) with overcapacity  $\phi_{\text{R},0}^{\text{WT}}$ , we can write this linear relation as

$$\lambda^*(\phi_{\text{R},0}) = \lambda_{\text{WT}}^* \frac{\phi_{\text{R}}^{\text{max}} - \phi_{\text{R},0}}{\phi_{\text{R}}^{\text{max}} - \phi_{\text{R},0}^{\text{WT}}}. \quad (2.14)$$

This expression allows us to compute the steady state growth rates corresponding to different combinations of nutrient sources (which affect  $\lambda_{\text{WT}}^*$ ) and ribosome overcapacity  $\phi_{\text{R},0}$ .

### 2.5.2 Fitness landscape for different upshifts

We show in Fig. 2.5A the optimal overcapacity  $\phi_{\text{R},0}^{\text{opt}}(T)$  with different feast time  $T$ , for upshifts from different pre-shift growth medium (characterized by the respective growth rates of the wild type,  $\lambda_i^{\text{WT}}$ ) to rich medium. The red line corresponds to shift from a very poor pre-shift medium (aspartate,  $\lambda_i^{\text{WT}} \approx 0.06/\text{h}$ ) to rich medium, and the dashed line shows the wild type overcapacity  $\phi_{\text{R},0}^{\text{WT}}$ . As the quality of the pre-shift medium improves (in the order of orange, green and light blue), the value of  $\phi_{\text{R},0}^{\text{opt}}(T)$  decreases more and more rapidly for increasing  $T$ . The reason is that as pre-shift growth rate increases, the ribosomal content of pre-shift cells also increases in accordance to the growth law Eq. (1.2). A small initial amount of R-proteins allows the cell to quickly build up the translation machinery (at a rate  $\dot{M}_{\text{R}}/M_{\text{R}} = \lambda_f$ , see Eq. (2.4)) needed for fast growth, therefore reducing the initial advantage of strains with higher overcapacities.

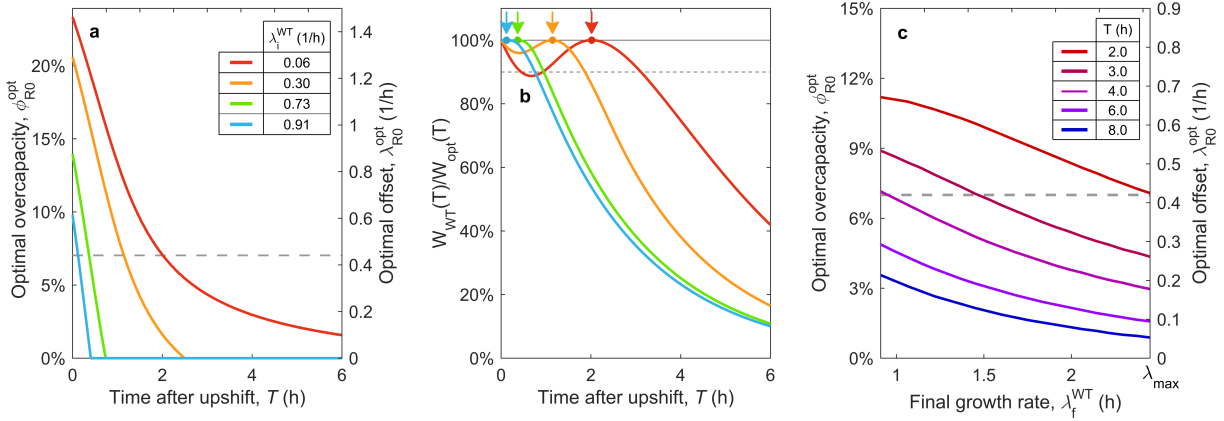


**Figure 2.5: Fitness landscape for different upshifts.** (A) Optimal overcapacity  $\phi_{R,0}^{\text{opt}}(T)$  as a function of feast time for four different shifts to rich media (from aspartate (red), mannose (orange), glycerol (green) and glucose (blue)), with the pre-shift growth rates for the wild-type strain reported in figure. The overcapacity for the wild type strain is shown as a dashed line. (B) Fitness of the wild type strain,  $W_{\text{WT}}(T) = W(\phi_{R,0}^{\text{opt}}(T), T)$ , compared to the optimal value  $W_{\text{opt}}(T) = W(\phi_{R,0}^{\text{opt}}(T), T)$  for the four shifts shown in panel (a). The wild type strain is optimal for feast times of two hours (red arrow), and close to optimal ( $W_{\text{WT}}/W_{\text{opt}} \gtrsim 90\%$ ) for shifts from poor to rich media (red) for about 3 hours. These times are decreased as the pre-shift media improves (orange, green and blue lines). (C) Optimal overcapacity  $\phi_{R,0}^{\text{opt}}$  as a function of the post-shift growth rate for the wild-type strain,  $\lambda_{\text{max}}^{\text{WT}}$ , varying between 0.91/h (corresponding to the growth rate in glucose minimal medium) and  $\lambda_{\text{max}}^{\text{WT}} = 2.45$ /h (rich media). Each line represents a given feast time  $T$ , ranging between three (red) and eight hours (blue); in all cases the pre-shift growth rate is set to  $\lambda_i^{\text{WT}} = 0.06$ /h (aspartate minimal medium). The dashed line indicates the overcapacity of the wild-type strain.

We show in Fig. 2.5B the fitness of the wild type strain  $W_{\text{WT}}(T) = W(T, \phi_{R,0}^{\text{WT}})$ , as a fraction of the optimal fitness,  $W_{\text{opt}}(T) = W(T, \phi_{R,0}^{\text{opt}}(T))$ , for the upshifts analyzed in Fig. 4a. We see that the fitness of the wild type strain in the shift from famine to feast (red line) is maximal for feast times  $T \approx 2$  h, as indicated by the red arrow, and does not drop much below 90% of the maximum (dashed line) for all feast times until  $T > 3.5$  h. In particular, for small feast times where in principle larger  $\phi_{R,0}$  would do better (since  $\phi_{R,0}^{\text{opt}}$  increases for smaller  $T$  as shown in Fig. 2.5A), not much advantage is gained in practice over wild-type strain. If the pre-shift medium supports larger growth rates (orange, green and blue lines), the fitness of the wild type strain drops quickly for feast time  $T$  exceeding 1-2 hours.

Our theory can also be extended to describe the case where the quality of the post-shift medium is reduced, i.e.  $\lambda_{\text{f}} < \lambda_{\text{max}}$ , if the instantaneous upshift kinetics assumed here still holds. This seems to be the case, e.g., for upshift from various poor medium to medium with amino acids but not other ingredients (nucleotides, vitamins, etc) contained in rich medium, or if cells growing in carbon-limited chemostat suddenly experience an increase in carbon flux [76]. We see that the optimal overcapacity  $\phi_{R,0}^{\text{opt}}$  increases as  $\lambda_{\text{f}}^{\text{WT}}$  is decreased from the maximum growth rate of the wild type strain,  $\lambda_{\text{max}}^{\text{WT}} = 2.45$ /h (Fig. 2.5C). This increase originates in the slower synthesis of R-proteins after the shift, due to the reduced final growth rate: as cells need more time to synthesize the ribosomes, the overcapacity becomes more valuable. A detailed analysis of the fitness landscape, including a derivation of the expressions involving  $\lambda_{\text{R}}^{\text{opt}}$ , can be found in Section A.2. Note, however, that for upshift to medium with a simple nutrient source whose uptake requires a large amount of a dedicated transporter, the instantaneous upshift kinetics requires a more elaborate model, which will be discussed in the following chapter.

## 2.6 Discussion

Proteome allocation has been widely studied in the context of cellular economics, both using coarse-grained [34, 42, 80–82] and genome-scale models [83–89]. All of the studies to date have been on steady state systems, and the presence of overcapacities in proteome allocation has been puzzling and counter-intuitive, as they clearly lead to reduced steady state growth [34, 44]. In this work, we characterized the effect of fluctuating environmental conditions on bacterial growth, in an ecological scenario of intermittent growth interrupted by starvation periods, such as the ones experienced by gut microbiota. Using a simple model of upshift kinetics based on the experimental observation for switch to rich medium [39, 78], we elucidated the impact of an overcapacity of the translation machinery (R-proteins) on the kinetics of growth recovery. This overcapacity, which is substantial at low growth rates [41], is suggested to be a reserve, intentionally kept by the cell to enable rapid growth upon improvement in nutrient conditions.

Strains that express different amounts of this reserve are predicted to perform differently in shifts from poor to rich medium. Using an evolutionary consideration, we derived a simple expression for the reserve amount that maximizes the fitness, defined as the gain in biomass during the feast period, for different lengths of the feast period. Analytical expressions are derived for this fitness gain, for different pre-shift and post-shift growth medium, leading to quantitative predictions for the performance of strains with different ribosome overcapacities in a variety of environments. The amount of ribosome reserve maintained by *E. coli* – different strains have similar overcapacities, see Fig. A.2 – coincides with what the model predicts to be optimal for feasts lasting 2-3 hours. Notably, this corresponds to the feast period for the human gut microbiota, since flow rates of nutrient from small to large intestine peak shortly after meals, and decrease considerably after a few hours [10, 11]. This coincidence raises the possibility that this reserve may have been optimized for the typical nutrient cycles in the gut.

At the regulatory level, synthesis of ribosomal proteins is known to be controlled mainly by the transcription of ribosomal RNA [90] via a tandem pair of promoters [91]. The P2 promoter is regulated by ppGpp to provide demand-dependent expression while the P1 promoter is constitutive [91]. Adjusting the strength of the P1 promoter may therefore be a convenient route for the cell to set the amount of the ribosomal reserve. Interestingly, varying the number of rRNA gene copies in *E. coli* has been found to modulate both the steady-state growth rate and the adaptation kinetics. Systematic, quantitative characterization of the growth kinetics of these strains may be effective ways to test these model predictions. A similar mechanism may underly earlier finding that soil bacteria adapting quickly to upshifts have more copies of rRNA genes compared to slowly adapting strains [92]. Adjusting the copy of rRNA genes may thus be another effective way for bacteria to modulate R-sector reserve, thereby allowing them to adjust the adaptation speed with respect to the time scale of environmental changes.

Ribosome reserve is of course not the only type of reserve cells keep for adaptation in fluctuating environments. Metabolically versatile organisms such as *E. coli* express many genes not needed in a given growth condition. One such class of proteome reserve is comprised of the biosynthetic enzymes, whose availability affect the ability of the cell to adjust its growth following up- or down-shifts to environments not containing all the metabolic precursors needed for cell growth. Examples include upshift from stationary phase or downshift from rich medium. In these cases, various biosynthetic pathways must be expressed to synthesize the needed precursors; merely keeping a reserve of translational machinery is not sufficient for rapid adaptation. Existing proteomic data shows that most biosynthetic pathways are indeed kept at large overcapacities compared to their metabolic needs in poor nutrient conditions [44]. Quantitative characterization of these shifts will require better description of growth shifts into incomplete medium, which is well beyond the simple kinetics for switch to rich medium used here.

Catabolic proteins comprise another class of protein reserves. For example during growth on a single carbon substrate the transporters and degradation enzymes of many absent sugars are co-expressed with the present carbon catabolic system, according to recent proteomic studies [44, 93, 94]. Also co-expressed with the carbon catabolic systems is the entire motility system (flagella and motor proteins) which is not needed in well-stirred laboratory culture [44]. The expressions of these proteins have detrimental effects on steady state growth, as shown by directly deleting the flagella system [82], and also in long-term evolution experiments where consistent increases in growth rate are seen for *E. coli* growing in glucose minimal medium, upon reduction in ribose/maltose catabolism and motility gene expression [95–97]. The fitness cost of expressing these proteins cannot be accounted for by a simple offset, whose effect is a linear reduction of steady state growth rate (as in Eq. (2.12)), since their expression levels increase upon carbon limitation [42, 44]. The fitness gain for carrying the catabolic reserves will surely depend on details of the environment, e.g., the amount and duration of the availability of specific types of nutrients [98–100].



# Chapter 3

## Growth transitions

### 3.1 Introduction

A grand challenge of systems biology is to predict the kinetic responses of living systems to perturbations starting from the underlying molecular interactions. Changes of the nutrient environment have long been used to study regulation and adaptation phenomena in microorganisms [67, 101, 102], and remain a topic of active investigation in the era of systems biology [75, 103–109]. While much is known about the molecular interactions governing the regulation of key metabolic processes in response to the applied perturbations [42, 43, 110–114], they remain insufficiently quantified for predictive bottom-up modeling. In the previous chapter, we discussed the impact of ribosomes reserves in upshifts using a simple kinetic model. While the simplicity of this model allowed us to probe connections between reserve size and adaptation speed, such models are inherently frail and restricted to the specific conditions to which they were developed for. Due to the lack of quantitative understanding underlying the kinetic response, such models will fail when different perturbations are applied, as detailed in Appendix B.1 for the model of Chapter 2.

Here we develop a top-down approach, expanding the recently established coarse-grained proteome allocation models [34, 42, 44, 115], and discussed in Section 1.3.2, from steady-state growth into the kinetic regime. Using only qualitative knowledge of the underlying regulatory processes and imposing the condition of flux balance, we derive a quantitative model of bacterial growth transitions independent of inaccessible kinetic parameters. The resulting flux-driven regulation model, applicable to growth transitions not involving prolonged periods of growth arrest, accurately predicts the time course of gene expression and biomass accumulation in response to both nutrient upshifts and downshifts (e.g., diauxic shifts) for many combinations of nutrients tested without adjustable parameters. As predicted by the model and validated by quantitative proteomics, cells exhibit slow recovery kinetics in response to nutrient shifts due to a coordinated global remodeling of the proteome that prevents channeling protein synthesis specifically into bottleneck proteins. Quantitative knowledge of these slow proteome-wide dynamics is foundational for predictive understanding of growth-dependent processes, including antibiotic inhibition and robust operation of genetic circuits *in vivo*. Importantly, the success of the coarse-grained top-down approach introduced here suggests that the adaptive dynamics at cellular scale is set by global strategies of resource allocation independent of the details of molecular control parameters. Our approach thus outlines a theoretical framework for describing a broad range of such adaptive processes without detailed knowledge of the underlying biochemical reactions.

Initially we focus on medium shifts between carbon substrates which can be co-utilized [116] or are closely related and hence readily switchable, thus avoiding long delays and heterogeneous

growth characteristic seen in complex transitions [107, 108]. We will further extend the theory to non co-utilized carbon substrates, i.e. diauxic shifts of sequentially utilized carbon substrates. As predicted by the model and validated by quantitative proteomics, cells exhibit slow recovery kinetics in response to nutrient shifts due to a coordinated global remodeling of the proteome that prevents channeling protein synthesis specifically into bottleneck proteins. Quantitative knowledge of this slow proteome-wide dynamics is foundational for predictive understanding of growth related processes, such as in vivo genetic circuits or antibiotic inhibition. More generally, the coarse-grained top-down approach introduced here suggests a path for understanding a broad range of adaptive processes without the need for detailed characterization of the underlying biochemical reactions.

### 3.1.1 Carbon co-utilization upshift

We first studied nutrient upshifts by growing a wild-type *E. coli* K-12 strain (NCM3722 [29]) in minimal medium (see Section B.5.1) in batch culture, with succinate as the sole carbon source. Subsequently, during exponential growth, gluconate, a co-utilized carbon substrate [116] was added directly to the medium; see Section B.5.2 for details of culture procedure. The time course of optical density ( $OD_{600}$ ) of the cell culture (a proxy for cell mass  $M$ , Fig. B.9A), was measured throughout the course of this nutrient upshift (red circles, Fig. 3.1A); faster growth occurred soon after the shift ( $t = 0$ , dashed vertical line). Ribosome content (reported by the RNA abundance [43], inverted blue triangles), increased faster than cell mass as is well known [102], while catabolic protein content (reported by LacZ expression in medium induced with IPTG [42], green triangles), took several hours to adapt. Eventually all these quantities grew at the final rate (dotted black line). The instantaneous growth rate of the biomass,  $\lambda \equiv d \ln M / dt$ , slowly converged to its final value  $\lambda_f^*$  over the course of several hours (dotted red line, Fig. 3.1B, and Fig. B.10 for long time data). In contrast to this slow adaptation of cellular components, the slope of  $M$ ,  $J \equiv dM/dt$ , a measure for biomass synthesis flux showed a much faster response (red squares, Fig. 3.1C): Within  $\sim 30$  min of the upshift, this flux increased exponentially at the final rate (dotted red line). Similarly, synthesis of new RNA and LacZ (Fig. 3.1D and E) showed fast response, with expression levels (slope of the data) being at the final level (slope of the dashed lines) less than a doubling after the upshift.

### 3.1.2 Carbon co-utilization downshift

Nutrient downshifts result from the depletion of some nutrient component in the medium as in Monod's study of diauxic growth [101]. They are complementary to nutrient upshifts, as they present the transition from fast to slow growth. In Fig. 3.2 we grow cells on succinate and glucose and observe bi-phasic growth of biomass (Fig. 3.2A), characteristic for diauxic shifts. As succinate is co-utilized with glucose, cells first grow on both carbon substrates, and switch to succinate only after glucose is depleted around  $t = 0$  (dashed vertical line). At this point the instantaneous growth rate  $\lambda(t)$  decreases sharply, followed by a recovery to the growth rate supported by succinate (red diamonds in Fig. 3.2B). During the recovery, biomass flux (red squares in Fig. 3.2C) showed growth at an increased rate (slope of the orange line), before settling to its final value (slope of the green dotted line). Similarly, expression of catabolic proteins (Fig. 3.2D) showed a transiently increased expression rate (slope of the orange line) before settling to the final rate (slope of the dotted green line).

These dynamics differ from those of nutrient upshifts. In upshift experiments the sudden increase of nutrient quality leads to an up-regulation of ribosomes and a down-regulation of catabolic proteins. As a consequence, the cell monotonically adapts growth rate to its new growth state. In contrast, in downshift experiments, the depletion of a nutrient leads to a

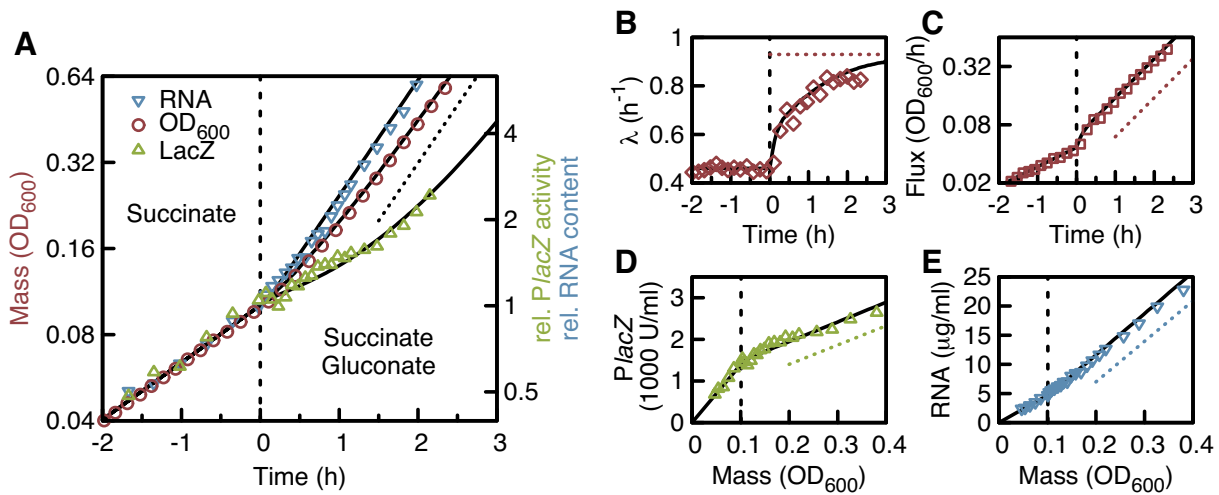


**Figure 3.1: Co-utilization upshift.** Cells grown exponentially on minimal medium with 20mM succinate (and IPTG to induce LacZ) are supplemented with 20mM gluconate at  $t = 0$  (dashed vertical line). **(A)** Optical density,  $OD_{600}$  (red circles), total amount of RNA relative to  $t = 0$  (blue inverted triangles), and LacZ activity relative to  $t = 0$  (green triangles) are plotted versus time. [Note that LacZ is used here as a general reporter of carbon catabolic protein expression, as detailed in Section 1.3.2.] Slope of the dotted black line indicates the rate of increase of all three quantities in the final steady state according to the final growth rate ( $\lambda_f^* = 0.98/\text{h}$ ). **(B)** Instantaneous growth rate  $\lambda(t)$ , computed as the time derivative of  $\ln(OD_{600})$  (red diamonds). Red dotted line indicates the final growth rate  $\lambda_f^*$ . **(C)** Time derivative of  $OD_{600}$  (biomass flux, red squares) grows exponentially at the final rate (slope of the red dotted line) within 30 minutes after the upshift. **(D, E)** The absolute activity of LacZ and absolute RNA content are plotted versus  $OD_{600}$ . Within one doubling after the upshift (dashed vertical line), expression of both quantities (i.e. the slope of the data) reached its final value (slope of the dotted line). In all panels, the black curves are predictions of the FDR model. Parameters defining the initial and final steady states are listed in Table B.1. All data shown here and throughout this manuscript are from individual experiments. The data is highly reproducible, see Fig. B.11 for a comparison of biological replicates.

sudden drop of carbon influx. The following recovery is dominated by excess ribosomes and biosynthesis pathways and insufficient carbon uptake.

Despite these seemingly different kinetics, we will attempt to formulate a common theory to describe the kinetics of growth transitions, including growth, fluxes, catabolic and ribosomal proteins, based on flux driven regulation. In Section 3.2 we explain the design of the model, which will be solved in Section B.3 and compared to experimental data in Section 3.3. It will be further extended to describe proteome remodeling during growth shifts in Section 3.4. The strategy behind the adaptation will be elucidated in Section B.4, where we will identify two adaptation regimes.

## 3.2 A flux-driven regulation (FDR) model

### 3.2.1 Design principle

We build a coarse-grained kinetic model that incorporates the regulation of catabolism and protein synthesis as illustrated in Fig. 3.3. The model contains two internal fluxes: Catabolism (red) and translation (orange), which both, sequentially contribute to growth. Key to understanding the dynamics of growth transitions is knowing the synthesis rates of core proteins of catabolism (green) and translation (blue), i.e. transporters (or other limiting catabolic proteins) and ribosomes, respectively. For simplicity our model includes two substrates, S1 and S2. Generally, it can be extended to include an arbitrary number of substrates. In upshift experiments, the cell culture grows exponentially on carbon substrate S1 and is upshifted by the addition of a second

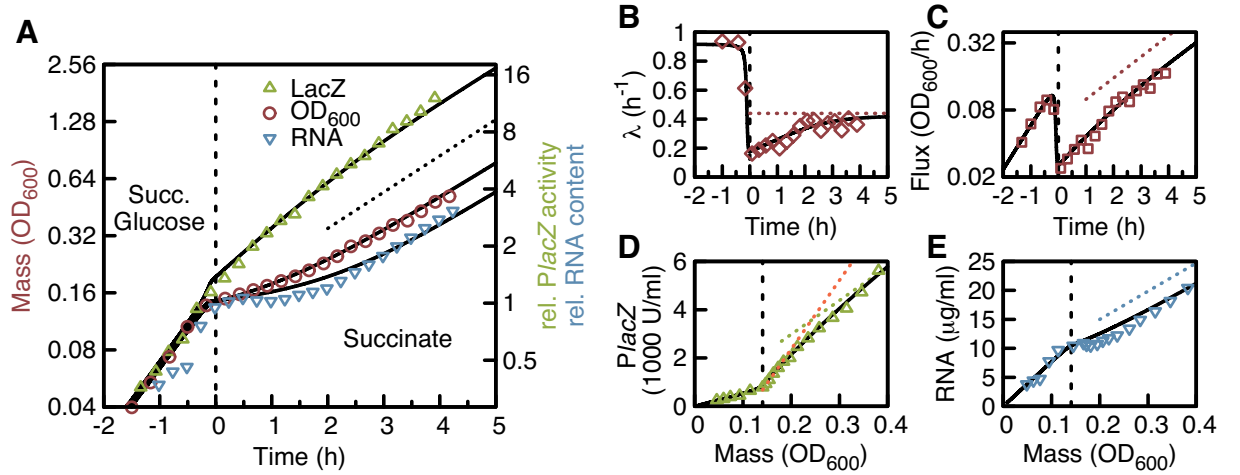


**Figure 3.2: Co-utilization downshift.** Cells were grown exponentially in minimal medium with glucose and succinate as carbon sources (and IPTG to induce LacZ). The dashed vertical line indicates the time ( $t = 0$ ) when glucose was depleted. **(A)** Optical density,  $OD_{600}$  (red circles), amount of total RNA relative to  $t = 0$  (blue inverted triangles) and the activity of LacZ relative to  $t = 0$  (green triangles) are plotted versus time. Several hours after the shift, all three quantities increased according to the final growth rate  $0.45/h$  (slope of the dotted line). **(B, C)** At the time of glucose depletion, the instantaneous growth rate (diamonds) and the biomass flux (squares) both decreased sharply, but remained finite due to continued supply of succinate. Dotted lines indicate the final state behavior, which is reached 3 hours after the shift (one mass doubling according to panel A). **(D)** Catabolic reporter LacZ (green triangles) was expressed at high levels for a fraction of mass doubling after diauxic shift (slope of the orange dotted line indicates the theoretical maximal expression  $\chi_{C,max}$ ), before settling down to its final value (slope of green dotted line). **(E)** The increase in RNA content (blue triangles) was reduced for a fraction of mass doubling after the shift, before approach its final behavior (slope of the blue dotted line). In all panels, the solid black curves are predictions of the FDR model. Variables defining the initial and final steady state are listed in Table B.1.

(co-utilized) substrate S2. The uptake of both substrates (by catabolic proteins Cat1 and Cat2) contribute to the carbon influx  $J_C$ . In downshift experiments, the cell culture grows on both substrates S1 and S2. Upon depletion of one substrate, the carbon influx  $J_C$  decreases.

The key element of the model is how to set the regulatory functions that control the synthesis of these proteins. In our coarse-grained model, the regulatory functions are set according to the metabolic fluxes, thus the name flux-driven regulation (FDR). We do not attempt to capture the details of metabolic changes (e.g., the concentrations of amino acids and carbon precursors) therefore do not need to explicitly consider the complex molecular details of the underlying regulations, e.g., the signaling by ppGpp [112] and cAMP [42] which are poorly characterized at a quantitative level. Instead we focus on describing the macroscopic outputs of the regulatory functions, because they govern bacterial growth and hence their quantitative forms are constrained by the steady state growth laws reviewed above. We will show how the growth laws and the known topology of the regulatory interactions [43] are sufficient to constraint completely the macroscopic outputs of the key regulatory functions. The resulting model is conceptually simple and analytically solvable, and accurately captures the kinetics of the growth transitions such as Figs. 3.1 and 3.2 and many more. The impatient reader may skip the mathematical discussion in the following sections and rejoin in Section 3.3, where the model solutions are compared to data.

### 3.2.2 Model components

In this section, we provide the details of each element of the model illustrated in Fig. 3.3.

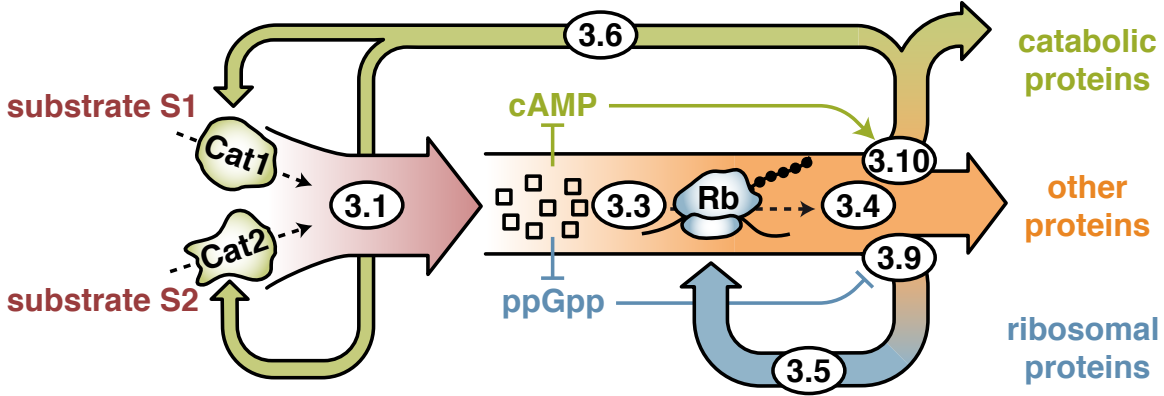


**Figure 3.3: Model of Flux-driven Regulation (FDR).** Flux balance and the allocation of protein synthesis. Carbon substrates S1, S2 are imported by uptake proteins Cat1, Cat2 of abundances  $M_{\text{Cat1}}$ ,  $M_{\text{Cat2}}$  at rates  $k_1$ ,  $k_2$ , respectively. Changes in the external concentrations of these substrates result in changes in the carbon influx  $J_C$  (red, Eq. (3.1)), which supplies a pool of central precursors (squares). These precursors are consumed by the ribosomes Rb for protein synthesis, whose flux  $J_R$  must balance the changes in the carbon influx (orange, Eq. (3.3)) at a coarse-grained time scale. Attaining this protein synthesis flux for a given amount of ribosomes (of abundance  $M_{\text{Rb}}$ ) demands changes in the translational activity  $\sigma$  as defined in Eq. (3.4), which arise molecularly due to changes in the precursor pools [43]. Parts of the protein synthesis are allocated to the expression of catabolic and ribosomal proteins,  $M_{\text{Rb}}$  and  $M_{\text{Cat1}}$ ,  $M_{\text{Cat2}}$ , Eqs. (3.5) and (3.6). This allocation is determined by the global regulation functions  $\chi_{\text{Rb}}(t)$  and  $\chi_{\text{Cat}}(t)$ , set molecularly by the precursor pool via ppGpp (blue arrows) [43, 91, 112, 113, 117] and the cAMP-CRP system (green arrows) [42, 118, 119], respectively, as well as the substrate-specific regulation  $h_{1,2}$ . The forms of the regulatory functions  $\hat{\chi}_{\text{Rb}}(\sigma)$  and  $\hat{\chi}_{\text{Cat}}(\sigma)$ , Eqs. (3.7) and (3.8) (black lines), can be determined from the known steady state measurements (colored triangles, see Section 1.3.2 and Tables B.1 and B.2 for data and fits) as derived in Eqs. (3.9) and (3.10). The central simplifying assumption of the model is that the time-dependence of the regulation functions during growth transition is determined solely through the changes in  $\sigma$ , as expressed explicitly in Eqs. (3.7) and (3.8)

### Carbon influx

To model the kinetic transition due to a change in carbon substrates, we consider the time-dependent abundances of the two relevant carbon-substrate uptake systems  $M_{\text{Cat1}}(t)$  and  $M_{\text{Cat2}}(t)$  (mass per standard culture volume, as defined in Section 1.3.2). These systems import their cognate substrates S1 and S2 at specific rates  $k_1$  and  $k_2$  when supplied with saturating concentrations of these substrates in the medium. We introduce constant conversion factors  $\beta_1$  and  $\beta_2$  to describe how much an imported substrate contributes to the carbon budget (see details in Section B.2 below), and write the metabolic influx of carbon substrates ( $J_C(t)$ , in number of carbon atoms assimilated per time per standard culture volume) as

$$J_C(t) = \beta_1 k_1 M_{\text{Cat1}}(t) + \beta_2 k_2 M_{\text{Cat2}}(t). \quad (3.1)$$

The carbon influx is depicted in Fig. 3.3 as a red arrow. During steady state growth,  $J_C(t)$ ,  $M_{\text{Cat1}}(t)$  and  $M_{\text{Cat2}}(t)$  all grow exponentially at the steady state growth rate  $\lambda^*$ . Generally, the uptake rates  $k_j$  are Michaelis-Menten functions of the concentration of the cognate carbon substrate  $n_j$

$$k_j = k_{j,\text{max}} \frac{n_j}{n_j + K_M} \quad (3.2)$$

with the Michaelis constant  $K_M$  in the sub millimolar range. During steady state and upshift experiments, we provide saturating amounts of carbon substrate,  $n_j \gg K_M$  so that Eq. (3.2)

reduces to  $k_j = k_{j,\max}$ . For diauxic shifts this is not possible, since when the substrate is depleted, the concentration  $n_j$  will inevitably decrease into the regime where the influx is sub-saturated.

### Central Precursor pool

Carbon influx leads into central metabolism and eventually to precursors required for biosynthesis, including ketoacids, amino acids and charged tRNAs. As these metabolites are connected by rapid reversible reactions [120], we coarse-grain them into a single pool of “central precursors” (open squares, Fig. 3.3). The increase or decrease of carbon influx leads to corresponding change in these key internal metabolites [75, 121]. The increase of these precursors leads to an increase in the ribosomes’ “translational activity”,  $\sigma(t)$ , such that the flux of protein synthesis  $J_R$  balances the increased carbon influx on a coarse-grained time scale (orange arrow in Fig. 3.3). The translational activity includes contributions from the active ribosome fraction (possible mechanism: inhibition of IF2-dependent translation initiation via low concentrations of ppGpp [37, 122]) and the elongation rate of active ribosomes.

### Protein synthesis flux

The central precursors are assembled into proteins by ribosomes and the associated protein synthesis machinery. As described in Section 1.3.2, the total protein synthesis flux is given by the ribosomal content  $M_{Rb}$  and translational activity  $\sigma$  as  $J_R(t) = \sigma(t)M_{Rb}(t)$ .

Molecularly, the translation rate and the fraction of active ribosomes (which collectively determine  $\sigma(t)$ ) depend on the concentrations of the central precursors, in particular on the abundance of charged tRNA. During nutrient upshifts, rapid increases in carbon uptake lead to rapid rises in the central precursor pools [75], which results in rapid increases in the translation rate and in the number of translating ribosomes [40, 43], amounting to a rise in  $\sigma(t)$ . The molecular details of these processes and their control are complex and not known quantitatively. We make the crucial simplifying assumption that the translational activity  $\sigma(t)$  takes on values such that the carbon influx  $J_C(t)$  and protein synthesis flux  $J_R(t)$  are always balanced, i.e.,

$$J_R(t) = \alpha J_C(t), \quad (3.3)$$

with a constant conversion factor  $\alpha$  to be discussed in Section B.2. Thus, an abrupt change in nutrients (hence  $J_C(t)$ ) is passed immediately onto an abrupt change in translational activity, i.e.,

$$\sigma(t) = \alpha J_C(t)/M_{Rb}(t), \quad (3.4)$$

where the ribosomal content  $M_{Rb}(t)$  cannot change abruptly.

This assumption makes the model incapable of describing metabolite build-up and inter-conversion at very short time scales (less than five minutes) [75], and consequently short period oscillations in macromolecular content ( $\sim 15$  minutes, [123]), and random fluctuations in the metabolic network [124]. However, it allows us to address the coarse-grained kinetics beyond the time resolution of  $\sim 15$  minutes where the growth data are taken in this study.

### Allocation of protein synthesis

$J_R(t)$  is the entire protein synthesis flux, the synthesis of specific proteins is specified by the regulation functions. We introduce the regulatory function  $\chi_{Rb}$  as the fraction of protein synthesis that is allocated to ribosomal proteins, and write

$$\frac{dM_{\text{Rb}}}{dt} = \chi_{\text{Rb}}(t)J_{\text{R}}(t). \quad (3.5)$$

Ribosome synthesis is depicted in Fig. 3.3 as a blue arrow. The regulation of ribosome synthesis itself is controlled via the ppGpp pathway [112] an important topic we will address in the next subsection.

Catabolic proteins are often controlled by a specific as well as a global regulation [42, 110, 125]. The specific regulation can be, for example an on-off switch that senses the presence of the metabolite taken up by the controlled proteins. For the well-studied lac operon, the specific regulation is the repression of the lac operon by LacI, which is relieved in the presence of allolactose, a lactose-derived metabolite. The global regulation of the catabolic genes is set by the cAMP-CRP signaling system and modulates the expression of all catabolic genes to balance internal fluxes [42]. We introduce the global regulatory function  $\chi_{\text{Cat}}(t)$  for the synthesis of catabolic proteins and the specific regulatory function  $h_j(t)$ . Then the abundance of a catabolic enzyme  $\text{Cat},j$ , which takes up substrate  $S_j$  (as shown in Fig. 3.3) and is denoted as  $M_{\text{Cat},j}$ , changes as

$$\frac{dM_{\text{Cat},j}}{dt} = h_j(t) \chi_{\text{Cat}}(t) J_{\text{R}}(t). \quad (3.6)$$

Synthesis of catabolic proteins is depicted as a green arrow in Fig. 3.3. The forms of these regulatory functions are discussed below.

### Global regulatory functions: strategy

A key challenge to describing the dynamics is to represent the time-dependent signals setting the global regulatory functions  $\chi_{\text{Rb}}(t)$  and  $\chi_{\text{Cat}}(t)$  controlling the synthesis of ribosomal and catabolic proteins during nutrient shifts. The typical approach to this task is based on bottom-up models that describe the known specifics of regulatory interactions mathematically; see Ref. [43], which provides some details of the form of the ppGpp-mediated function  $\chi_{\text{Rb}}$ . There are several problems with this approach which we illustrate with the ppGpp pathway: First, although it is known that RelA is the enzyme primarily responsible for the synthesis of ppGpp in response to changes in the tRNA charging level [112, 117, 126], quantitative details of this interaction (e.g., the binding and rate constants, the abundance of RelA) are missing. Second, quantitative details of how ppGpp affect rRNA transcription [117], and through it, exerts its effect on ribosomal protein synthesis [113, 127] are missing. Third, the details of ppGpp hydrolysis by SpoT [114] are missing (even at the molecular level). And most importantly, completing such a bottom-up approach would require a dynamic description of the tRNA-charging levels, which would in turn require a much larger description of metabolism covering the conversion of the carbon taken-up to tRNA charging, and thus calling upon an even larger number of molecular processes with unknown kinetic parameters. It should also be kept in mind that the abundances of many of the enzymes involved are growth-condition dependent [44]. Hence to describe growth transition from different initial states to final states, it is also necessary to determine the changes in the enzyme levels themselves during the transition. All of these problems add up to make the bottom-up approach a daunting task, and render the resulting model weak in predictive power.

In this work, we adopt a top-down approach, which bypasses the above-mentioned problems, allowing accurate prediction of growth transition kinetics based on the initial and final growth rates of the culture. Inspecting the known topology of factors regulating the synthesis of catabolic and ribosomal proteins, we observe that while ppGpp-mediated regulation is set by the charging of tRNA by amino acids [112, 117, 126] cAMP-CRP regulation is set by  $\alpha$ -ketoacids [42], which are connected to the amino acids by rapidly reversible trans-amination reactions

[120]. We note that these metabolites, which are the drivers of ppGpp and cAMP signaling, are the same ‘‘pool of central precursors’’ discussed in Section 3.2.2 that molecularly set the magnitude of the translational activity  $\sigma(t)$  in 3.4. This leads us to our central approximation that the (time-dependent) effects that these central precursors exert on the regulatory functions  $\chi_{\text{Rb}}(t)$  and  $\chi_{\text{Cat}}(t)$  during growth transitions can be mimicked through their effect on the translational activity  $\sigma(t)$ . As we will show in the next subsection, the latter can be determined through the relation between the values of the regulatory functions and translational activity in the steady state,  $\hat{\chi}_{\text{Rb}}(\sigma^*)$  and  $\hat{\chi}_{\text{Cat}}(\sigma^*)$ , such that our central approximation can be stated mathematically as

$$\chi_{\text{Rb}}(t) = \hat{\chi}_{\text{Rb}}(\sigma(t)), \quad (3.7)$$

$$\chi_{\text{Cat}}(t) = \hat{\chi}_{\text{Cat}}(\sigma(t)). \quad (3.8)$$

The above relations provide a ‘closure’ to our coarse-grained model of growth transition: Eq. (3.4) specifies how  $\sigma(t)$  change in response to changes in flux  $J_C(t)$ , Eqs. (3.7) and (3.8) then specifies how the regulatory functions are affected, and finally Eqs. (3.5) and (3.6) dictates how the proteome is affected. Together, Eqs. (3.4) to (3.8) define a mathematical scheme to describe gene regulation changes in response to changes in metabolic fluxes, hence the name Flux-Driven Regulation (FDR). Note that this FDR scheme does not require knowledge about quantitative details of the complex molecular interactions that ultimately yield the dynamic responses  $\sigma(t)$  and  $\chi_{\text{Rb}}(t)$ ,  $\chi_{\text{Cat}}(t)$ .

We further assume that all other regulatory functions (of other proteome sectors not described in this model) vary depending on the same parameter as the regulatory functions  $\hat{\chi}_{\text{Rb}}(\sigma(t))$  and  $\hat{\chi}_{\text{Cat}}(\sigma(t))$ , i.e.  $\sigma(t)$ , such that proteome partitioning is still valid.

### Global regulatory functions: form

Here we derive the steady state relations between the regulatory functions  $\chi_{\text{Rb}}$  and  $\chi_{\text{Cat}}$  and the translational activity  $\sigma$ , using the steady state growth laws in Eqs. (1.2) and (1.5). As introduced above, the proteome fractions of ribosomal and catabolic proteins  $\text{Cat},j$  are  $\phi_{\text{Rb}}(t) = M_{\text{Rb}}(t)/M_{\text{P}}(t)$  and  $\phi_{\text{Cat},j}(t) = M_{\text{Cat},j}(t)/M_{\text{P}}(t)$ , respectively. On the other hand, the regulatory functions  $\chi_{\text{Rb}}(t)$  and  $\chi_{\text{Cat}}(t)$ , as defined in Eqs. (3.5) and (3.6), can be written as  $\chi_{\text{Rb}}(t) = \dot{M}_{\text{Rb}}/\dot{M}_{\text{P}}$  and  $h_j(t)\chi_{\text{Cat}}(t) = \dot{M}_{\text{Cat},j}/\dot{M}_{\text{P}}$  (since  $J_{\text{R}} \equiv \dot{M}_{\text{P}}$ , with the dot representing a time derivative). During steady state growth, all quantities, including  $M_{\text{Rb}}(t)$ ,  $M_{\text{Cat}}(t)$  and  $M_{\text{P}}(t)$ , grow exponentially at rate  $\lambda^*$ ; see Eq. (1.1). Hence the values of the regulatory functions in steady state,  $\chi_{\text{Rb}}^* \equiv \chi_{\text{Rb}}(t \rightarrow \infty)$ ,  $\chi_{\text{Cat}}^* \equiv \chi_{\text{Cat}}(t \rightarrow \infty)$  and  $h_j^* \equiv h_j(t \rightarrow \infty)$  can be fixed by the steady-state proteome fractions, i.e.,  $\chi_{\text{Rb}}^* = M_{\text{Rb}}(t \rightarrow \infty)/M_{\text{P}}(t \rightarrow \infty) = \phi_{\text{Rb}}^*$  and  $h_j^*\chi_{\text{Cat}}^* = M_{\text{Cat},j}(t \rightarrow \infty)/M_{\text{P}}(t \rightarrow \infty) = \phi_{\text{Cat},j}^*$ . From Eqs. (3.7) and (3.8), we make the identification  $\chi_{\text{Rb}}^* = \hat{\chi}_{\text{Rb}}(\sigma^*) = \phi_{\text{Rb}}^*$ . For catabolic proteins, we let the specific regulatory function to carry the scale such that  $h_j^* = \phi_{\text{Cat},j,\text{max}}$ . It then follows that  $\phi_{\text{Cat},j,\text{max}}\hat{\chi}_{\text{Cat}}(\sigma^*) = \phi_{\text{Cat},j}^*$ .

The steady state values of the proteome fractions  $\phi_{\text{Rb}}^*$  and  $\phi_{\text{Cat},j}^*$  are related to the growth rate  $\lambda^*$  by the growth laws, Eqs. (1.2) and (1.5). Furthermore, the steady-state value of the translational activity  $\sigma^*$  is related to the growth rate by Eq. (1.4). Together, we can obtain the relations between the regulatory functions and translational activity in steady state,

$$\hat{\chi}_{\text{Rb}}(\sigma^*) = \phi_{\text{Rb}}^*(\lambda^*(\sigma^*)) = \frac{\phi_{\text{Rb},0}}{1 - \sigma^*/\gamma} \quad (3.9)$$

and

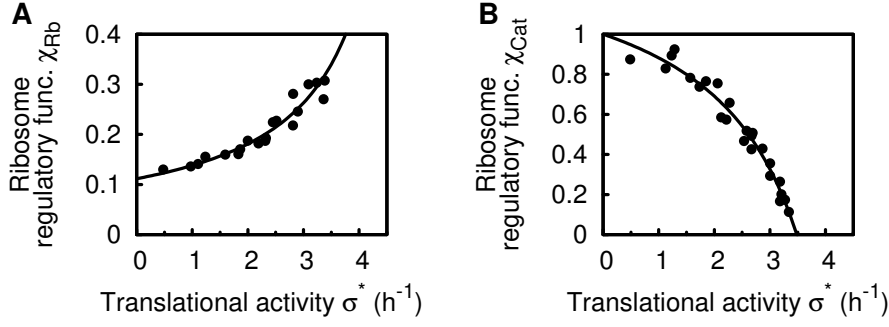


**Figure 3.4: Regulatory functions.** The regulatory functions  $\hat{\chi}_{\text{Cat}}(\sigma^*)$  and  $\hat{\chi}_{\text{Rb}}(\sigma^*)$  as a function of the translational activity  $\sigma^*$ , obtained as explain in the text. Symbols shows experimental data from Figs. 1.3 and 1.5 plotted versus the translational activity Fig. 1.4.

$$\hat{\chi}_{\text{Cat}}(\sigma^*) = \frac{\phi_{\text{Cat},j}^*(\lambda^*(\sigma^*))}{\phi_{\text{Cat},j,\text{max}}} = 1 - \frac{\sigma^*}{\lambda_{\text{C}}} \hat{\chi}_{\text{Rb}}(\sigma^*), \quad (3.10)$$

which are shown in Fig. 3.4. The parameters  $\phi_{\text{Rb},0}$  (vertical intercept of the ribosome line),  $\gamma$  (inverse slope of the ribosome line, maximal translation rate) and  $\lambda_{\text{C}}$  (horizontal intercept of the catabolic line) are defined by the growth laws Eqs. (1.2) and (1.5) and measured experimentally, see Figs. 1.3 and 1.5. Together Eqs. (3.9) and (3.10) specify the time-dependent regulatory functions  $\chi_{\text{Rb}}(t)$  and  $\chi_{\text{Cat}}(t)$  via our central approximation, Eqs. (3.7) and (3.8).

### Global regulatory functions: Beyond $\lambda_{\text{C}}$

The above definitions of the global regulatory functions are technically valid only until a value of  $\sigma^*$  that corresponds to  $\lambda^*(\sigma_{\text{C}}^*) = \lambda_{\text{C}}$ . For  $\sigma^* > \sigma_{\text{C}}^*$ , the regulatory function  $\hat{\chi}_{\text{Cat}}(\sigma^*)$  would become negative. While this limit cannot be reached during steady state growth ( $\lambda_{\text{C}}$  is the maximal steady state growth rate in this minimal medium), it can be reached transiently during nutrient shifts. An example is the mannose adding OAA upshift presented in Fig. 3.8, later in this chapter. We observe in Fig. 3.8 panel D, that LacZ activity remains constant after the upshift and thus ask if we can extend the model to describe this data. We implement  $\hat{\chi}_{\text{Cat}}(\sigma^* > \sigma_{\text{C}}^*) = 0$ , and keep the relation  $\hat{\chi}_{\text{Rb}}(\sigma^*)$ , as presented in Eq. (3.10). Fig. 3.8 is further discussed in Section 3.3.

### Substrate-specific regulatory functions

The specific regulation functions  $h_j(t)$  are usually characterized by steep response curves to the substrate concentrations, as many uptake systems are tightly repressed in the absence of the cognate substrate. For nutrient upshifts, we simply model  $h_j(t)$  by a step function, depending on the presence or absence of the cognate carbon substrate, i.e.

$$h_j(t) = \begin{cases} 0 & \text{for } t < 0 \\ \phi_{\text{Cat},j,\text{max}} & \text{for } t \geq 0 \end{cases} \quad (3.11)$$

When the carbon substrate is added at  $t = 0$ . For pre-expressed uptake systems, we choose

$$h_j(t) = \begin{cases} x\phi_{\text{Cat},j,\text{max}} & \text{for } t < 0 \\ \phi_{\text{Cat},j,\text{max}} & \text{for } t \geq 0 \end{cases} \quad (3.12)$$

and refer to  $x$  as the pre-expression level. Since the catabolic protein are rarely expressed above 1% of the proteome [44], we assume that the additional expression of one catabolic protein does not alter the expression of other proteins.

Some carbon uptake systems are repressed in the presence of other, preferred carbon substrates, leading to an exclusive consumption of the preferred carbon substrate [101]. Glucose and lactose is such a combination [128], with glucose being preferred by *E. coli* over lactose. Generally, the inferior carbon substrate is only consumed by the cell once the preferred carbon substrate is depleted and the uptake system for the inferior carbon is de-repressed. The molecular details of this repression are substrate specific and generally not quantitatively known, so we model the expression of the inferior carbon uptake system analogously to above as a step function,

$$h_j = \begin{cases} x\phi_{\text{Cat},j,\text{max}} & \text{for } t < t_{\text{sw}} \\ \phi_{\text{Cat},j,\text{max}} & \text{for } t \geq t_{\text{sw}} \end{cases} \quad (3.13)$$

where  $x$  is the pre-expression level and  $t_{\text{sw}}$  is the time-point when expression of the inferior carbon uptake system is switched on. For growth on glucose and lactose, the expression levels are presented in Table B.4, which yields a pre-expression level of only  $x = 98 \text{ MU}/1557 \text{ MU} = 6\%$ .

### Biomass and growth rate

A large part of the cell's biomass is proteins, which were discussed in the previous section. Other parts, such as RNA, DNA or lipids also contribute to the cell's biomass. Since optical density  $\text{OD}_{600}$  is a good measure for dry biomass, across all growth states, see Fig. B.9, we introduce biomass  $M$  and the biomass flux  $J \equiv \dot{M}$  and the conversion factor  $\alpha_M$ , from carbon influx to biomass flux,  $J = \alpha_M J_C$ . The instantaneous growth rate is defined as the derivative of the natural logarithm of biomass  $\lambda \equiv d \ln M / dt = J / M$ .

### 3.2.3 Analytical solution

We refer to the model of gene regulation derived in this section as Flux-Driven Regulation (FDR), since the key dynamic variable  $\sigma(t)$  which controls gene expression, Eqs. (3.5) and (3.6) is set by the condition of flux balance, Eqs. (3.3) and (3.4). Our approach of using  $\sigma$  as a proxy for the precursors themselves, thus avoiding explicitly referencing the dependence of the regulatory interactions  $\chi_{\text{Rb}}(t)$  and  $\chi_{\text{Cat}}(t)$  on the precursor molecules and circumventing the unknown details of these interactions and their parameters, is central to making the FDR model quantitatively predictive. Combining all the equations, as detailed in Section B.3.1, above results in a single nonlinear differential equation describing the kinetics after the shift ( $t > 0$ ):

$$\frac{d\sigma}{dt} = \sigma(t) [\mu_f \hat{\chi}_{\text{Cat}}(\sigma(t)) - \sigma(t) \hat{\chi}_{\text{Rb}}(\sigma(t))] \quad (3.14)$$

where  $\hat{\chi}_{\text{Cat}}$  and  $\hat{\chi}_{\text{Rb}}$  are the regulatory functions given in Eqs. (3.9) and (3.10). The lone parameter in Eq. (3.14),  $\mu_f$ , characterizes the uptake rate of the newly added substrate in the post-shift medium; its value can be fixed through its relation with the steady-state growth rate  $\lambda_f$  in the post-shift medium,  $\mu_f \equiv \lambda_f / (1 - \lambda_f / \lambda_C)$ , where  $\lambda_C$  is a known, strain specific constant of the growth laws; see Section 1.3.2. This logistic-like kinetic Eq. (3.14) can be solved analytically, see Section B.3.2, yielding the time courses of mass  $M(t)$ , ribosomes  $M_{\text{Rb}}(t)$ , and all other quantities introduced in this section. The complete solution requires also the specification of the initial condition  $\sigma(0)$ , the translational activity right after shift ( $t = 0^+$ ), which is discussed in Section B.3.3.

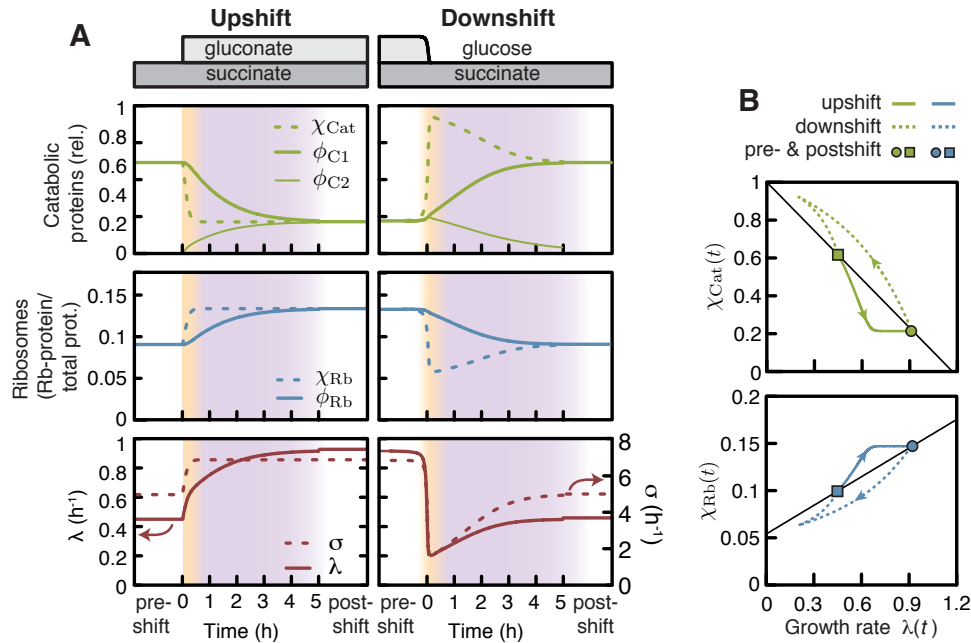


**Figure 3.5: Proteome remodeling.** (A) Synthesis and abundance of catabolic proteins (rel. to maximal expression), ribosomes (abs. in mg RNA per mg protein) as well as growth rate  $\lambda(t)$  and translational activity  $\sigma(t)$  during growth shifts for the upshift and downshift of Figs. 3.1 and 3.2. Rapid initial adaptation (orange band) of the regulatory functions of catabolic proteins  $\chi_{Cat}(t)$  and ribosomes  $\chi_{Rb}(t)$ , driven by the translational activity  $\sigma(t)$  (green, blue and red dashed lines) is followed by slow adaptation (purple band) of the abundance of catabolic proteins  $\phi_{Cat1}(t)$ ,  $\phi_{Cat2}(t)$  and ribosomes  $\phi_{Rb}(t)$  and growth rate  $\lambda(t)$  (green, blue and red solid lines). (B) The regulatory functions  $\chi_{Cat}(t)$  and  $\chi_{Rb}(t)$ , set by the translational activity  $\sigma(t)$ , plotted versus growth rate  $\lambda(t)$ . Thin black lines show the steady state growth laws; see Figs. 1.3 and 1.5 and Section 1.3.2.

As illustrated in Fig. 3.5A and discussed extensively in Section 3.5, both the up- and downshifts feature rapid responses in gene regulatory activities, reflected by abrupt changes in  $\chi_{Rb}(t)$  and  $\chi_{Cat}(t)$  (dashed blue and green lines) immediately after the shifts (orange band). This is followed by slow recovery in the abundances of catabolic proteins and ribosomes (solid lines) towards their final states (purple band). Note that although the forms of the regulatory functions are derived from steady-state growth laws, Figs. 1.3 and 1.5, the transition kinetics, driven by the translational activity  $\sigma(t)$  (red dashed line in Fig. 3.5A), does not simply slide along the steady-state lines of Figs. 1.3 and 1.5 but exhibits distinct hysteresis behavior (black vs colored lines in Fig. 3.5B).

The complete adaptation after nutrient shifts (purple band) is surprisingly slow, considering that the amount of desired proteins needed to overcome the metabolic bottleneck is small, e.g., Cat2 for upshift and Cat1 for downshift, Fig. 3.3 both comprise no more than a few percent of the entire proteome. They should thus take only a few percent of the doubling time to synthesize, if cells direct protein synthesis exclusively on the limited number of bottleneck proteins, as proposed by recent theories of optimal growth transition strategies [129, 130]. Instead, according to the FDR model, cells adopt a regulatory strategy featuring coordinated global remodeling of the proteome well beyond the adjustment of a few specific proteins, which will be discussed in Section 3.4.

### 3.3 Comparison of the FDR model with data

#### 3.3.1 Upshifts without pre-expression

Many uptake systems are not pre-expressed, i.e., not expressed in the absence of their cognate substrates. Consequently, cells cannot take up the added substrate at the instant of the upshift. In these cases, the biomass flux  $J(t)$  and thus  $\sigma(t)$  are continuous and the solution of Eq. (B.11) is able to describe the entire upshift kinetics without adjustable parameters: The black lines in the panels of Fig. 3.1 are solutions of the model for the addition of gluconate to succinate. The agreement between theory (black line) and data (red symbols) is not limited to this particular upshift, but extends to most upshifts studied in this work, such as those presented in Figs. 3.6 and 3.7, without adjustable parameters. The quantitative agreement of the model output with the different types of measured quantities is remarkable, given the simplicity of the model, and especially the lack of free parameters: the only parameters used to generate the model predictions are the steady-state growth rates measured in the pre-shift and post-shift medium.

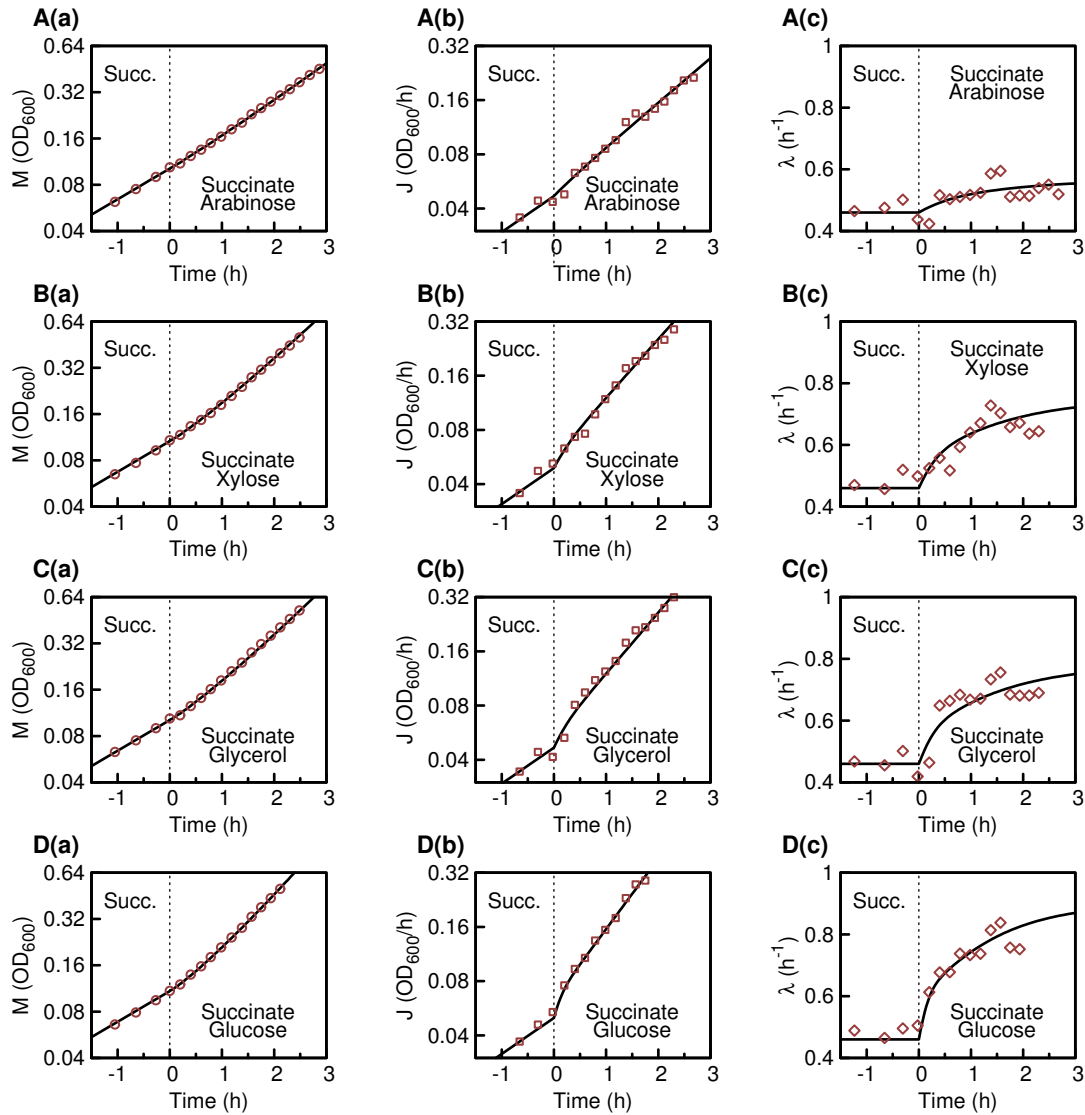


**Figure 3.6: Upshifts from succinate.** NCM3722 grown exponentially on 20mM succinate as the sole carbon substrate. At  $t = 0$  a second, subsequently co-utilized carbon substrate was added: **(A)** 0.2% arabinose, **(B)** 0.2% xylose, **(C)** 0.2% glycerol and **(D)** 0.2% glucose. First column **(a)** shows optical density  $OD_{600}$ , a measure of biomass  $M(t)$ , (red circles), second column **(b)** the derivative of  $OD_{600}$ , a measure for biomass flux  $J(t)$  (red squares), and the third column **(c)** shows growth rate  $\lambda(t) = J(t)/M(t)$  (red diamonds). Theory lines for  $M(t)$ ,  $J(t)$  and  $\lambda(t)$  were calculated using Eq. (B.41), Eq. (B.35) and Eq. (B.42) using the initial condition Eq. (B.18) for upshift without pre-expression. Initial and final growth rates were measured during steady state growth on the respective carbon substrates and are shown in Table B.1 and Table B.7

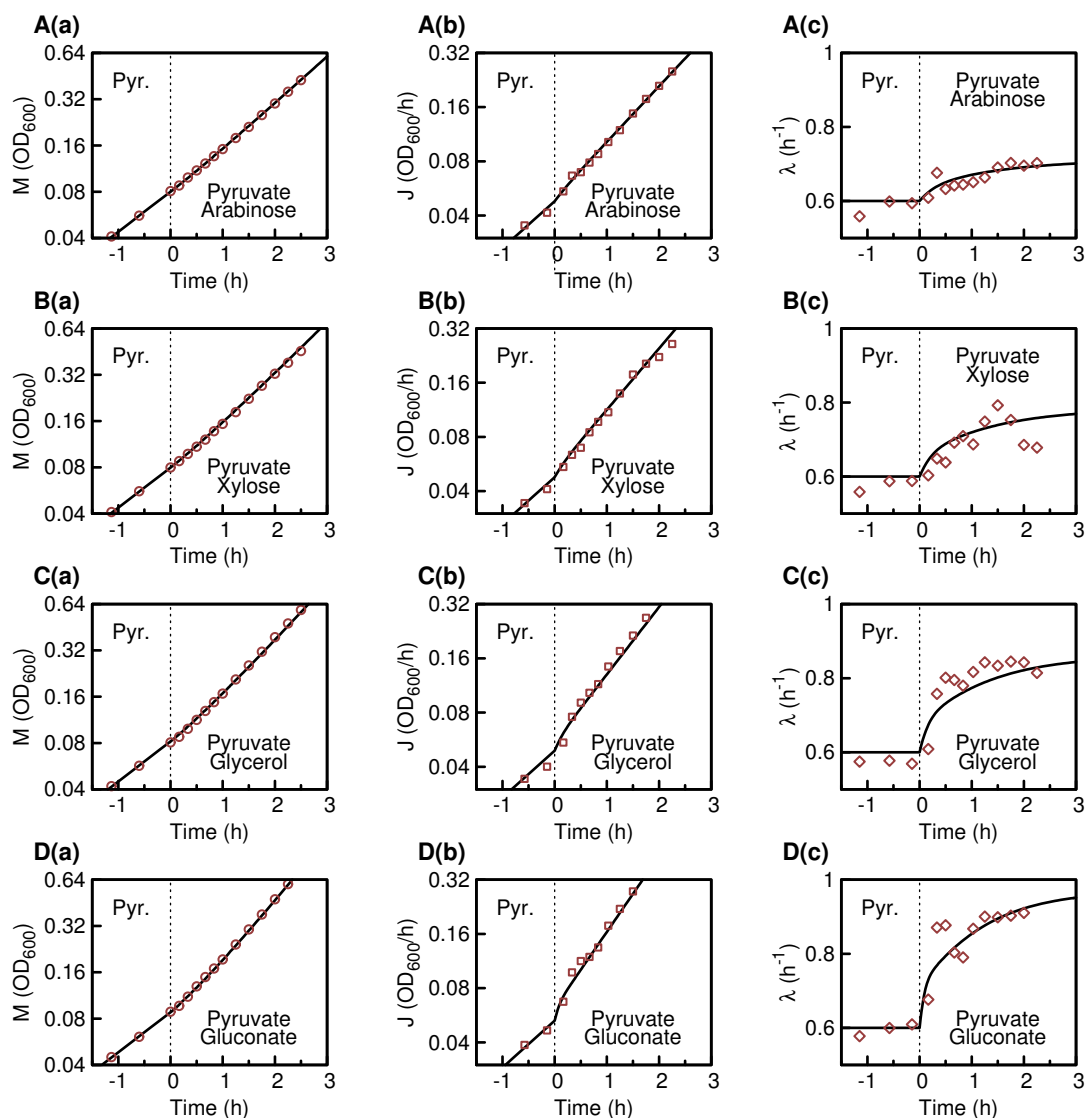


**Figure 3.7: Upshifts from pyruvate.** NCM3722 grown exponentially on 20mM pyruvate as the sole carbon substrate. At  $t = 0$  a second, subsequently co-utilized carbon substrate was added: **(A)** 0.2% arabinose, **(B)** 0.2% xylose, **(C)** 0.2% glycerol and **(D)** 20mM gluconate. First column **(a)** shows optical density  $OD_{600}$ , a measure of biomass  $M(t)$  (red circles), second column **(b)** the derivative of  $OD_{600}$ , a measure for biomass flux  $J(t)$  (red squares), and the third column **(c)** shows growth rate  $\lambda(t) = J(t)/M(t)$  (red diamonds). Theory lines for  $M(t)$ ,  $J(t)$  and  $\lambda(t)$  were calculated using Eq. (B.41), Eq. (B.35) and Eq. (B.42), using the initial condition Eq. (B.18) for upshift without pre-expression. Initial and final growth rates were measured during steady state growth on the respective carbon substrates and are shown in Table B.1 and Table B.7

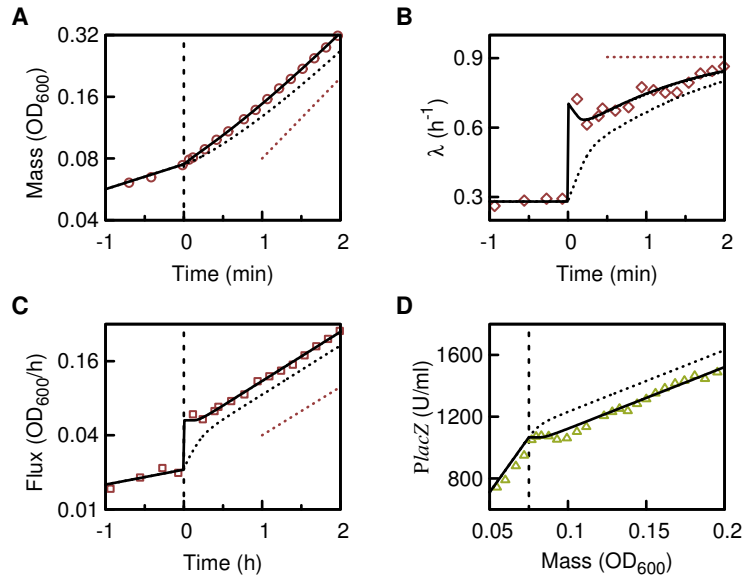


**Figure 3.8: Mannose adding oxaloacetic acid (OAA).** NCM3722 grown exponentially on 0.1% mannose as the sole carbon substrate. At  $t = 0$  a second, subsequently co-utilized carbon substrate was added: 20mM oxaloacetic acid (OAA). (A) Biomass, (B) growth rate and (C) biomass flux quickly increases, beyond the expected kinetics for no pre-expression (black dashed lines). Using the initial condition Eq. (B.19) and fitting  $\sigma(0)$ , the theory Eq. (B.41), Eq. (B.35) and Eq. (B.42) can describe the experimental data (red symbols). (D) Catabolic proteins, reported by lacZ expression (green symbols), show a strong repression after the upshift, as predicted from the theory. Red dashed lines show the final growth rate.

### 3.3.2 Upshifts with pre-expression

The addition of some carbon substrates did result in an abrupt jump of flux  $J(t)$  at the instant of upshift, suggesting some level of pre-expression of the uptake proteins, see Fig. 3.8 for an example of cells grown on mannose, with oxaloacetic acid (OAA) added. In these cases, the biomass flux  $J(t)$  and thus  $\sigma(t)$  are not continuous and the solution of Eq. (B.11) requires the fitting of the initial condition  $\sigma(0)$ . Fitting the initial condition to the biomass  $M$  allows accurate description of the increase of biomass  $M$ , flux  $J$  and growth rate  $\lambda$  shown in panels A-C. The solution is plotted in Fig. 3.8 with solid black lines, and compared to the continuous solution expected for no pre-expression, displayed as dotted black lines. Due to the sudden increase of the carbon influx after OAA addition leads to a sudden increase of the precursor pool. As a consequence the theory predicts strong repression of the catabolic proteins, which is experimentally validated in panel D.

### 3.3.3 Upshifts with titratable pre-expression

To test the hypothesis that pre-expression leads to the sudden increase of flux after upshift to some carbon substrates, we used a titratable construct to express varying levels of the succinate transporter DctA in the pre-shift phase ( $t < 0$ ) which had mannose as the sole carbon source; see Fig. 3.9A. After adding succinate to the medium and setting DctA expression to a common final level, the culture with higher DctA pre-expression level adapted faster (compare purple and green circles in Fig. 3.9B), with both of which faster than the expected time course in the absence of pre-expression (orange curve). Both the biomass flux and the instantaneous growth rate of the cultures with pre-expression exhibited saltatory increases at the time of upshift, followed by gradual approaches towards the final steady state behavior, see Fig. 3.9C and D respectively.

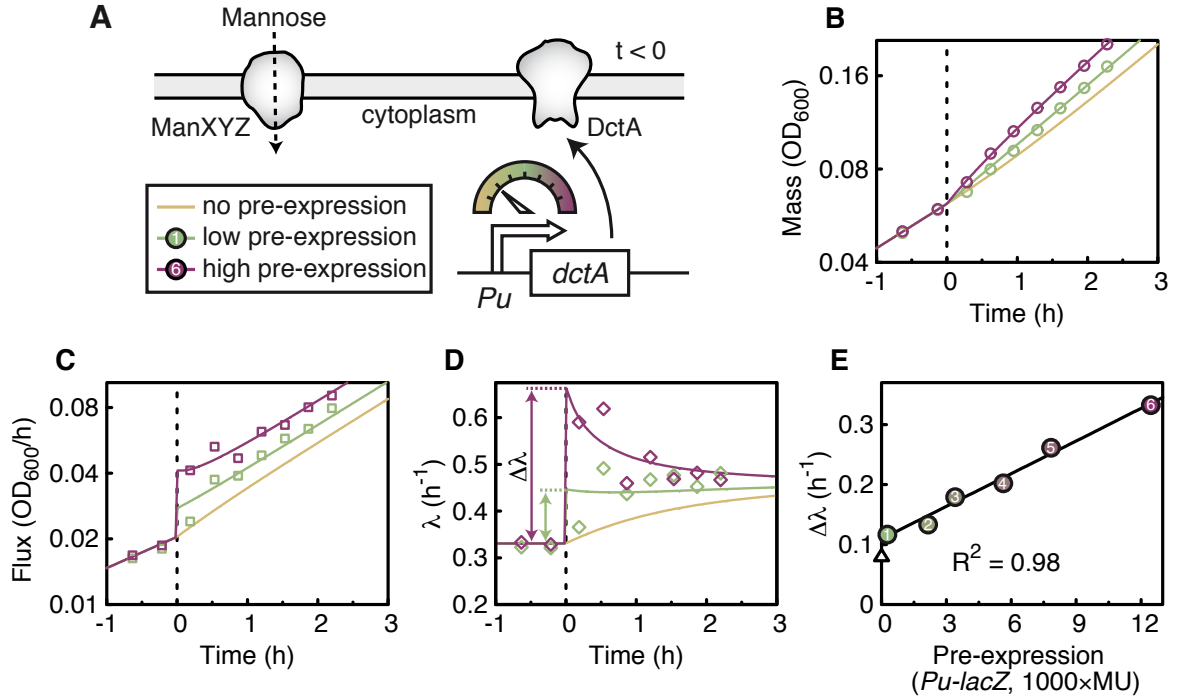


**Figure 3.9: Effect of pre-expression on upshift kinetics.** (A) *E. coli* NQ530 grown exponentially in mannose minimal medium with different levels of succinate transporter (DctA) pre-expressed via the titratable Pu promoter, as described in Section B.5. At time  $t = 0$ , medium was supplemented with 20mM succinate and DctA expression is set to a common level for all upshifts. (B) DctA pre-expression positively effects post-shift growth. (C) The biomass flux  $J(t)$  (squares) shows a saltatory increase followed by exponential growth at final rate  $\lambda_f^*$ . (D) For the strain with high level of pre-expression, the instantaneous growth rate  $\lambda(t)$  (diamonds) transiently overshoot before relaxing to the final value  $\lambda_f^*$ . The kinetic theory quantitatively captures the upshift kinetics for all pre-expression levels, when using the initial condition  $\sigma(0)$  as the single fit parameter (solid lines). (E) Validation of theoretical prediction. The magnitude of saltatory increase in growth rate  $\Delta\lambda$  (indicated in panel D) depends linearly on the pre-expression levels ((1), (6) shown in panels B-D, intermediate levels (2-5) shown in Fig. B.12; Pre-expression was characterized by the level of Pu-lacZ reporter obtained at the same Pu titration level; Table B.3. Zero pre-expression extrapolates towards  $\Delta\lambda$  for *dctA* knock-out mutants NQ1324 (triangle), see Fig. B.12.

High pre-expression levels even led to a transient over-shoot of the instantaneous growth rate (purple diamonds in Fig. 3.9D). This overshoot is a direct result of the low translational activity and thus sub-optimal usage of ribosomes during slow pre-shift growth. Without this sub-optimal use the cell would not have enough ribosomes to balance the sudden increase in carbon influx.

Pre-expressing DctA leads to an additional carbon influx at the time of upshift, which is captured by the initial condition  $\sigma(0)$  in the model. Using this as a fit parameter, the FDR model quantitatively describes the two cases of upshift kinetics shown in Fig. 3.9 with high and low DctA pre-expression (purple and green lines), as well as intermediate levels of pre-expression, see Fig. B.12. The theory predicts that the magnitude of the saltatory increase of the growth rate ( $\Delta\lambda$ , defined in Fig. 3.9D) to be linear with the pre-expression level of DctA, which is directly verified in Fig. 3.9E.

### 3.3.4 Diauxic shifts with co-utilized substrates

We next characterized the kinetics of nutrient downshifts, resulting, e.g., from the depletion of some nutrient component in the medium as in Monod's study of diauxic growth [101]. We grow cells on succinate and glucose and observe bi-phasic growth of biomass (Fig. 3.2A), characteristic

for diauxic shifts. As succinate is co-utilized with glucose, cells first grow on both substrates first, and switch to succinate after glucose is depleted around  $t = 0$  (dashed vertical line). At this point the instantaneous growth rate  $\lambda(t)$  decreases sharply, followed by a recovery to the growth rate supported by succinate (red diamonds in Fig. 3.2B). During the recovery, biomass flux (red squares in Fig. 3.2C) showed growth at an increased rate (slope of the orange line), before settling to its final value (slope of the green dotted line). Similarly, expression of catabolic proteins (Fig. 3.2D) showed a transiently increased expression rate (slope of the orange line) before settling to the final rate (slope of the dotted green line).

These dynamics are in contrast to upshifts, which show monotonous adaptation, see Fig. 3.1A–B, with constant levels of catabolic and ribosomal gene expression rates during the recovery; see Fig. 3.1D–E. Nevertheless the same FDR model quantitatively captures diauxic shifts, too: Depletion of substrate S1 leads to a drop of the central precursor pool to the level supported by the influx of the remaining substrate S2. This decrease results in a down-regulation of ribosome synthesis on the one hand and up-regulation of catabolic protein synthesis on the other hand, as expected based on the qualitative knowledge of how these processes are regulated [42, 43, 110–112, 114]. Biosynthesis flux recovers (Fig. 3.2C) at rate  $\mu_f$  (see Eq. (B.11) , slope of orange line), because catabolic protein expression rate (Fig. 3.2D) increases close to maximal levels (slope of the orange dotted line). Using initial and final growth rates and the known affinity of the glucose uptake system PtsG [131] to model glucose depletion, the FDR model is able to capture all major features of the downshift kinetics presented in Fig. 3.2 (black lines), including the non-trivial change of synthesis rate of catabolic proteins. This degree of quantitatively accurate description extends to diauxic shifts between other pairs of co-utilized carbon substrates; see Fig. 3.10 for data for another four combinations of substrates. In these cases, the initial condition  $\sigma(0)$  is given by the contribution of the remaining substrate to co-utilization growth and full description involves no fitting parameters.

As outlined in Section 3.2.2, depletion of a carbon substrate leads to an impaired uptake rate, following a Michaelis-Menten type uptake kinetics, Eq. (3.2). This is most prominent in diauxic shifts including gluconate (panels A and C in Fig. 3.10), due to the low uptake affinity of the gluconate transporter gntU, see Table B.5 for a list of uptake affinities used in this work. The FDR model can be solved numerically and can describe diauxic shifts of co-utilized carbon substrates with low or high affinities without adjustable parameters.

### 3.3.5 Diauxic shifts with non co-utilized substrates

We can further expand the FDR model to describe diauxic shifts between non co-utilized carbon substrates. We choose glucose and lactose as a combination, as carbon hierarchy and diauxic shifts in this combination is well studied [101]. When grown on both glucose and lactose, the cell utilizes glucose, and switches to lactose utilization only when glucose is depleted, see Fig. 3.11. After glucose depletion, growth rate recovers quickly, within 30 min, to its final value. During the recovery, flux  $J$  grows exponentially at an increased rate, that is compatible with the theoretical prediction of the maximal uptake rate, Eq. (1.10), (orange line). In synchrony with increased flux recovery, catabolic protein expression is also increased initially, compatible with the maximal expression level of the steady state growth law.

The switching time point of substrate preference from glucose to lactose, shortly before glucose depletion, determines the initial condition  $\sigma(0)$  and was used as the lone fitting parameter. The theoretical prediction (black lines) can accurately describe the entire dynamics of the glucose lactose diauxie.

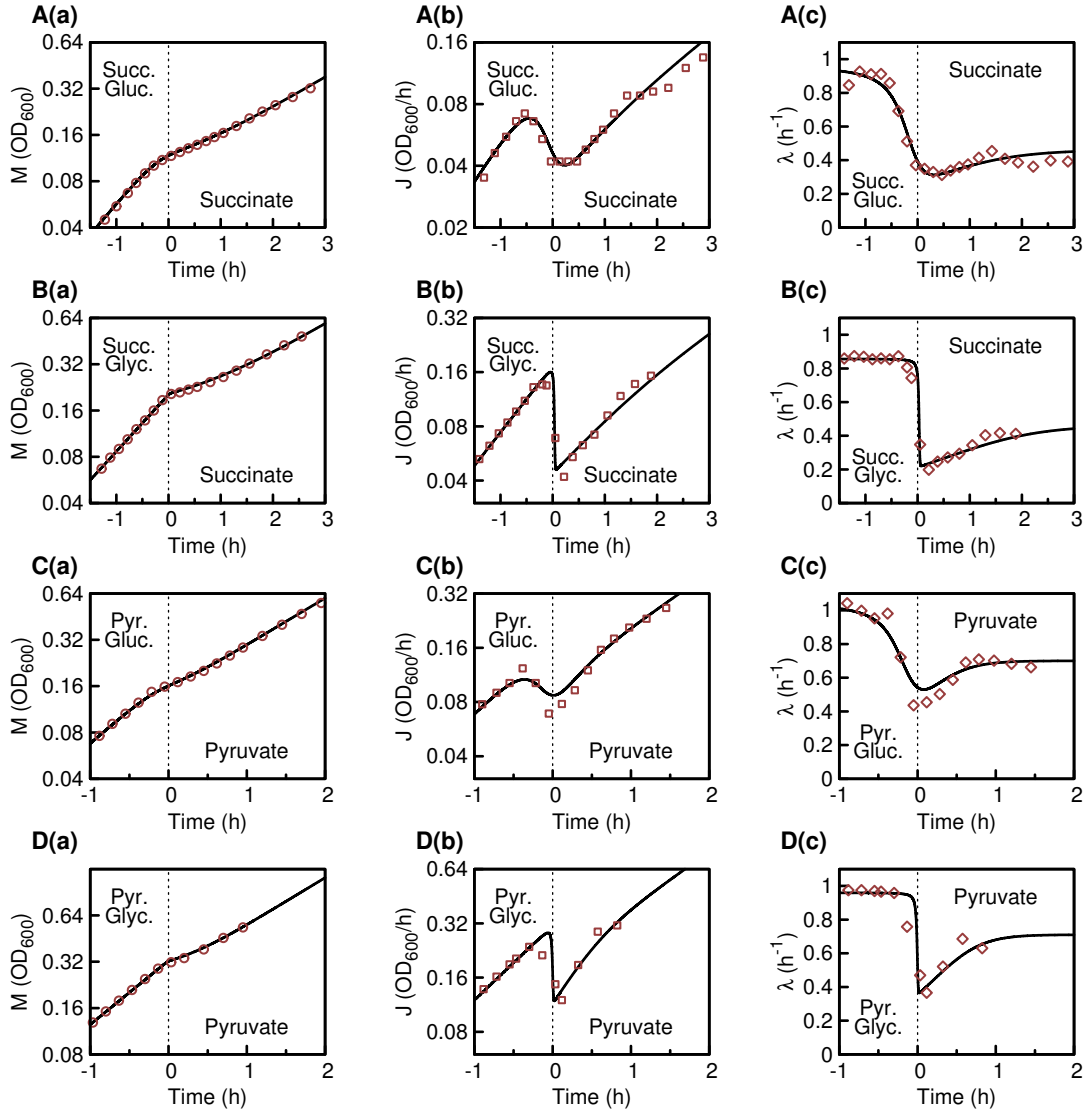


**Figure 3.10: Diauxic shift with co-utilized carbon substrates.** NCM3722 grown exponentially on (A, B) 20mM succinate (abbr. Succ.) or (C, D) 20mM pyruvate (Abbr. Pyr), combined with either (A, C) 0.56mM gluconate (abbr. Gluc) or (B, D) 1.11mM glycerol (abbr. Glyc). At around  $t = 0$  Gluconate or Glycerol were depleted. (a) shows optical density  $OD_{600}$ , a measure of biomass  $M(t)$  (red circles), (b) the derivative of  $OD_{600}$ , a measure for biomass flux  $J(t)$  (red squares), and the third column (c) shows growth rate  $\lambda(t) = J(t)/M(t)$  (red diamonds). Theory lines for  $M(t)$ ,  $J(t)$  and  $\lambda(t)$  were calculated solving the differential equation for the translational activity  $\sigma(t)$ , Eq. (B.11), and those defining the internal fluxes and protein content Eqs. (3.1) and (3.6) numerically. The uptake of the depleting substrate (glycerol or gluconate) was calculated from Eq. (3.2). This was necessary since some substrates (e.g. gluconate) have low affinities (see Table B.5 for a list of the used affinities) and thus deplete slowly (see panel B and D). Initial and final growth rates were measured during steady state growth on the respective carbon substrates and are shown in Table B.7.

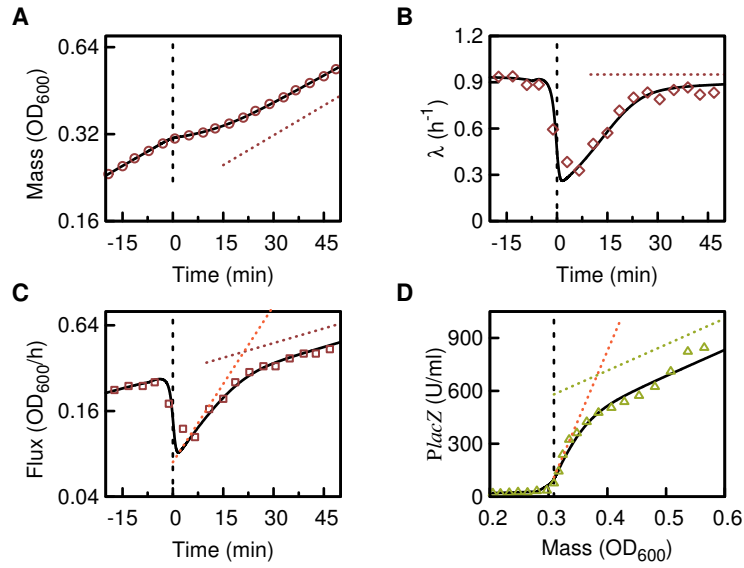


**Figure 3.11: Diauxic shift between hierarchically utilized carbon substrates.** (A) Growth curve for NCM3722 cells growing on 0.03% glucose and 0.2% lactose; initially, only glucose was utilized [101]. Around time  $t = 0$  (dashed vertical line) glucose was depleted and lactose uptake and metabolism was activated. Dashed red line indicates the rate of growth on lactose only. (B) As glucose was depleted, the instantaneous growth rate dropped abruptly, followed by a sharp recovery to the final growth rate ( $\lambda_f^* = 0.95/\text{h}$ , dotted horizontal line) within 30 min. (C) After glucose depletion biomass flux increased at elevated rate, before settling to the final rate (slope of the red dotted line, given by  $\lambda_f^*$ ). The slope of the orange dotted line is given by  $\mu_f = (\lambda_f^{*-1} - \lambda_C^{-1})^{-1} = 5.1/\text{h}$ , the predicted initial increase in flux, where  $\lambda_C = 1.17/\text{h}$  is obtained from the steady-state growth law, Eq. (1.10). (D) Lactose catabolic enzyme LacZ (green triangles) is tightly repressed before the shift, then increases rapidly following the shift, before settling to the final expression level indicated by the slope of the green dotted line (1557 U/ml OD<sub>600</sub>, obtained from steady state growth in lactose only Table B.4). Slope of the dotted orange line is the predicted maximal expression level,  $\mu_f/\lambda_f^* \times 1557 \text{ U/ml OD}_{600} = 7866 \text{ U/ml OD}_{600}$ . The black curves in the four panels are predictions of the FDR theory using the time-point of lac operon activation as the single fitting parameter; see Eq. (3.13).

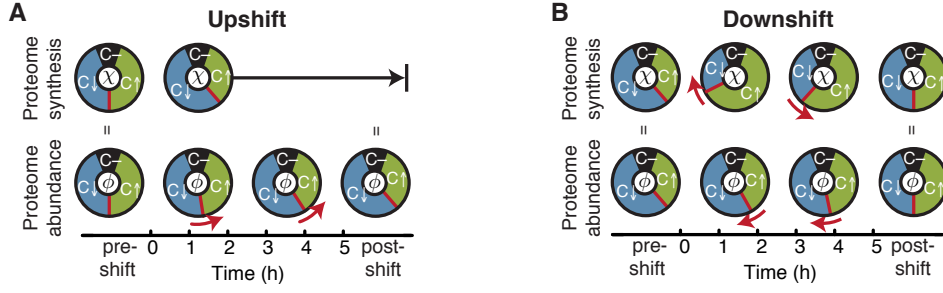


**Figure 3.12: Graphical synopsis of the proteome remodeling.** Pie charts show the allocation of protein synthesis (top row) and proteome abundance (bottom row), as predicted by the FDR model in Eqs. (3.15) to (3.18). Red boundary and arrows show dynamic. In upshifts regulatory functions  $\chi$  rapidly relax to their final states; in downshifts regulatory functions initially overshoot and relax slowly to the final states, see Section 3.5 for extended discussion.

### 3.4 Proteome sectors during growth transitions

The adaptation after nutrient shifts is surprisingly slow, considering that the amount of newly desired proteins needed to overcome metabolic bottleneck is small, e.g., Cat2 for upshift and Cat1 for downshift, both being typically at most a few percent of the entire proteome. Indeed, the FDR model does not channel resources just into the synthesis of the limited number of bottleneck proteins, as proposed by a recent theory of optimal transition strategy [129]. Rather, since the FDR model is based on steady state proteome partitioning laws validated by Hui et al [44], it prescribes a regulatory strategy featuring coordinated global remodeling of the proteome well beyond the adjustment of a few specific catabolic proteins and the ribosomes, but including for example a large number of anabolic proteins and catabolic proteins unrelated to the specific sugars in the medium. Classifying the proteome according to the steady-state response under carbon limitation [44], we group proteins increasing/decreasing/not changing under carbon limitation by  $C\uparrow$ ,  $C\downarrow$ , and  $C^-$  “sectors”.

Since catabolic proteins are part of  $C\uparrow$ -sector and ribosomes are part of  $C\downarrow$ -sector, dynamics of these proteome sectors, allocated by the regulatory functions  $\chi_{C\uparrow}$  and  $\chi_{C\downarrow}$ , is given in the FDR model by the regulatory functions  $\chi_{Cat}(t)$  and  $\chi_{Rb}(t)$  according to the linear relations Eqs. (1.20) and (1.21), with all constants fixed by the steady state proteome partitioning. This global co-regulation, established by the growth laws during steady state exponential growth is assumed by the FDR model to hold during growth transitions for the regulatory functions,

$$\chi_{C\downarrow} = a_{C\downarrow} + b_{C\downarrow}\chi_{Rb}, \quad (3.15)$$

and

$$\chi_{C\uparrow} = a_{C\uparrow} + b_{C\uparrow}\chi_{LacZ}. \quad (3.16)$$

The dynamics of the proteome sectors  $C\uparrow$  and  $C\downarrow$ ,  $\phi_{C\uparrow}(t)$  and  $\phi_{C\downarrow}(t)$  respectively, is then prescribed by

$$\frac{d\phi_{C\downarrow}}{dt} = \lambda(\chi_{C\downarrow} - \phi_{C\downarrow}) \quad (3.17)$$

and

$$\frac{d\phi_{C\uparrow}}{dt} = \lambda(\chi_{C\uparrow} - \phi_{C\uparrow}). \quad (3.18)$$

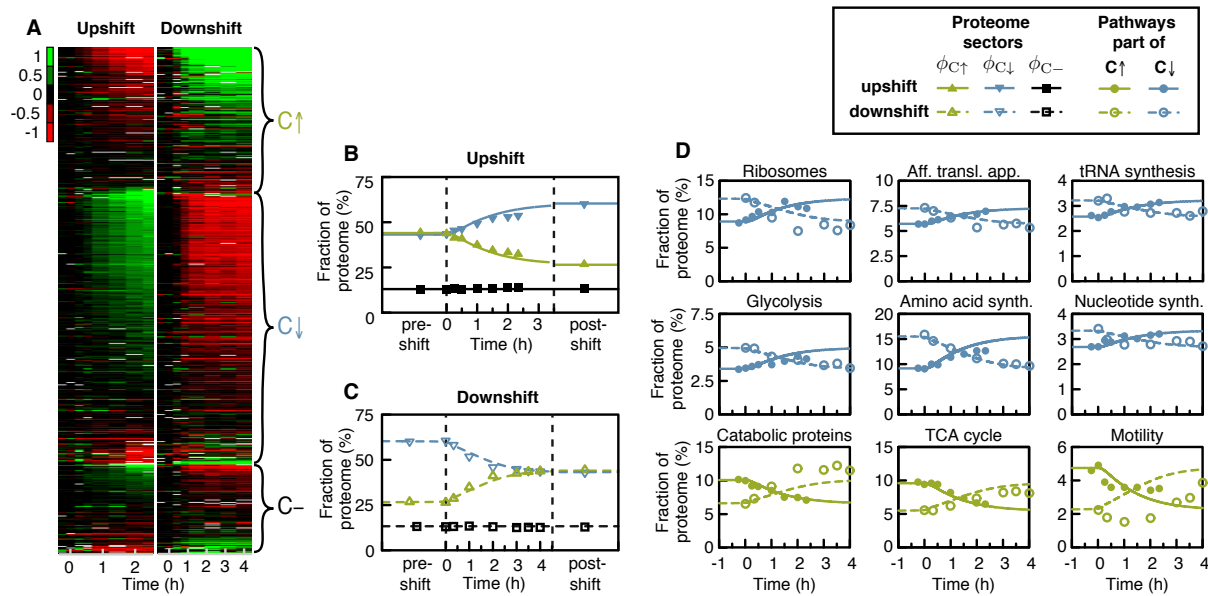


**Figure 3.13: Proteome composition during adaptation.** (A) Expression of individual proteins during the up- and downshifts of Figs. 3.1 and 3.2, relative to the pre-shift steady state (scale:  $\log_2$ ). Proteins are grouped according to their steady state response to decreasing growth rate by carbon limitation: C<sup>↑</sup> (increase; includes reporter LacZ; green), C<sup>↓</sup> (decrease; includes ribosomes; blue) and C<sup>-</sup> (no response; black) [44]. (B–C) Absolute proteome fractions of the protein sectors  $\phi_{C^\uparrow}$ ,  $\phi_{C^\downarrow}$  and  $\phi_{C^-}$  (symbols) respond following the fit parameter free prediction (lines), derived under the assumption that all proteins in sectors  $\chi_{C^\uparrow}$  and  $\chi_{C^\downarrow}$  and C<sup>-</sup> follow a global remodeling, derived in Eqs. (3.17) and (3.18). (D) Mass fraction of individual pathways or protein groups during upshift (solid lines and symbols) and downshift (dashed lines and open symbols). Colors denote sector affiliation. All biosynthetic pathways follow the theoretical prediction assuming co-regulation. Motility (top right) is a clear exception, showing transient repression in downshifts, opposed to an expected increase in expression (dashed line). Mass spectrometry data was taken by, and analysed with Vadim Patsalo and Jamie Williamson (Scripps Institute, UC San Diego, USA).

While the allocation functions  $\chi_{C^\uparrow}$  and  $\chi_{C^\downarrow}$  are not directly observable, we can follow the resulting proteome mass fractions  $\phi_{C^\uparrow}$  and  $\phi_{C^\downarrow}$  through the course of the growth transition, using the quantitative mass spectrometry approach of Hui et al [44]. Figure 3.13A shows the abundances of many hundreds of proteins during both up- and downshifts presented in Figs. 3.1 and 3.2, relative to their respective pre-shift abundances. We observe that proteins responded dynamically according to their steady state categorization; see Fig. 3.13A–C: After carbon downshift, C<sup>↑</sup> proteins increased and C<sup>↓</sup> proteins decreased, while the opposite occurred in upshift. The majority of C<sup>-</sup> proteins showed little to no response to nutrient shifts. The change of protein abundance is dominated by expression of new proteome, with degradation playing a negligible role, see Fig. 3.14. We estimated the total abundances of proteins belonging to each of these 3 sectors (see Section B.5) and plotted their time dependences following upshift and downshift; symbols in Fig. 3.13B, C. The dynamics of these proteome mass fractions follow closely model predictions (lines) throughout the transitions. The same approach was applied in Fig. 3.13D to characterize the total abundances of proteins belonging to various major metabolic pathways or functional groups, see Section B.5 for details. The dynamics of these groups in upshifts (closed symbols) or downshifts (open symbols) again followed largely the model predictions, except for motility proteins, which clearly deviated under nutrient downshift.

The quantitative matches of the model with the proteome data without adjustable parameters suggests that the majority of the proteome is indeed co-regulated as assumed in the model, following a *single* dynamic control variable throughout the growth shifts. In our model, this

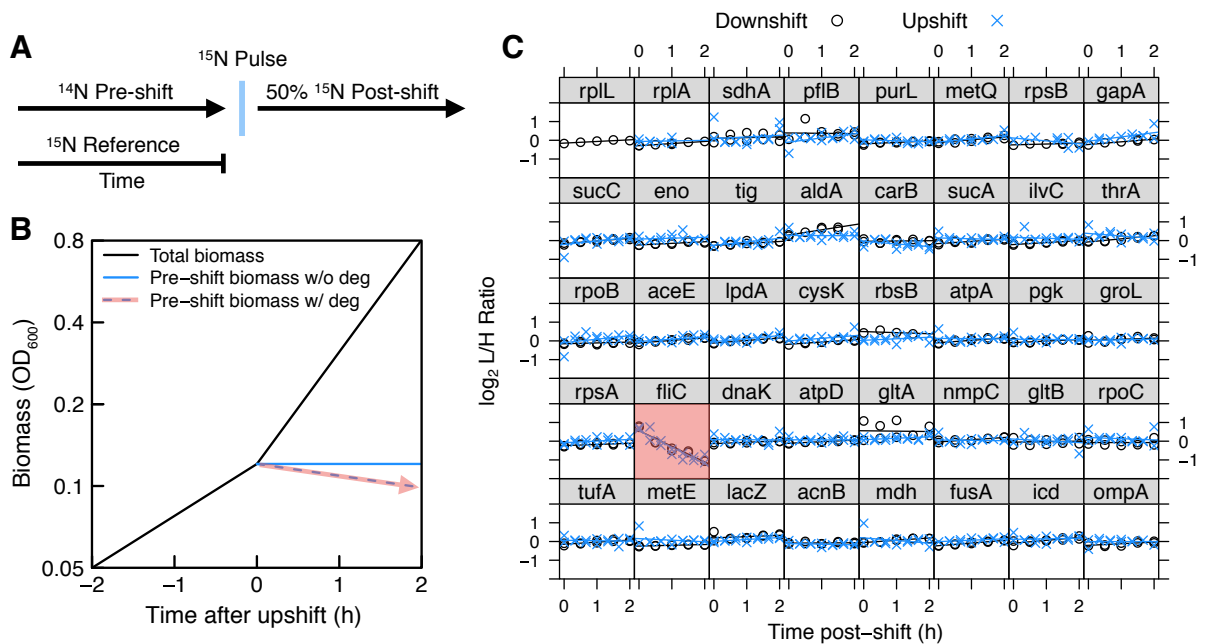


**Figure 3.14: Protein degradation.** (A) Pulse-labelling allows the differentiation of pre-pulse and post-pulse protein mass, as detailed in Section B.5. We added concentrated  $^{15}\text{NH}_4\text{Cl}$  into the culture at the moment of gluconate upshift or a few minutes prior to glucose exhaustion during the downshift. Comparing to a third isotope species (spiked-in  $^{15}\text{N}$ -reference culture) allows tracking the levels of pre-shift proteins over time. (B) A schematic showing the levels of total cellular protein (black) and cellular protein existing at pulse time (blue) as the culture is instantaneously upshifted. Stable protein levels are evidenced by a zero-slope line (blue solid line), while degrading or exported cellular proteins exhibit a negative-slope line (blue dashed line, red arrow). (C) The post-shift levels of 40 cellular proteins of highest mass fraction were quantified using the pulse-labelling approach. Light (L,  $^{14}\text{N}$ ) over heavy (H,  $^{15}\text{N}$ ) relative protein levels are plotted as a function of time. These proteins span diverse biological function, cellular localization, size and structure. Together, they account for 35-40% of the total protein mass detected throughout the shift (estimated by adding up their mass abundances for each condition). With the exception of flagellin (fliC, red box), we did not observe decreasing protein levels for either the upshift or downshift series on the two-hour timescale for large-abundance proteins which we could confidently quantify. Flagellin is exported to the cell periphery by a dedicated transport system, and likely shed into the medium during steady-state growth. As shed proteins are not collected at the same efficiency as proteins in cells, the decline of pre-labeled FliC serves as a positive control for the method. Protein degradation data was taken, and analysed by Vadim Patsalo and Jamie Williamson (Scripps Institute, UC San Diego, USA).

dynamic variable is the translational activity  $\sigma(t)$ , which is itself a proxy for the intermediate metabolite pools (e.g., the ketoacids and amino acids) as illustrated in Fig. 3.3. Since molecularly the control is exerted via the secondary messengers cAMP and ppGpp, our results suggest that these two signaling pathways are tightly coupled, and that they largely dictate the responses proteome-wide following carbon shifts, even for many pathways where direct regulation by cAMP or ppGpp is not known. Interestingly, even pathways not known to be directly regulated by cAMP or ppGpp, e.g. amino acid synthesis, are seen to follow the predicted global response following carbon shifts, possibly due to competition for transcriptional or translational resources [42, 43].

### 3.5 Adaptation strategy according to the FDR model

Given the predictability of the FDR model, we next use it to reveal the essential feature of the growth transition kinetics, a constrained interplay between catabolic and ribosomal proteins, which underlies the different behaviors observed Figs. 3.1, 3.2, 3.6 to 3.11 and 3.13. In this

section, we will use the mathematical solutions to reveal a simple, qualitative picture underlying the adaptation kinetics observed in all these shifts.

Central to the analysis of the adaptation strategy is the observation from Section 1.3.3 and Fig. 3.13 that the proteome follows a global regulation. After a nutrient shift, the cell needs to produce individual proteins, such as those catabolic proteins Cat1, Cat2, etc. that transport the carbon substrates present in the medium, or ribosomes. These individual proteins are part of the proteome sectors and which are globally regulated by the cell. Thus protein synthesis is always directed towards the synthesis of the entire sector, rather than just a few catabolic proteins. This can have dramatic effects, for example if a carbon substrate S1 is suddenly depleted or replaced by a different substrate S2, then the entire sector is synthesized together with the new catabolic protein Cat2, even if it already was previously synthesized together with Cat1. This repeated, futile production at a moment when the cell would most benefit from channeled synthesis of a bottleneck-protein leads to the slow adaptation of bacterial growth transitions.

The kinetic process can be most directly revealed by plotting the concentration of ribosomes Rb against the concentration of the newly synthesized catabolic protein Cat2 (needed for the uptake of post-shift substrate S2). Figure 3.15A shows the kinetic trajectories of two simplest shifts, corresponding to cells in slow and fast pre-shift growth (orange and green lines, respectively) switched abruptly to the same post-shift medium and hence with the same final state (indicated by the black cross). We see that regardless of the pre-shift state, the trajectories contain two distinct regimes separated by the colored circles: Starting from the initial condition (colored squares, specified by pre-shift growth rate), the trajectories exhibit steep increase of the new uptake protein Cat2 in the first regime, reflecting active adaptation by the cell to changes in the environment. Through much of this regime, the trajectories follow the dashed grey lines, which correspond to maximal synthesis rates for Cat2 and minimal rate for the ribosomes. We will discuss this first regime in Section B.4.2 in detail.

When the trajectories hit the dotted black line (open circles), they entered the second regime and slide along this line towards the final steady state (indicated by the black cross). This dotted line, which is obtained by connecting the final state with the origin, describes proportionality of catabolic and ribosomal proteins, along which the translational activity  $\sigma(t)$  has reached its final value, see Fig. 3.15B. Since the regulatory functions depend only on the value of  $\sigma(t)$  (see Eqs. (3.9) and (3.10)), they have also reached their final values throughout the second regime, while the instantaneous growth rate  $\lambda(t)$  continues to recover, see Fig. 3.15C. Thus the second regime represents a passive *dilution* of the proteome composition towards the final state without changing the rate of protein synthesis and is discussed in Section B.4.3.

Recovery of growth rate is generally faster during adaptation, due to the maximal expression of catabolic proteins, and thus the resulting total recovery time, plotted in Fig. 3.15D, depends on how much recovery is achieved in each regime. Recovery is fastest when both pre- and post-shift growth rates are fast, a setting typical for diauxic shifts like Fig. 3.11. This situation is described by the green trajectory in Fig. 3.15A and represented by the green "D" in Fig. 3.15D. In contrast, recovery in upshift experiments like Fig. 3.1, where the cell adapts from slow pre- to fast post-shift growth, is slower. This situation is captured by the orange trajectory in Fig. 3.15A and represented by the orange "U" in Fig. 3.15D. A detailed discussion of the time scales is given in Section B.4.4.

In summary, growth transitions from one state to another involve a rapid adaptation of the proteome to the new medium, followed by a slow dilution of the inherited proteome. The cell's decision of how much new proteins to synthesize in a new environment depends on the inherited proteome defined by pre-shift growth, and can lead to seemingly very different transition kinetics despite the same underlying principle.

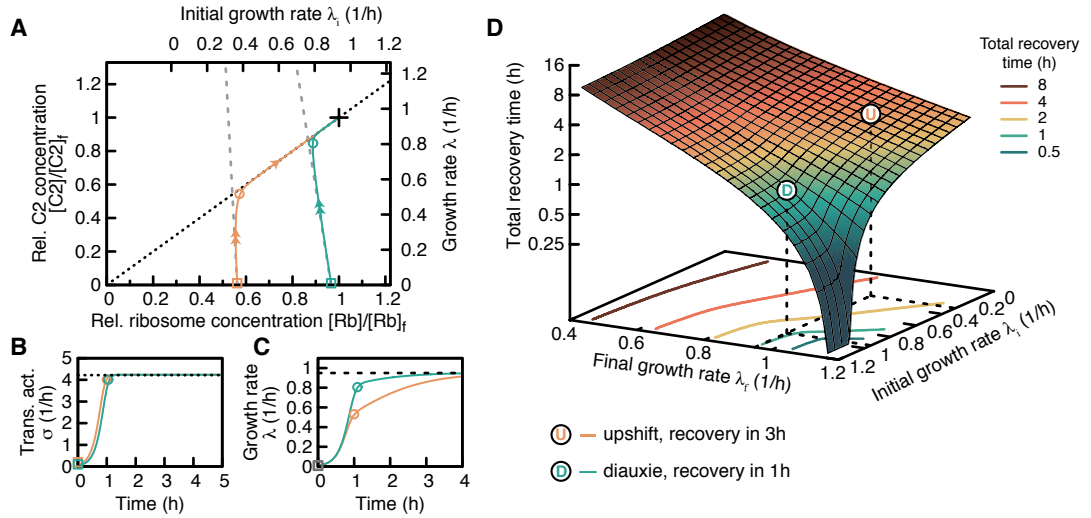


**Figure 3.15: Trajectories and time scales of growth transition.** (A) Growth recovery trajectories in the phase space spanned by two key dynamic variables: the abundance of the new catabolic protein Cat2,  $\phi_{\text{Cat}2}$ , which is proportional to the instantaneous growth rate  $\lambda(t)$  (right y-axis), and the abundance of ribosomes,  $\phi_{\text{Rb}}$ . Both quantities are normalized to their final steady-state values,  $\phi_{\text{Cat}2,f}$  and  $\phi_{\text{Rb},f}$ . Initial condition of the latter is set by the pre-shift growth rate  $\lambda_i^*$  (top x-axis) according to the steady state growth law. Two trajectories starting with low  $\phi_{\text{Cat}2}$  and  $\lambda_i^* = 0.3/\text{h}$ ,  $\lambda_i^* = 0.95/\text{h}$  (orange, green squares), both ending at  $\lambda_f^* = 0.95/\text{h}$  (black cross), are shown according to the theory. In both cases, the trajectories rise steeply upward initially (*first* regime), following the dashed grey lines, which reflect the regulatory functions ( $\hat{\chi}_{\text{Cat}}$ ,  $\hat{\chi}_{\text{Rb}}$  in Fig. 3.3B and Eqs. (3.9) and (3.10)) set to their extreme values; see Section B.4.2. Upon reaching the dotted diagonal (indicated by the colored circles), the trajectories turn sharply and glide along the diagonal towards the final state (black cross) (*second* regime). (B) Translational activity  $\sigma(t)$  rises sharply during the first regime and settles to the final value (dashed line) upon entry to the second regime at times indicated by the circles. (C) The instantaneous growth rate  $\lambda(t)$  recovers fast during the first regime (square to circle), followed by slow recovery in the second regime to the final state (dashed line). (D) The total recovery time, defined as the time for the growth rate to reach 90% of its final value, plotted for various initial and final growth rates. The fastest recovery occurs when the pre- and post-shift growth rates  $\lambda_i^*$  and  $\lambda_f^*$  are both large.

## 3.6 Discussion

The ability of the kinetic theory based on the coarse-grained FDR model to accurately describe a broad range of growth transitions is rather remarkable given the complexity of the underlying signaling networks [40, 42, 112]. The predictability of the theory depends crucially on the phenomenological growth laws established from previous studies [34, 40, 42, 44]. To extend to the kinetic regime, we introduced a single dynamic variable, the translational activity  $\sigma$ , which lumps together actions of the key signaling molecules and metabolites. By construction, the coarse-grained model does not attempt to address the very rapid kinetic processes, e.g. ribosomal oscillation during upshift to rich medium [123]. But the FDR model has been very successful in capturing the kinetics of cell growth and gene expression at slower time scales, from  $\sim 15$  min to several hours as demonstrated in this study.

Despite the central regulatory roles of the cAMP and ppGpp signals, the growth transition kinetics itself is not sensitive to the details of signaling kinetics, as evidenced by the predictive power of the FDR model which does not explicitly describe signaling. Rather, the adaptation kinetics is governed by the slow time scale of global proteome remodeling and growth. The observed resource allocation strategy maintains global coordination of the proteome, instead of sequentially prioritizing the expression of various bottleneck proteins as demanded by schemes of optimal adaptation [129, 130]. This conservative control strategy may be more robust by confining the metabolic bottleneck to the central precursors, which drive global regulatory control Fig. 3.3. The slow proteome-wide dynamics sheds light on a well-known empirical rule in classical bacteriology, that a culture should be adapted in a growth medium for  $\sim 10$  generations before it is to be regarded as in steady state. Quantitative understanding of such proteome remodeling processes is a prerequisite for predicting the dynamics of both endogenous and synthetic genetic circuits, whenever circuit operation involves changes in the cell's growth state, as in responses to stresses and antibiotics, making the framework established here foundational in understanding a broad spectrum of other adaptation phenomena.



## Chapter 4

# Death during carbon starvation

### 4.1 Introduction

Microbes have developed a multitude of strategies to cope with starvation that help them to survive from days to years and millennia. While microbes like *Bacillus subtilis*, a soil bacterium, can develop spores to survive, others like *Escherichia coli* are less fortunate. Without a sporulation program, a slow decay of viability of these microbes sets in soon after nutrient exhaustion [45–48]. Several molecular processes occurring inside cells during starvation were identified [49], such as a down-regulation of the metabolism [121] and an activation of the stress response system via the alternative sigma factor rpoS [50, 132]. On the population level it was noticed early that cannibalism occurs [64, 133, 134]). In its extreme, cannibalistic use of deceased cells can lead to a growing subpopulation of cells called cryptic growth [45, 135, 136], most prominent in oscillatory decay patterns [46, 47], but not always detectable [45, 62].

Generally, the decay of viability depends on the environmental conditions [47] and can be delayed by several days by residual nutrients [48]. If bacteria are carefully starved of all energetic substrates, they show an exponential decay of viability ranging several orders of magnitude of viability [46, 48, 134], when held at optimal temperature and pH. This simple experimental phenomenon is intriguing, since the entire dynamics can be described by one parameter: the death rate of the population. In the literature, changes of the death rate are often used as an indicator to classify the cost or benefit of genes [48, 50] or the quality of environments [47, 137]. However, it remains unclear why the viability of the population decreases exponentially, and which consequences provoke a changes of the death rate.

In this chapter we establish a quantitative understanding cells in starvation. Only when carefully starved of all energetic substrates, *E. coli* shows an exponential decay of viability, with the rate depending on environment and genetics. We identify the exponential decay to be a consequence of the energetic needs of the cell for maintenance. When no carbon resources are available in the medium, the only external possibility for energy production are resources freed by lysed cells in the population. Such a cannibalistic process, in which dying cells release nutrients that can sustain the remaining viable cells, naturally leads to an exponential decay of viability. The death rate of a starved population is thus a measure for the maintenance rate, and allows quantitative studies of environmental and genetic perturbation, as exemplified by the study of knock-outs of the stress response sigma factor rpoS.

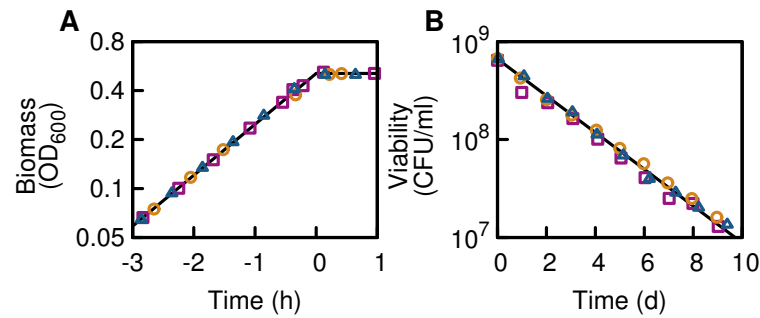


**Figure 4.1: Exponential growth and death.** (A) Growth of *E. coli* K-12 strain NCM3722 in glycerol minimal medium at growth rate  $\lambda = 0.70\text{h}$  abruptly halts when Glycerol is depleted ( $t = 0$ ). Colors denote three independent repeats. (B) The starvation following glycerol depletion leads to an exponential decay of bacterial viability, measured in colony forming units (CFU) per ml. The death rate  $\mu = 0.43\text{d}$  (black line) is very reproducible.

## 4.2 Characterizing the starvation state

### 4.2.1 Exponential decay of viability during starvation

We focus on carbon starvation, the only energetic nutrient for a chemoorganotrophic bacterium like *E. coli*. The challenge lies in finding a simple, well-defined and reproducible environment to study carbon starvation. Several complications are encountered in the experimental design, in particular the removal of all carbon from the medium. For instance, many nutrients are taken up with a low affinity during growth. In the gluconate-succinate downshift in Fig. 3.10A discussed in the previous chapter, the phase of gluconate depletion takes about one hour, while glycerol depletion (with high affinity) in Fig. 3.2 is completed within few minutes. It was speculated that during the depletion period the cells could adapt to the coming starvation, e.g. by storing nutrient [48, 138]. Even worse, after growth on a rich nutrient mixture, such as casamino acids or lysogenic broth (LB), as studied in Chapter 2, some nutrients remain in the medium and allow for prolonged survival of the cells for several days, compared to when the spent medium was replaced by fresh medium. Carbon starvation should thus be studied in a medium with a single carbon substrate to which the cell has a high affinity.

#### Carbon starvation leads to exponential decay of viability

When cells grow there exists the possibility of them excreting fermentation products, even in anaerobic conditions. For *E. coli* it was shown that this bacterial Crabtree effect leads to the excretion of acetate [82, 139–141]. After starvation, the excreted acetate can be utilized as a secondary nutrient, potentially influencing the survival physiology during starvation. However, acetate excreting is growth rate dependent and absent below a growth rate threshold of about  $0.76/\text{h}$  [82].

In *E. coli* (K-12 strain NCM3722) Glycerol lies below the acetate excretion threshold, but still allows relatively fast growth ( $\lambda = 0.70/\text{h}$ ). At the same time, the cell has a high affinity for glycerol, see Table B.5, making growth in minimal medium with glycerol as the sole carbon substrate the ideal experimental condition. We further minimize stresses caused by temperature and pH, by keeping these at optimal conditions ( $37^\circ\text{C}$ , pH 7). With this experimental protocol, which was first used in Ref. [48], cells grow exponentially until growth abruptly halts when glycerol is depleted, see Fig. 4.1A.

After growth, cells enter a phase of starvation, in which bacterial viability, recorded by

colony forming units per ml (CFU/ml), decreases; see Fig. 4.1B, and Section C.1 for details on the plating method. The decay of viability is very reproducible; compare the three different repeats in Fig. 4.1B and consistently exponential, with the death rate  $\mu = 0.43/\text{d}$  being constant over 2 orders of magnitude of viability.

### Entry to the exponential phase

In the most common notion of the post-growth phase, the cells will first go through a phase of no-growth and no-death, often called "stationary phase", see the bacterial life cycle drawn in Fig. 1.2. This phase is reported to be somewhere between negligible [46–48] and up to several days [14, 66], and its origins are unknown. To investigate the extent of an initial phase of no decay of viability, we stained cells using an established set of Live/Dead stains that measure the membrane integrity, see Section C.1 for details. After nutrient depletion, almost the entirety of bacteria were stained 'live', see Fig. 4.2A, with this amount decreasing to about 50 % after 48 h, see Fig. 4.2B. After about a day of starvation, the decrease of viability has reached the death rate  $\mu = 0.43/\text{d}$ , see Fig. 4.2C.

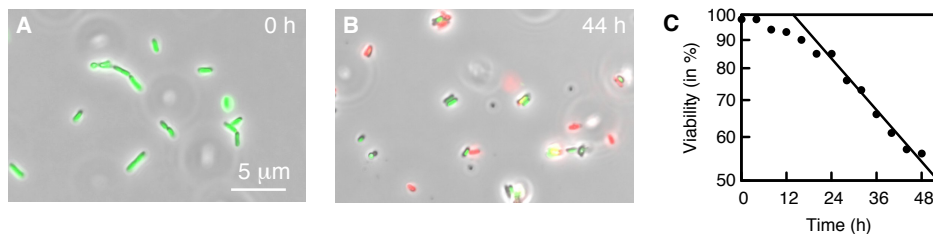


**Figure 4.2: Decrease of viability after entry into starvation.** (A) Cells were stained using a Live/Dead stain, see Section C.1 and counted manually using light microscope images. Green stained cells were counted as viable. Red stained, Green-red stained and un-stained cells were counted as unviable, see images. (B) After exhaustion of glycerol ( $t = 0$ ), cells enter starvation. During the first hours into starvation cell death is slow, increasing to the final death rate  $\mu = 0.43/\text{d}$  (black line) after about 24h.

## 4.2.2 Carbon starvation is a static phase

### Absence of cryptic growth

During the subsequent exponential decay of viability the question arises if there is a turn-over of cells, i.e. if there exists a cryptically growing subpopulation slowly replacing the existing population. Using time-lapse microscopy in a microfluidic channel, see Fig. 4.3A, we did not observe a single growing cell among a sample size of  $\sim 10.000$  cells over the time course of 5 days, see Fig. 4.3B. Consequently, growth-dependent antibiotic treatment (cell wall synthesis inhibition by Ampicillin) during the entire starvation did not alter death, see Fig. 4.3C. This suggests that a cryptic growth is absent on the population level and non-essential.

### Cell size during starvation

During growth, cell size and shape are known to change depending on steady state growth rate [32] and during growth transitions [67]. During carbon starvation we characterized cell width and length and found that after an initial decrease of length in the first hour after entry to starvation, see Fig. 4.4A, both cell length and width remained constant during the entire starvation Fig. 4.4A, B. Comparison of cell width and length during growth and starvation, Fig. 4.4C, D, revealed substantial loss of elongated cells and gain of cells about half this size.

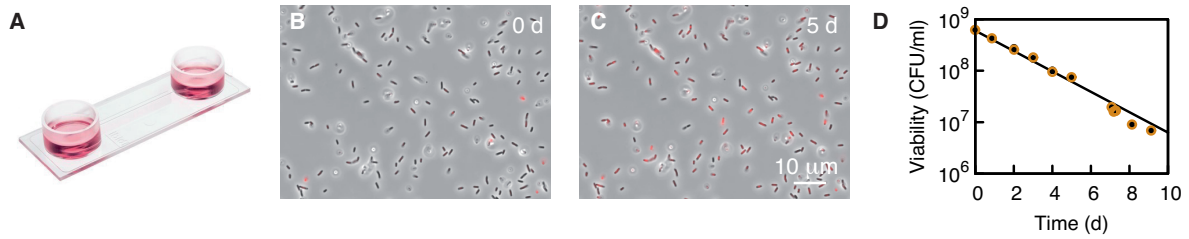


**Figure 4.3: Cryptic growth.** (A) An uncoated Ibidi  $\mu$ -slide<sup>®</sup> was used to culture starved *E. coli* for several days. (B) After an initial period of about 1 h, all cells settled to the bottom of the slide. Propidium iodide stain (red) was used to identify cell death (loss of membrane integrity). (C) After three days of starvation the vast majority of cells were stained dead (either still, or they lost their stain by bleaching or DNA loss). From the imaged  $\sim 10,000$  cells, not a single growing cell could be identified. (D) Inhibition of growth by Ampicillin (inhibition of cell wall synthesis) did not alter cell death, indicating that cryptic growth is not only small, but also non-essential for the exponential survival. Data in panel D was taken by Elena Biselli (LMU, Germany).

This indicates that during the first hour after starvation long cells complete their division, while smaller cells do not manage to finish their division cycle.

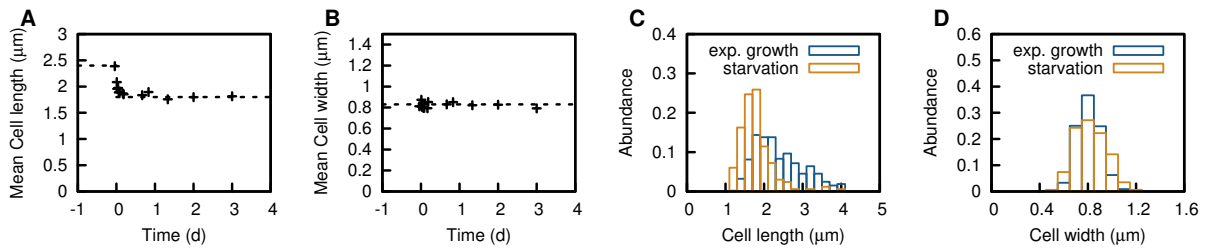


**Figure 4.4: Cell size during exponential growth and starvation.** (A) Mean cell length  $\langle l \rangle$  measured by light microscopy images relaxes from the lengths during exponential growth,  $\langle l \rangle = 2.4 \mu\text{m}$ , to the mean length during starvation  $1.8 \mu\text{m}$ , in less than one hour. (B) Cell width does not change significantly after entry into starvation. (C-D) Distribution of cell lengths and widths during exponential growth and 2 days into starvation.

### Protein synthesis during starvation

Protein synthesis during carbon starvation could play an important role for survival, as suggested previously [62]. We tested the magnitude of protein synthesis by inducer dependent gene expression of the lac operon, see Fig. 4.5. At several time points during starvation, indicated by differently colored symbols in Fig. 4.5A), we added 1 mM IPTG, a lactose analog, to express the lac operon. By quantifying the absolute amount of LacZ synthesized by the starved population, Fig. 4.5B), we determined the expression of LacZ per viable cell, relative to the expression during steady state growth, see Fig. 4.5C). We observed a phase of constant LacZ expression at around 1% of the steady state value, similar to the “constant activity in stationary phase” (CASP) state found in Ref. [66], yet at lower expression levels. Inhibition of translation by Chloramphenicol did not alter death, indicating that this protein synthesis plays a non-essential role, see Fig. 4.5D), in contrast to previous findings [62].

### Mutations and long-term survival

Mutants appear when cells are starved for longer than ten days or when viability decreases below  $10^7$  CFU/ml. These mutants allow long-term survival, similar to previous observation [14, 60, 64]; see Fig. 4.6A). These mutants are characterized by a smaller colony size, see Fig. 4.6B).

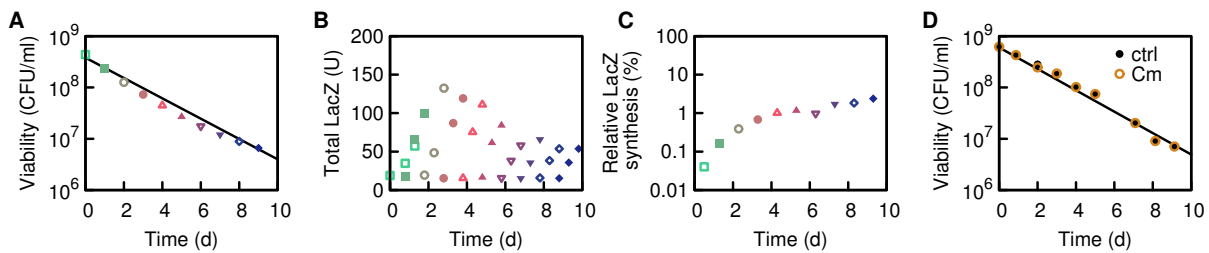


**Figure 4.5: Gene expression during starvation.** A large culture of cells is starved (125 ml) and subcultures (5 ml) split off daily. After splitting, each subculture is supplemented with 1 mM IPTG to induce the lac operon and LacZ activity is assayed using the Miller Assay [142] every 12 h. (A) Viability at the extraction points of ten different cultures (symbols). After extraction, viability follows the main culture (data not shown). (B) Total LacZ expression (see Section C.1) of each of the ten cultures is recorded for two days. Units U = MU · OD<sub>600</sub> are defined as activity per unit volume, as opposed to MU, which are defined per OD<sub>600</sub>. (C) LacZ synthesis per viability, normalized to the value during exponential growth prior to starvation,  $11 \cdot 10^3$  MU/(h · 10<sup>9</sup>CFU). After about two days of starvation, LacZ expression levels increase to a constant rate of about 1% of the pre-starvation level. Samples of panels A to C were taken by and analysed together with Elena Biselli (TUM, Germany). Data in panel D was taken by Elena Biselli (TUM, Germany).

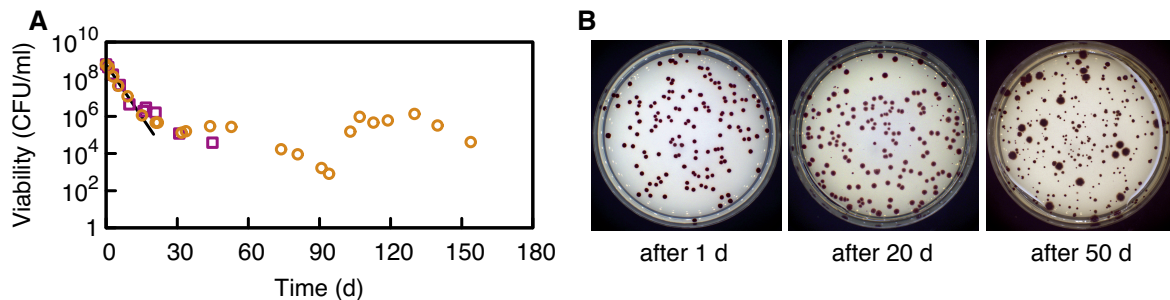


**Figure 4.6: Long-term survival of adapted mutants.** (A) Two independent cultures are shown as orange circles and purple squares. After about 20 days of exponential starvation (black line:  $\mu = 0.43$  d), the decrease of viability halts and cells enter a phase of long-term survival. Long-term survival can last at least several months to years and is characterized by regrowth of mutated subpopulations [14, 60, 64]. (B) Change of the colony size and shape during the starvation. After 1 days of starvation colony shapes are homogenous. After 20 days of starvation, size and shape begin to show heterogeneity, a sign for mutations [14]. After 50 days of starvation only micro-colonies prevail (plate incubated for 72 h, in contrast to 24 h for day 1 and 20.). Long-term starvation experiment was performed by Elena Biselli (TUM, Germany).

The function of these mutants, as well as the reduced size and altered shape remain obscure, despite considerable effort to shed light on this issue, see e.g. Ref. [14] for a review.

### 4.2.3 Cannibalisms during starvation

The apparent absence of mutation, growth and protein synthesis raises the question which other processes occur that could lead the observed exponential decay. Cannibalism was suggested long ago to play a potential role for the survival of bacteria during starvation [64, 133, 134], but its influence remained obscure. To probe a possible influence of cannibalistic catabolism of dead biomatter on survival, we starved a culture of cells, see Fig. 4.7A, and extracted the supernatant by filtration after 44 h at a viability of  $N(44 \text{ h}) = 2.5 \cdot 10^8$  CFU/ml, see black arrow in panel A. We inoculated a small amount of starved cells from this culture ( $6 \cdot 10^7$  CFU/ml) into the filtrate, see Fig. 4.7B purple squares, and observed that death halts and cell maintain their viability for about  $8.5 \pm 0.5$  h, compared to an inoculation of identical population into fresh, carbon-free medium, Fig. 4.7B open black circles. If an even smaller number of viable

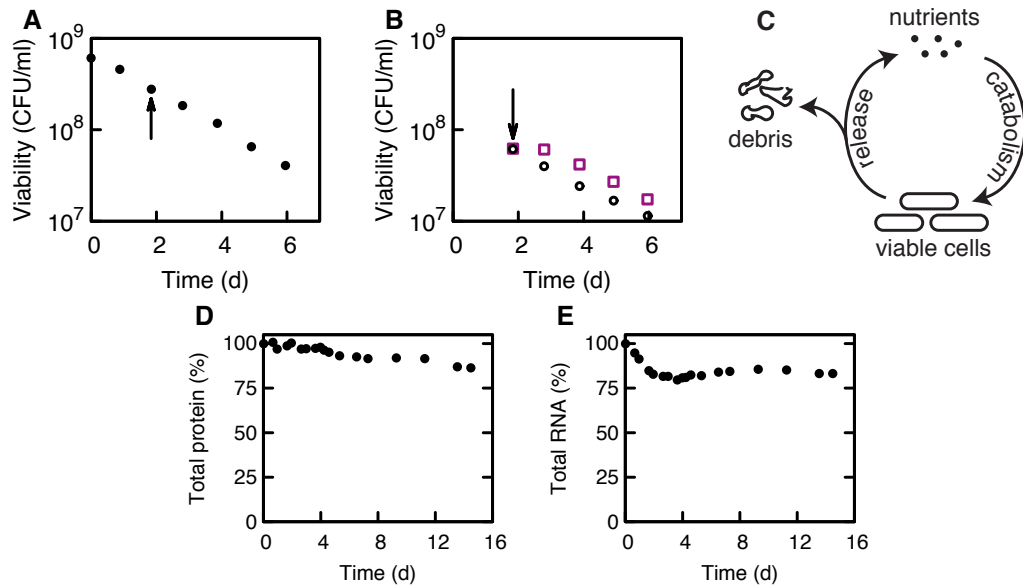


**Figure 4.7: Cannibalism during starvation.** (A) At 44 h into starvation, indicated by the arrow, the culture was filtered and the supernatant extracted. Viability at extraction was  $2.5 \cdot 10^8$  CFU/ml. (B) When a small number of cells ( $6 \cdot 10^7$  CFU/ml) from the culture of panel A is inoculated inside the filtrate (at the arrow), death halts compared to inoculation into fresh, carbon-free medium. (D-E) Total protein, RNA and carbon content of a starved culture over 16 days, relative to the first extraction point shortly after glycerol exhaustion, see Section C.1 for details. Data in panels a and b, and samples of panels d and e were taken by Elena Biselli (TUM, Germany).

cells is inoculated into the filtrate, e.g.  $10^4$  CFU/ml, then growth to a maximal density of about  $2 \cdot 10^6$  CFU/ml is observed (data not shown).

The survival on the supernatant shows the importance of nutrients released by loss of membrane integrity. We hypothesize a biomass recycling process, sketched in Fig. 4.7C: Cell death and loss of membrane integrity leads to release of nutrients by dead cells (up arrow), while unmetabolizable biomatter accumulates as debris (left arrow). Nutrients are subsequently taken up and catabolized (down arrow), and metabolism (e.g. respiration) leads to excretion of waste production such as  $\text{CO}_2$ ,  $\text{H}_2\text{O}$  and other small molecules.

This biomass recycling can be directly observed as a loss of biomolecules from the culture. In Fig. 4.7D-F we show the loss of total protein and total RNA over a 16 day period. Total protein shows a gradual decrease from to about 80% of the original content during the starvation period. RNA initially decreases fast, possibly due to turn-over of ribosomes after entry to starvation [143] and degradation of mRNAs. After the initial period, RNA content in the culture remains constant. Since the majority of RNA is ribosomal rRNA folded into ribosomes ( $\sim 85\%$  [68, 144]) this finding implies that ribosomes are stable even after cell death, in contrast to other types of starvation [143]. The decrease of biomass is surprisingly small, a bizarre result given that bacteria like *E. coli* are usually thought to be versatile scavengers.

### 4.3 Origin of the exponential decay of viability

Recycling of nutrients after cell death are key for the survival of the remaining viable cells. We hypothesize that the exponential decay of viability originates from this recycling process and corresponds to state where nutrient supply by cell death balances an energetic need for maintenance. Generally, in a population of viable cells, the death rate is given by,

$$\mu(t) = -\frac{d \ln N(t)}{dt} = -\frac{\dot{N}}{N} \quad (4.1)$$

At this rate, biomolecules are leaked into the medium. Some of these can be used as nutrients and are subsequently taken up and catabolized by the remaining viable cells (under excretion of  $\text{CO}_2$ ,  $\text{H}_2\text{O}$ ,  $\text{NH}_4$  etc.), while others remain as un-metabolizable debris accumulates, see Fig. 4.7. The metabolism of nutrients increases the energetic state of the cell  $\epsilon$ , with the conversion given by a yield  $\alpha$ , which is defined as the energy that can be scavenged from a dead cell. If the turn-over of free nutrients in the medium is fast, then the increase of the energetic state of a cell is directly given by the death rate times the energetic yield,  $\alpha\mu$ . At the same time, the cell spends energy on maintenance at rate  $\beta$ , a biological necessity of non-sporulating cells [145, 146], which continuously decreases the energetic state of the cell. Taken together, the change of the energetic state of the cell is given by

$$\frac{d\epsilon}{dt} = \alpha\mu - \beta \quad (4.2)$$

Here the death of other cells at rate  $\mu$  increases the energetic state  $\epsilon$  of the particular cell studied. We make the fundamental assumption that all cells are in the same energetic state and write the death rate  $\mu(\epsilon)$  as being dependent on the internal energy state of the cells,  $\epsilon$ , based on the knowledge that the addition of nutrients, e.g. via the filtrate of a starved culture in Fig. 4.7B, will decrease death rate. The energetic state<sup>1</sup> of the cells can be itself dynamic and depend on time  $\epsilon(t)$ . However, assuming that yield  $\alpha$  and maintenance rate  $\beta$  are fairly constant, the dynamics of the energetic state of the cell derived in Eq. (4.2), will inevitably converge towards a steady state  $d\epsilon/dt = 0$ . In this steady state, the nutrient leakage by cell death balanced the maintenance rate, and the steady state death rate is given by

$$\mu^* = \frac{\beta}{\alpha}. \quad (4.3)$$

As a result, in this balanced steady state the number of viable cells  $N(t)$  continuously decreases exponentially,

$$N(t) = N(0) \exp(-\mu^*t). \quad (4.4)$$

which can be obtained by plugging in Eq. (4.3) into Eq. (4.1). The theoretical finding that the steady state death rate  $\mu^*$  is given by the ratio of maintenance rate  $\beta$  to yield  $\alpha$  is the central result of this chapter, and its validity will be extensively tested. We begin by investigating the maintenance rate  $\beta$  and yield  $\alpha$  individually. Since all experiments below will be performed inside the steady state exponential death, we omit the asterisk on the death rate  $\mu$ .

### 4.3.1 Maintenance rate

At the heart of the balanced exponential decay underlies the assumption that viable cells  $N(t)$  must constantly consume nutrients  $R(t)$  at maintenance rate  $\beta$ ,

$$\frac{dR}{dt} = -\beta N(t). \quad (4.5)$$

The energetic need can be quantified by the addition of a small amount of nutrients. After the addition of a small amount of glycerol, death halts for a short period of time, see Fig. 4.8A,

<sup>1</sup>Here we implicitly assume that energy is the only requirement for survival. Nutrients could also be used as nutrients, e.g. to repair or re-synthesize essential proteins. Since we previously showed that protein synthesis is small and non-essential (Fig. 4.5) we assume that it is negligible compared to the energetic need.

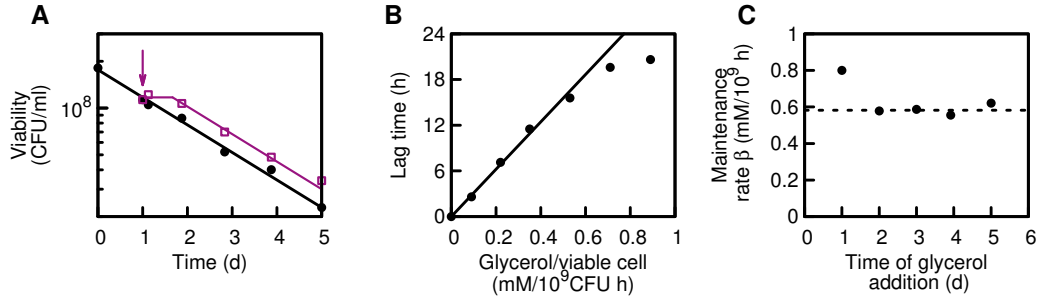


**Figure 4.8: Maintenance rate.** (A) After supplementing a starved culture with glycerol (purple open squares shows addition of 60  $\mu\text{M}$  after 24 h at the arrow) survival is prolonged compared to a control (black circles). (B) Lag time increases linearly with the supplemented glycerol, and the slope of the black line is the maintenance rate  $\beta$ . (C) The maintenance rate  $\beta$ , is constant after an initial 24 h, at  $\beta = 0.58 \text{ mM}/(10^9 \text{ CFU/ml} \cdot \text{d})$ , indicated by the black line. Data was taken by Elena Biselli (TUM, Germany).

with this period linearly increasing with glycerol concentration, see Fig. 4.8B. The maintenance rate can be calculated using Eq. (4.5) under the assumption that during the utilization of the added nutrient  $R_0$  no cell death occurs, i.e.  $\mu(t) = 0$ ,

$$R_0 = - \int_0^T \frac{dR}{dt} = \beta NT, \quad (4.6)$$

which can be reformulated as

$$T = \frac{1}{\beta} \frac{N}{R_0}. \quad (4.7)$$

The maintenance rate is thus the slope of Fig. 4.8B, in the regime of small external nutrient additions. When the lag time  $T$  is plotted against the supplemented glycerol  $R_0$  per viable cell  $N$ , yields a maintenance rate  $\beta = 0.58 \text{ mM}/(10^9 \text{ CFU/ml} \cdot \text{d})$ , in units of glycerol. During growth, about 5 mM glycerol yield  $5 \cdot 10^8$  cells, thus the amount of glycerol that supports one doubling during growth can maintain the viability for more than two weeks. The maintenance rate  $\beta$  is constant during the starvation, Fig. 4.8C, as pervasively assumed in Eq. (4.2). The maintenance rate can be converted into units of ATP molecules consumed per cell per second  $\beta = 3.7 \cdot 10^6 \text{ ATP/s}$ , using the conversion of 15 ATP per glycerol<sup>2</sup>.

### 4.3.2 Yield

In the biomass recycling process, nutrients are released, taken up and metabolized. As a consequence of the constant consumption of nutrients, the nutritional value of the entire culture, including both viable cells and dead cells, should decrease. Inserting the exponential decay Eq. (4.4) into the expression for maintenance rate Eq. (4.5), we get that the model predicts that the total amount of nutrients  $R(t)$  in the culture should linearly decrease with viability  $N(t)$ ,

$$R(t) = \alpha N(t), \quad (4.8)$$

where the total energetic yield per cell was previously defined as  $\alpha = \beta/\mu$ . This relation is tested in Fig. 4.9. At different time points during starvation a sample is extracted and killed by irradiation with UV light, see Fig. 4.9A (arrows indicate sterilization times). This

<sup>2</sup>Total yield of glycerol catabolism: 4 NADH (1 from pyruvate oxidation, 3 from TCA cycle), 1 FADH<sub>2</sub> and 1 ATP (both from TCA). Taking standard conversion from the electron transfer chain yields 3 ATP per NADH and 2 ATP per FADH<sub>2</sub> and a total yield of 15 ATP/glycerol.

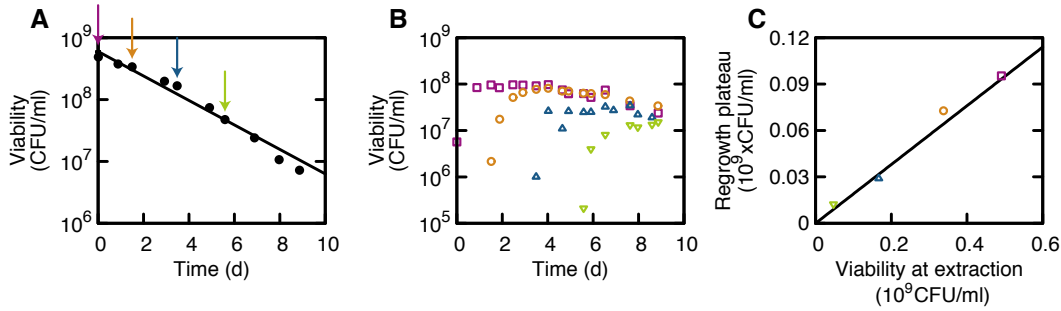


**Figure 4.9: Yield.** (A) At different times during carbon starvation, samples are extracted and UV-sterilized (arrows). (B) UV-sterilized cultures are inoculated with a small amount of viable cells and growth is recorded by plating. The growth-yield (plateau after growth) is a measure for the nutrient content. (C) The growth-yield of a culture decreases proportionally with the viability at the extraction, showing viable cell contain the dominant nutrient source as assumed by the model. Slope of the black line: 0.19. Data was taken by Constantin Ammar (TUM, Germany).

UV-sterilization efficiently induces cell death and loss of membrane integrity, see Fig. C.1 and Section C.1, thus freeing all potential nutrients from previously intact, viable cells. When the UV-sterilized culture is inoculated with a small amount of viable cells, these can regrow on the nutrients released by cell death, see Fig. 4.9B (colors correspond to arrows in panel A). Cells grown on samples extracted at different time points reach a different maximal level. This plateau level decreases with time into starvation, indicating that less nutrients were available to the cells. When the regrowth plateau level is plotted against the viability at extraction they exhibit a clear proportionality, see Fig. 4.9C (colors correspond to arrows in panel A). This validates a key assumption of our hypothesis, i.e. that the dominant nutrient source are kept inside viable cells. Released nutrients are quickly taken up and the remaining dead cell mass accumulates as un-metabolizable debris.

The proportionality constant of the black line in Fig. 4.9C, 0.19, means that for every 5 killed cell, one new cell can regrow. This value agreement with findings from Fig. 4.7, that show that protein and RNA decrease by about 20%.

The yield  $\alpha$  can be calculated from the maintenance rate  $\beta$  measured in the above section,

$$\alpha = \frac{\beta}{\mu} = \frac{0.58 \text{ mM}/(10^9 \text{ CFU} \cdot \text{d})}{0.43/\text{d}} = \frac{1.35 \text{ mM}}{10^9 \text{ CFU/ml}}. \quad (4.9)$$

In comparison, during growth 10 mM glycerol yield about (10<sup>9</sup> CFU/ml). This growth-yield is about eight fold higher than the maintenance-yield  $\alpha$

## 4.4 Perturbing the steady state state

Above we proposed that the exponential decay of viability in starvation originates from a balance of nutrient release with maintenance. In this section we probe this steady state exponential decay by either increasing maintenance or added a defined amount of nutrients.

### 4.4.1 Titratable maintenance rate

We test the exponential decay by increasing the maintenance rate  $\beta$  of the cell during starvation, by varying the import of non-metabolizable, synthetic IPTG via the lactose transporter, see Fig. 4.10A, a known energetically costly process [147]. While for low LacY activity (blue triangles) the death rate is virtually unchanged, for higher expression of LacY (yellow circles

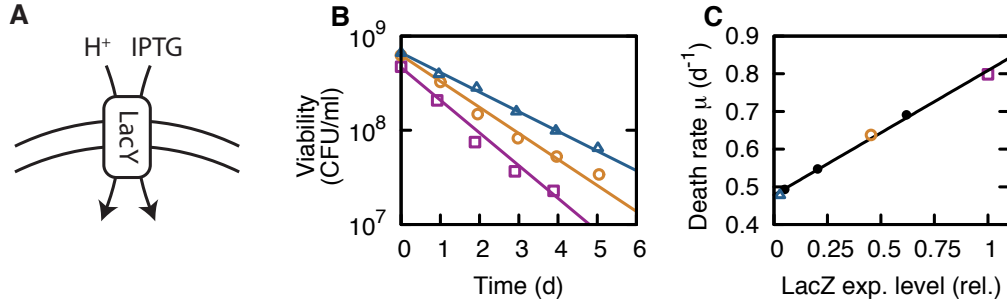


**Figure 4.10: Titrating the maintenance rate.** (A) The lactose permease LacY can import the unmetabolizable lactose analog IPTG using symport with one proton. (B) Cells starved in the presence of IPTG. Cells with high levels of *lac* expression (pink) die faster than intermediate (orange) or low levels (blue), presumably because of high energetic costs of LacY activity [147]. (C) Death rate linearly increases with LacZ expression (a reporter for LacY activity). LacZ expression is normalized to the highest level (pink). Viability curves were taken by Elena Biselli (TUM, Germany).

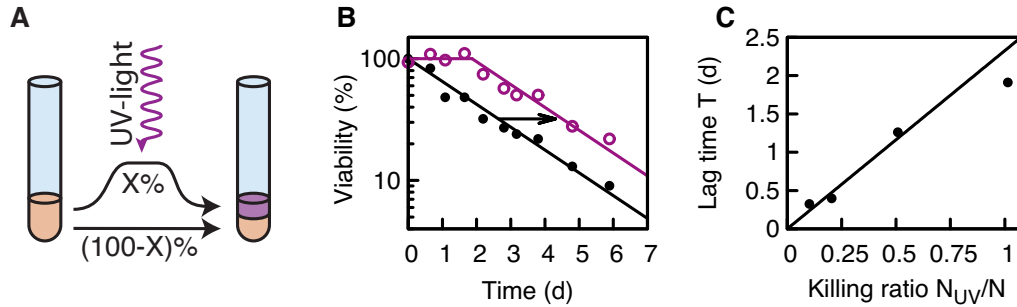


**Figure 4.11: Inducing cell death.** (A) A fraction of the population is extracted, UV-sterilized and mixed with a part of the original culture. (B) A culture mixed 50% original culture, 50% UV-sterilized culture can survive for up to two days (arrow indicated lag time  $T$ ), compared to a control. (C) The lag time  $T$  increases linearly with the mixing ratio of UV-sterilized cells to viable cells,  $N_{UV}/N$ . The black line shows the fit parameter free prediction of the model in Eq. (4.13),  $\mu^{-1}$ . Viability curves were taken by Constantin Ammar (TUM, Germany).

and purple squares), the death rate of the bacterial culture increases, see Fig. 4.10B. According to our theory of steady state exponential death, the death rate will linearly increase when an additional energy consumption rate  $\Delta\beta$  is introduced,

$$\mu = \frac{\beta}{\alpha} = \frac{\beta_0 + \Delta\beta}{\alpha} \quad (4.10)$$

where  $\beta_0$  is the basal maintenance rate. The additional energy consumption rate  $\Delta\beta$  should increase with LacY expression. The expression level can be readily measured using the co-expressed LacZ. When death rate  $\mu$  is plotted against the expression level of LacZ, we observe the predicted linear increase of death rate, see Fig. 4.10C.

#### 4.4.2 Inducing cell death

We further test the above theory by artificially killing a fraction  $X$  of the population, see Fig. 4.11A. The survival kinetics of viable cells upon 50-50 mixing of UV-sterilized cells and original cells is shown in Fig. 4.11B. Viable cells in the culture can survive for up to two days before the exponential decay of viability sets in. This lag time  $T$  increases linearly with the killing ratio, see Fig. 4.11C.

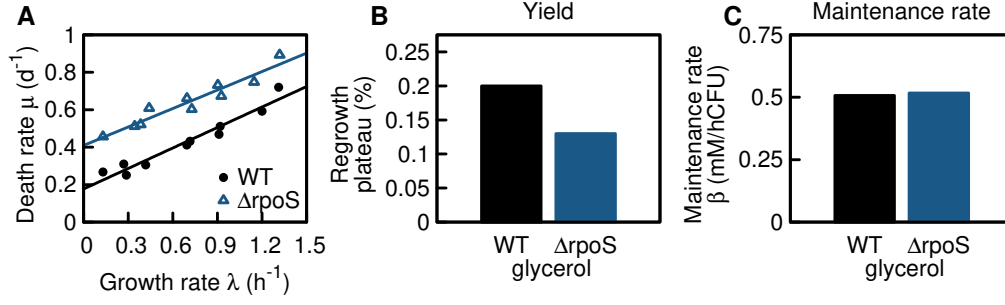


**Figure 4.12: Environmental and genetic dependence of the death rate.** (A). Death rate of wild type (WT) previously grown at different rates  $\lambda$  (different substrates) increases with growth rate (black dots).  $rpoS$  knockout mutant ( $\Delta rpoS$ ) increases death rate at all growth rates (blue triangles). (B-C). Histograms of maintenance-yield  $\alpha$  and maintenance rate  $\beta$  for WT (black) and  $\Delta rpoS$  (blue) previously grown in minimal medium with glycerol. Note that the maintenance rate  $\beta$  remains constant respect to the wild type case, while the metabolizable resources released by dead cells,  $\alpha$ , decrease. Data was taken by Elena Biselli (TUM, Germany).

The lag time  $T$  can be obtained from our model by calculating the time it takes to consume the energy provided by UV-sterilized cells,  $R_0 = \alpha N_{UV}$ .

$$R_0 = \alpha N_{UV} = - \int_0^T \frac{dR}{dt} = \beta NT, \quad (4.11)$$

The result,

$$T = \frac{\alpha N_{UV}}{\beta N}, \quad (4.12)$$

includes the ratio of metabolizable resources per biomass  $\alpha$  to maintenance rate  $\beta$ , and can be simplified using Eq. (4.3) to

$$T = \mu^{-1} \frac{N_{UV}}{N}. \quad (4.13)$$

The lag time is thus entirely determined by the killing ratio  $N_{UV}/N$  and the death rate  $\mu$ . Comparing this parameter free prediction to the experimentally extracted lag times  $T$  in Fig. 4.11C, shows quantitative agreement.

## 4.5 Effect of genetic and environmental conditions on the death rate

We further test the consequences of environmental and genetic perturbations on the death rate of *E. coli*. By varying the nutrient substrates, growth rate prior to starvation can be changed. We observe an increase of death rate with growth rate, black points in Fig. 4.12A. In addition, knockout of  $rpoS$ , an alternative sigma factor controlling the expression of around 40 genes, including the stress response system [50, 52, 148], increases death rate at all growth rates, blue triangles in Fig. 4.12A. Under both perturbations, starved populations still decrease their viability exponentially; see Fig. C.2.

According to Eq. (4.3), the change of death rate with these environmental or genetic perturbations could originate in either the metabolizable resources released by dead cells  $\alpha$ , the maintenance rate  $\beta$  or a combination of both. Following the approach introduced in Fig. 4.9,

we identify that the yield  $\alpha$  decreases for rpoS knock-out mutants, see Fig. 4.12B. In contrast, the maintenance rate  $\beta$  remains constant Fig. 4.12C.

This clear result points towards an inefficiency of the rpoS knock-out mutant to catabolize dead cell matter. Such inability to catabolize biomatter can be induced by sequential knock-out of proteases, and was shown to increase death rate [149]. However, only few genes regulated by rpoS have a known potential to increase catabolism, e.g. ansP (arginine transporter), sdaA (serine deaminase) or ydcS (polyamine transporter), and no proteases are affected by the absence of RpoS [52, 148]. It thus remains obscure how rpoS knock-out mutants can lose  $\sim 40\%$  of their catabolic potential.

## 4.6 Discussion

Surviving nutrient limitation is an important, yet poorly understood part of the life cycle of microbes like *E. coli* and crucial for its overall fitness [49]. Progress in understanding the processes underlying death and survival still remains in its infancy, to great extent due to the lack of a well-defined survival state. In this work we identified the exponential decay of viability during carbon starvation to be such a simple, reproducible and well-controlled steady state, analogously to the steady-state exponential growth that revolutionized studies on growth mid last century. The steady state exponential decay originates in the basic need of the cell for maintenance. After depletion of all carbon substrates, the only substrates for energy production by viable cells are biomolecules released into the medium by cell death and loss of membrane integrity of other members of the population. Such a biomass recycling process, in which dying cells release nutrients that can sustain the remaining viable cells, naturally leads to an exponential decay of viability.

As a result, the death rate is determined by the ratio of maintenance rate to the energetic yield of a dead cell. We use this fundamental insight to uncover that knock-outs of the stress response sigma factor rpoS die at an accelerated rate during starvation due to an impaired utilization of released biomolecules. We further uncover a fundamental trade-off between fast growth and slow death, when cells are grown on nutrients allowing different growth rates prior to starvation.

This theory furthers the understanding of bacteria, away from the monolithic fixation on growth, towards a more complete understanding of the bacterial life cycle and broad implications for bacterial ecology, evolution and physiology. A better understanding of the mechanisms allowing bacterial survival will open new doors for investigation of contexts in which non-growing states are probably required and regulated, such as symbiotic associations with plants and animals, and stable, structured microbial communities in both natural and applied settings.

## Chapter 5

# Preventing systemic spread of pathogens

### 5.1 Introduction

Bacterial infections remain a leading cause of death in both developed and developing countries, a problem that is aggravated by the global rise in antibiotic resistance. Opportunistic infections caused by normally harmless or beneficial strains when introduced to sick hosts or to parts of a host's body outside of the gut pose a substantial threat to human health [3]. The immune system protects the organism from such harmful infections. It provides a complex array of molecular and cellular structures shielding the organism from infectious diseases. To function properly, an immune system must detect a wide variety of agents, known as pathogens, from viruses to parasitic worms, and distinguish them from the organism's own healthy tissue. The immune system protects the host's organism with a layered defense system of increasing specificity. Once physical barriers are breached by pathogens such as bacteria or viruses, the innate immune systems is triggered immediately and acts as the first defense barrier in a non-specific manner. The response is evoked by pattern recognition receptors, that are preserved among broad groups of microorganisms [150], such as the lipopolysaccharide (also called LPS, or endotoxins) found in the outer membrane of Gram-negative bacteria such as *E. coli* [151, 152]. As part of the innate immune response, immune cells (also called leukocytes or white blood cells) are recruited to the site of inflammation through chemical signaling. Further, the complement cascade activates macrophages, which identify bacteria and clear the organism of antibody complexes or dead cells. Foreign substances are identified and removed. In addition, the complement cascade guides leukocytes to the site of inflammation using chemotaxis.

Inadequate innate immune responses favors the systemic dissemination of pathogens which may result in life-threatening septic conditions, such as septic shock and multi organ dysfunction [153–155]. As a final step of the innate immune response, the next layer of the defense is activated: the adaptive immune system. This adaptive response is highly specialized and allows recognition of antigens, to specifically target pathogens or pathogen infected host cells in a process called antigen presentation. This specificity of the antigens allows a cellular memory of the antigen structure of previous infections. In this project we focus on the first defense layer of the immune response, the protection of the host's organism after breaching of physical barriers by pathogens such as *E. coli*.

## 5.2 Thrombus formation in the microvasculature

Recently, it was proposed that hemostasis (the process that stops bleeding) contributes to the first defense layer of the innate immune system [156–158], as an instrument of the body to limit the systemic dissemination of pathogens by interrupting the blood flow in once pathogens have breached the physical barriers and infected the circulatory system. Together with platelets and the coagulation system, leukocytes have been reported to collaborate for clot formation in larger vessels (e.g., arteries and veins) and in sinusoids of the liver, a process termed ‘immunothrombosis’: Under exposure to relatively low shear stress, neutrophils support thrombus growth by the release of extracellular traps (NETs; network of extracellular fibers containing DNA and other molecules which are instrumental for the clearance of pathogens [159] which, in turn, activate components of the coagulation system and facilitate platelet aggregation [160–163]. The entry of pathogens into the body, however, predominantly occurs in tissues that are supplied by microvessels typically exhibiting high shear rates (e.g., in the respiratory and urinary tract or in the skin). Whether leukocyte-driven events are also relevant for thrombus formation in this most common type of microvasculature is still unknown.

### 5.2.1 The mouse cremaster muscle model

For this study we employed the well-established mouse cremaster muscle model [164–167], see Sections D.1.1 and D.1.2, which allows *in vivo* light microscopy of the capillary vessel network in a thin, 2D-like tissue. Microvascular thrombus formation was induced by phototoxic injury [166], where animals received an intraarterially injection of a FITC-dextran solution, and continuous epi-illumination, see Section D.1.2 for details. Fig. 5.1A shows a time series of thrombus formation in an unstimulated venule. Less than a minute after beginning of the phototoxic illumination, platelets began to adhere to the surface of microvascular endothelial cells ( $55 \text{ s} \pm 12 \text{ s}$ , “onset”). The thrombus eventually occluded the entire vessel and blood flow has ceased ( $386 \text{ s} \pm 19 \text{ s}$  “cessation”).

Inflammation is induced locally in the cremaster muscle by intrascrotal injection of lipopolysaccharide (LPS, from *E. coli* O111:B4). This inflammation model allows the separation of effects by free-floating bacteria to be separated from the inflammation response due to LPS. The local administration of LPS produces a single primary site of injury, similar to an inflammation due to vessel injury after pathogen breach. Six hours after induction of the inflammation, thrombus formation is significantly accelerated ( $279 \text{ s} \pm 39 \text{ s}$  until cessation), suggesting a potential interplay between thrombus formation and inflammation. Such interplay, called ‘immunothrombosis’, was recently reported in low-shear vessels (e.g., arteries and veins sinusoids of the liver [156–158]), but was previously un-described in the high-shear microvasculature. A trend towards faster onset of platelet adhesion was noted, although not reaching statistical significance. Alternatively to the local inflammation, LPS administered intraperitoneally allows studies in systemic inflammation. Such experiments were performed too, and discussed in below in Section 5.2.4.

Generally, both platelet aggregation and fibrin generation contribute to hemostasis [156, 157]. In the high shear microvasculature of this work, thrombus formation critically involved platelets (as assessed in platelet-depleted animals), but did not require fibrin generation by the coagulation system (as observed upon anti-coagulation with heparin); see Fig. 5.1D, E, which is in line with previous reports [166] and in contrast to thrombosis in vessels exposed to lower shear stress such as arteries, veins, or hepatic sinusoids [156–158]. Interestingly, inflammation accelerated thrombus formation in venules, but not in arterioles (Fig. D.1), i.e. only in the draining part and not the feeding part of the microvasculature.

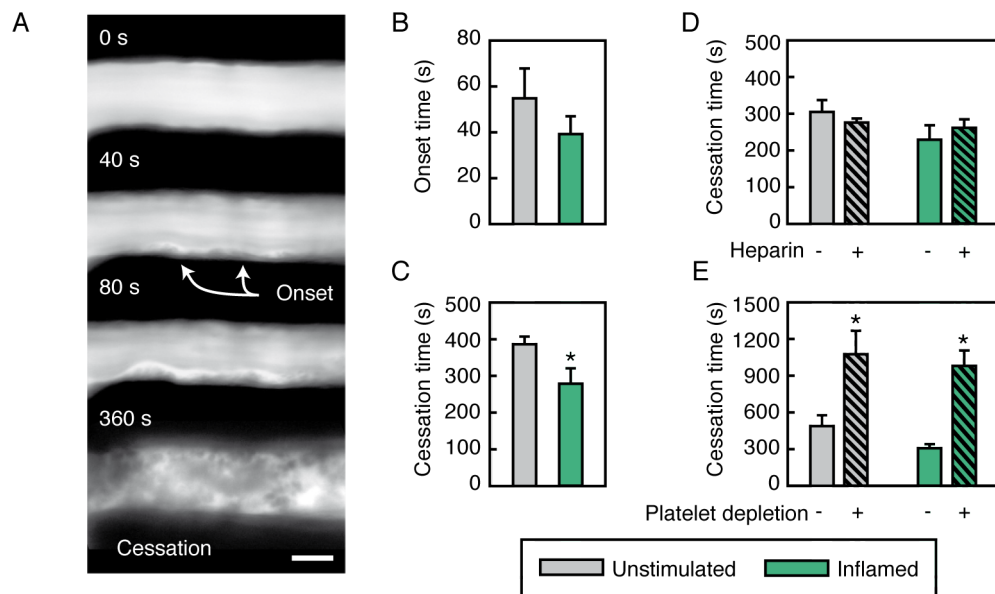


**Figure 5.1: Spatiotemporal dynamics of thrombus formation in inflamed venular microvessels.** Thrombus formation in post-capillary venules of the mouse cremaster muscle was induced by phototoxic injury as detailed in Section D.1.3; representative *in vivo* fluorescence microscopy images of time lapse video recordings are shown (A; scale bar: 20  $\mu\text{m}$ ). Panels show quantitative data for onset and cessation times in WT mice receiving an intrascrotal injection of PBS or LPS (B, C; mean  $\pm$  standard error of mean (SEM) for  $n=9$  per group;  $*p<0.05$  vs. unstimulated control) and undergoing treatment with heparin (D), platelet-depleting antibodies, or vehicle/isotype control antibodies (E; mean  $\pm$  SEM for  $n=3-4$  per group;  $*p<0.05$  vs. vehicle/isotype control). Experiments were performed by Daniel Puhr-Westerheide and Matthias Fabritius (LMU, Germany).

### 5.2.2 Restricting dissemination of pathogens by thrombosis

The breaching of pathogens into the circulatory system is associated with prior inflammation due to pathogen spread inside the tissue. We disentangle the presence of bacteria in the circulatory system from the inflammation by inducing inflammation by intrascrotal injection of *E. coli* LPS six hours and intraarterially injection of non-pathogenic *E. coli* immediately prior to thrombus formation. Fig. 5.2A shows a thrombus in a postcapillary venule of the inflamed cremaster muscle with systemically circulating, fluorescently stained bacteria. After thrombus formation, bacteria (cyan) are highly localized with the platelets (red), showing that bacteria are captured during thrombosis formation in the microvasculature. The number of bacteria, Fig. 5.2B, or alternatively fluorescence-labeled micro-beads, Fig. 5.2C, retained is drastically increased after "phototoxic injury" (leading to thrombus formation) compared to an un-inflamed, non-thrombotic, control group (intrascrotal PBS, "baseline"). Thus thrombus formation is essential for retaining bacteria.

A lack of retention close to breaching site leads to a systemic spread of the pathogens, in which pathogens adhere in the capillary vessels of vital organs, such as lung, liver or brain. Efficient compartmentalization of pathogens is thus a core requirement of the immune response. Indeed, we observe that retention is significantly increased, if an inflammation was previously induced by intrascrotal injection of LPS from pathogenic *E. coli* O111:B4 ("inflamed"), see Fig. 5.2, compare green to grey, indicating that the immune response actively accelerates thrombus formation.

### 5.2.3 Accelerated thrombus formation in the inflamed microvasculature

To investigate if and how inflammation enhances thrombus formation, we next investigated the dynamics of thrombus formation; see Fig. 5.3 for snapshots of a time lapse movie. In un-

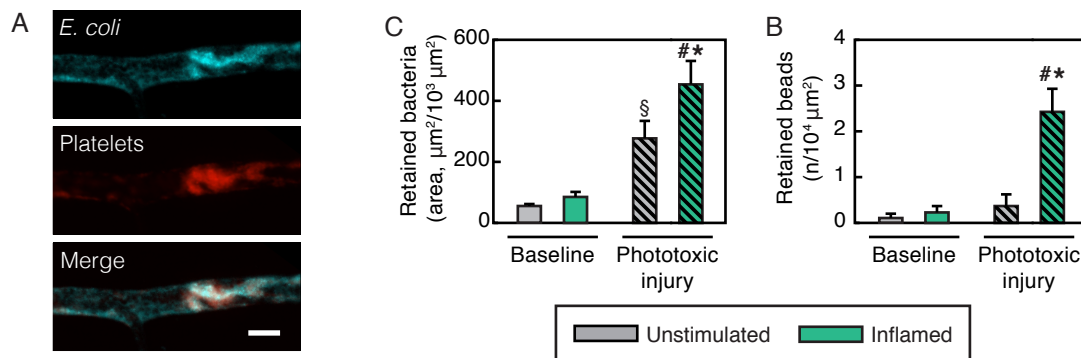


**Figure 5.2: Capturing of pathogens in microvascular thrombosis.** Thrombus formation in postcapillary venules of the cremaster muscle of WT mice was induced by phototoxic injury. (A) *E. coli* K-12 strain NCM3722 (cyan) and platelets (red) are co-localized during thrombus formation as analyzed during microvascular thrombosis by multi-channel *in vivo* fluorescence microscopy as detailed in Section D.1.3 (scale bar: 40  $\mu\text{m}$ ). Panels (B, C) show quantitative data for *E. coli* or alternatively fluorescence-labeled beads retained in thrombi during clot formation in WT mice undergoing intrascrotal stimulation with PBS or LPS (mean $\pm$ SEM for  $n=4$  per group; \* $p<0.05$  vs. unstimulated). Experiments were performed by Daniel Pühr-Westerheide (LMU, Germany).

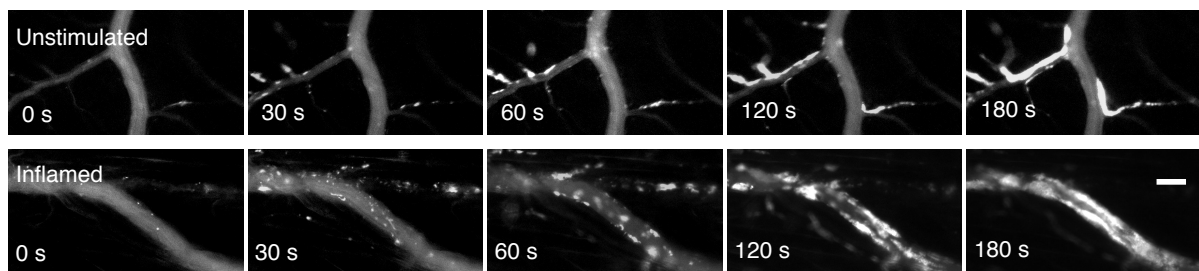


**Figure 5.3: Spatiotemporal dynamics of thrombus formation in inflamed venular microvessels.** Aggregation patterns of fluorescence-labeled platelets during thrombus formation in unstimulated or inflamed capillary and venular cremasteric vessels are visualized by multi-channel *in vivo* fluorescence microscopy as detailed in Section D.1.3; platelets in white, scale bar: 40  $\mu\text{m}$ ). In the unstimulated cremaster muscle (top row), the thrombus grows from the capillaries into lumen. In contrast, in the inflamed cremaster muscle (bottom row), platelets immediately adhere at multiple adhesion sites inside the lumen, suggesting an additional recruitment mechanisms enabled by the immune response.

stimulated tissue thrombi originate from capillaries and progressively grow into the lumen of postcapillary venules ultimately occluding these vessel segments; see Fig. 5.3, top. Virtually no platelets adhered directly in the lumen of the venules. In inflamed tissue, however, platelets directly accumulate at multiple sites in postcapillary venules thereby leading to multiple adhesion hotspots, see Fig. 5.1; bottom, that are likely responsible for the observed accelerated cessation of blood flow in the capillary and venular vasculature. Thus, inflammation changes the spatiotemporal interaction patterns of platelets in the microvasculature which effectively promotes microvascular clot formation.

#### 5.2.4 Immune cells drive platelet recruitment in the microvasculature

Leukocyte recruitment to the site of inflammation is an integral part of the inflammatory response and leukocytes are known to collaborate with platelets and the coagulation system for the propagation of thrombus growth in low-shear vessels [160–163]. We thus suspect that adherent leukocytes contribute to the platelet recruitment in the venule, a high-shear vessel, and

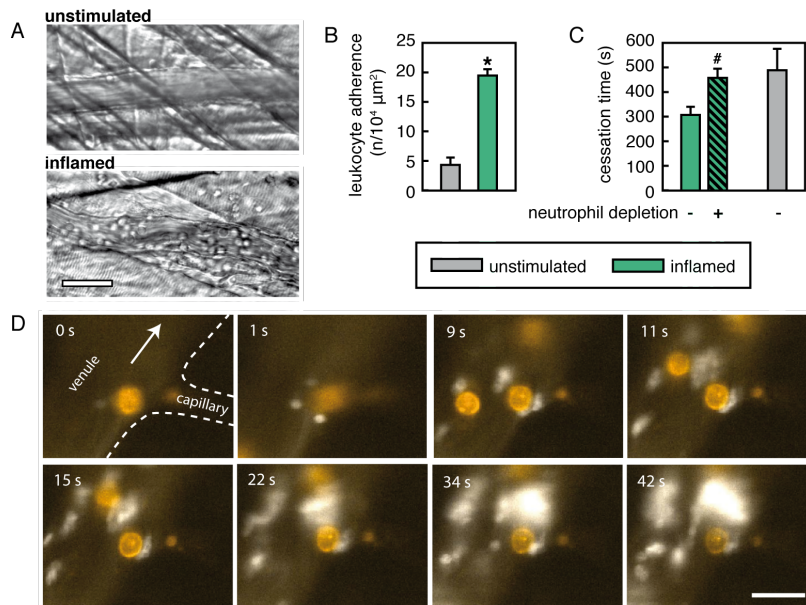


**Figure 5.4: Role of leukocytes for thrombus formation in inflamed venular microvessels.** Intravascular adherence of leukocytes was analyzed in postcapillary venules of the cremaster muscle of WT mice receiving an intrascrotal injection of PBS or LPS by RLOT *in vivo* microscopy as detailed in Section D.1.3, representative images are shown (A; scale bar: 40 μm). Panel (B) shows quantitative data for leukocyte intravascular adherence (mean±SEM for n=4 per group; \*p<0.05 vs. unstimulated control). Thrombus formation in postcapillary venules of the cremaster muscle of WT mice was induced by phototoxic injury as detailed in Section D.1.2. (C) shows quantitative data for cessation times in WT mice undergoing intrascrotal stimulation with LPS after treatment with neutrophil-depleting or isotype control antibodies (mean±SEM for n=4 per group; \*p<0.05 vs. isotype control). Interactions of platelets (white) and neutrophils (orange) during thrombus formation in postcapillary venules of the cremaster muscle of WT mice induced by phototoxic injury were visualized by multi-channel *in vivo* fluorescence microscopy as detailed in Section D.1.3, representative images are shown (D; arrow indicates flow direction, scale bar: 20 μm). Experiments were performed by Daniel Pühr-Westerheide and Matthias Fabritius (LMU, Germany).

locally promote the adhesion of platelets. During thrombus formation in inflamed tissue, we above found that platelets primarily accumulated in postcapillary venules, see Fig. 5.3, which is the vessel segment, where leukocytes arrest on the endothelium upon induction of inflammation; see Fig. 5.4A, B. We thus proposed that the presence of leukocytes is essential for platelet recruitment. Consistent with this assumption, the acceleration of thrombus formation in the inflamed venular microvasculature was completely abolished in mice with anti-body depleted neutrophils, see Fig. 5.4C.

To test whether the effect of neutrophils on platelet recruitment is global or local, we used multi-channel fluorescence microscopy and investigated the co-localization of neutrophils (orange) and platelets (white); see Fig. 5.4D. We found that platelets predominantly adhered at the vessel wall of postcapillary venules in areas downstream of adherent leukocytes during early clot formation. At these ‘hot spots’, platelets immediately formed aggregates that gradually merged into a large thrombus occluding the entire vessel segment. Hence, intravascularly adherent leukocytes recruit platelets to specific sites in the inflamed microvasculature, from which thrombus formation can emerge.

In systemic inflammations, performed by administering LPS intraperitoneally, significant immunothrombotic effects were identified, too. In contrast to local inflammations, this effect was independent of local adherent leukocytes. In particular, leukocyte adhesion during inflammation

was not significantly increased, and depletion of leukocytes did not alter the cessation times significantly, see Fig. D.2.

### 5.3 *In vitro* analysis of the platelet capture

#### 5.3.1 Rheological perturbations inside a microfluidic device

We next investigated whether the recruitment of platelets by leukocytes is based on biochemical interactions, physical properties, or a combination of both. With respect to the distinct interaction patterns of platelets in microvascular thrombosis observed in Fig. 5.4 and previous reports on the shear-dependency of platelet interactions [168, 169], we hypothesized that intravascularly adherent leukocytes promote platelet aggregation by perturbing the blood flow in the microvasculature, similar to micro-stenosis [170], yet on a much smaller scale. To separate leukocyte specific, biochemical effects from rheological effects we constructed a polydimethylsiloxane (PDMS) microfluidic device, which mimics the surface geometry of postcapillary venules and is uniformly thrombogenic Fig. 5.5A. The design and manufacturing process is described in Section D.1.4.

In summary, the device contains one sink and one drain, where tubing and reservoirs are connected. The height difference between the reservoirs at the end of the tubing sets the hydrostatic pressure, which was used to flush blood through the device. Inside the device, a single channel (40  $\mu\text{m}$  height) connects sink and drain, which splits up in the middle section of the chip into four parallel channels, see Fig. 5.5B. Each one of the channels has a different density of bump structures, constructed by two-layer soft lithography; see Section D.1.4. The bump structures are designed to mimic adherent leukocytes and are roughly cylindrical with a diameter of 8  $\mu\text{m}$ . This small dimension of the bump structure is at the precision edge of PDMS microfluidics, yielding a slightly amorphous shape. By design, bump structures and surrounding flat walls are made of the same, thrombogenic material [170], PDMS, avoiding surface specific interactions to lead to geometry dependent adhesion. Bump structures were placed at random, non-overlapping positions. Eventually all four channels merged, and fed a hydrostatic resistance, designed to support a shear rate of  $\gamma = 1500 \text{ s}^{-1}$  at a hydrostatic pressure of 50 mmH<sub>2</sub>O ( $\approx 5 \text{ mbar}$ ), which was confirmed and calibrated using fluorescence beads.

#### 5.3.2 Rheological perturbations are essential for platelet recruitment

Mouse blood was perfused in the microfluidic device for 10 min and adherence of platelets counted. In flat channels, virtually no platelets were adherent, while in channels with micro-bumps, platelets could be found in the wake of the bumps. At the highest bump density, the adherence was 100 fold increased over flat channels; see Fig. 5.5C. Time lapse microscopy revealed the capture dynamics: platelets were observed to initially adhere to the top of the bump structure, before these cellular blood components migrated to the downstream face of the obstacle; see Fig. 5.5D. Having arrived in the wake of a bump, platelets formed tethers anchoring to the bump which allow them to freely rope down in the bloodstream; see Fig. 5.5E. These platelet structures, in turn, promoted the capturing of following platelets ultimately mediating aggregation of these cellular blood components and facilitating thrombus growth; see Fig. 5.5D, E.

The adhesion of platelets was almost completely abrogated when blood was incubated with GPIIb $\alpha$  Fab' fragments (to block VWF) before the onset of microfluidic experiments Fig. 5.5C, showing the adhesion process does not only involve rheology around the bump structure, but also bio-chemical interactions.

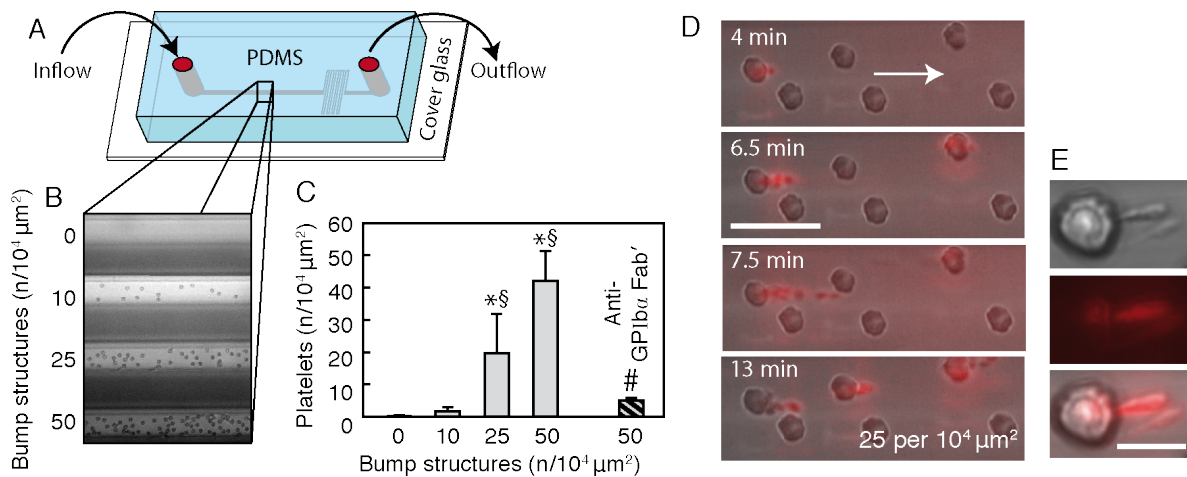


**Figure 5.5: Rheological effects of adherent leukocytes on platelet aggregation under flow.** Interactions of fluorescence-labeled platelets were analyzed *in vitro* in custom-made PDMS microfluidic devices as detailed in Section D.1.4. (A) A schematic illustration of the device and (B) transillumination microscopy images of the flow channels. (C) shows quantitative data for the number of platelets adhering to the wall of flow channels exhibiting varying densities of bump structures (mimicking intravascularly adherent leukocytes) and receiving antibodies directed against GPIb $\alpha$  (highest bump density) after 10 min of perfusion with mouse blood (mean $\pm$ SEM for n=3-4 per group; \*p<0.05 vs. flat devices, §p<0.05 vs. lowest bump density, #p<0.05 vs. highest bump density). Interactions of fluorescence-labeled platelets with bump structures were analyzed *in vitro* in custom-made PDMS microfluidic devices by high-resolution microscopy as detailed in Section D.1.5, representative images are shown (D; scale bar: 20  $\mu$ m). In panel (E; scale bar: 10  $\mu$ m), formation of GPIb $\alpha$ -positive tethers in platelets (red) adhering to bump structures is shown (scale bar=10  $\mu$ m). In-vitro experiments were performed together with Daniel Puhr-Westerheide (LMU, Germany).

## 5.4 Theoretical investigation of platelet capture

To understand the interplay of rheology and platelet capture, we next investigated the dynamics theoretically. Generally, hemodynamics is an active field of research, and its complexity should not be underestimated. Careful modeling of platelet hydrodynamics performed in the literature include wall effects [171, 172], Brownian motion [173], elasticity [174], biochemical interactions [175] and the effect of whole blood (e.g. red blood cells) on platelets [176, 177]. One dominant effect of the platelet hydrodynamics is a flipping motion, due to high shear rates, which can bring platelets into close contact with each other [172] and the endothelium in micro-stenosis [177].

Due to these studies, we postulated that the flipping motion can bring the platelet into close proximity with the micro bump structures (or adherent leukocytes) of this work, and focused on a theoretical approach that correctly describes the flipping motion, while neglecting other aspects, like Brownian motion, elasticity of the impact of whole blood. We chose a combination of Navier-Stokes equations to describe the blood flow around the bump structures and Stokes drag to describe the platelet motion. Platelets were spawned close to the endothelium, to account for the near-wall excess of platelets caused by red blood cells [176].

### 5.4.1 Fluid flow

#### General formulation of the Navier-Stokes equation

Generally, the Navier-Stokes equations describe the motion of fluids and are derived from Newton's second law of motion. In the case of a compressible Newtonian fluid, this yields

$$\rho \left( \frac{\partial \mathbf{u}}{\partial t} + \mathbf{u} \cdot \nabla \mathbf{u} \right) = -\nabla p + \nabla \cdot \left( \mu \left( \nabla \mathbf{u} + (\nabla \mathbf{u})^T \right) - \frac{2}{3} \mu (\nabla \cdot \mathbf{u}) \mathbf{I} \right) + \mathbf{F} \quad (5.1)$$

where  $\mathbf{u}$  is the fluid velocity,  $p$  is the fluid pressure,  $\rho$  is the fluid density and  $\mu$  the fluid dynamic viscosity.  $\mathbf{F}$  is an external force applied to the fluid. The different terms in the Navier-Stokes equation correspond to different forces: The first term  $\rho (\partial \mathbf{u} / \partial t + \mathbf{u} \cdot \nabla \mathbf{u})$  describes the inertia of the fluid, the second,  $-\nabla p$  the pressure forces, the third term,  $\nabla \cdot \left( \mu \left( \nabla \mathbf{u} + (\nabla \mathbf{u})^T \right) - \frac{2}{3} \mu (\nabla \cdot \mathbf{u}) \mathbf{I} \right)$ , describes viscous forces. The final term describes external forces. The Navier-Stokes equation are solved together with the continuity equation

$$\frac{\partial \rho}{\partial t} + \nabla \cdot (\rho \mathbf{u}) = 0. \quad (5.2)$$

The Navier-Stokes equations represent the conservation of momentum, while the continuity equation represents the conservation of mass.

### Mach number and incompressibility

Depending on the flow regime of interest, it is often possible to simplify these equations. In the field of fluid dynamics, the different flow regimes are categorized using non-dimensional numbers: the Reynolds number and the Mach number. The Mach number corresponds to the ratio of fluid velocity to speed of sound

$$M = U/c, \quad (5.3)$$

and measures the compressibility of the fluid. In the experiments of this work, the fluid velocity  $U \approx 2$  mm/s is much smaller than the speed of sound  $c \approx 1500$  m/s, leading to a minuscule Mach number of  $M = 10^{-6}$ . In this regime, we can neglect density changes  $\partial \rho / \partial t$  in Eq. (5.2) and rewrite the continuity equation as

$$\nabla \cdot \mathbf{u} = 0. \quad (5.4)$$

Because the divergence of the velocity field  $\mathbf{u}$  is zero, we can neglect the term  $2/3 \mu (\nabla \cdot \mathbf{u}) \mathbf{I}$  in the viscous term of the Navier-Stokes equation, Eq. (5.1).

### Reynolds number and laminar flow

The Reynolds number corresponds to the ratio of internal forces to viscous forces,

$$\text{Re} = \frac{\rho U L}{\mu} \quad (5.5)$$

Here  $U$  is the characteristic velocity and  $L$  the characteristic dimension of the system. In the venule and the microfluidic device, the fluid flow is around  $U \approx 2$  mm/s at a diameter of the venule or channel of  $L \approx 40$   $\mu\text{m}$ . Together with  $\rho = 1$  kg/m<sup>3</sup> and  $\mu = 0.89$  mPa  $\cdot$  s at 25°C, this results in a very low Reynolds number  $\text{Re} \approx 10^{-4}$ .

In this regime, inertial forces are very small compared to viscous forces and can thus be neglected. In the absence of external forces, the Navier-Stokes equation then reads

$$0 = -\nabla p + \nabla \cdot \left( \mu \left( \nabla \mathbf{u} + (\nabla \mathbf{u})^T \right) \right). \quad (5.6)$$

The steady state solutions of the Navier-Stokes equation in this regime are exclusively laminar, with cross-currents, eddies or swirls being forbidden mathematically.

### Boundary conditions

The solution of the Navier-Stokes equation for laminar flow, Eq. (5.6), requires the definition of boundary conditions. We choose no-slip boundaries, i.e. the velocities are zero, at all interfaces of liquid and solid,

$$\mathbf{u} = 0, \quad \text{at } \partial V \quad (5.7)$$

and a pressure difference  $\Delta p$  between inlet and outlet

$$p = \Delta p, \quad \text{at inlet} \quad (5.8)$$

$$p = 0, \quad \text{at outlet} \quad (5.9)$$

that reproduces the physiological flow velocities of about 2 mm/s.

### 5.4.2 Platelet motion

Prior to adhesion, platelets are biconvex discoid (lens-shaped) structures, 2-3  $\mu\text{m}$  in greatest diameter, and show only a small amount of irregularity, including occasional marginal filaments or pseudopods [178]. After adhesion, filaments can form; see Fig. 5.5E. We are interested in the capture process prior to final adhesion and thus approximate the platelet shape to be an oblate discoid, with a equatorial diameter of 2  $\mu\text{m}$  and a small diameter of 1  $\mu\text{m}$ . We further assume that platelets are inelastic and neglect deformations, as well as Brownian motion.

In general, the surface of the platelet requires a no-slip condition, and the motion of the platelet will be governed by the momentum and angular momentum transferred to the platelet by the fluid. Since the platelet is small compared to the dimensions of the system, we assume that it does not alter the fluid velocity field. This assumption greatly simplifies the simulations, as the fluid velocity and platelet motion can be solved sequentially.

Motion of the inelastic platelet requires two components, motion of the center of mass and rotation. Due to the laminar flow regime encountered in this work, we approximate drag by Stoke's law to describe motion of the center of mass of the platelet. For a discoid particle, the drag force is given by

$$\mathbf{F}_d(t) = 6\pi\mu a K \Delta \mathbf{v}(t) \quad (5.10)$$

where  $a = 2 \mu\text{m}$  is the equatorial diameter,  $\mu$  is dynamic viscosity of water and  $\Delta \mathbf{v}(t) = \mathbf{v}(t) - \mathbf{u}(\mathbf{x}(t))$  the velocity difference between the platelet and fluid. The shape factor  $K = \mathcal{O}(1)$  depends on the orientation of the platelet relative to the fluid flow.

In addition, an adhesive force, pulling the platelet towards surface can be implemented. In this work we use a Lennard-Jones potential

$$V_a(\mathbf{x}) = \epsilon \left( \left( \frac{d_m}{d(\mathbf{x})} \right)^{12} - \left( \frac{d_m}{d(\mathbf{x})} \right)^6 \right), \quad (5.11)$$

with  $d(\mathbf{x})$  being the nearest distance between the platelet at position  $\mathbf{x}$  and the wall, and  $\epsilon$  is the depth of the potential. The equilibrium distance  $d_m$  of the platelet in the adhesion state was estimated with  $d_m = 200$  nm, the typical length of VWF in whole blood<sup>1</sup>. The adhesive force

$$\mathbf{F}_a(\mathbf{x}) = -\nabla \cdot V_a(\mathbf{x}) \quad (5.12)$$

acts on the center of mass of the platelet,  $\mathbf{x}$ , pulling it towards the wall. We choose the strength of this force, i.e.  $\epsilon$ , such that adhesion is 50% stronger than drag in the wake of the micro-bump (at 200 nm distance and half height of the bump structure).

Rotation of the platelet is calculated by matching the angular velocity of the platelet  $\omega$  to minimize the surface integral of relative velocities of platelet wall and fluid at the surface of the platelet

$$0 = \int_S (\mathbf{u}(\mathbf{x} + \mathbf{r}) - \hat{\mathbf{t}}|\mathbf{r}|\omega) d\Sigma. \quad (5.13)$$

Here  $\mathbf{x}$  is the center of mass of the platelet,  $\mathbf{r}$  the position of a surface element relative to the center of mass, and  $\hat{\mathbf{t}}$  the tangential normal vector. This formula essentially measures the fluid velocity difference at the top and bottom of the platelet, and induces a rotational motion accordingly.

### 5.4.3 Simulation results

The previous *in-vitro* analysis of platelet capture in microfluidics, Fig. 5.5, revealed that the capture process happens on top of the bump structure. We thus choose a trajectory that is centered relative to the bump structure and reduce the dimensions to 2D. We then sequentially solve the fluid flow, using Eq. (5.6) and the boundary conditions Eqs. (5.7) and (5.9), and platelet motion using Eq. (5.10). We initially omitted adhesive forces, to isolate the effect of fluid motion around the bump structure on the platelet capture.

In vicinity of the bump structures, blood flow is accelerated, see Fig. 5.6A. The increased velocity of the blood leads to an increase in shear rate at the top of the bump structure. This increases the velocity of the platelet Fig. 5.6B, and accelerates the flipping motion of the platelet Fig. 5.6C. As a result of these events, one part of the rotating discoid platelet is brought in close proximity to the bump's surface (Fig. 5.6D), thus allowing bimolecular binding and arrest. From these simulations we conclude that a micro bump of just 8  $\mu\text{m}$  diameter can alter the rheological environment around it just enough to capture freely flowing platelets from the near-wall vicinity.

## 5.5 Biochemistry of platelet adhesion in the microvasculature

While the micro bump structures can bring platelets into close vicinity of the surface, at the capture location there still exists a high shear rate, which results in a strong drag force. The complete arrest of the platelets required for thrombus formation, thus requires additional, biochemical interactions, which keep the platelets in place. Evidence of the necessity of such

<sup>1</sup>VWF multimerizes in physiological conditions: VWF size distribution in whole blood is roughly exponential, with an average length of 4.7 monomers, with each monomer being cylindrical with around 42 nm length and 3 nm diameter, leading to an average VWF length of about 200 nm [179]. Under pathogenic shear conditions VWF forms ultra-large multimers (ULVWF), reaching from several  $\mu\text{m}$  to mm in size [180]. As adhesion was observed to be locally restricted within less than a few  $\mu\text{m}$  around the center-top of the bump structures, we assume that ULVWF do not play a significant role in the capture process.

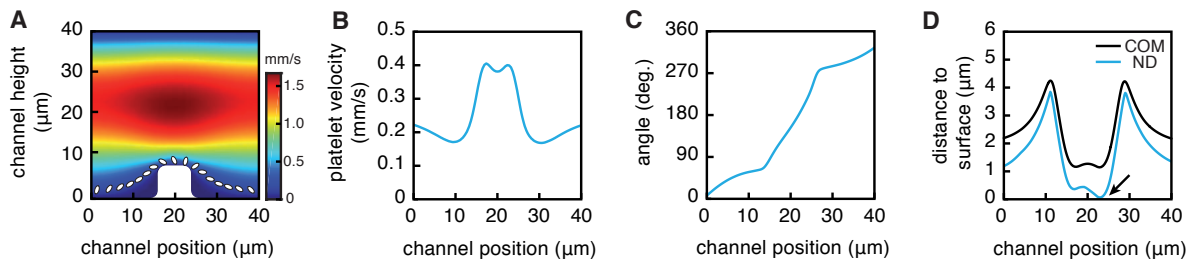


**Figure 5.6: Theoretical analysis of platelet capture by intravascularly adherent leukocytes.** Platelet motion in a flow channel exhibiting a bump structure was modeled along a longitudinal cross-section with a fluid dynamics simulation of an ellipsoid as detailed in Methods. **(A)** The blood flow velocity profile (pseudo-colors) and the motion kinetics of a platelet moving over the bump structure (white; assuming the absence of bimolecular interactions) in a flow channel. Platelet velocity **(B)** and its relative angle **(C)** during its movement over the bump structure are shown. **(D)** Distance to surface of the platelet's center of mass to the bump surface ('COM') is approximated to the surface during passage of the micro bump. Additionally, a flipping motion brings one end of the platelet into close proximity to the bump surface, further reducing the nearest distance ('ND') and thus bringing it to  $\approx 100$  nm distance, which would allow biochemical binding (arrow).

biochemical interactions was observed in the *in-vitro* experiments, too, see Fig. 5.5C: When VWF-GPIb $\alpha$  interactions were inhibited, platelet adherence was drastically reduced.

Towards a more comprehensive understanding of the biochemical mechanisms underlying the arrest of platelets, in particular the immune cell-driven thrombus formation in the microvasculature, we systematically screened a variety of candidate adhesion and signaling molecules for their functional relevance in this particular biological process. To avoid interference with inflammatory processes arising during the pre-stimulation period of the cremaster muscle (6 h stimulation with LPS), blocking antibodies directed against the target proteins were applied 10 min prior to the induction of phototoxic injury and *in vivo* microscopy. In line with studies in different experimental models [166, 181–191], clot formation in the inflamed venular microvasculature required vWF (which is scattered throughout the thrombus) and its platelet counter receptor GPIb $\alpha$ , which manifests in a prolonged cessation time upon upon inhibition with the respective antibody; see Fig. 5.7A. In contrast, inhibition of the alternative platelet receptor GPIIb/IIIa did not alter cessation times; see Fig. 5.7A).

Blockade of CD40 or its ligand CD40L/CD154 lead to a significant prolongation of thrombus formation in the inflamed venular microvasculature as compared to controls, whereas blockade of P-selectin/CD62P (facilitating platelet- or leukocyte-endothelial cell and platelet- leukocyte interactions through leukocyte PSGL-1/CD162 [166, 192–194]) or Mac-1/CD11b (facilitating interactions of leukocytes with fibrin(ogen) or platelet GPIb $\alpha$  [195]) did not significantly alter thrombus formation in inflamed venular microvessels; see Fig. 5.7A).

In addition to adhesion and signaling molecules, NETs released by neutrophils have recently been demonstrated to activate platelets and bind components of the coagulation system thereby promoting thrombosis in lower-shear vessels such as liver sinusoids, arteries, and veins [160–163]. To our surprise, however, application of DNase I (which degrades NETs) did not significantly alter thrombus formation in the inflamed microvasculature, see Fig. 5.7A, indicating that NETosis is negligible microvascular thrombosis. This might be due to the limited mechanical stability of complexes between DNA and other proteins (e.g., fibrin) under high shear stress [196]. Consequently, the inhibition of either vWF, GPIb $\alpha$ , CD40, and CD40L lead to significantly less platelet aggregates after phototoxic injury; see Fig. 5.7B. Collectively these bimolecular findings emphasize that immune cell-driven thrombosis in the microvasculature requires a combination of physical and biochemical effects.

Employing *in vivo* immunostaining and multi-channel fluorescence microscopy as well as

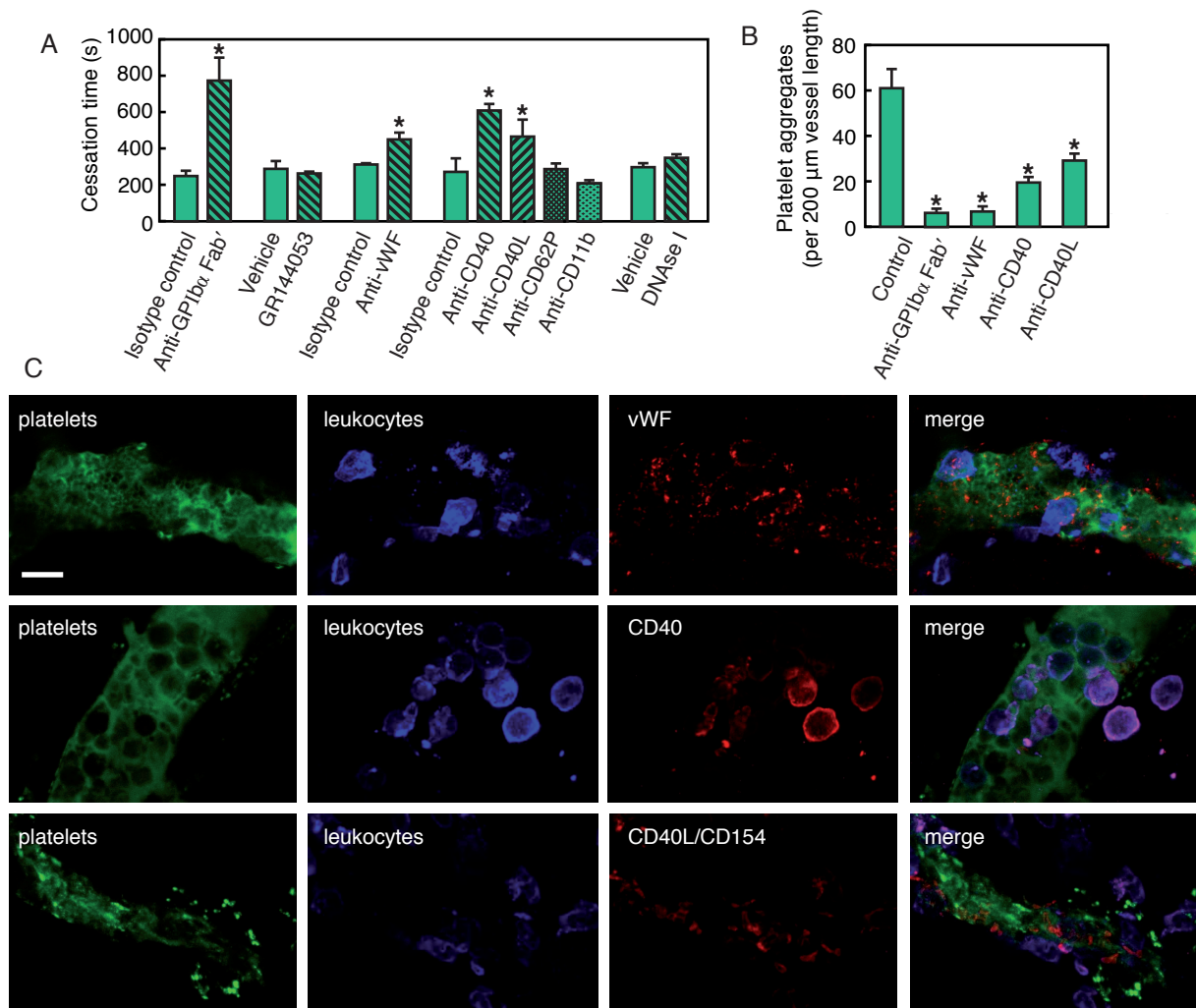


**Figure 5.7:** Molecular mechanisms underlying thrombus formation in inflamed venular microvessels. Thrombus formation in postcapillary venules of the cremaster muscle of WT mice was induced by phototoxic injury as detailed in Sections D.1.3 and D.1.7. **(A)** Quantitative data for cessation times in animals undergoing intrascrotal stimulation with LPS and treatment with antibodies directed against P-selectin/CD62P, Mac-1/CD11b, vWF, GPIIb/IIIa, CD40, or CD40L/CD154, with compound GR144053 (inhibitor of GPIIb/IIIa), with DNase I (NET-degrading enzyme), or vehicle/isotype control antibodies (mean±SEM for n=4 per group; \* $p < 0.05$  vs. vehicle/isotype control, 'One way ANOVA' followed by 'Dunnett's test' for comparison of > 2 groups, 't-test' for comparison of 2 groups). **(B)** Platelet aggregates in animals undergoing intrascrotal stimulation with LPS and treatment with antibodies directed against vWF, GPIIb/IIIa, CD40, CD40L/CD154, or isotype control antibodies (mean±SEM for n=3 per group; \* $p < 0.05$  vs. baseline non-related to leukocytes, # $p < 0.05$  vs. baseline related to leukocytes; 'One way ANOVA' followed by 'Dunnett's test'). **(C)** Representative confocal microscopy images of neutrophils/classical monocytes (Ly-6G/C; blue), platelets (GPIIb/IIIa; green), and vWF, CD40, or CD40L/CD154 (red) in thrombi occluding postcapillary venules of the inflamed cremaster muscle of WT mice. Data suggests that vWF is spread through the entire thrombus, with non-co-localized local aggregates (top row); CD40 is co-localized with leukocytes (middle row); CD40L is co-localized with both platelets and leukocytes (bottom row); scale bar: 10 μm. Data in panels A and B was taken by Daniel Puhr-Westerheide and Matthias Fabritius (LMU, Germany), images in panel C were taken by Gabriele Zuchtriegel (LMU, Germany).

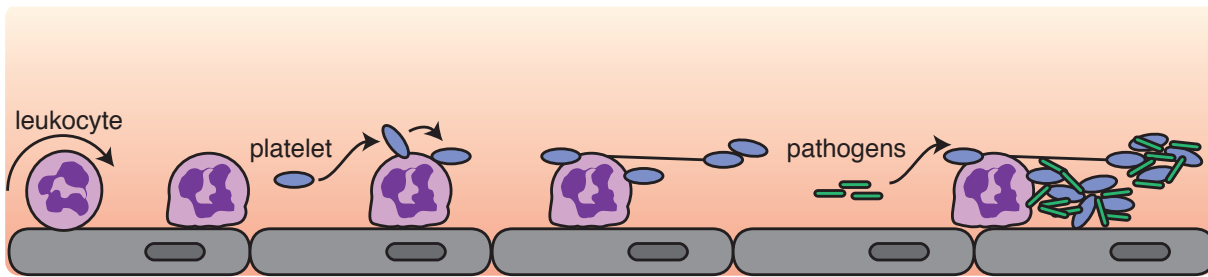


**Figure 5.8: Graphical synopsis** In injured tissue, circulating leukocytes (purple) are recruited to postcapillary venules where they arrest on endothelial cells (grey). Supported by hydrodynamic forces, circulating platelets (blue) get in close contact with leukocytes. This enables platelets to form tethers anchoring to adherent leukocytes thus initiating thrombus formation. Subsequently, pathogens (green) invading the microvasculature of injured tissue get trapped in the forming thrombus preventing them from systemic dissemination.

*ex vivo* confocal microscopy analyses, the location of vWF, CD40, and CD40L/CD154 in the venular microvascular thrombus formation was analyzed; see Fig. 5.7C. Platelets are stained green (GPIIb/IIIa/FITC dextran), leukocytes are stained blue (Ly-6G/C), the receptor of interest is stained red. vWF appears to be spread throughout the entire thrombus, with local aggregates that are not co-localized with neither platelets nor leukocytes. CD40 is clearly co-localized with leukocytes and CD40L, the ligand of CD40, is localized with platelets and leukocytes. This suggests that while vWF is generally necessary thrombosis at high shear rates, and thus found throughout the entire thrombus, it is not contributing to the interaction between leukocytes and platelets. Rather the co-localization of CD40 on leukocytes and its ligand CD40L on platelets suggests a specific interaction that contributes to immunothrombosis.

## 5.6 Discussion

In this work we studied how the immune system enhances thrombus formation in the microvasculature. Using bio-mimicking microfluidic devices and theoretical fluid dynamics simulation, we showed that local perturbations of the blood flow around adherent leukocytes are essential to platelet recruitment. In addition, successful recruitment of platelet requires biochemical interactions. In contrast to larger (lower-shear) vessels, successful recruitment of platelets in high-shear microvessels does not require fibrin generation or extracellular trap formation, but involves GPIIb/IIIa-vWF and CD40-CD40L-dependent platelet interactions.

The enhanced thrombotic effect was only found in the draining part of the microvasculature (venules) and not in the feeding part (arterioles). In addition, a leukocyte-dependent enhanced thrombogenic effect was only found in local inflammations, found typically at a site of vessel injury and barrier breach of pathogens, in contrast to leukocyte-independent immunothrombosis in systemic inflammation. These findings lead us to speculate that a potential physiological function of this directed immunothrombosis is the efficient combat of pathogens that breached the barrier into the host's system. As a result of the immunothrombosis, the infected draining part of the microvasculature can be isolated from the blood system, so that the systemic dissemination of pathogens can be prevented. In addition, we found that pathogens became trapped in the thrombus. The strategy of the host's organism to capture and eliminate pathogens in targeted manner by immunothrombosis, could be a major factor in the battle against infections.

This previously unanticipated function of leukocytes, the shaping of the rheological environment for platelet aggregation, leads to a new understanding of the platelet recruitment in the inflamed microvasculature, see Fig. 5.8 for a graphical synopsis. First, leukocytes adhere on the endothelium by rolling and subsequent arrest. Thereafter, the stationary leukocyte recruits

platelets, which adhere due to a flipping motion, form tethers and accumulate in a process that requires both physical and biochemical effects. The resulting thrombus can capture free floating pathogens, and thus contributes to the immune response.

Even with controlled thrombus formation being beneficial for preventing hemorrhage or the systemic spread of pathogens, exaggerated vascular clotting (e.g., under severe inflammatory conditions) leads to the interruption of blood supply and provokes ischemic tissue injury [153–155]). In the past decades, the application of endovascular intervention techniques for the removal of thrombi from arteries and veins in clinical routine revolutionized the treatment of thromboembolic pathologies including myocardial infarction [197] and stroke [198, 199]. Therapeutic options for the dissolution of blood clots from the microvasculature, however, are still limited due to its inaccessibility to interventional procedures and demand for the development of powerful pharmaceutical strategies. In this context, our present findings urgently suggest the inclusion of immune cells as targets in treatment regimens for thromboembolic events.

# Appendices



# Appendix A

## The benefit of a proteome reserve

### A.1 Theoretical analysis of the instantaneous model

We will describe in this section a kinetic model for upshifts, already introduced by several authors such as Schleif [79] and Dennis & Bremer [71, 78] and link the kinetics to the protein allocation model introduced in [34].

#### A.1.1 Kinetic modeling of the proteome composition

The starting point in assumption is that proteome production rate, or protein flux, is assumed to be proportional to the mass of the total ribosome mass  $M_R$  through a (time-dependent) proportionality constant  $\sigma_R(t)$ , as follows:

$$\frac{dM(t)}{dt} = \sigma_R(t)M_R(t), \quad (\text{A.1})$$

$$\lambda(t) = \frac{1}{M(t)} \frac{dM(t)}{dt} = \sigma_R(t)\phi_R(t). \quad (\text{A.2})$$

with  $\phi_R(t) = M_R(t)/M(t)$  is the mass fraction of the R-sector.

The parameter  $\sigma_R$  is an average translation rate, being proportional to the protein flux per “extended ribosome” mass unit. In particular, this quantity does not distinguish between active and inactive ribosomes. If we consider that at any moment only a fraction  $f_{\text{act}} = M_R^{\text{act}}/M_R$  is translating at a rate  $k$ , we may write:

$$\frac{dM}{dt} = kM_R^{\text{act}} = kf_{\text{act}}M_R \equiv \sigma_R M_R. \quad (\text{A.3})$$

Therefore,  $\sigma_R$  can be decomposed as the product of the elongation rate and the active ribosome fraction,  $\sigma_R(t) = k(t)f_{\text{act}}(t)$ . A recent study [41] highlighted the contribution of the translation rate  $k_{\text{el}}$  and the fraction of active ribosomes  $f_{\text{act}}$  to  $\sigma_R$ . As the nutrient source is decreased from rich to poor media, the steady state elongation rate  $k^*$  drops slightly below  $\lambda = 1/h$  (from  $\sim 17$  aa/s to about 8 aa/s in poor nutrient conditions or stationary state). Given the elongation rates  $k$ , the fraction of active ribosomes  $f_{\text{act}}$  can be computed from the known ribosome abundances and the protein flux;  $f_{\text{act}}$  seems to be close to one for growth rates larger than 0.5/h, and rapidly decreasing below that [41]. Therefore,  $\sigma_R = kf_{\text{act}}$  is constant above  $\lambda = 1/h$ , and decreases for smaller growth rates.

### A.1.2 Protein allocation

In order to solve the kinetic system, one also needs to know how the total protein flux is partitioned, or allocated, to the different proteins (or, equivalently, protein sectors). The protein flux of any given protein  $j$  is a fraction of the total protein flux. We will this fraction as  $\chi_j(t)$ :

$$\frac{dM_j(t)}{dt} = \chi_j(t) \frac{dM(t)}{dt} = \chi_j(t) \sigma_R(t) M_R(t), \quad (\text{A.4})$$

The value of  $\chi_j(t)$  is set by several factors, such as the abundance of mRNA of the species  $j$  and/or the translation efficiency of the specific transcript. Of course, the sum over the masses of the individual proteins must be equal to with the total proteome mass,  $\sum_j M_j(t) = M(t)$ . This condition implies the constraint  $\sum_j \chi_j(t) = 1$ . We can now compute the time derivative of the protein fraction  $\phi_j$ :

$$\frac{d\phi_j(t)}{dt} = \frac{d}{dt} \left( \frac{M_j(t)}{M(t)} \right) = \frac{1}{M(t)} \frac{dM_j(t)}{dt} - \frac{M_j(t)}{M(t)} \frac{dM(t)}{dt} \quad (\text{A.5})$$

Using equations Eq. (A.1) and Eq. (A.4) we obtain:

$$\frac{d\phi_j(t)}{dt} = \sigma_R(t) \phi_R(t) (\chi_j(t) - \phi_j(t)) = \lambda(t) (\chi_j(t) - \phi_j(t)). \quad (\text{A.6})$$

Summarizing, Eq. (A.4) or, equivalently, Eqs. (A.2) and (A.6), depend on the translation rate  $\sigma_R(t)$  and on the “flux fractions”  $\chi_j(t)$ , setting the ratios of the production rates of the individual proteins. The knowledge of these functions allows to completely solve the dynamic system.

### A.1.3 R-proteins dynamics for constant $\sigma_R$ and $\chi_R$ with a generic initial state

Let us now consider Eq. (A.4) in the case of  $j$  being the R-sector itself,  $j = R$ . One obtains the following expression:

$$\frac{d\phi_R(t)}{dt} = \sigma_R(t) \phi_R(t) (\chi_R(t) - \phi_R(t)) . \quad (\text{A.7})$$

This equation is a closed equation for  $M_R$ , and can be easily integrated in the particular case of constant  $\sigma_R$  and  $\chi_R$ . We will indicate with the asterisk (\*) the steady state value of dynamic quantities, like the instantaneous growth rate ( $\lambda^*$ ) or the R-sector proteome fraction ( $\phi_R^*$ ). One obtains:

$$M_R(t) = M_R(0) e^{\lambda^* \sigma_R^* t} = M_R(0) e^{\lambda^* t} . \quad (\text{A.8})$$

We can then plug this expression in Eq. (A.1) and integrate, obtaining:

$$M(t) = M(0) \left( 1 + \frac{\phi_R(0)}{\chi_R} \left( e^{\lambda^* t} - 1 \right) \right) . \quad (\text{A.9})$$

Here,  $M(0)$  and  $M_R(0)$  represent two independent initial conditions of the system. It is convenient to introduce  $\phi_R(0) = M_R(0)/M(0)$ , so that we use  $M(0)$  and  $\phi_R(0)$  as initial conditions. Then, the instantaneous growth rate and the R-sector proteome fractions are easily computed from their definitions:

$$\lambda(t) = \lambda_0 + \frac{\lambda^* - \lambda_0}{1 + (\lambda^*/\lambda_0)/(e^{-\lambda^*t} - 1)}, \quad \frac{\lambda_0}{\lambda^*} = \frac{\phi_R(0)}{\chi_R^*} \quad (\text{A.10})$$

The R-sector proteome fraction  $\phi_R(t)$  is always proportional to  $\lambda(t)$ , with  $\phi_R(t)/\chi_R^* = \lambda(t)/\lambda^*$  at any time  $t \geq 0$ . The steady state equations  $\phi_R^* = \chi_R^*$  and  $\lambda(t) = \lambda^*$  are then recovered in the  $t \rightarrow \infty$  limit, or if the initial conditions satisfy  $M_R(0) = \chi_R^* M(0)$ .

If we further suppose that for any protein  $j$  the functions  $\chi_j$  do not depend on time, the kinetics of each protein fraction is obtained solving Eq. (A.6), where  $\lambda(t)$  is given by Eq. (A.10). Let us define the fractional mass increase  $W(t) = M(t)/M(0)$ , whose expression is:

$$W(t) = \exp\left(\int_0^t \lambda(s) ds\right) = 1 + \frac{\lambda_0}{\lambda^*} (e^{\lambda^*t} - 1). \quad (\text{A.11})$$

where we used the result in Eq. (A.9). Then, one can easily check that the proteome fraction for a generic protein  $j$  is given by:

$$\phi_j(t) = \frac{1}{W(t)} \phi_j(0) + \left(1 - \frac{1}{W(t)}\right) \chi_j^*. \quad (\text{A.12})$$

This expression is linear in the protein fractions, so that to obtain the time-dependence of any set  $\mathcal{S}$  of proteins one only has to sum over the proteins  $j \in \mathcal{S}$ . In particular, if we sum over the ribosomal proteins ( $\mathcal{S} = R$ ), and we use the relation  $\phi_R(t) = \chi_R^* \lambda(t)/\lambda^*$ , one obtains an alternate form for the growth kinetics:

$$\lambda(t) = \frac{1}{W(t)} \lambda_0 + \left(1 - \frac{1}{W(t)}\right) \lambda^*. \quad (\text{A.13})$$

#### A.1.4 Upshifts and the R-sector offset

Schleif and Dennis & Bremer showed [71, 78, 79] that the proteome production rates stabilize within a few minutes to their final values after an upshift. The obvious approximation is to consider this first phase of the upshift instantaneous, meaning that both  $\gamma$  and the ribosomal production rate  $f_R$  are discontinuous at the upshift ( $t = 0$ ), being constant before and after it. In this situation Eq. (A.10) can be used, since we can solve for constant  $\sigma_R$  and  $\chi_R$  in the two regions  $t < 0$  and  $t > 0$ , and then match the solutions. Let us assume that the growth rate and the proteome fractions are at steady state before the upshift. Then, an upshift at  $t = 0$  is described from the following choice:

$$\sigma_R(t) = \begin{cases} \sigma_{R,i}^*, & t < 0, \\ \sigma_{R,f}^*, & t \geq 0. \end{cases} \quad \chi_R(t) = \begin{cases} \chi_{R,i}^*, & t < 0, \\ \chi_{R,f}^*, & t \geq 0. \end{cases} \quad (\text{A.14})$$

We will label  $\lambda_i^*$  and  $\lambda_f^*$  the initial and final (in the  $t \rightarrow \infty$  limit) growth rates, respectively. Then we have Eq. (2.8) from the main text:

$$\lambda(t) = \begin{cases} \lambda_i^*, & t < 0, \\ \frac{\lambda_f^*}{1 + \left(\frac{\lambda_f^*}{\lambda_0} - 1\right) e^{-\lambda_f^*t}}, & t \geq 0. \end{cases} \quad (\text{A.15})$$

where the constant  $\lambda_0$  is computed by imposing that the R-sector proteome fraction  $\phi_R(t)$  is continuous at  $t = 0$ :

$$\lambda_0 = \lambda_f^* \chi_{R,i}^* / \chi_{R,f}^* = \sigma_{R,f}^* \chi_{R,i}^*. \quad (\text{A.16})$$

This quantity is the growth rate attained immediately after the upshift, as a function of the initial and final steady state proteome fractions  $\chi_{R,i}^* = \phi_{R,i}^*$  and  $\chi_{R,f}^* = \phi_{R,f}^*$ . Therefore, the upshift kinetics can be summarized as follows:

- The first phase is a rapid increase in the instantaneous growth rate from  $\lambda_i^* = \sigma_{R,i}^* \phi_{R,i}^*$  to a larger value  $\lambda_0 = \sigma_{R,f}^* \phi_{R,i}^*$ . The jump in growth rate is uniquely due to the increase in ribosome efficiency:

$$\lambda_0 - \lambda_i^* = (\sigma_{R,f}^* - \sigma_{R,i}^*) \phi_{R,i}^* . \quad (\text{A.17})$$

- The second phase is a much slower increase in the growth rate from  $\lambda_0 = \sigma_{R,f}^* \phi_{R,i}^*$  to the final value  $\lambda_f^* = \sigma_{R,f}^* \phi_{R,f}^*$ . This time, the further increase in growth rate is uniquely due to the increase in ribosomes, with no variation in the utilization efficiency:

$$\lambda_f^* - \lambda_0 = \sigma_{R,f}^* (\phi_{R,f}^* - \phi_{R,i}^*) . \quad (\text{A.18})$$

### Lag time

The lag time  $\tau_{\text{lag}}$  can be computed from Eq. (A.11). Asymptotically, to  $t \rightarrow \infty$ , the fractional mass increase  $W(t)$  can be written as:

$$W(t) \sim \frac{\lambda_0}{\lambda_f^*} \exp(\lambda_f^* t) . \quad (\text{A.19})$$

From the definition of lag time, this expression is equal to  $W(t) = \exp(\lambda_f^*(t - \tau_{\text{lag}}))$ . Therefore, we can solve for the lag time as:

$$\tau_{\text{lag}} = \frac{1}{\lambda_f^*} \log \left( \frac{\lambda_f^*}{\lambda_0} \right) = \frac{1}{\lambda_f^*} \log \left( \frac{\chi_{R,f}^*}{\chi_{R,i}^*} \right) . \quad (\text{A.20})$$

Also, we can express  $\lambda_0$  in terms of the lag time:

$$\lambda_0 = \lambda_f^* e^{-\lambda_f^* \tau_{\text{lag}}} . \quad (\text{A.21})$$

## A.2 Fitness landscape in upshifts to rich media

The aim of this section is to describe how strains with different  $\phi_{R0}$  perform in different environments, that is, for different uptakes, doing analytical and numerical calculations based on Eq. (A.15). We will restrict ourselves to the simple situation in which the cell culture undergoes a nutritional upshift at time  $t = 0$ , and we study the fractional, or relative, mass increase  $M(T)/M(0)$  after a fixed amount of time  $T$ . This models a real experiment in which the cells are supplied with high quality nutrients for a time interval  $T$ . The strain which produces more mass in the time window has an obvious selective advantage on the others. The reciprocal fitness measure is given by the effective growth rate for a fixed fractional mass increase: this corresponds to the biological situation in which the cells can grow until they reach a certain total mass, or density. In this case the analytical treatment is more complex, but the numerical results are analogous. For this reason we will discuss the first case only.

As a warm-up exercise, consider two identical cell populations, whose growth kinetics are both described by Eq. (A.15), undergoing an upshift at time  $t = 0$ . In the simple case in which the initial populations are the same ( $M^{(1)}(0) = M^{(2)}(0)$ ) and the final growth rates are the same ( $\lambda_f^{*(1)} = \lambda_f^{*(2)} \equiv \lambda_f^*$ ), one can compute the ratio of the bacterial (protein) masses using Eq. (A.11) as:

$$\frac{M^{(1)}(t)}{M^{(2)}(t)} = \frac{W^{(1)}(t)}{W^{(2)}(t)} = \frac{1 + (\lambda_0^{(1)}/\lambda_f^*)(e^{\lambda_f^* t} - 1)}{1 + (\lambda_0^{(2)}/\lambda_f^*)(e^{\lambda_f^* t} - 1)} \quad (\text{A.22})$$

From this equation we can see that the mass ratio asymptotically reaches the value  $\lambda_0^{(1)}/\lambda_0^{(2)}$  as  $T \gg \lambda_f^*$ . This simple example shows that a large value of  $\lambda_0$ , and thus of the ribosomal offset  $\lambda_R = \nu_R \phi_{R0}$ , may provide a large increase in the mass of the cell population in dynamic environments. However, if the final growth rates  $\lambda_f^{*(1)}$  and  $\lambda_f^{*(2)}$  are not equal, the fastest growing strain will always dominate in the long run.

### A.2.1 Analysis of the fitness landscape

The upshifts in rich media are fully specified described by the kinetics shown before, plus steady state informations on the proteome allocation. In particular, given the proteome partitioning model in Scott et al., 2010 [34], the kinetics are fully specified by the initial ( $\nu_P^i$ ) and final ( $\nu_P^f$ ) quality of the nutrients, by the duration of the upshift experiment  $T$ , and by the other parameters appearing in the proteome partitioning model ( $\phi_{R0}$ ,  $\nu_R$ ,  $\phi_Q$ ). The proteome mass increase at time  $T$ , which coincides with our definition of absolute fitness  $W$ , is shown in Eq. (A.11), which we rewrite here as:

$$\begin{aligned} W(T, \phi_{R0}, \dots) &= \frac{M(T, \phi_{R0}, \dots)}{M_0} = \exp\left(\int_0^T \lambda(s) ds\right) \\ &= 1 + \frac{\lambda_R + \lambda_i^*}{\lambda_R + \lambda_f^*} \left(e^{\lambda_f^* T} - 1\right) \quad \text{for } T \geq 0, \end{aligned} \quad (\text{A.23})$$

An alternate form for the same quantity can be obtained in terms of the lag time  $\tau_{\text{lag}}$ :

$$W = 1 + \left(e^{-\lambda_f^* \tau_{\text{lag}}}\right) \left(e^{\lambda_f^* T} - 1\right). \quad (\text{A.24})$$

According to the model from [34], the initial and final growth rates are functions of the nutritional qualities  $\nu_P^{i/f}$  as follows:

$$\lambda_{i/f}^* = (\phi_{R0}^{\max} - \phi_{R0}) \nu_R \frac{\nu_P^{i/f}}{\nu_P^{i/f} + \nu_R} = (\lambda_R^{\max} - \lambda_R) \frac{\nu_P^{i/f}}{\nu_P^{i/f} + \nu_R}. \quad (\text{A.25})$$

where we defined  $\phi_{R0}^{\max} = 1 - \phi_Q = 55\%$  and  $\lambda_R^{\max} = \phi_{R0}^{\max} \nu_R \sim 3.2/\text{h}$ . The proteome mass  $M$  is a function of three environmental variables  $T$ ,  $\nu_P^i$  and  $\nu_P^f$ , and three strain variables  $\phi_{R0}$ ,  $\phi_{R0}^{\max}$  and  $\nu_R$  (or  $\lambda_R$ ,  $\lambda_R^{\max}$  and  $\nu_R$ ). However, dynamics is specified by less than six variables. We can reduce the number of variables to four by defining:

$$x = \frac{\phi_{R0}}{\phi_{R0}^{\max}} = \frac{\lambda_R}{\lambda_R^{\max}}, \quad \tau = \lambda_R^{\max} T, \quad z_{i/f} = \frac{\nu_P^{i/f}}{\nu_P^{i/f} + \nu_R}. \quad (\text{A.26})$$

These quantities allow us to rewrite Eqs. Eq. (A.23) and Eq. (A.25) with only four variables, instead of six. The mass production  $W$  is therefore only a function of the rescaled R-sector overcapacity,  $x = \phi_{R0}/\phi_{R0}^{\max}$ , the rescaled feast time  $\tau \sim 3.2 T/\text{h}$  and the initial and final nutrient source qualities  $z_i$  and  $z_f$ . Equation Eq. (A.23) reduces to a very simple form:

$$W(x|\tau, z_i, z_f) = 1 + \frac{x + z_i(1-x)}{x + z_f(1-x)} \left(e^{(1-x)z_f\tau} - 1\right). \quad (\text{A.27})$$

The optimal value of the overcapacity  $x^*(\tau, z_i, z_f)$  for a given environment is obtained by setting to zero the partial derivative of  $W$  with respect to  $x$ . In general, the resulting equation is impossible to be solved exactly. On the other hand, an analytical expression for the optimal value  $x^*$  as a function of the rescaled initial nutritional quality  $z_i$  can be obtained in the limit of either small or large  $\tau$ . We will consider in the following a few particular cases.

### Small time limit, upshift to rich media

In this case consider the limit  $\tau \rightarrow 0$ , and we will only consider upshifts to high quality nutrients, that is,  $\nu_P^f \gg \nu_R$ , or  $z_f = 1$ . For small  $\tau$ , one can approximate  $e^{(1-x)\tau} - 1 \sim (1-x)\tau$ , obtaining:

$$W \sim 1 + (x + z_i(1-x))(1-x)\tau, \quad (\text{A.28})$$

$$\frac{\partial W}{\partial x} \sim 2\tau(1-z_i) \left( \frac{1-2z_i}{2(1-z_i)} - x \right), \quad (\text{A.29})$$

$$x^*(\tau \rightarrow 0, z_i) \sim \frac{1-2z_i}{2(1-z_i)}. \quad (\text{A.30})$$

We notice that the condition which favors the largest possible offset is very low nutritional quality ( $z_i = 0$ , corresponding to  $x^* = 1/2$ ), while the optimal overcapacity goes to zero when  $z_i = 1/2$ . Given that the value of the offset maximizing the fitness is a monotonously decreasing function of the feast time  $T$  (see Main Text Fig. 2d), the strains with  $x > 1/2$ , or  $\phi_{R0} > \phi_{R0}^{\max}$ , are always suboptimal.

### Large time limit, upshifts to rich media

In the opposite limit, i.e.  $\tau \gg 1$ , one can write  $e^{(1-x)\tau} - 1 \sim e^{(1-x)\tau}$ . Imposing  $z_f = 1$  we have:

$$W \sim 1 + (x + z_i(1-x))e^{(1-x)\tau}, \quad (\text{A.31})$$

$$\frac{\partial W}{\partial x} \sim \left( 1 - z_i - \tau(x + z_i(1-x)) \right) e^{(1-x)\tau}, \quad (\text{A.32})$$

$$x^*(\tau \gg 1, z_i) \sim \frac{1}{\tau} - \frac{z_i}{1-z_i}. \quad (\text{A.33})$$

In this limit one obtains a nice expression for the optimal offset  $\lambda_R^*$ . Using the definitions of  $x$ ,  $\tau$  and  $z_i$ :

$$\lambda_R^* = \nu_R \phi_{R0}^* = \frac{1}{T} - \phi_{R0}^{\max} \nu_P^i \quad (\text{A.34})$$

In the limit of  $\nu_P^i \rightarrow 0$ , the optimal offset is simply given by the inverse of the feast time,  $T$ . If, instead, the initial nutritional quality is larger than zero, the optimal offset is reduced by a quantity similar to the initial growth rate  $\lambda_P^*$ , Eq. (A.25), computed using  $\phi_{R0} = 0$  and  $\nu_P^i \ll \nu_R$ .

Corrections to Eq. (A.34) are exponentially small, as can be easily seen in the case  $z_i = 0$ . We can rewrite the equation  $\partial W / \partial x = 0$  as:

$$(1 - \tau x)e^{1-\tau x} = e^{1-\tau}, \quad (\text{A.35})$$

which is solved in terms of Lambert's W function (which we denote as  $W_L$ ) as:

$$1 - \tau x = W_L(e^{1-\tau}). \quad (\text{A.36})$$

Lambert's W function admits a power series expansion around 0 as  $W_L(z) \sim z - z^2 + \dots$ , with a convergence radius of  $1/e$ . Therefore, one obtains:

$$x = \frac{1}{\tau} (1 - W_L(e^{1-\tau})) \sim \frac{1}{\tau} (1 - e^{1-\tau} + e^{2(1-\tau)} + \dots) \quad (\text{A.37})$$

The series converges for  $\tau > 2$ , or  $T > 2/\lambda_R^{\max} \sim 0.6$  h.

### Large time limit, upshifts from poor media

Here we consider instead the situation in which  $z_i$  is set to zero, while  $z_f$  can be smaller than 1, still in the large time limit ( $z_f\tau \gg 1$ ). One has:

$$W \sim 1 + \frac{x}{x + z_f(1-x)} e^{(1-x)z_f\tau}, \quad (\text{A.38})$$

$$\frac{\partial W}{\partial x} \sim \left( (1 - z_f\tau x)(x + z_f(1-x)) - x(1 - z_f) \right) \frac{e^{(1-x)z_f\tau}}{(x + z_f(1-x))^2}, \quad (\text{A.39})$$

$$(1 - z_f)(x^*)^2 + z_f x^* - \frac{1}{\tau} = 0, \quad (\text{A.40})$$

$$x^*(\tau \gg 1, z_i) \sim \frac{1}{z_f\tau} \frac{z_f^2\tau}{2(1 - z_f)} \left( \sqrt{1 + \frac{4(1 - z_f)}{z_f^2\tau}} - 1 \right). \quad (\text{A.41})$$

If again one assumes that  $\tau$  is large enough, this expression reduces to  $x^* = 1/(\tau z_f)$ , or  $\lambda_R^* = 1/(T z_f)$ . However, this asymptotic expression only holds when  $\tau \gg 1/z_f$ . If  $z_f \sim 1$ ,  $T$  as large as 1 hour is enough to guarantee a good match of Eq. (A.31) and Eq. (A.38) with the exact solutions computed numerically. However, if  $z_f < 1$  this time increases proportionally.

#### A.2.2 Comparing different environments

The quantity  $x^*$  studied in the previous section only yields the best strain for one particular environment. In order to compare different strains in different environmental conditions, we have to introduce a properly normalized fitness  $W_{\text{rel}}$ , which is proportional to the fractional mass increase  $W$ , Eq. (A.23), but is normalized by some quantity which is not a function of the R-sector overcapacity. In order to do so, one can either introduce a reference strain, or some average of them. We choose to normalize the fitness using the average fitness among all possible strains (with different values of  $\phi_{R0}$ ):

$$W_{\text{rel}}(\phi_{R0}, T, z_i, z_f) = \frac{W(\phi_{R0}, T, z_i, z_f)}{\frac{1}{\varphi_{\text{max}}} \int_0^{\varphi_{\text{max}}} W(\varphi, T, z_i, z_f) d\varphi}. \quad (\text{A.42})$$

where  $\varphi_{\text{max}}$  identifies a maximum value for the R-sector overcapacity. The denominator is the average mass produced by the strains in a given upshift, identified by the environmental variables  $T$ ,  $z_i$  and  $z_f$ . Such a normalization is quite natural, since each bacterial strain has to outperform other bacterial populations. Since we found in the previous section that every strain with a rescaled overcapacity  $x > 1/2$  is always suboptimal, we set  $\varphi_{\text{max}} = \phi_{R0}^{\text{max}}/2$ . The resulting fitness landscape is shown in Main Text Figure 2C in the case  $z_i = 0$ ,  $z_f = 1$ ; contour plots of the fitness for different values of the parameters are shown in Fig. A.3–A.6. In all plots the values  $\phi_{R0}^{\text{max}} = 0.55$  and  $\nu_R = 5.9/\text{h}$  [34] have been used.

- Fig. A.3 shows the relative fitness  $W_{\text{rel}}$  (Eq. (A.42)) as a function of the normalized offset. We see that the experimental strain  $\phi_{R0} \sim 6\%$  performs well for upshifts from poor ( $z_i \lesssim 0.2$ – $0.3$ ) to rich substrates for a quite large window of time. Furthermore, the strains with small ( $\phi_{R0} \lesssim 3\%$ ) offsets are not competitive in upshifts from very poor nutrient sources ( $z_i \lesssim 1$ ), even for very long times.
- As the previous figure, Fig. A.4 shows the relative fitness  $W_{\text{rel}}$  as a function of the normalized offset and feast time. However, we set  $z_f = 0.3$  in this case, corresponding to a growth rate close to  $1/\text{h}$  for the wild-type strain. The picture emerging from the previous

figure is not altered: however, since the final steady state growth rate is reduced, strains with larger offsets are more advantaged in the case  $z_f = 0.3$  with respect to the case with  $z_f = 1$ , at least for upshifts from very low growth rates.

- Fig. A.5 shows  $W_{\text{rel}}$  as a function of feast time  $T$  and the normalized initial nutrient quality  $z_i$ . The different plots refer to different values for the R-sector overcapacity  $\phi_{R0}$ , with  $z_f = 1$ . These plots highlight the best and worst upshift conditions for each strain. (i) Strains with small overcapacities  $\phi_{R0} \lesssim 3\%$  are heavily penalized in upshifts from low growth rates, when  $z_i \lesssim 0.05$  or  $0.1$ . In particular, the strain with  $x = 0$  is the most penalized, even for very long times after the upshift. However, they grow very quickly if the initial nutrient quality is even just moderately large. (ii) Strains with large overcapacities are always disadvantaged, especially for large feast times  $T$ . (iii) Strains with intermediate overcapacities,  $3\% \lesssim \phi_{R0} \lesssim 6\%$ , perform in an average manner for a wide set of conditions. Notably, the experimental value obtained for the R-sector overcapacity (6–7%) places itself at the upper edge of this range, with best performance in upshifts from low initial growth rates (small  $z_i$ ).
- As the previous figure, Fig. A.6 shows  $W_{\text{rel}}$  as a function of feast time  $T$  and the normalized initial nutrient quality  $z_i$ , but using  $z_f = 0.3$ . Also in this case, strains with large overcapacities behave consistently for a wide range of initial nutrient qualities  $z_i$ .

### A.3 Supplementary Materials and Methods

Growth was performed in a shaking water bath at 250 rpm and 37 °C, using N<sup>-</sup>C<sup>-</sup> minimal medium [119], containing K<sub>2</sub>SO<sub>4</sub> (1 g), K<sub>2</sub>HPO<sub>4</sub> · 3 H<sub>2</sub>O (17.7 g), KH<sub>2</sub>PO<sub>4</sub> (4.7 g), MgSO<sub>4</sub> · 7 H<sub>2</sub>O (0.1 g), and NaCl (2.5 g), supplemented with 20 mM NH<sub>4</sub>Cl. The pre-shift medium was supplemented with the indicated carbon substrates and *E. coli* K-12 strain NCM3722 [29] grown exponentially as described in [42] until an optical density OD<sub>600</sub> of about 0.3. Upshift was performed by dilution of the pre-shift culture into fresh, pre-warmed N<sup>-</sup> C<sup>-</sup> medium containing 2% (w/v) LB, 2% glucose and 20 mM NH<sub>4</sub>Cl to OD<sub>600</sub> 0.075. Growth was followed until OD<sub>600</sub> 0.5 and growth rate measured over a 10 min window.

## A.4 Supplementary Figures

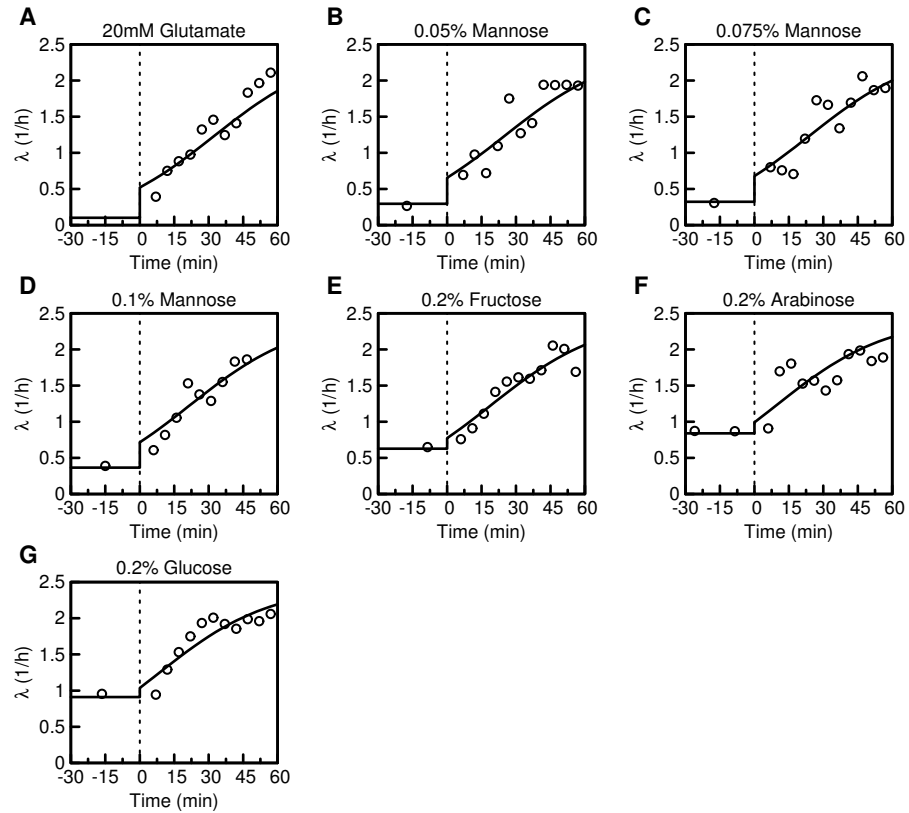


**Figure A.1: Upshifts to rich medium.** (A-G) Cells grown exponentially on N-C- minimal medium supplemented with 20mM  $\text{NH}_4$  and the carbon substrate indicated above panel are subjected to an upshift to rich medium (LB + 0.2% glucose) at  $t = 0$  (symbols). Using the final growth rate  $\lambda_f^* = 2.45/\text{h}$ , the upshift kinetics in Chapter 2. Eq. (2.8) is fitted to the data (solid lines). Fit results, summarized in Table A.1, are plotted in Fig. 2.3D of Chapter 2.

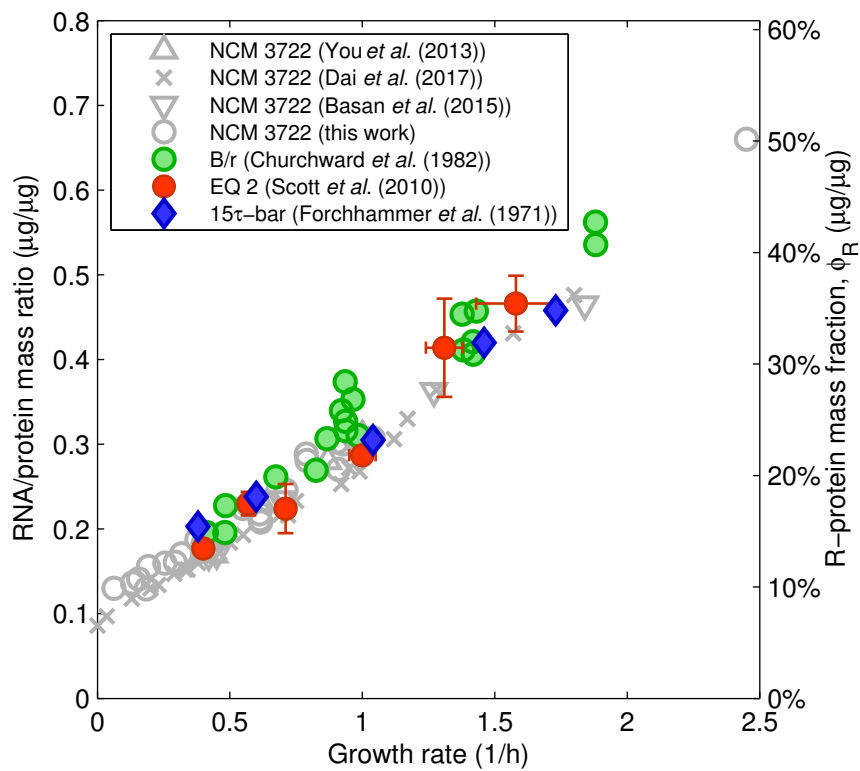


**Figure A.2: RNA to protein mass ratio for different *E. coli* strains.** NCM3722, in grey ([41, 42, 82]); EQ2 (derived from MG 1655), red circles [34]; B/r, green circles [200]; 15 $\tau$ -bar (an auxotroph, non-K-12, strain), blue diamonds [71]. We show on the right axis the corresponding R-protein mass fraction, using the same conversion factor (0.76 grams of R-proteins per gram of RNA).

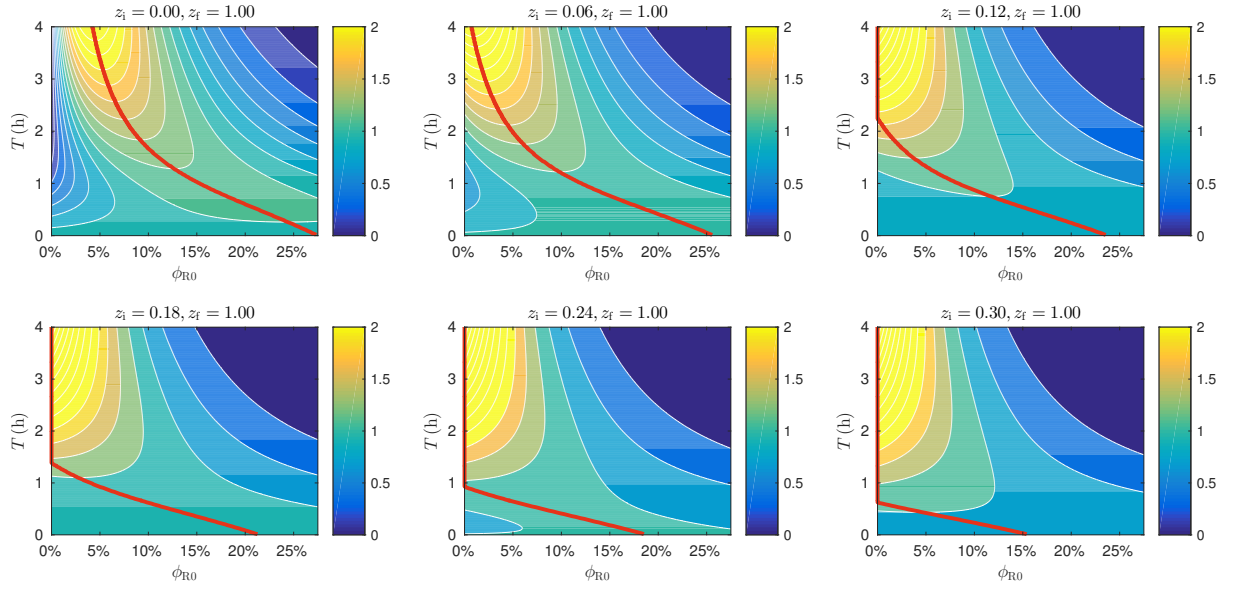


**Figure A.3:** Relative fitness  $W_{\text{rel}}$ , Eq. (A.42), as a function of the R-sector overcapacity  $\phi_{\text{R0}}$  and time  $T$  for six different values of the initial nutrient level,  $z_i = \nu_{\text{P}}^i / (\nu_{\text{P}}^i + K_M)$  and  $z_f = 1$ . The red line shows the optimal overcapacity and offset for a given feast time  $T$ . The wild type strain ( $\phi_{\text{R0}} \sim 6\%$ ) performs the best for  $z_i \lesssim 0.1$  and  $T \lesssim 3$  h.

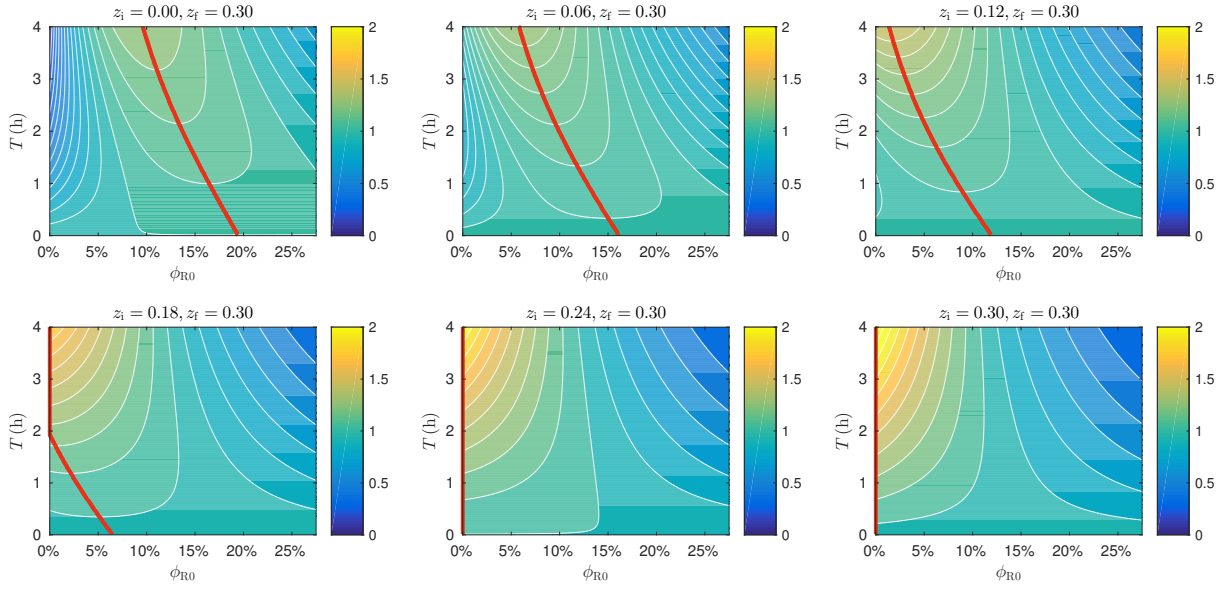


**Figure A.4:** Relative fitness  $W_{\text{rel}}$ , Eq. (A.42), as a function of the R-sector overcapacity  $\phi_{R0}$  and time  $T$  for six different values of the rescaled initial nutrient quality  $z_i = \nu_P^i / (\nu_P^i + K_M)$  and  $z_f = 0.3$ . The red line shows the optimal overcapacity and offset for a given feast time  $T$ . The scenario is qualitatively similar to the one emerging in Fig. A.3. Note that the case  $z_i = z_f = 0.3$  simply corresponds to exponential growth with growth rate  $\lambda^*(\phi_{R0}) = 0.3 * (\phi_{R0}^{\text{max}} - \phi_{R0})$ , with no shift at all.

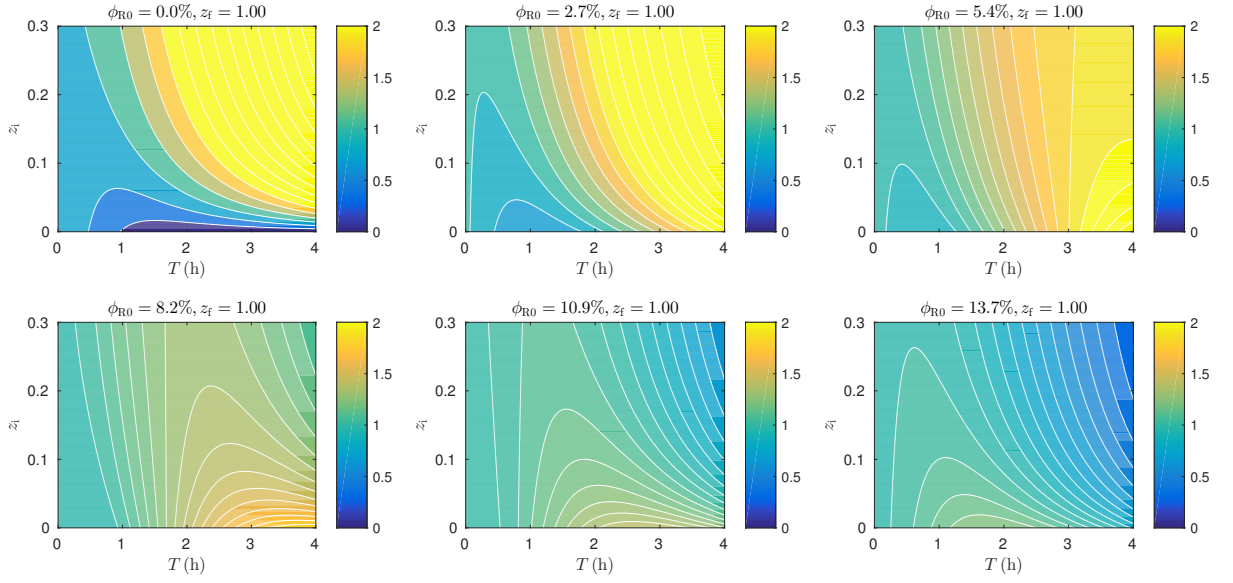


**Figure A.5:** Relative fitness  $W_{\text{rel}}$ , Eq. (A.42), as a function of time  $T$  and normalized initial nutrient quality  $z_i = k_P^i / (k_P^i + K_M)$  for six different values of the R-sector overcapacity  $\phi_{R0}$  and  $z_f = 1$ . The strain with zero overcapacity clearly disadvantaged for small initial growth rates ( $z_i \lesssim 0.1$ ) even for long feast times. Strains with large overcapacities, instead, are almost always disadvantaged. Strains with R-sector proteome offset between 3% and 6% appear to be competitive in any situation (relative fitness close to 1).

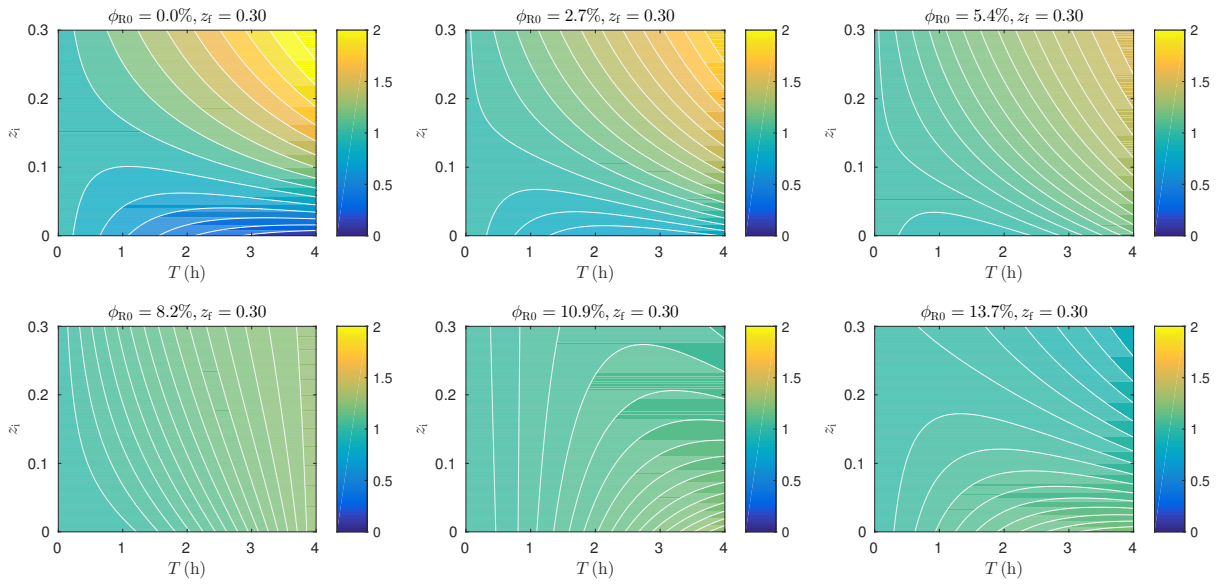


**Figure A.6:** Relative fitness  $W_{\text{rel}}$ , Eq. (A.42), as a function of time  $T$  and normalized initial nutrient quality  $z_i = k_P^i / (k_P^i + K_M)$  for six different values of the R-sector overcapacity  $\phi_{R0}$  and  $z_f = 0.3$ .

## A.5 Supplementary Tables

**Table A.1: Fit results for the instantaneous growth rate  $\lambda(t)$  in various upshift experiments.** Equation (2.8) of the main text was fitted to the data presented in Fig. 2.3 C and Fig. A.1 using  $\lambda_0$  as the only fitting parameter. Pre-shift growth rates  $\lambda_i^*$  are computed from the pre-shift growth curves or from separate steady state experiments; the final growth rate is in all cases set to  $\lambda_f^* = 2.45/\text{h}$ , obtained for steady state exponential growth on LB + 0.2% glucose medium. The results of the fit are shown in Fig. 2.3D.

C-substrate	$\lambda_i^*$ (1/h)	$\lambda_0$ (1/h)
0.2% Glucose	0.91	1.04
0.2% Arabinose	0.84	0.99
0.2% Glycerol	0.72	0.87
0.2% Fructose	0.63	0.77
0.2% Mannose	0.45	0.72
0.1% Mannose	0.37	0.72
0.075% Mannose	0.32	0.68
0.05% Mannose	0.30	0.66
20mM Glutamate	0.10	0.52
20mM Aspartate	0.06	0.51

# Appendix B

## Growth transitions

### B.1 Limits of the instantaneous model

In a seminal work done in the early 1970s, Bremer and Dennis studied the kinetics of bacterial growth following nutritional upshifts and established a quantitative phenomenological model [39, 78], which we applied in Chapter 2 to describe upshifts from poor to rich media.

Fig. B.1A compares this prediction to our data for the upshift from succinate to succinate plus gluconate. The comparison reveals that the very simple assumptions of the Bremer-Dennis model indeed yield a strikingly good description of the data, with the rapid initial rise of the growth rate right after the shift approximate here by a sudden jump. As a reference, the prediction of our FDR model to be discussed in detail below is also shown. The FDR model predicts a more gradual initial rise, but yields almost identical behavior at later times.

Given the favorable comparison between prediction of the Bremer-Dennis model and the data in Fig. B.1A, it is natural to ask whether the model can be extended to describe bacterial growth shifts more generally. However, as Bremer and Dennis already noted, their model is agnostic of the control mechanism underlying the dynamics. While it considers the dynamics of protein synthesis, it completely ignores catabolism. As a consequence, it posits that the cell jumps to the final steady-state parameters,  $\sigma_f^*$  and  $\chi_{\text{RB}}^f$ , immediately after the shift, without addressing how the cell could anticipate the new growth state in the new environment. In reality, the jump of the translational activity requires a jump in catabolism supplying the necessary precursors for translation. In growth shifts where a co-utilized carbon substrate is added, the required increase in catabolism is small and can be achieved by synthesis of an additional, small amount of catabolic proteins. Consequently, the resulting quick increase of flux and translational activity is reasonably approximated by Bremer and Dennis instantaneous-jump assumption.

However, if growth shifts involve major changes in catabolism, e.g. due to depletion of a nutrient (downshift; diauxic shift), then Dennis and Bremer's assumption of an instantaneous jump of  $\sigma_f^*$  fails, because this assumption would require synthesis of a large amount of catabolic proteins to balance the depletion of a nutrient.<sup>1</sup> As a result, the theory fails entirely to describe the kinetics of downshifts and diauxic shifts, as shown in panels B and C of Fig. B.1. This shortcoming cannot be overcome by a simple fix to match the observed flux after nutrient depletion in diauxic shifts, see Fig. B.1C, since flux in diauxic shifts initially grows at a faster rate than the final growth rate  $\lambda_f^*$ , potentially due to a transient change of regulation, as proposed by the FDR model.

We therefore find it difficult to use the Bremer-Dennis model as a starting point to construct a general kinetic theory of bacterial growth shifts. Instead, we must incorporate metabolism

---

<sup>1</sup>The addition of a nutrient with pre-expressed catabolic proteins (e.g. the upshift in Fig. 3.8, is another case that cannot be described by the Bremer-Dennis model.

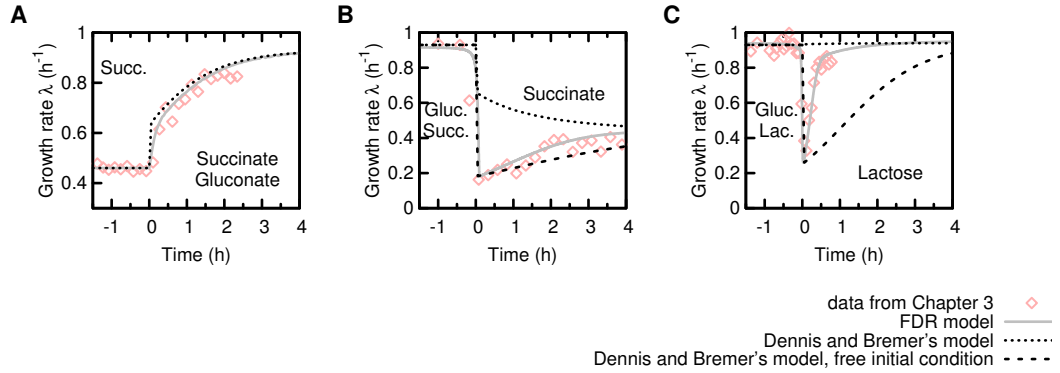


**Figure B.1: Comparison of Dennis and Bremer's model to experimental data and the FDR model.** Light red data and grey lines are experiments and FDR model. Solutions of Dennis and Bremer's model derived in Chapter 2 are shown as a dotted lines. For the downshift and diauxic shift, the initial condition  $J(0)$  is fitted to match flux after glucose depletion (at  $t = 0$  in panels B and C), yielding the black dashed lines. (A) Succinate gluconate upshift from Fig. 3.1B; (B) Succinate glucose downshift from Fig. 3.2G (C) Glucose-lactose diauxic from Fig. 3.11B. Dennis and Bremer's model very well for the upshift shown in panel A, but since it does not include catabolism it fails at describing both downshift in panel B and the diauxic shift in panel C. Fitting the initial condition  $J(0)$  cannot fix Dennis and Bremer's model, most prominent in the mismatch of the black dashed line and red symbols in panel C. Only the FDR model (grey line) can describe all shifts consistently.

(specifically catabolism) from the beginning, and we will do so by starting from the steady-state growth laws which incorporates both protein synthesis and its upstream metabolism.

## B.2 Parameters of the FDR model

The FDR model is thus far self-contained but still requires the specification of several of molecular parameters, including the conversion factor from substrate flux to carbon influx  $\beta_j$ , the conversion factor from carbon influx to protein synthesis  $\alpha$  and to biomass flux  $\alpha_M$ , the uptake rates of the substrates  $k_j$ , and the maximal value of the specific regulation functions,  $\phi_{\text{Cat},j,\text{max}}$ . The values of these parameters determine the quantitative details of the growth transitions. In the following subsections, we show that these microscopic parameters come in combinations such that their effect can be captured simply through the steady state growth rates before and after the shift and constants appearing in the growth laws. Thus the FDR model can be formulated as an entirely macroscopic model without references to molecular parameters.

### B.2.1 Conversion factor $\beta$ , substrate to carbon flux

The conversion factor from imported substrate to metabolic influx (which has the unit of number of carbon atoms assimilated per time per standard culture volume),  $\beta_j$ , is specific for each carbon substrate  $j$ , and counts the number of carbon atoms per substrate. We thus take  $\beta_j$  to be a substrate specific constant.

### B.2.2 Conversion factors $\alpha$ and $\alpha_M$ , carbon flux to protein synthesis and biomass

The conversion factors from carbon influx to protein synthesis and biomass are subject to small changes, depending on the growth state of the cell. We define the conversion factor from carbon influx (in number of carbon atoms assimilated per time per standard culture volume) to biomass flux (weight per standard culture volume per time) as  $\alpha_M$ , as introduced in Section 3.2.2. The

conversion factor thus comprises the conversion from 1) biomass to number of carbon atoms in the biomass  $e_C$ , and 2) the yield  $Y_C$  (unit-less), defined as the fraction of carbon atoms used for biomass production:  $\alpha_M = e_C Y_C$ . While  $e_C$  can be safely assumed to be constant (around  $\sim 50\%$  of the dry mass are carbon atoms [201], and the molecular weight of carbon  $M = 12\text{g/mol}$ , thus  $e_C \approx 50\%/M \approx 0.04\text{mol/g}$ ), the yield is dependent on the growth state of the cell. This is partly because the energy demand of the cell is growth rate dependent, as energy is needed for biomass synthesis, as well as for maintenance energy [202]. Furthermore, the yield crucially depends on the metabolic pathway used, and the cell's choice which pathway to use varies with growth rate. Cells growing faster than some threshold ( $\sim 0.76/\text{h}$  for NCM3722, the strain used in this study) excrete acetate, in amounts increasing with growth rate, thus lowering the yield [115, 140]. While there is knowledge on the yield during steady state growth, we have no quantitative information on how the yield changes during growth transitions. We assume the changes in the yield  $Y_C$  to be small during the growth transitions studied in this paper and take it to be a substrate specific constant.

The conversion factor from carbon flux (carbon atoms assimilated per time per standard culture volume) to protein synthesis (protein mass synthesized per time per standard culture volume),  $\alpha$ , can be similarly calculated as  $\alpha = e_P e_C Y_C = e_P \alpha_M$ . Here  $e_P$  is the ratio of protein mass to total dry mass, which shows a slight dependence on growth rate, as shown in Fig. B.9. Since the changes are relatively small in the growth rate regime probed in this paper, we assume  $e_P$  and thus  $\alpha$  to be a constant throughout growth shifts.

### B.2.3 Constraining the microscopic parameters

Having approximated the parameters  $\alpha$  and  $\beta_j$  as substrate-specific constants, we can further impose the constraint that the values of these parameters must reproduce macroscopic parameters defining steady state growth. Consider the steady state growth of cells under a single carbon substrate  $j$ , such that the carbon influx is given by  $J_C = \beta_j k_j M_{\text{Cat},j}$ . Synthesis of the catabolic protein  $\dot{M}_{\text{Cat},j}$  is given by Eq. (3.6). Using Eq. (3.3) for the protein flux  $J_R(t)$  and taking  $h_j(t) = \phi_{\text{Cat},j,\text{max}}$  for the specific regulation (defined in Eq. (3.11)), Eq. (3.6) becomes

$$\dot{M}_{\text{Cat},j} = \alpha \beta_j k_j \phi_{\text{Cat},j,\text{max}} \chi_{\text{Cat}}(t) M_{\text{Cat},j}. \quad (\text{B.1})$$

Since  $\dot{M}_{\text{Cat},j} = \lambda_j^* M_{\text{Cat},j}$  during steady state exponential growth, with  $\lambda_j^*$  being the steady state growth rate on substrate  $j$ , and in steady state  $\phi_{\text{Cat},j,\text{max}} \chi_{\text{Cat}}^* = \phi_{\text{Cat},j}^*$ , we can express the combination of parameters as

$$\alpha \beta_j k_j = \lambda_j^* / \phi_{\text{Cat},j}^* (\lambda_j^*), \quad (\text{B.2})$$

i.e., in terms of only the steady-state growth rate and constants of growth law appearing in  $\phi_{\text{Cat},j}^*$  (Eq. (1.11)). Alternatively, Eq. (B.2) together with Eq. (1.5) and Eq. (1.10) can be turned around to read

$$\alpha \beta_j k_j \phi_{\text{Cat},j,\text{max}} = \lambda_j^* / (1 - \lambda_j^* / \lambda_C) = \mu_j, \quad (\text{B.3})$$

an expression which specifies the growth rate in terms of the molecular parameters ( $\alpha, \beta_j, k_j, \phi_{\text{Cat},j,\text{max}}$ ) and  $\lambda_C$ , constant appearing in the growth law Eq. (1.5).

### B.2.4 Growth rate composition formula for co-utilized substrates

For growth on two co-utilized carbon substrates, S1 and S2, the carbon influx is given by Eq. (3.1). Repeating the above analysis leads to the following expression for the steady-state growth rate  $\lambda_{12}^*$  on the two substrates:

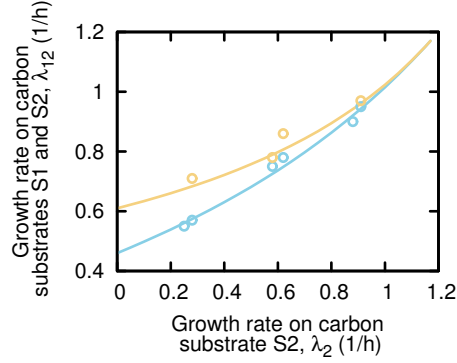


**Figure B.2: Growth rate addition.** Growth rates of co-utilized carbon substrates. The combinations either involve Succinate (blue) or Pyruvate (yellow), and one additional glycolytic carbon substrate. Growth rates of carbon substrate S1 (succinate and pyruvate) are the vertical intercepts of the blue and yellow lines, respectively. Growth rates of substrate S2 is plotted versus the co-utilization growth rate. Data from Table B.7. Theoretical lines are calculated from the growth rate composition formula derived in Eq. (B.6), and based on Ref. [116].

$$\lambda_{12}^* = \alpha (\beta_1 k_1 \phi_{\text{Cat1}}^* (\lambda_{12}^*) + \beta_2 k_2 \phi_{\text{Cat2}}^* (\lambda_{12}^*)). \quad (\text{B.4})$$

Using Eq. (1.11), the above can be expressed as

$$\lambda_{12}^* = \alpha (\beta_1 k_1 \phi_{\text{Cat1,max}} + \beta_2 k_2 \phi_{\text{Cat2,max}}) \left( 1 - \frac{\lambda_{12}^*}{\lambda_C} \right). \quad (\text{B.5})$$

Further using Eqs. (B.3) and (B.5) and simplifying, we obtain

$$\lambda_{12}^* = \frac{\lambda_1^* + \lambda_2^* - \frac{\lambda_1^* \lambda_2^*}{\lambda_C}}{1 - \frac{\lambda_1^* \lambda_2^*}{\lambda_C^2}}. \quad (\text{B.6})$$

This growth-rate composition formula, first derived in Ref. [116], holds for all co-utilized carbon pairs used in this paper, as shown in Table B.7 and Fig. B.2.

### B.3 Analytical analysis of the FDR model

The FDR model described in Section 3.2 can be reduced to an ordinary differential equation for a single variable, the translational activity  $\sigma(t)$ , and solved analytically if the uptake rates defined in Eq. (3.2) are constant (e.g., when the substrates are supplied at saturating concentration). Once the solution is found, we can compute all other variables since they are solely functions of  $\sigma(t)$ . If the substrates are not supplied at saturating concentrations, then the model described in Section 3.2 can be solved numerically. The latter was chosen for diauxic shifts, where one substrate is depleted during the growth.

#### B.3.1 Derivation of the central differential equation

To obtain the central differential equation, we take the time derivative of the translational activity  $\sigma$ , see Eq. (1.3), and find

$$\frac{d}{dt} \sigma = \frac{d}{dt} \left( \frac{J_R}{M_{\text{Rb}}} \right) = \frac{1}{M_{\text{Rb}}} \left( \frac{d}{dt} J_R \right) - \frac{J_R}{M_{\text{Rb}}^2} \left( \frac{d}{dt} M_{\text{Rb}} \right). \quad (\text{B.7})$$

Enforcing the condition of internal flux balance  $J_R(t) = \alpha J_C(t)$  (Eq. (3.3)) and inserting the form of carbon influx  $J_C(t)$  from Eq. (3.1), we obtain an equation relating  $d\sigma/dt$  to the synthesis of catabolic and ribosomal proteins,

$$\frac{d}{dt}\sigma = \sum_j \alpha\beta_j k_j \frac{1}{M_{Rb}} \left( \frac{d}{dt} M_{Cat,j} \right) - \frac{J_R}{M_{Rb}^2} \left( \frac{d}{dt} M_{Rb} \right). \quad (\text{B.8})$$

Note that this equation applies to the post-shift condition ( $t > 0$ ) and the summation includes all carbon substrates present in the medium. Thus for upshifts such as described in Fig. 3.1, the sum is over both substrate types, S1 and S2, while for downshifts e.g. Fig. 3.2, only substrate S2 is involved.

We then use the allocation of protein synthesis for ribosomal and catabolic proteins (Eqs. (3.5) and (3.6), respectively), to relate  $d\sigma/dt$  to the flux of total protein synthesis  $J_R$ ,

$$\frac{d}{dt}\sigma = \sum_j \alpha\beta_j k_j h_j(t) \chi_{Cat}(t) \frac{J_R}{M_{Rb}} - \chi_{Rb}(t) \frac{J_R^2}{M_{Rb}}. \quad (\text{B.9})$$

In the post-shift medium, the specific regulatory function  $h_j(t)$  very quickly approaches its asymptotic value,  $\phi_{Cat,j,max}$ . Using  $J_R/M_{Rb} = \sigma(t)$  and identifying<sup>2</sup> the parameters  $\sum_j \alpha\beta_j k_j \phi_{Cat,j,max} = \lambda_f^*/(1 - \lambda_f^*/\lambda_C) \equiv \mu_f$  (Eq. (B.3)) where  $\lambda_f^*$  is the final steady-state growth rate in the post-shift medium and  $\mu_f$  is the corresponding maximum carbon uptake rate (as introduced in Eq. (1.11)) we obtain

$$\frac{d}{dt}\sigma = \sigma(t) \cdot (\mu_f \chi_{Cat}(t) - \sigma(t) \chi_{Rb}(t)), \quad (\text{B.10})$$

which is an equation relating  $d\sigma/dt$  to the regulatory functions  $\chi_{Cat}(t)$  and  $\chi_{Rb}(t)$ . By our central approximation (Eqs. (3.7) and (3.8)), the regulatory functions themselves are functions of  $\sigma$ , leading to

$$\frac{d}{dt}\sigma(t) = \sigma(t) \cdot (\mu_f \hat{\chi}_{Cat}(\sigma(t)) - \sigma(t) \hat{\chi}_{Rb}(\sigma(t))), \quad (\text{B.11})$$

which is the central equation of FDR model.

This equation has a simple biological interpretation: change in translational activity (and the central precursors it represents) is increased by carbon uptake (first term), which supplies the precursor pool, and slowed down by protein synthesis (second term), which drains the precursor pool. Eq. (B.11) contains a number of macroscopic parameters:  $\lambda_C$  in  $\hat{\chi}_{Cat}(\sigma)$  and  $\mu_f$ , see Eqs. (1.10) and (3.10) respectively,  $\phi_{Rb,0}$  and  $\gamma$  in  $\hat{\chi}_{Rb}(\sigma)$  (Eq. (3.9)), and the final growth rate  $\lambda_f^*$  in  $\mu_f$ . The explicit dependence of  $\hat{\chi}_{Rb}(\sigma)$  on  $\phi_{Rb,0}$ , see Eq. (3.9), can be eliminated by introducing  $\sigma_f^*$ , the steady-state value of  $\sigma$ , defined as  $\sigma_f^* \equiv \lambda_f^*/\phi_{Rb}^*(\lambda_f^*)$ : For each occurrence of  $\hat{\chi}_{Rb}(\sigma)$ , divide by the factor  $\sigma_f^* \hat{\chi}_{Rb}(\sigma_f^*)/\lambda_f^*$  (which has the value 1 since  $\hat{\chi}_{Rb}(\sigma_f^*) = \phi_{Rb}^*(\lambda_f^*)$ ) to obtain

$$\hat{\chi}_{Rb}(\sigma(t)) = \frac{\lambda_f^*}{\sigma_f^*} \frac{1 - \sigma_f^*/\gamma}{1 - \sigma(t)/\gamma}. \quad (\text{B.12})$$

Using the above expression in Eq. (B.11), along with Eq. (3.10) for  $\hat{\chi}_{Cat}(\sigma)$ , we obtain a very simple equation for  $\sigma(t)$ ,

<sup>2</sup>For downshift where only substrate 2 is present in the post-shift medium,  $\sum_j \alpha\beta_j k_j h_{j,max} = \alpha\beta_2 k_2 h_{2,max} = \lambda_2^*/\phi_{Cat}^*(\lambda_2^*)$  according to Eq. (B.2). For upshift, both substrate 1 and 2 are present in the post-shift medium, and  $\sum_j \alpha\beta_j k_j h_{j,max} = \lambda_{12}^*/\phi_{Cat}^*(\lambda_{12}^*)$  according to Eq. (B.4). In the first case, the final growth rate is  $\lambda_f^* = \lambda_2^*$ ; in the second case,  $\lambda_f^* = \lambda_{12}^*$ . So we have  $\sum_j \alpha\beta_j k_j h_{j,max} = \lambda_f^*/\phi_{Cat}^*(\lambda_f^*)$  for both cases.

$$\frac{d}{dt}\sigma = \mu_f \sigma(t) \left[ \frac{1 - \sigma(t)/\sigma_f^*}{1 - \sigma(t)/\gamma} \right], \quad (\text{B.13})$$

with  $\mu_f = \lambda_f^*/(1 - \lambda_f^*/\lambda_C)$  being the maximum carbon uptake rate in the final growth medium as defined in Eq. (1.10). If  $\sigma$  starts close to zero (i.e., near starvation as right after the diauxic shift shown in Fig. 3 and 4 of the main text), then  $\mu_f$  gives the rate of exponential accumulation of  $\sigma$ . It is the rate obtained when catabolic proteins are synthesized at maximal level.

Eq. (B.13) is the central equation describing the kinetics of the growth transitions. All other dynamic variables in the model can be expressed as functions of  $\sigma(t)$  and are thus fully specified through solution of Eq. (B.13), and their respective initial conditions. This equation contains only 3 effective parameters: Given the final growth rate  $\lambda_f^*$ , the values of  $\gamma$  and  $\sigma_f^*$  can be obtained from the growth law 1.2 and the value of  $\mu_f$  from the growth laws Eq. (1.10). Note that the maximal abundance of the relevant catabolic protein  $\text{Cat}_j$ ,  $\phi_{\text{Cat},j,\text{max}}$ , is not involved, making it possible to fix the remaining constant  $\lambda_C = 1.17/\text{h}$  just by using a LacZ reporter (data in Tables B.1 and B.2, visualized in Fig. 1.5.).

### B.3.2 Solution of the central differential equation

Here we provide the solution to the differential equation for the translational activity  $\sigma(t)$ , Eq. (B.13). We rearrange the differential equation for  $dt$  and find

$$dt = \frac{d\sigma}{\mu_f \sigma} \left( \frac{1 - \sigma/\sigma_f^*}{1 - \sigma/\gamma} \right). \quad (\text{B.14})$$

This equation can be integrated to yield,

$$\mu_f t = \ln \left[ \left( \frac{\sigma(t)}{\sigma(0)} \right) \left( \frac{1 - \sigma(0)/\sigma_f^*}{1 - \sigma(t)/\gamma} \right)^{1 - \sigma_f^*/\gamma} \right], \quad (\text{B.15})$$

with the solution depending on the initial condition  $\sigma(0)$ . Inverting the above function numerically yields  $\sigma(t)$ . Fig. B.3A, Fig. B.4A, Fig. B.5A show the solution of  $\sigma(t)$  according to Eq. (B.15) for three cases of different initial conditions  $\sigma(0)$ . The value of the initial condition depends on pre-shift growth, as ribosomal and catabolic proteins are inherited from the pre-shift. The following section will discuss this in detail.

#### Initial condition: general formulation

While the parameters of Eq. (B.13) depend on cell properties in the post-shift medium (through the final growth rate  $\lambda_f^*$ ), the initial condition  $\sigma(0)$  is determined by cell properties setup by pre-shift growth. We use the definition of  $\sigma(t)$  in Eq. (1.3) and apply the flux balance constraint Eq. (3.3) to write

$$\sigma(0) = \alpha \frac{J_C(0)}{M_{\text{Rb}}(0)}. \quad (\text{B.16})$$

This equation can be rewritten entirely in terms of catabolic and ribosomal protein abundances before the shift, by using Eq. (3.1),

$$\sigma(0) = \frac{\alpha \sum_j \beta_j k_j M_{\text{Cat},j}(0)}{M_{\text{Rb}}(0)}. \quad (\text{B.17})$$

As described in Section B.2, we assume the conversion factors  $\alpha$  and  $\beta_j$ , as well as the uptake rates  $k_j$  to be constant throughout the growth transition. The initial condition is thus only a

function of the pre-shift protein abundances  $M_{\text{Rb}}(0)$  and  $M_{\text{Cat},j}(0)$ . Note that as the medium is changed abruptly at time  $t = 0$ , the carbon influx  $J_{\text{C}}(0)$  depends on the abundance of the uptake system(s)  $M_{\text{Cat},j}(0)$  for all substrates  $S,j$  present in the post-shift medium. The value of  $M_{\text{Cat},j}(0)$  thus depends on the detail of the shift and is described below for each case studied.

### Upshift without pre-expression

In an upshift experiment, the medium is comprised of only carbon substrate S1 during pre-shift, and is supplemented with carbon substrate S2 at  $t = 0$  (see e.g., Fig. 3.1). If the uptake system for substrate 2 is not pre-expressed, i.e.,  $M_{\text{Cat}2}(0) = 0$ , then the initial condition only involves the uptake system for substrate S1, of abundance  $M_{\text{Cat}1}(0)$ . The latter is readily obtained during exponential pre-shift growth by using Eq. (3.6) together with Eq. (1.1):  $M_{\text{Cat}1}(t) = \phi_{\text{Cat},j}^*(\lambda_1^*) M_{\text{P}}(t)$ , where  $\lambda_1^*$  is the pre-shift growth rate,  $\phi_{\text{Cat}1}^*(\lambda_1^*)$  is the fraction of protein C1 before the shift. Similarly, the use of Eq. (3.5) gives  $M_{\text{Rb}}(t) = \phi_{\text{Rb}}^*(\lambda_1^*) M_{\text{P}}(t)$  for the abundance of the ribosomal fraction before the shift. It then follows that  $M_{\text{Cat}1}(0)/M_{\text{Rb}}(0) = \phi_{\text{Cat}1}^*(\lambda_1^*)/\phi_{\text{Rb}}^*(\lambda_1^*)$ , and

$$\sigma(0) = \frac{\alpha\beta_1 k_1 \phi_{\text{Cat}1}^*(\lambda_1^*)}{\phi_{\text{Rb}}^*(\lambda_1^*)} = \frac{\lambda_1^*}{\phi_{\text{Rb}}^*(\lambda_1^*)} = \sigma_i^* \quad (\text{B.18})$$

where  $\sigma_i^*$  is the steady state value of the translational activity in the pre-shift medium, and Eq. (B.2) and Eq. (1.4) are used in simplifying Eq. (B.18). The above result shows that in the absence of pre-expression, the translational activity is continuous. The result is plotted in Fig. B.3A, for an upshift without pre-expression and to the final growth rate  $\lambda_f^* = 0.9/\text{h}$ . The translational activity  $\sigma$  relaxes monotonically from the initial to the final value. Panels B and C show the resulting regulatory functions, according to Eqs. (3.9) and (3.10).

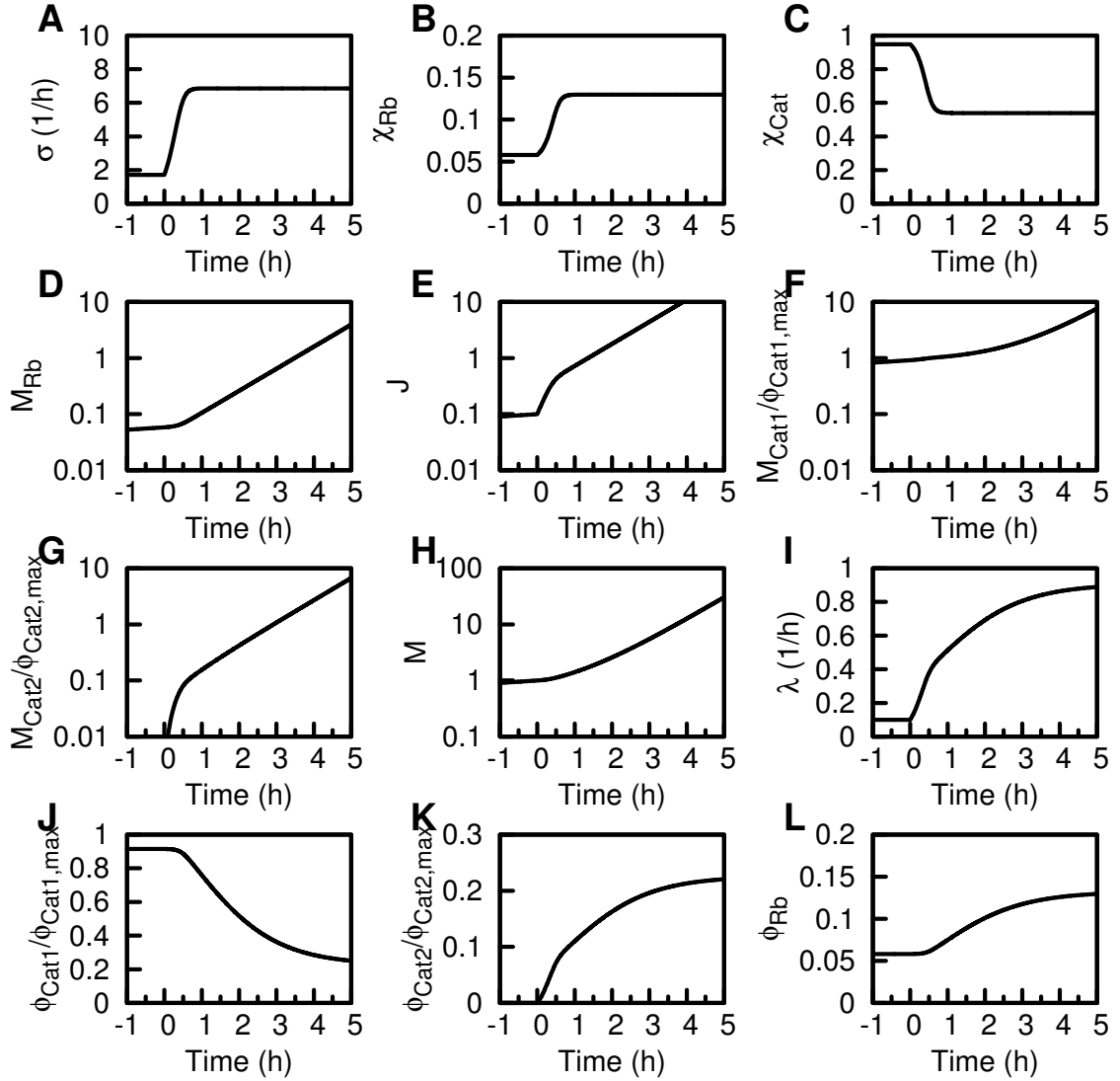


**Figure B.3: Theoretical result for an upshift without pre-expression.** Cells grown exponentially on substrate S1 at initial growth rate  $\lambda_i^* = 0.1/\text{h}$ , when at  $t = 0$ , substrate S2 (subsequently co-utilized with substrate S1) was added to the medium. Co-utilization growth rate in the final  $\lambda_f^* = 0.9/\text{h}$ . Uptake system for substrate 2 is not expressed in the pre-shift state. (A-C) Translational activity  $\sigma(t)$  and ribosomal and catabolic regulation functions  $\chi_{\text{Rb}}(t)$ ,  $\chi_{\text{Cat}}(t)$  relax quickly and monotonically from their initial to their final states. (D) Ribosomal protein synthesis quickly responds and grows exponentially. (E) Biomass flux  $J(t) = \alpha_M M_{\text{Rb}}(t) \sigma(t)$  shows an initial quick increase ( $\sim 15\text{min}$ ) resulting from the increase of  $\sigma(t)$ . Thereafter flux grows exponentially as  $\sigma(t)$  has settled and ribosomal proteins grow exponentially. (F-G) catabolic proteins  $M_{\text{Cat1}}(t)$  and  $M_{\text{Cat2}}(t)$  are synthesized proportionally after the shift. The high initial content of  $M_{\text{Cat1}}(t)$ , however, dominates over newly synthesized proteins for several hours, as the regulation of catabolic proteins  $\chi_{\text{Cat}}(t)$  (panel C), is generally lower than in the pre-shift. H total biomass increases after the shift, with growth rate, (I), first shown a quick increase ( $\sim 15\text{min}$ ) due to  $\sigma(t)$  increasing, followed by slow adaptation (logistic function) to the final state. (J-L) The proteome fractions slowly adapt from the initial to the final states.

### Upshift with pre-expression

Next we consider the case where the uptake system for substrate S2 is pre-expressed already during pre-shift growth. The pre-expression level is characterized by the specific regulatory function  $h_2(t)$  taking on the value  $h_2(t < 0) = x\phi_{\text{Cat2,max}}$ , where  $\phi_{\text{Cat2,max}}$  is the fraction of catabolic protein synthesis that is allocated to the catabolic proteins Cat2 during growth on substrate S2, and  $x$  describes the relative degree of pre-expression. Then Eq. (B.17) becomes

$$\sigma(0) = \frac{\alpha\beta_1 k_1 \phi_{\text{Cat1}}^*(\lambda_1^*)}{\phi_{\text{Rb}}^*(\lambda_1^*)} + x \frac{\alpha\beta_2 k_2 \phi_{\text{Cat2}}^*(\lambda_1^*)}{\phi_{\text{Rb}}^*(\lambda_1^*)}. \quad (\text{B.19})$$

This can be reformulated by replacing the molecular parameters with macroscopic parameters, Eq. (B.2),

$$\sigma(0) = \sigma_1^* \left( 1 + x \frac{\lambda_2^* \phi_{\text{C}}^*(\lambda_1^*)}{\lambda_1^* \phi_{\text{C}}^*(\lambda_2^*)} \right) = \sigma_1^* \left( 1 + x \frac{\mu_2}{\mu_1} \right), \quad (\text{B.20})$$

where in the last step, we used the carbon uptake efficiency for substrate S $j$  according to Eq. (1.9). The result is plotted in Fig. B.4A for an upshift with pre-expression and to the final growth rate  $\lambda_f^* = 0.3/\text{h}$ . The translational activity  $\sigma$  suddenly increases as the carbon influx suddenly increases. Thereafter  $\sigma$  relaxes to the final value. Panels B and C show the resulting regulatory functions, according to Eqs. (3.9) and (3.10).

### Diauxic shifts from co-utilized substrates

For downshift experiments (diauxic shifts), a carbon substrate is depleted during growth, leading to a sudden decrease in carbon influx and a drop of translational activity  $\sigma$ . If the pre-shift growth is on two co-utilized carbon substrates, S1 and S2, and the remaining substrate is substrate S2, then the initial condition reads

$$\sigma(0) = \frac{\alpha\beta_2 k_2 \phi_{\text{Cat2}}^*(\lambda_{12}^*)}{\phi_{\text{Rb}}^*(\lambda_{12}^*)} \quad (\text{B.21})$$

with  $\lambda_{12}^*$  being the steady state growth rate in the pre-shift on co-utilized carbon substrates S1 and S2. This can be further simplified using Eqs. (1.9) and (B.2) to

$$\sigma(0) = \sigma_{12}^* \frac{\lambda_2^* \phi_{\text{C}}^*(\lambda_{12}^*)}{\lambda_{12}^* \phi_{\text{C}}^*(\lambda_2^*)} = \sigma_{12}^* \frac{\nu_2}{\nu_{12}}. \quad (\text{B.22})$$

Note that for diauxic shifts, the initial condition  $\sigma(0)$  is smaller than the pre-shift value  $\sigma_{12}$  since  $\nu_2 < \nu_{12}$ . The result is plotted in Fig. B.5A for a diauxic shift with the final growth rate  $\lambda_f^* = 0.9/\text{h}$ . The translational activity  $\sigma$  suddenly decreases as the carbon influx drops. Thereafter  $\sigma$  quickly relaxes to the final value. Panels B and C show the resulting regulatory functions, according to Eqs. (3.9) and (3.10), which first shoot to extreme values, before relaxing to their final states.

### B.3.3 Continuity at the instant of shift

While the cellular content, such as proteins or the total biomass are naturally continuous at the shift, internal fluxes can undergo abrupt changes when substrates are added or depleted. In this section we trace the discontinuities of the fluxes to the initial condition  $\sigma(0)$  and the protein contents inherited from the pre-shift.

Generally, the kinetics of the growth shifts are determined by the solution to Eq. (B.15) given the initial condition  $\sigma(0)$ . The experimental observables, e.g., cell dry mass  $M(t)$ , protein

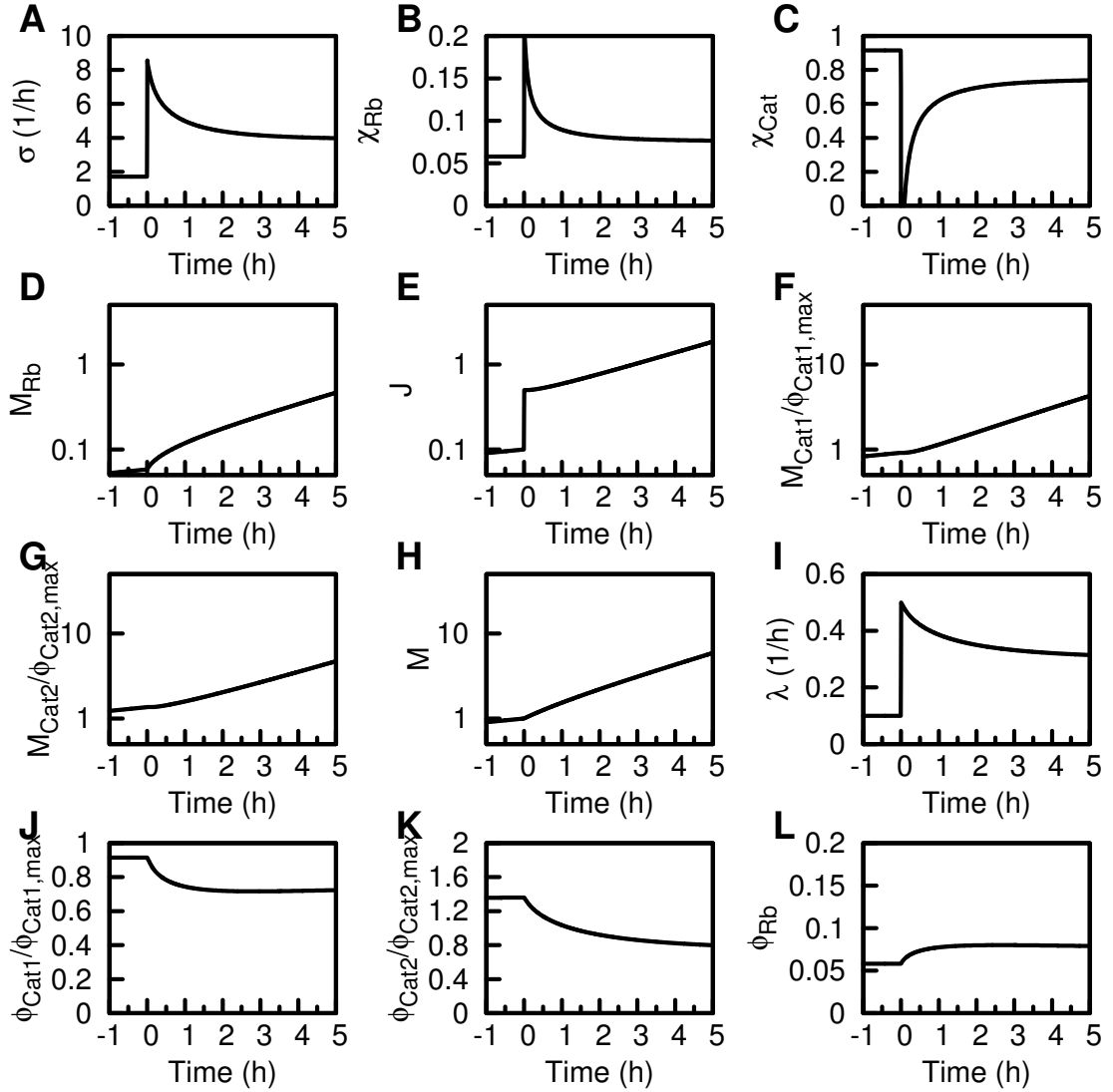


**Figure B.4: Theoretical result for an upshift with pre-expression.** Cells grown exponentially on substrate S1 at initial growth rate  $\lambda_i^* = 0.1/\text{h}$ , when at  $t = 0$ , substrate S2 (subsequently co-utilized with substrate S1) was added to the medium. Co-utilization growth rate in the final  $\lambda_f^* = 0.3/\text{h}$ . Uptake system for substrate S2 is expressed in the pre-shift state and can be utilized immediately after the shift up. (A) Translational activity  $\sigma(t)$  jumps at the upshift, to cope with the sudden increase of carbon influx and central precursors. (B-C) The ribosomal and catabolic regulation functions  $\chi_{\text{Rb}}(t)$  and  $\chi_{\text{Cat}}(t)$  jump to extreme values as the new carbon substrate is added, followed by a relaxation to the final states. (D) Ribosomal protein synthesis quickly responds. Transiently ribosomal proteins are expressed higher than in the initial or final state (see  $\chi_{\text{Rb}}(t)$  in panel B for the regulation function) (E) Biomass flux  $J(t) = \alpha_M M_{\text{Rb}}(t) \sigma(t)$  jumps at the upshift, as the additional carbon influx provides additional pre-cursors at the upshift. After the initial jump flux grows exponentially at final rate  $\lambda_f^*$ . (F-G) catabolic proteins  $M_{\text{Cat1}}(t)$  and  $M_{\text{Cat2}}(t)$  are synthesized proportionally after the shift, with slightly different initial conditions inherited from the pre-shift. H total biomass increases after the shift, with growth rate, (I), first shown a quick increase ( $\sim 15\text{min}$ ) due to  $\sigma(t)$  increasing, followed by slow adaptation (logistic function) to the final state. (J-L) The proteome fractions slowly adapt from the initial to the final states.

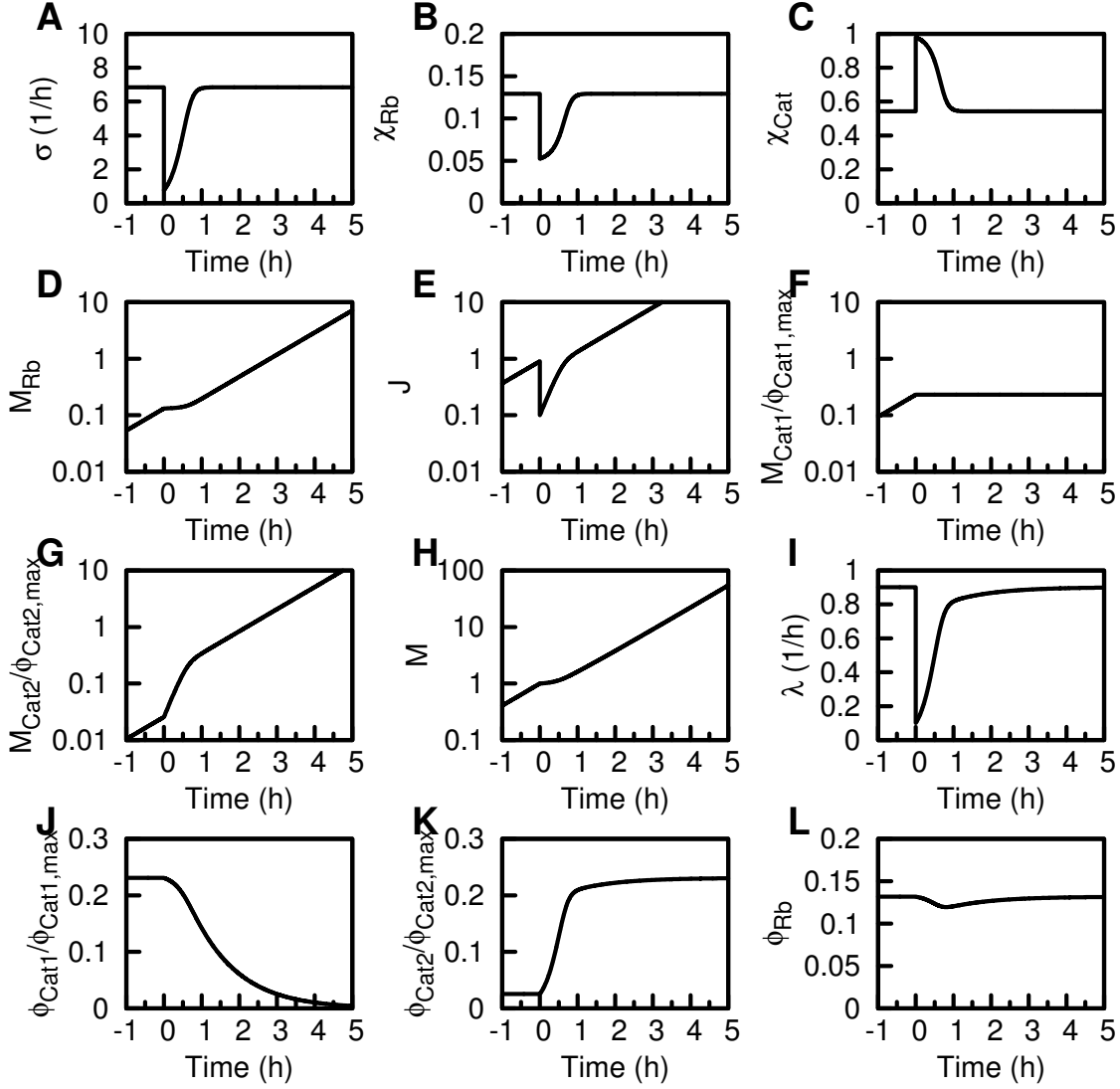


**Figure B.5: Theoretical result for a downshift.** Cells grown exponentially on substrate S1 at initial growth rate  $\lambda_f^* = 0.9/\text{h}$ , when at  $t = 0$ , substrate S1 was removed and the cells grown on substrate S2 only at the rate  $\lambda_f^* = 0.3/\text{h}$ . Uptake system for substrate S2 is expressed in the pre-shift state to support the a growth rate of  $0.1/\text{h}$  at  $t = 0$  (same growth rate at  $t = 0$ , as in Fig. B.3). (A) Translational activity  $\sigma(t)$  decreases sharply at the upshift, as the influx of carbon and central precursors suddenly drop. (B-C) The ribosomal and catabolic regulation functions  $\chi_{\text{Rb}}(t)$  and  $\chi_{\text{Cat}}(t)$  jump to extreme values as the carbon substrate is removed, followed by a relaxation to the final states. (D) Ribosomal protein synthesis is repressed after the shift (see  $\chi_{\text{Rb}}(t)$  in panel B for the regulation function), but recovers as growth is resumed. (E) Biomass flux  $J(t) = \alpha_M M_{\text{Rb}}(t) \sigma(t)$  decreases sharply at the upshift, as the carbon influx providing precursors is suddenly decreased. After the initial decrease flux first grows at a rate  $\nu_{C,f}^{\text{max}}$  ( $0$  to  $\sim 45\text{min}$ ), followed by exponential growth at final rate  $\lambda_f^*$ . (F) Catabolic proteins  $M_{\text{Cat1}}(t)$  are repressed and not expressed since substrate S1 was removed. (G) Catabolic proteins  $M_{\text{Cat2}}(t)$  respond quickly and provide the entire carbon influx. (H) total biomass increases after an initial lag. (I) Growth rate shows very fast recovery, reaching a value close to the final growth rate after merely 1h. (compare to Fig. B.3, where growth rate started from the same initial condition, but took several hours to reach the final state (J) The proteome fraction  $\phi_{\text{Cat1}} = M_{\text{Cat1}}(t)/M(t)$  is slowly diluted as no more  $M_{\text{Cat1}}(t)$  is synthesized. (K) The proteome fraction  $\phi_{\text{Cat2}} = M_{\text{Cat2}}(t)/M(t)$  quickly reaches its final state, as expression of  $M_{\text{Cat2}}(t)$  is transiently increased (see  $\chi_{\text{Cat}}(t)$  in panel C for the regulation function). (L) The proteome fraction of ribosomal proteins remains at high levels, as initial and final growth rates are identical.

mass  $M_P(t)$ , the fluxes  $J(t)$ ,  $J_C(t)$  and  $J_R(t)$ , and the protein levels  $M_{\text{Cat},j}(t)$  and  $M_{\text{Rb}}(t)$ , can be calculated from the translational activity  $\sigma(t)$ . These variables require their own initial conditions, which we get from the pre-shift growth state and the requirement that protein content and biomass are continuous. If the translational activity  $\sigma(t)$  is also continuous, e.g. for upshift without pre-expression, see Section B.3.2, then the fluxes  $J(t)$ ,  $J_C(t)$  and  $J_R(t)$  are continuous. Else, if the translational activity  $\sigma(t)$  is not continuous, then  $J(t)$ ,  $J_C(t)$  and  $J_R(t)$  aren't either. The latter is the case for upshift with pre-expression or diauxic shifts; see Sections B.3.2 and B.3.2.

### Pre-shift growth

By experimental design, the cell grow exponentially before the shift, thus all extensive quantities grow exponentially at the initial growth rate  $\lambda_i^*$ :

$$M(t < 0) = M(0) \exp(\lambda_i^* t) \quad (\text{B.23})$$

$$J(t < 0) = \frac{dM}{dt} = \lambda_i^* M(t) \quad (\text{B.24})$$

$$M_P(t < 0) = M_P(0) \exp(\lambda_i^* t) = \frac{\alpha}{\alpha_M} M(t) \quad (\text{B.25})$$

$$J_R(t < 0) = \frac{dM_P}{dt} = \lambda_i^* M_P(t) \quad (\text{B.26})$$

$$J_C(t < 0) = \alpha J_R \quad (\text{B.27})$$

$$M_{\text{Cat},j}(t < 0) = M_{\text{Cat},j}(0) \exp(\lambda_i^* t) = h_{j,\max} \phi_{\text{Cat}}^*(\lambda_i^*) M_P(t) \quad (\text{B.28})$$

$$M_{\text{Rb}}(t < 0) = M_{\text{Rb}}(0) \exp(\lambda_i^* t) = \phi_{\text{Rb}}^*(\lambda_i^*) M_P(t) \quad (\text{B.29})$$

### At the instant of shift

At the instant of the nutrient shift,  $t = 0$ , all protein levels ( $M_P$ ,  $M_{C,j}$  and  $M_{\text{Rb}}$ ) and the biomass  $M$  must be continuous. Fluxes, however, can abruptly change at the instant of upshift, depending on the initial condition  $\sigma(0)$  discussed in the previous section. We use the definition of the translational activity Eq. (3.4), as well as the conversion factors discussed in Section B.2 and write

$$J(0) = \alpha_M J_C(0) = \frac{\alpha_M}{\alpha} J_R(0) = \frac{\alpha_M}{\alpha} \sigma(0) \phi_{\text{Rb}}^*(\lambda_i^*) M_P(0) \quad (\text{B.30})$$

### B.3.4 Post-shift growth

For the kinetics after the upshift, we use solution of the translational activity  $\sigma(t)$ , from Eq. (B.15), to calculate the experimental observables. The subscripts  $i$  and  $f$  denote steady state values in the initial and final states.

### Ribosomal content

We start with the kinetics of ribosomal proteins  $M_{\text{Rb}}(t)$ . From Eq. (3.5) and 1.3, we have  $\dot{M}_{\text{Rb}} = \chi_{\text{Rb}}(t) \sigma(t) M_{\text{Rb}}(t)$ . Together with our central assumption Eq. (3.7), this can be rewritten as  $d \ln M_{\text{Rb}} = \hat{\chi}_{\text{Rb}}(\sigma) dt$ . Substituting  $dt$  using Eq. (B.14), using Eq. (B.15) for  $\hat{\chi}_{\text{Rb}}(\sigma)$  and integrating, we find

$$M_{\text{Rb}}(t) = M_{\text{Rb}}(0) \left( \frac{1 - \sigma(0)/\sigma_f^*}{1 - \sigma(t)/\sigma_f^*} \right)^{(1-\lambda_f^*/\lambda_C)(1-\sigma_f^*/\gamma)}. \quad (\text{B.31})$$

Where the translational activity in the final state is denoted by  $\sigma_f^*$ . Using the solution for the translational activity  $\sigma(t)$  from Eq. (B.29), the above equation reduces to

$$M_{\text{Rb}}(t) = M_{\text{Rb}}(0) \left( \frac{\sigma(t)}{\sigma(0)} \right)^{\lambda_f^*/\lambda_C - 1} \exp(\lambda_f^* t). \quad (\text{B.32})$$

The solution is plotted in Fig. B.3D for an upshift without pre-expression, in Fig. B.4D for an upshift with pre-expression and in Fig. B.5D for a diauxic shift.

The temporal change of the ribosomal content comprises two distinct contributions. As the translational activity adapts from the initial  $\sigma(0)$  to the final state  $\sigma_f$ , the ribosomal content increases by the factor  $(\sigma(t)/\sigma(0))^{\lambda_f^*/\lambda_C - 1}$ . This dynamics happens at the time scale of the relaxation  $\sigma(t)$ , which is given by  $\mu_f$ , according to Eq. (B.15). Once the translational activity has settled, the ribosomal content keeps increasing exponentially at the final growth rate  $\lambda_f^*$ , as expected for long times.

At the end of this section, once all experimental observables are derived, we will discuss the physical origin of the pre-factor  $(\sigma(t)/\sigma(0))^{\lambda_f^*/\lambda_C - 1}$ , and we will estimate the time to reach this increase.

### Fluxes: Protein synthesis, carbon influx and biomass flux

We can directly derive the protein synthesis flux  $J_{\text{R}}(t) = \sigma(t) M_{\text{Rb}}(t)$ , from Eq. (B.32) as

$$J_{\text{R}}(t) = J_{\text{R}}(0) \left( \frac{\sigma(t)}{\sigma(0)} \right)^{\frac{\lambda_f^*}{\lambda_C}} \exp(\lambda_f^* t). \quad (\text{B.33})$$

Here the initial condition of the protein synthesis rate  $J_{\text{R}}(0)$  is set by the translational activity via  $J_{\text{R}}(0) = \sigma(0) M_{\text{Rb}}(0)$ . The ribosomal content  $M_{\text{Rb}}(0)$  is continuous and determined from the pre-shift, while  $\sigma(0)$  is determined according to Section B.3.2. Using flux balance from Eq. (3.4) we calculate the carbon influx as

$$J_{\text{C}}(t) = \alpha^{-1} J_{\text{R}}(t) = J_{\text{C}}(0) \left( \frac{\sigma(t)}{\sigma(0)} \right)^{\frac{\lambda_f^*}{\lambda_C}} \exp(\lambda_f^* t). \quad (\text{B.34})$$

The initial condition is determined by flux balance:  $J_{\text{C}}(0) = \alpha^{-1} J_{\text{R}}(0)$ . The total biomass flux is calculated analogously using  $J(t) = \alpha_{\text{M}} J_{\text{C}}(t)$  as

$$J(t) = \alpha_{\text{M}} J_{\text{C}}(t) = J(0) \left( \frac{\sigma(t)}{\sigma(0)} \right)^{\frac{\lambda_f^*}{\lambda_C}} \exp(\lambda_f^* t), \quad (\text{B.35})$$

with the initial condition  $J(0) = \alpha_{\text{M}} J_{\text{C}}(0)$ . The solution for  $J(t)$  is plotted in Fig. B.3E for an upshift without pre-expression, in Fig. B.4 E for an upshift with pre-expression and in Fig. B.5E for a diauxic shift.

The biomass flux is directly coupled to the ribosomal content, as  $J(t) = \alpha_M/\alpha \sigma(t) M_{\text{Rb}}(t)$ . Thus the temporal changes of the flux are based on a change in the translational activity, on the one hand, and the change of the ribosomal content on the other. As we have noted in the previous section, the ribosomal content increases with two distinct contributions: A fast initial increase, followed by an exponential increase at the final rate. The fast initial increase of the ribosomal content, combined with the increase of translational increase translates into an increase of the biomass flux by a factor  $(\sigma(t)/\sigma(0))^{\lambda_f^*/\lambda_C}$ , on the fast time scale  $\mu_f$ .

### Catabolic proteins

We can further use Eq. (B.34) to derive the content of catabolic proteins  $M_{\text{Cat1}}$  and  $M_{\text{Cat2}}$  after the upshift, using the definition of the carbon influx from Eq. (3.1). We discuss two cases, either both carbon substrate systems are expressed and contribute to carbon influx, or only one substrate remains in the medium and provides the entire carbon flux.

We first discuss the simpler case where only one substrate, e.g. substrate S2, is in the post-shift medium. In this case, we have  $J_C(t) = \beta_2 k_2 M_{\text{Cat2}}(t)$ . Plugging in the solution of  $J_C(t)$  from Eq. (B.34) and using Eq. (B.2) to substitute constants, we derive

$$M_{\text{Cat2}}(t) = M_{\text{Cat2}}(0) \left( \frac{\sigma(t)}{\sigma(0)} \right)^{\frac{\lambda_f^*}{\lambda_C}} \exp(\lambda_f^* t) . \quad (\text{B.36})$$

The initial condition  $M_{\text{Cat2}}(0) = \phi_{\text{Cat2}}^*(t < 0) M_{\text{P}}(0)$  is determined by the expression level in the pre-shift  $h_2$  ( $t < 0$ ), according to Eq. (3.13), Eq. (B.2). The uptake system for substrate S1 is not expressed in this case,  $M_{\text{Cat1}}(t) = 0$ , thus the total content remains constant at  $M_{\text{Cat1}}(0)$ . The diauxic shift presented in Fig. B.5 is calculated under the above assumptions. The content of catabolic enzymes  $M_{\text{Cat1}}$  and  $M_{\text{Cat2}}$  are shown in panel Fig. B.5F-G.

If both substrates S1 and S2 are in the medium after the shift, and both uptake systems are expressed, then  $M_{\text{Cat1}}$  and  $M_{\text{Cat2}}$  show different kinetics. Since both uptake systems are under the global control of  $\chi_{\text{Cat}}$ , see Eq. (3.6), they will be produced proportionally to one another, according to the specific regulation discussed in Section 3.2.2

$$\frac{M_{\text{Cat2}}(t) - M_{\text{Cat2}}(0)}{h_2} = \frac{M_{\text{Cat1}}(t) - M_{\text{Cat1}}(0)}{h_1} . \quad (\text{B.37})$$

The carbon influx is provided by both uptake systems, according to Eq. (3.1). Plugging in Eqs. (B.34) and (B.37) into Eq. (3.1), we obtain an expression for the catabolic protein content valid for either uptake system

$$M_{\text{Cat},j}(t) = M_{\text{Cat},j}(0) + \phi_{C,j,\max} \frac{J_{\text{R}}(0)}{\mu_f} \left[ \left( \frac{\sigma(t)}{\sigma(0)} \right)^{\frac{\lambda_f^*}{\lambda_C}} \exp(\lambda_f^* t) - 1 \right] . \quad (\text{B.38})$$

The initial condition can be derived either by the catabolic protein content inherited from pre-shift as  $J_C(0) = \beta_1 k_1 M_{\text{Cat1}}(0) + \beta_2 k_2 M_{\text{Cat2}}(0)$ , or equivalently from the ribosomal content and the translational activity as  $J_C(0) = \alpha^{-1} J_{\text{R}}(0) = \alpha^{-1} \sigma(0) M_{\text{Rb}}(0)$ .

Note that although both catabolic proteins are expressed proportionally, they can show different kinetics due to the different initial conditions  $M_{\text{Cat},j}(0)$ . To illustrate this, we show two upshifts (substrate S2 added to substrate S1, co-utilization of substrates S1 & S2) in Fig. B.3F-G and Fig. B.4F-G, respectively, with different initial conditions for  $M_{\text{Cat2}}(0)$ . In Fig. B.3G the second uptake system is not pre-expressed in pre-shift,  $M_{\text{Cat2}}(0) = 0$ , in contrast to Fig. B.4G where the second uptake system is pre-expressed, with  $M_{\text{Cat2}}(0) > 0$ . The abundances of the uptake systems according to Eq. (B.38) are shown in panels F and G.

### Biomass

We now integrate biomass flux  $J(t)$  to obtain the biomass  $M(t)$ . We calculate the biomass flux from the ribosomal content  $M_{\text{Rb}}(t)$  by multiplying it with  $\sigma(t)$  to obtain and the appropriate conversion factors. Integrating biomass flux gives an expression for biomass,

$$M(t) = \int \frac{\alpha_M}{\alpha} \sigma(t) M_{\text{Rb}}(t) dt. \quad (\text{B.39})$$

Using Eq. (B.29), the above equation can be solved and yields

$$\begin{aligned} M(t) = & M(0) \left( 1 - \frac{\lambda_i^* \sigma_f^*}{\lambda_f^* \sigma_i^*} \cdot \frac{1 + \left(\frac{\lambda_C}{\lambda_f^*} - 1\right) \frac{\sigma(0)}{\gamma}}{1 + \left(\frac{\lambda_C}{\lambda_f^*} - 1\right) \frac{\sigma_f^*}{\gamma}} \right) \\ & + M(0) \left( \frac{\lambda_i^* \sigma_f^*}{\lambda_f^* \sigma_i^*} \cdot \frac{1 + \left(\frac{\lambda_C}{\lambda_f^*} - 1\right) \frac{\sigma(t)}{\gamma}}{1 + \left(\frac{\lambda_C}{\lambda_f^*} - 1\right) \frac{\sigma_f^*}{\gamma}} \right) \left( \frac{1 - \sigma \frac{\sigma(0)}{\sigma_f^*}}{1 - \frac{\sigma(t)}{\sigma_f^*}} \right)^{(1-\lambda_f^*/\lambda_C)(1-\sigma_f^*/\gamma)} \end{aligned} \quad (\text{B.40})$$

which is further simplified using Eq. (B.15) to

$$\begin{aligned} M(t) = & M(0) \left( 1 - \frac{\lambda_i^* \sigma_f^*}{\lambda_f^* \sigma_i^*} \cdot \frac{1 + \left(\frac{\lambda_C}{\lambda_f^*} - 1\right) \frac{\sigma(0)}{\gamma}}{1 + \left(\frac{\lambda_C}{\lambda_f^*} - 1\right) \frac{\sigma_f^*}{\gamma}} \right) \\ & + M(0) \left( \frac{\lambda_i^* \sigma_f^*}{\lambda_f^* \sigma_i^*} \cdot \frac{1 + \left(\frac{\lambda_C}{\lambda_f^*} - 1\right) \frac{\sigma(t)}{\gamma}}{1 + \left(\frac{\lambda_C}{\lambda_f^*} - 1\right) \frac{\sigma_f^*}{\gamma}} \right) \left( \frac{\sigma(t)}{\sigma(0)} \right)^{\frac{\lambda_f^*}{\lambda_C} - 1} \exp(\lambda_f^* t) \end{aligned} \quad (\text{B.41})$$

The initial condition  $M(0)$  comes from enforcing continuity of the biomass and protein mass.

The solution for  $M(t)$  is plotted in Fig. B.3H for an upshift without pre-expression, in Fig. B.4H for an upshift with pre-expression, and in Fig. B.5H for a diauxic shift. We note that for long times, after  $\sigma(t)$  has relaxed to its final value  $\sigma_f^*$ , that the biomass grows as  $M(t) = A + B \exp(\lambda_f^* t)$ , with the pre-factors having complicated dependencies on the pre- and post-shift state, as visible in Eq. (B.41).

### Growth rate

We use the resulting expression for the biomass  $M(t)$ , Eq. (B.41), and biomass flux  $J(t)$ , Eq. (B.35) to derive growth rate  $\lambda(t) = d \ln M / dt = J(t) / M(t)$ ,

$$\lambda(t) = \frac{\lambda_f^* \sigma(t) / \sigma_f^*}{\left( \frac{\lambda_f^* \sigma_i^*}{\lambda_i^* \sigma_f^*} - \frac{1 + (\lambda_C / \lambda_f^* - 1) \frac{\sigma(0)}{\gamma}}{1 + (\lambda_C / \lambda_f^* - 1) \frac{\sigma_f^*}{\gamma}} \right) \left( \frac{\sigma(0)}{\sigma(t)} \right)^{\frac{\lambda_f^*}{\lambda_C} - 1} \exp(-\lambda_f^* t) + \frac{1 + (\lambda_C / \lambda_f^* - 1) \frac{\sigma(t)}{\gamma}}{1 + (\lambda_C / \lambda_f^* - 1) \frac{\sigma_f^*}{\gamma}}} \quad (\text{B.42})$$

The solution is for  $\lambda(t)$ , Eq. (B.42), is plotted in Fig. B.3I for an upshift without pre-expression, in Fig. B.4I for an upshift with pre-expression and in Fig. B.5I for a diauxic shift.

### Relative catabolic and ribosomal protein content

To obtain relative quantities of ribosomal proteins, or catabolic proteins, we divide the solutions of the total content (ribosomal proteins, Eq. (B.32), catabolic proteins Eq. (B.38) by the total protein mass  $M_P(t) = \alpha M(t)$  and use the solution for biomass in Eq. (B.41). We plot the resulting ribosomal protein fraction  $\phi_{\text{Rb}}(t) = M_{\text{Rb}}(t)/M_P(t)$  and the fraction of catabolic proteins Cat1 and Cat2,  $\phi_{\text{Cat1}}(t) = M_{\text{Cat1}}(t)/M_P(t)$  and  $\phi_{\text{Cat2}}(t) = M_{\text{Cat2}}(t)/M_P(t)$  in panels J-L in Fig. B.3 for an upshift without pre-expression, in Fig. B.4 for an upshift with pre-expression and in Fig. B.5 for a diauxic shift.

We note that even though the synthesis of ribosomal and catabolic proteins can quickly adapt to their final rates, the proteome fractions adapt slowly. This is because even if synthesis is at increased, old biomass still dominates the proteome fractions. Only as more and more new biomass is synthesized, the relative proportion of old biomass decreases. The basis of this effect is identical to the slow adaptation of growth rate that will be discussed in the following section.

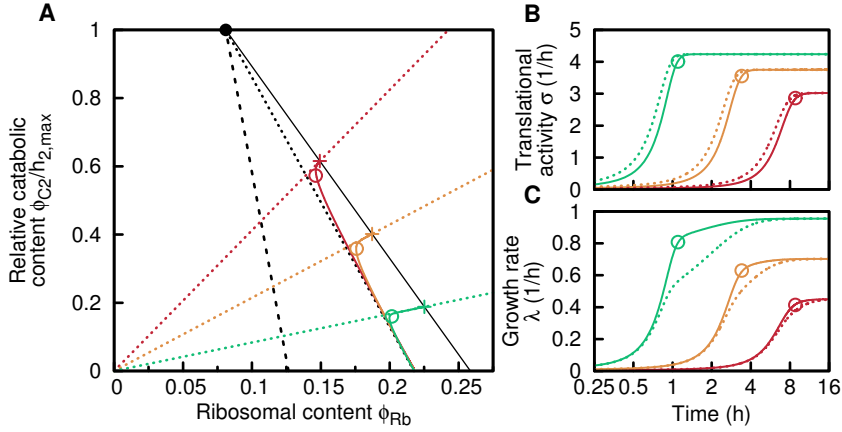


**Figure B.6: Adaptation strategy of the cell during upshifts (slow initial growth).** (A) Relative catabolic content  $\phi_{C2}(t)/\phi_{C2,\max}$  plotted versus ribosomal content  $\phi_{Rb}(t)$ . The solid lines represent trajectories of the full solution described in section 3, starting at the initial condition  $\phi_{Rb}(0) = \phi_{Rb,0} + \lambda_i^*/\gamma$  with  $\lambda_i^* = 0.3/\text{h}$  and  $\phi_{C2}(0) = 0.01 \phi_{C2,f}$  and ending at final states (colored crosses, green:  $\lambda_f^* = 0.95/\text{h}$ , orange:  $\lambda_f^* = 0.7/\text{h}$  and red:  $\lambda_f^* = 0.45/\text{h}$ ). Initially gene regulation is set to the extreme values,  $\chi_{Cat}(t) = 1$  and  $\chi_{Rb}(t) = \phi_{Rb,0}$  (black dashed lines, slope from Eq. (B.54)) and thus catabolic protein content quickly rises, while ribosomal protein content is diluted as cells grow. The filled circle indicates  $\phi_{C2}(t) = \phi_{C2,\max}$  and  $\phi_{Rb}(t) = \phi_{Rb,0}$ . The diagonal, colored dotted lines indicate the ratio of catabolic to ribosomal proteins such that the translational activity  $\sigma$  is at its final value  $\sigma_f^*$ . Once the trajectory is close to the colored dotted line (indicated by a circle), it follows the dotted line to the final state (crosses). (B) The translational activity  $\sigma$  is proportional to the ratio of catabolic to ribosomal proteins, see Eq. (B.47). The circles correspond to the positions in panel A. (C) Growth rate during the recovery. Recovery is slower than translational activity for fast growth rate (green). For slow final growth rate (red) translational activity and growth rate relax in synchrony. Circles correspond to panels B and A.

## B.4 Adaptation strategy according to the FDR model

In this appendix section we discuss the adaptation strategy of Section 3.5 in detail. For simplicity we discuss here a gedanken experiment where nutrient is abruptly shifted from a pre-shift medium containing only saturating amounts of substrate S1 as the sole carbon source to one a post-shift medium containing only saturating amounts of substrate S2 as the sole carbon source. By choosing appropriately the steady-state growth rate in the pre- and post-shift medium ( $\lambda_i^*$  and  $\lambda_f^*$ , respectively), the results below mimic closely nutrient up-shift ( $\lambda_f^* > \lambda_i^*$ ) or diauxie shift ( $\lambda_f^* \lesssim \lambda_i^*$ ) described in the main text.

### B.4.1 A geometric view of adaptation kinetics

As we will show, the key feature of the adaptation kinetics is an interplay between the synthesis of the catabolic enzyme Cat2 for the post-shift substrate S2 (defined in Fig. 3.3), and adjusting the ribosomal abundance for what is needed for growth. To capture this interplay, we follow the content of Cat2,  $\phi_{C2}(t)$ , and the ribosomal content,  $\phi_{Rb}(t)$ .

Solutions for  $\phi_{C2}(t)$  and  $\phi_{Rb}(t)$  are obtained using the following initial conditions:  $\phi_{C2}(0) = 10^{-2} \phi_{C2,f}^*$  is used for C2, i.e. 1% of the final proteome fraction  $\phi_{C2,f}^*$ , reflecting the typical extent of repression in the regulatory function  $h_2$ , whereas  $\phi_{Rb}(0)$  is set by the pre-shift growth rate  $\lambda_i^*$  according to the steady state growth law of Eq. (1.2),

$$\phi_{Rb}(0) = \phi_{Rb,0} + \frac{\lambda_i^*}{\gamma}. \quad (\text{B.43})$$

In Fig. B.6A, we plot the trajectories  $\phi_{C2}(t)$  vs  $\phi_{Rb}(t)$  for growth transitions from the same (slow) pre-shift growth rate  $\lambda_i^* = 0.3/\text{h}$  (which defines the initial condition indicated by

the grey square) to 3 different final states. These final states are defined by  $\lambda_f^* = 0.45/h$  (red),  $\lambda_f^* = 0.7/h$  (orange),  $\lambda_f^* = 0.95/h$  (green) and span the range of final growth rates used in this paper. The corresponding trajectories are shown as solid lines in red, orange, and green.

Mathematically, the final states are defined by the growth laws Eqs. (1.2) and (1.5), rewritten here as

$$\phi_{\text{Rb}}^*(\lambda_f^*) = \phi_{\text{Rb},0} + \frac{\lambda_f^*}{\gamma} \quad (\text{B.44})$$

and

$$\phi_{\text{Cat2}}^*(\lambda_f^*) = \phi_{\text{Cat2,max}} \left( 1 - \frac{\lambda_f^*}{\lambda_C} \right) \quad (\text{B.45})$$

And indicated with crosses of the respective colors in Fig. B.6A. Thus the final states  $\phi_{\text{Rb}}^*(\lambda_f^*)$  and  $\phi_{\text{Cat2}}^*(\lambda_f^*)$  for all  $\lambda_f^*$  lie along the line

$$\frac{\phi_{\text{Cat2}}^*(\lambda_f^*)}{\phi_{\text{Cat2,max}}} + (\phi_{\text{Rb}}^*(\lambda_f^*) - \phi_{\text{Rb},0}) \cdot \gamma / \lambda_C = 1, \quad (\text{B.46})$$

which is indicated in Fig. B.6A as the thin black line. For convenience, the vertical axis is shown as  $\phi_{\text{Cat2}}(t) / \phi_{\text{Cat2,max}}$ .

As seen in Fig. B.6A, the trajectories  $\phi_{\text{Cat2}}(t)$  versus  $\phi_{\text{Rb}}(t)$  comprise of two regimes: First, there is a regime of steep increase of catabolic proteins  $\phi_{\text{Cat2}}(t)$  regardless of the final state; the initial part of this steep rise is along the dashed grey line which is obtained by simply connecting the initial position (defined by pre-shift growth) with the position when the cell has maximal catabolic content,  $\phi_{\text{Cat2}} = \phi_{\text{Cat2,max}}$ , and minimal ribosomal content  $\phi_{\text{Rb}} = \phi_{\text{Rb},0}$  (filled black circle in Fig. B.6). As we discuss in Section B.4.2, the trajectory along this line means that the cell has set its regulatory functions  $\chi_{\text{Cat}}(t)$  and  $\chi_{\text{Rb}}(t)$  to the extreme values, with maximal catabolic expression  $\chi_{\text{Cat}}(t) = 1$  and minimal ribosomal expression  $\chi_{\text{Rb}}(t) = \phi_{\text{Rb},0}$ .

At some point the trajectories cross over to a phase along the thin dashed lines of corresponding colors, which are obtained by connecting the origin  $(0, 0)$  to the final coordinates  $(\phi_{\text{Cat2},f}^* / \phi_{\text{Cat2,max}}, \phi_{\text{Rb},f}^*)$  marked by the crosses. These colored lines define a constant ratio of catabolic to ribosomal proteins, thus in this regime  $\phi_{\text{Cat2}}(t)$  and  $\phi_{\text{Rb}}(t)$  increase in synchrony, such that the ratio remains constant. As we discuss in Section B.4.3 the trajectory along this diagonal line means that the cell has set the regulatory functions  $\chi_{\text{Cat}}(t)$  and  $\chi_{\text{Rb}}(t)$  into the final state,  $\chi_{\text{Cat}}(t) = \phi_{\text{Cat2},f}^* / \phi_{\text{Cat2,max}}$  and  $\chi_{\text{Rb}}(t) = \phi_{\text{Rb},f}^*$ .

To investigate the time dependence of trajectories, we look at the translational activity, Fig. B.6B, and growth rate, Fig. B.6C. The translational activity is proportional to the ratio of catabolic to ribosomal proteins,

$$\sigma(t) = \frac{\alpha\beta_2 k_2 M_{\text{Cat2}}(t)}{M_{\text{Rb}}(t)} = \mu_f \frac{\phi_{\text{Cat2}}(t) / \phi_{\text{Cat2,max}}}{\phi_{\text{Rb}}(t)}, \quad (\text{B.47})$$

according to Eq. (3.1) and Eq. (3.4). Thus, the dashed colored lines are of constant  $\sigma(t)$ , and the slopes are given by  $\sigma_f^* / \mu_f$ . On the dashed lines the translational activity has its final value  $\sigma_f^*$ , outside the diagonal the translational activity decreases linearly with distance. When translational activity increased to its final value (time point marked with colored circles in Fig. B.6B), then the trajectory of  $\phi_{\text{Cat2}}(t)$  vs  $\phi_{\text{Rb}}(t)$  in Fig. B.6A goes along the dotted, colored diagonal (corresponding point marked with colored circles in Fig. B.6A). At this point growth rate in Fig. B.6C has not fully relaxed to its final state (compare colored circles in Fig. B.6B and C). Growth rate is directly proportional to the relative protein content of Cat2,

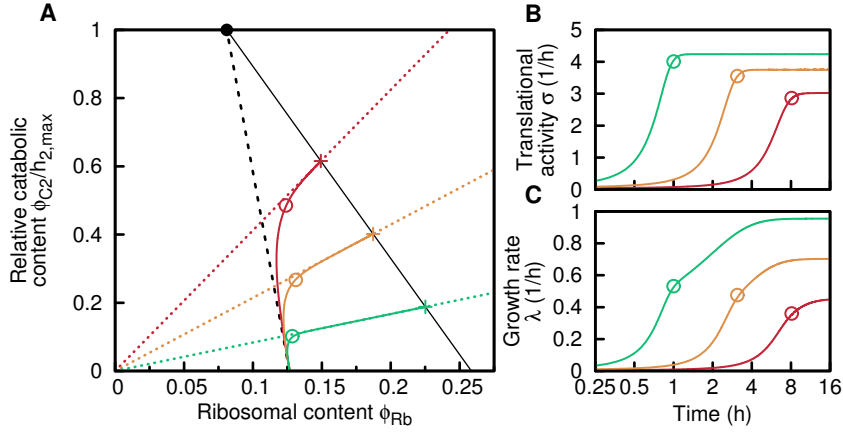


**Figure B.7:** Adaptation strategy of the cell during diauxic shifts (slow initial growth). Colors and final states correspond to those in Fig. B.6. **(A)** Trajectories in this figure start at the initial condition  $\phi_{Rb}(0) = \phi_{Rb,0} + \lambda_i^*/\gamma$  with  $\lambda_i^* = 0.9/h$  and  $\phi_{Cat2}(0) = 0.01 \phi_{C2,f}$ . As in Fig. B.6, regulation is initially set to the extreme values,  $\chi_{Cat}(t) = 1$  and  $\chi_{Rb}(t) = \phi_{Rb,0}$  (black dotted lines, slope from Eq. (B.54)). Black dashed line taken from Fig. B.6A) and thus catabolic protein content quickly rises, while ribosomal protein content is diluted as cells grow. The filled circle indicates  $\phi_{Cat2}(t) = \phi_{Cat2,max}$  and  $\phi_{Rb}(t) = \phi_{Rb,0}$ . The trajectories meet the diagonal colored dotted lines closer to the final states (crosses), than in Fig. B.6. **(B)** The translational activity  $\sigma$  recovers similarly to Fig. B.6 B. The circles correspond to the positions in panel A. **(C)** Growth rate relaxed almost entirely when translational activity has relaxed (circles). This is in contrast to upshifts presented in Fig. B.6C. The differences in the green lines of this figure and Fig. B.6 are highlighted in Fig. 3.15.

$$\lambda(t) = \mu_f \frac{\phi_{Cat2}(t)}{\phi_{Cat2,max}}, \quad (B.48)$$

according to Eq. (3.1) and Eq. (B.2), and thus measures the vertical distance to final state.  $\mu_f$  is the maximal carbon uptake rate, defined in Eq. (1.10). From Fig. B.6C we read that while the cell quickly recovers from the initial state to the circle indicated in all panels of Fig. B.6, it spends many hours gliding along the diagonal towards the final state. We will investigate these two time scales in the following Sections B.4.2 and B.4.3.

A similar picture for the trajectories is obtained for adaptation from a fast pre-shift growth rate ( $\lambda_i^* = 0.9/h$ ) to the same 3 post-shift growth rates (colored crosses in Fig. B.7A), except that the initial increase of catabolic proteins  $\phi_{Cat2}(t)$ , along the dashed grey line, is much more slanted. Again,  $\sigma(t)$  approaches its final value  $\sigma_f^*$  as the trajectories join the dashed colored dotted lines (indicated by the colored circles in Fig. B.7. The adaptation kinetics of  $\sigma(t)$  is in fact very similar to the case with slow pre-shift growth (colored lines of Fig. B.6B, shown as dashed lines again in Fig. B.7B for the ease of comparison). However for the faster pre-shift growth, the instantaneous growth rate  $\lambda(t)$  also nearly approaches its final value when  $\sigma(t)$  reaches  $\sigma_f^*$  (Fig. B.7C), since the locations where the trajectories join the colored dashed lines are all close to the final coordinates (the colored crosses). Thus, the late adaption phase is nearly avoided for shift from fast pre-shift growth.

The above analysis of the trajectories indicates that the adaptation kinetics can be characterized approximately by a simple geometrical construction based on the orientations of the few lines (color, grey and black) and their intersections. In the following section, we will derive the grey lines mathematically and show that they are completely determined by steady-state properties in the pre- and post-shift medium as we find empirically in the two cases examined above. We will also provide a simple expression describing the time scale separating the two phases.

### B.4.2 First regime

During the first regime of recovery, the catabolic protein content  $\phi_{\text{Cat}2}$  is low and as a result the translational activity  $\sigma(t)$  as given by Eq. (B.47) is low, too. In the beginning of this regime,  $\sigma(t)$  is small compared to the final state  $\sigma_f^*$ , i.e.,  $\sigma(t) \ll \sigma_f^*$ , and thus the regulatory functions  $\chi_{\text{Rb}}(t)$  and  $\chi_{\text{Cat}}(t)$  as defined in Eqs. (3.9) and (3.10) are set at their extreme values, i.e.,

$$\chi_{\text{Rb}}(t) = \phi_{\text{Rb},0}, \quad (\text{B.49})$$

and

$$\chi_{\text{Cat}}(t) = 1. \quad (\text{B.50})$$

This setting of the regulatory functions makes the cells quickly increase the catabolic protein content, whereas ribosomal proteins are weakly synthesized and hence largely diluted during this first regime of growth. We estimate the initial slope of the trajectories,  $d\phi_{\text{Cat}2}/d\phi_{\text{Rb}}$ , in Fig. B.6A using the change of the relative protein contents

$$\frac{d\phi_{\text{Cat}2}}{d\phi_{\text{Rb}}} = \frac{\dot{\phi}_{\text{Cat}2}(t)}{\dot{\phi}_{\text{Rb}}(t)}, \quad (\text{B.51})$$

where the change of the relative protein contents can be calculated from Eqs. (3.5) and (3.6),

$$\dot{\phi}_{\text{Rb}}(t) = \lambda(t) (\chi_{\text{Rb}}(t) - \phi_{\text{Rb}}(t)), \quad (\text{B.52})$$

and

$$\dot{\phi}_{\text{Cat}2}(t) = \lambda(t) (h_{2,\text{max}}\chi_{\text{Cat}}(t) - \phi_{\text{Cat}2}(t)). \quad (\text{B.53})$$

By setting the regulatory functions to the extreme values, Eqs. (B.49) and (B.50), and using the initial conditions  $\phi_{\text{Cat}2}(0) = 0$  and  $\phi_{\text{Rb}}(0) = \phi_{\text{Rb},0} + \frac{\lambda_i^*}{\gamma}$ , we obtain the solution

$$\frac{d\phi_{\text{Cat}2}}{d\phi_{\text{Rb}}} = -\frac{\phi_{\text{Cat}2,\text{max}}}{\lambda_i^*/\gamma} = -\frac{\phi_{\text{Cat}2,\text{max}}}{\phi_{\text{Rb}}(0) - \phi_{\text{Rb},0}}, \quad (\text{B.54})$$

which exactly describes the geometric construction used to draw the grey lines in Fig. B.6A and Fig. B.7A.

As catabolic protein content increases, the translational activity  $\sigma$  increases. In Fig. B.6A we observe that the cells at some point reach the diagonal that connects the final state (colored crosses) with the origin. Along this diagonal the ratio of catabolic to ribosomal proteins  $\phi_{\text{Cat}2}(t)/\phi_{\text{Rb}}(t)$  is constant, and thus the translational activity is in its final state  $\sigma_f^*$ ,

$$\sigma(t) = \frac{\mu_f \phi_{\text{Cat}2}(t)}{\phi_{\text{Rb}}(t)} = \sigma_f^*. \quad (\text{B.55})$$

On this diagonal also the regulatory functions have relaxed from their extreme values, Eqs. (B.49) and (B.50), to their final, asymptotic values

$$\chi_{\text{Rb}}(t) = \hat{\chi}_{\text{Rb},f} = \phi_{\text{Rb},0} + \frac{\lambda_f^*}{\gamma}, \quad (\text{B.56})$$

and

$$\chi_{\text{Cat}}(t) = \hat{\chi}_{\text{C},f} = 1 - \frac{\lambda_f^*}{\lambda_{\text{C}}}. \quad (\text{B.57})$$

However, the proteome composition, e.g., the ribosomal content  $\phi_{\text{Rb}}(t)$  and the catabolic content  $\phi_{\text{Cat2}}(t)$ , has not yet reached the final steady state value. We can estimate how far the proteome contents relaxed during the early stage of relaxation by calculating the intersection of the lines defined by Eq. (B.54) and Eq. (B.55). We find

$$\phi'_{\text{Rb}} \approx \frac{\mu_{\text{f}}}{\sigma_{\text{f}}^*} \frac{\phi_{\text{Rb}}(0)}{\phi_{\text{Rb}}(0) - \phi_{\text{Rb},0} + \mu_{\text{f}}/\sigma_{\text{f}}^*}, \quad (\text{B.58})$$

and

$$\phi'_{\text{Cat2}} \approx \phi_{\text{Cat2},\text{max}} \frac{\phi_{\text{Rb}}(0)}{\phi_{\text{Rb}}(0) - \phi_{\text{Rb},0} + \mu_{\text{f}}/\sigma_{\text{f}}^*}. \quad (\text{B.59})$$

For growth rate, this implies an increase from  $\lambda(0)$  to

$$\lambda' \approx \beta_2 k_2 \phi'_{\text{Cat2}} = \lambda_{\text{f}}^* \frac{\phi'_{\text{Cat2}}}{\phi_{\text{C2,f}}^*}. \quad (\text{B.60})$$

We conclude this subsection by estimating the time it takes for the first regime to reach  $(\phi'_{\text{Cat2}}, \phi'_{\text{Rb}})$ . Since this point sits on the diagonal given by Eq. (B.55), the translational activity  $\sigma(t)$  has relaxed to its final state  $\sigma_{\text{f}}^*$ . We take the differential equation governing the relaxation of  $\sigma(t)$ , Eq. (B.13), and note that the initial regime where  $\sigma(t) \ll \sigma_{\text{f}}^* < \gamma$ , the translational activity  $\sigma$  grows exponentially at rate  $\mu_{\text{f}}$ . Based on this exponential increase, we estimate the time  $\tau_{\sigma}$  it takes for  $\sigma$  to reach the final value  $\sigma_{\text{f}}^*$  from the initial value  $\sigma(0)$  to be about

$$\tau_{\sigma} = \frac{1}{\mu_{\text{f}}} \ln \left( \frac{\sigma_{\text{f}}^*}{\sigma(0)} \right) = \left( \frac{1}{\lambda_{\text{f}}^*} - \frac{1}{\lambda_{\text{C}}} \right) \cdot \ln \left[ \frac{\phi_{\text{Rb}}(0)}{\phi_{\text{Rb},\text{f}}^*} \frac{\phi_{\text{Cat2},\text{f}}^*}{\phi_{\text{Cat2}}(0)} \right]. \quad (\text{B.61})$$

The major contribution to this time  $\tau_{\sigma}$  stems from the pre-factor, which can be quite small for fast final growth (and vanishes for  $\lambda_{\text{f}}^* = \lambda_{\text{C}}$ ). E.g., for  $\lambda_{\text{f}}^* = 0.95/\text{h}$ , it is only 12 min, while for  $\lambda_{\text{f}}^* = 0.45/\text{h}$ , the pre-factor is 2.5 hr, a 10-fold slow down. In the logarithmic term, the initial condition for Cat2 is set so that  $\phi_{\text{Cat2},\text{f}}^*/\phi_{\text{Cat2}}(0)$  is 100, while  $\phi_{\text{Rb},\text{f}}^*/\phi_{\text{Rb}}(0)$  is of the order unity (with  $\phi_{\text{Rb}}(0)$  given by the pre-shift growth). Including this initial condition dependence, we obtain a time scale of 1hr and 10 hr for  $\lambda_{\text{f}}^* = 0.95/\text{h}$  and  $\lambda_{\text{f}}^* = 0.45/\text{h}$ , respectively, corresponding approximately to the time scales observed in Fig. B.6 and Fig. B.7B (with very weak dependence on the pre-shift state as expected). In Fig. B.8A, we plot the direct comparison of the recovery time  $\tau_{\sigma}$  for  $\sigma(t)$  according to Eq. (B.61) above, and the solution of the full model (defined as the time to reach 90% of  $\sigma_{\text{f}}^*$ ) for initial conditions spanning the whole range  $0 \leq \lambda_{\text{f}}^* < \lambda_{\text{C}}$  and the final growth rates of Fig. B.6 and Fig. B.7. We see a very good correspondence across two orders of magnitude.

### B.4.3 Second regime

We now study the course of growth recovery after translational activity  $\sigma(t)$  has settled from its initial value  $\sigma(0)$  to its final state  $\sigma_{\text{f}}^*$ . This phase is marked by the gradual recovery of the instantaneous growth rate,  $\lambda(t) \equiv \dot{M}/M = J(t)/M(t)$ . As fluxes grow exponentially in this phase, Eq. (B.35), but not the biomass, Eq. (B.41), the slow adaptation of growth rate  $\lambda(t)$  is due to the dilution of inherited biomass.

A time-evolution equation for  $\lambda(t)$  can be obtained by differentiating this expression for  $\lambda(t)$ , and using Eqs. (3.1) and (3.6) for  $J_{\text{C}}(t)$  and its time derivative, with the result

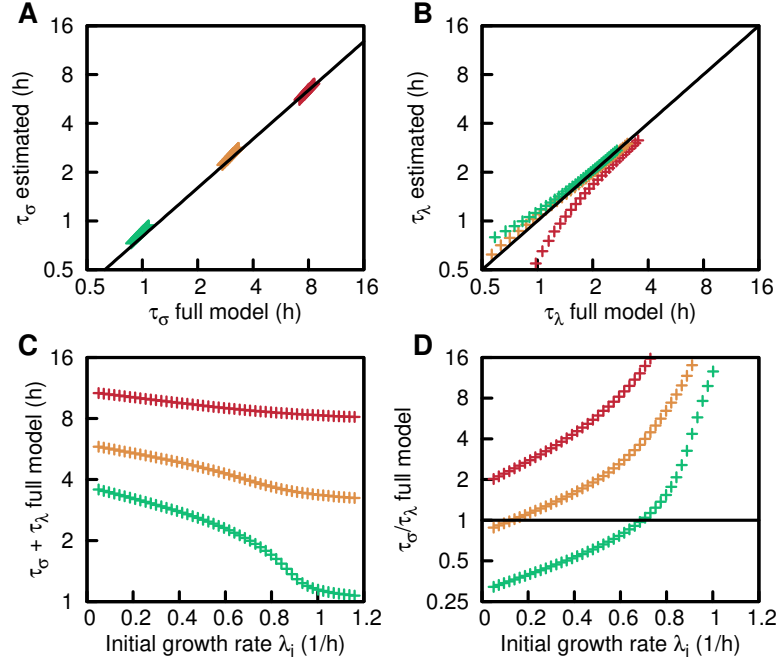


**Figure B.8: Relaxation times.** The system has two relaxation time scales,  $\tau_\sigma$  for the relaxation of the translational activity  $\sigma$  and  $\tau_\lambda$  for the relaxation of growth rate  $\lambda$ ,  $\tau_\sigma$  and  $\tau_\lambda$  are estimated in Eq. (B.61) and Eq. (B.65) and discussed in the surrounding text. Colors correspond to the final growth rates of Fig. B.6 and Fig. B.7, green:  $\lambda_f^* = 0.95/\text{h}$ , orange:  $\lambda_f^* = 0.7/\text{h}$  and red:  $\lambda_f^* = 0.45/\text{h}$ , crosses are calculated for different  $0 < \lambda_i^* < \lambda_C$  (A) Estimated  $\tau_\sigma$  compared to the full solution. Black line shows proportionality factor 1. (B) Estimated  $\tau_\lambda$  compared to the full solution. Black line shows proportionality factor 1. (C) Total relaxation time  $\tau_\sigma + \tau_\lambda$  (according to the full model) depends heavily on initial condition for fast final growth (green), but only weakly on initial condition for slow final growth. (D) Ratio  $\tau_\sigma/\tau_\lambda$  (according to the full model) identifies which time scale is dominant. Black horizontal line shows  $\tau_\sigma/\tau_\lambda = 1$ . For slow final growth rates  $\tau_\sigma$  always dominates (red). For fast growth rates (green),  $\tau_\sigma$  dominates for fast initial growth rates, while  $\tau_\lambda$  dominates for slow initial growth rates.

$$\frac{d\lambda}{dt} = \lambda(t) [\mu_f \chi_{\text{Cat}}(t) - \lambda(t)]. \quad (\text{B.62})$$

Since  $\sigma(t) = \sigma_f^*$  in this phase, then according to our central assumption Eqs. (3.7) and (3.8) we have  $\chi_{\text{Cat}}(t) = \chi_{\text{Cat}}^*(\sigma(t)) = \phi_C^*(\lambda_f^*)$ . Moreover,  $\mu_f \phi_C^*(\lambda_f^*) = \lambda_f^*$  according to the growth law Eq. (1.8). Thus, the evolution equation for  $\lambda(t)$  becomes a logistic equation

$$\frac{d\lambda}{dt} = \lambda(t) \cdot [\lambda_f^* - \lambda(t)], \quad (\text{B.63})$$

which manifests the simple dynamics of dilution by growth in this phase. The solution is a simple exponential approach to  $\lambda_f^*$ :

$$\lambda(t > \tau_\sigma) = \frac{\lambda_f^*}{1 + A \exp(-\lambda_f^*(t - \tau_\sigma))}. \quad (\text{B.64})$$

The constant  $A = \lambda_f^*/\lambda' - 1$  can be fixed by the point of entry to this regime at time  $t = \tau_\sigma$ , using  $\lambda' = \lambda(\tau_\sigma)$  as the growth rate at  $t = \tau_\sigma$  according to the full model. Entry into this phase is indicated in Fig. B.6C and Fig. B.7C with circles drawn at  $(\tau_\sigma, \lambda')$ .

We estimate the time  $\tau_\lambda$  to recover growth rate by calculating the time it takes to reach 90% of the final growth rate,

$$\tau_\lambda = \frac{\ln 10A}{\lambda_f^*} \quad (\text{B.65})$$

This estimate is compared to the full model in Fig. B.8B. Even for fast final growth rate  $\lambda_f^* \approx \lambda_C$ , the time  $\tau_\lambda$  remains finite, which is in contrast to the time scale  $\tau_\sigma$ , which vanishes in this limit. Which time scale dominates in which regime is discussed in the next section.

Finally, we remark that due to the proportionality between  $\lambda(t)$  and  $\phi_{\text{Cat}2}(t)$ , and between  $\phi_{\text{Cat}2}(t)$  and  $\phi_{\text{Rb}}(t)$  during the second regime, the logistic dynamics exhibited by  $\lambda(t)$  (Eq. (B.64)) is shared by  $\phi_{\text{Cat}2}(t)$  and  $\phi_{\text{Rb}}(t)$ , i.e.,

$$\phi_X(t) = \frac{\phi_X^*}{1 + B \exp(-\lambda_f^* t)} \quad (\text{B.66})$$

along the diagonals in Fig. B.6A. This effect is clearly seen here as a dilution of the old proteome.

#### B.4.4 Impact of the two regimes on total recovery

The two regimes of recovery, completely determine the adaptation of the cell to the final state. The first regime happens on a time scale  $\tau_\sigma$  (given approximately by Eq. (B.61)), while the second regime happens on the time scale  $\tau_\lambda$  (given approximately by Eq. (B.65)). The dynamics of the recovery, and the total recovery time  $\tau = \tau_\lambda + \tau_\sigma$ , depend heavily on which regime dominates the recovery.

The dependence of the total recovery time  $\tau = \tau_\lambda + \tau_\sigma$  on both initial and final growth rates is plotted in Fig. 3.15D as a 3D plot. The dependence of the total recovery time on the initial and final growth rates used in Fig. B.6 and Fig. B.7 is shown in Fig. B.8C.

The general trend is that the total recovery time decreases with final growth rate, which we expected as both  $\tau_\sigma$  and  $\tau_\lambda$  decrease with increasing growth rate. For fast initial and fast final growth rate, recovery is fastest. In this regime, when the final growth rate is close to  $\lambda_C$ , the time scale  $\tau_\sigma$  becomes vanishingly small, with only a small (logarithmic) dependence on the initial growth rate, see Eq. (B.61), and the total recovery time is then highly dependent on how long the cell spends in each phase. For slow initial growth rates, the cell is forced into a long second regime, and this regime dominates the recovery as can be seen in the ratio of time scales  $\frac{\tau_\sigma}{\tau_\lambda} \ll 1$ , plotted in Fig. B.8D in green. In contrast fast initial growth rates can help the cell to avoid the second regime almost completely, and the total recovery becomes dominated by the first regime  $\frac{\tau_\sigma}{\tau_\lambda} \gg 1$ , in which recovery is faster. This manifests itself in a 4-fold change of recovery rate over the whole range of initial growth rates in Fig. B.8C.

For slower final growth rates the adaptation time  $\tau_\sigma$  becomes longer, as can be seen in Fig. B.8A, while the recovery time  $\tau_\lambda$  stays of same magnitude. Thus these cases are always dominated by long first regime, as can be seen in Fig. B.8D, where the ratio of time scales is dominated by  $\tau_\sigma$  for all initial growth rates,  $\frac{\tau_\sigma}{\tau_\lambda} \gg 1$ . The impact of the initial growth rate, which can reduce the time spend in the late second regime is very small for slow final growth rates, as the recovery is dominated by the adaptation time scale. This manifests itself with a mere 30% change of recovery time over the whole range of initial growth rates.

## B.5 Supplementary Materials and Methods

### B.5.1 Growth medium

All growth media used in this study were based on "N<sup>-</sup>C<sup>-</sup>" minimal medium [119], containing K<sub>2</sub>SO<sub>4</sub> (1 g), K<sub>2</sub>HPO<sub>4</sub> · 3 H<sub>2</sub>O (17.7 g), KH<sub>2</sub>PO<sub>4</sub> (4.7 g), MgSO<sub>4</sub> · 7 H<sub>2</sub>O (0.1 g), and NaCl (2.5 g) per liter. The medium was supplemented with 20mM NH<sub>4</sub>Cl as Nitrogen source, and various carbon sources. 1mM IPTG was added to media when necessary to fully induce the native lac operon, or 0.1mM IPTG to induce PLlac-O1 promoter driving XylR for titratable expression of DctA in strain NQ537. B.1 includes steady state growth rates supported by the medium for all carbon sources used.

### B.5.2 Culture procedure

Each experiment was carried out in three steps: seed culture, pre-culture and experimental culture. Cells taken from -80°C Glycerol stock were struck out on an LB Agar plate before the experiment. A single colony was picked and grown on fresh LB in a shaken water bath at 37°C and 250 rpm. Media in the pre-culture were chosen to be identical medium to the experimental culture. Inoculation of the pre-culture with washed seed culture was chosen such that the pre-culture grown overnight were still growing exponentially in the morning of the experiment. Cells spend at least ten doublings (at least five for growth rates below 0.4/h) in the pre-culture at 37°C, shaken at 250 rpm. Inoculation into pre-warmed exponential culture in the morning was chosen such that cells spend at least an additional three doublings at 37°C and shaken at 250 rpm in the experimental culture before growth was measured.

For small culture volumes, 5ml of experimental culture were grown in 20 mm x 150 mm glass test tubes. For larger volumes 25 ml (100 ml) were grown in 125 ml (500 ml) baffled Erlenmeyer flasks. At each time point, a 200 μ sample was extracted and optical density was measured using a 1 mm path length Starna Sub-Micro Cuvette at 600 nm in a ThermoScientific Genesys 20 Spectrophotometer.

### B.5.3 Strains

All strains used in this study are derived from wild type *E. coli* K-12 strain NCM3722 [29] and are summarized in B.6. Titratable *dctA* expression strain was constructed as described previously [42]. In brief, the region containing the Kanamycin resistance gene *km* and *Pu* promoter was PCR amplified from plasmid pKDPu and integrated into the chromosome of *E. coli* strain NQ351 upstream of *dctA* (-1 to -182 bp relative to translational start point of *dctA*), by using the λ Red system [203]. The resulting *km-Pu-dctA* in above strain was transferred into strain NQ386 containing P<sub>Llac-O1</sub>-*xylR* by P1 transduction, resulting in strain NQ530. To construct titratable *lacZ* expression strain, *km-Pu-lacZ* in EQ40 was transferred into strain NQ386 by P1 transduction, resulting in strain NQ537. Strains NQ381 and NQ399 are described in Ref. [42]. A *dctA* knockout was transferred from JW3496-1 to NCM3722 via P1 transduction to yield strain NQ1324.

### B.5.4 β-galactosidase quantification

The β-galactosidase quantification is based on the Miller assay [142] and used as described in Ref. [42].

### B.5.5 Total RNA quantification

The RNA quantification method is based on the method used by [204] with modifications as described previously [42].

### B.5.6 Total protein quantification

Total protein was quantified using commercial microBCA assay. In summary, 1ml samples were collected via centrifugation and stored at  $-80^{\circ}\text{C}$  until the analysis. For the analysis, cells were washed again and resuspended in  $\text{N}^{-}\text{C}^{-}$  medium and diluted 1:10.  $200\ \mu\text{l}$  of diluted sample and  $200\ \mu\text{l}$  of microBCA working reagent were incubated at  $60^{\circ}\text{C}$  in a water bath. After one hour, samples were put on ice, cell debris was removed via centrifugation and absorbance at 592 nm was recorded. Each analysis was calibrated individually using bovine albumin serum (BSA) standards.

### B.5.7 Dry mass quantification

150 ml cell culture was grown in baffled 250 ml flasks to an optical density ( $\text{OD}_{600}$ ) of about 0.5 at  $37^{\circ}\text{C}$  in a water-bath shaker. Triplicates of 50 ml cell culture were subsequently collected, cooled by shaking in an ice-water bath, and concentrated via centrifugation. Supernatants were recorded at every step and subtracted from the  $\text{OD}_{600}$  reading. The resulting pellet was transferred to 1.5 ml tubes and dried at  $80^{\circ}\text{C}$  overnight. The resulting weight of the pellet was determined with a high precision balance.

### B.5.8 Growth transition mass spectrometry (MS) protocol

#### MS sample collection

We used quantitative mass spectrometry to analyze the kinetic series of the up- and down-shift of Figs. 3.1 and 3.2. Over approximately two doublings we collected 2 pre-shift and 6 logarithmically-spaced post-shift samples for each kinetic transition, each containing  $1\ \text{OD}_{600} \times \text{ml}$  total biomass (centrifugation at 17000 g for 2 min). To enable light/heavy relative quantitation using mass spectrometry, we prepared a  $^{15}\text{N}$  stable-isotope labeled reference containing 1:1 w/w mixture of steady state glucose and succinate-minimal medium cultures grown in the presence of  $^{15}\text{NH}_4\text{Cl}$ .

After resuspension in pure water,  $100\ \mu\text{l}$  of the mixed  $^{15}\text{N}$  reference containing  $1\ \text{OD}_{600} \times \text{ml}$  cell biomass was added to each sample cell pellet previously stored frozen at  $-20^{\circ}\text{C}$ . Subsequent sample processing, including TCA-precipitation, cysteine reduction, alkylation, tryptic digestion, and desalting procedures were performed as previously described [41].

#### MS data acquisition

Tryptic peptides were separated on an Eksigent NanoLC Ultra system coupled to a Sciex 5600 TripleTOF system and analyzed in data-dependent shotgun mode (250 ms MS1 scan, followed by 40 cycles of 150 ms MS2 scans) [41]. Each sample was injected twice, yielding two technical replicates.

#### MS data processing

As in Ref. [41], vendor WIFF-format instrument data files were converted to profile and centroid MZML formats using Sciex software. Using the Trans-Proteomic Pipeline [205] centroided mzML files were converted to mzXML and searched using X!Tandem [206] against a custom *E. coli*

database (derived from UniProt organism 83333). The MS2 search results were combined into raw and consensus spectral libraries using SpectraST.

### MS data quantitation

MS1 intensity envelopes containing light  $^{14}\text{N}$ - and heavy  $^{15}\text{N}$ -labeled ions were fit using a least-squares Fourier transform convolution algorithm [44] implemented using isodist [207] as implemented in the Perl program massacre [208]. Relative  $^{14}\text{N}/^{15}\text{N}$  ratios were corrected for unbalanced  $^{15}\text{N}$ -reference pipetting by the quotient of the cumulative light (sample) and heavy (reference) X!Tandem spectral counts for *E. coli* peptides on a per-sample basis. Protein absolute abundances was estimated by spectral counting X!Tandem peptide-spectrum matches.

## B.5.9 Pulse-labeling MS Protocol

### MS sample collection

Cells were grown in  $\text{N}^- \text{C}^-$  medium with 10 mM  $^{14}\text{NH}_4\text{Cl}$  as the sole source of nitrogen. At the time of glucose exhaustion (downshift) and gluconate addition (upshift), cells were  $^{15}\text{N}$ -isotopically labelled by adding a pulse of  $^{15}\text{NH}_4\text{Cl}$  to 10 mM. The pulse allows the differentiation of protein made pre-shift ( $^{14}\text{N}$ ) from protein made post-shift (50%  $^{15}\text{N}$ ). We collected 2 pre-shift and 6 post-shift samples (1  $\text{OD}_{600} \times \text{ml}$  total biomass) for each series. A  $^{15}\text{N}$ -isotopically-enriched reference was prepared as a 1:1 w/w mixture of steady-state succinate- and glucose minimal-medium cultures grown in the presence of  $^{15}\text{NH}_4\text{Cl}$  and added to each sample as above.

### MS data acquisition and processing

Performed as described above.

### MS data quantitation

MS1 intensity envelopes containing  $^{14}\text{N}$ -labelled (pre-shift) ions, 50%  $^{15}\text{N}$  (post-shift) ions, and 100%  $^{15}\text{N}$ -labelled (constant reference) ions were quantified using isodist [207] to fit a three-species model including the 50%  $^{15}\text{N}$ -labelled envelope.

## B.5.10 Data analysis

### Expression matrices

For each upshift and downshift, the time series of expression data can be represented in the form an expression matrix  $E_{m,n}$ , with the time series ( $n = 1 \dots 8$ ) along the columns, and number of proteins,  $m$ , as rows.

### Sector affiliation

Proteins previously classified to increase, decrease or show no response under carbon limitation [44] were classified as the  $\text{C} \uparrow$ ,  $\text{C} \downarrow$  and  $\text{C}^-$  sectors. 24 proteins not detected by Hui et al [44], were classified according to the nearest distance of their linear response (average of both upshift and downshift) and the average linear response of proteins belonging to each sector.

### Relative expression data

Data shown in Fig. 3.13A uses relative expression data, obtained as described in “Quantitative Mass Spectrometry” section of the Methods, normalized to the pre-shift expression data (average of one data point at  $t = -15$  min, and a second data point immediately before the shift). If both pre-shift entries were empty, data could not be normalized and was removed from the analysis. Additionally, to focus on high-quality expression data, rows (protein) with more than four empty entries are removed, yielding a total of  $m = 647$  proteins. Data was  $\log_2$  transformed and plotted as a heat map in Fig. 3.13A. Raw data is available upon request.

### Sectors and protein groups

Data shown in Fig. 3.13B and C uses absolute mass fractions of proteins, obtained as described above in “Quantitative Mass Spectrometry”. Single protein data is available upon request.. The abundance of a sector  $X$  at time entry  $n$ ,  $\phi_{X,n}$ , was calculated by summing protein expression  $p_{m,n}$  over all entries  $m$ , under the condition that protein  $m$  is element of the sector  $X$ ,

$$\phi_{X,n} = \sum_{\substack{m=1 \\ m \in X}}^{1583} p_{m,n} \quad (\text{B.67})$$

and is provided in Table B.8. Protein groups were calculated analogously to the protein sectors, with the mass fraction of all protein groups is approximately 60% of the proteome. Data is provided in Table B.9. Classifications of proteins (sectors and groups) are provided upon request.

## B.6 Supplementary Figures

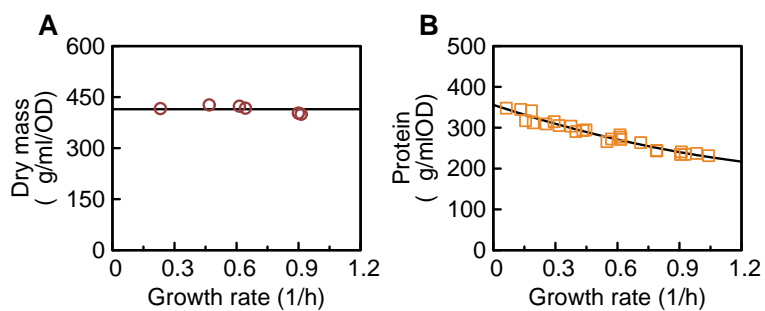


**Figure B.9:** Dry mass and protein mass during steady state growth. **(A)** Dry mass per optical density  $OD_{600}$  is independent of the growth rate in the investigated conditions with an average of  $414 \mu\text{g}$  dry weight per  $\text{ml} \times OD_{600}$  (black line). **(B)** Protein mass per optical density  $OD_{600}$  (orange squares) shows a slight dependence on growth rate (black line: quadratic fit), in accordance with the cell's increase of RNA and DNA at higher growth rates [32]. Since the change is small in the range of growth rates of the up- and downshifts presented in this paper, we take the conversion from dry mass to total protein to be constant throughout the shifts the presented in this paper. All data shown in Table B.1 and Table B.2.

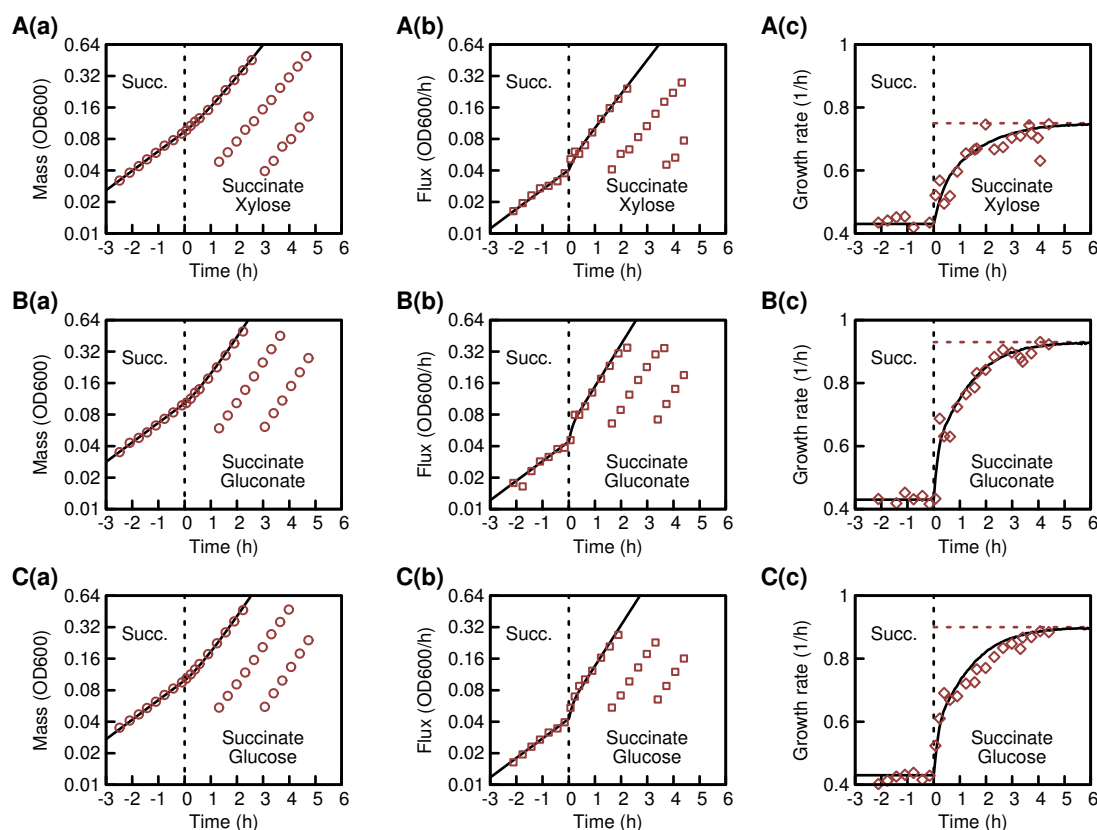


**Figure B.10: Serial dilution experiments.** At  $t = 0$  a second, subsequently co-utilized carbon substrate was added: (A) 0.2% xylose, (B) 0.2% gluconate or (C) 0.2% glucose. First column, (a), shows optical density  $OD_{600}$ , second column, (b), the derivative of  $OD_{600}$ , and the third column, (c), shows growth rate  $\lambda(t) = J(t)/M(t)$ . Shortly after the upshift the cell culture was diluted 4 and 16 fold in fresh medium, grown in parallel to the original culture and optical density was recorded for the diluted cultures once they reached an optical density of around 0.05. As growth rate is independent of the cell density, data from the original and the diluted cultures collapse, showing that for long times growth rate indeed reaches its final level (dashed line). Theory lines for  $M(t)$ ,  $J(t)$  and  $\lambda(t)$  were calculated using Eq. (B.41), Eq. (B.35) and Eq. (B.42) using the initial condition Eq. (B.18) for upshift without pre-expression. Initial and final growth rates were measured during steady state growth on the respective carbon substrates and are shown in Table B.1 and Table B.7.

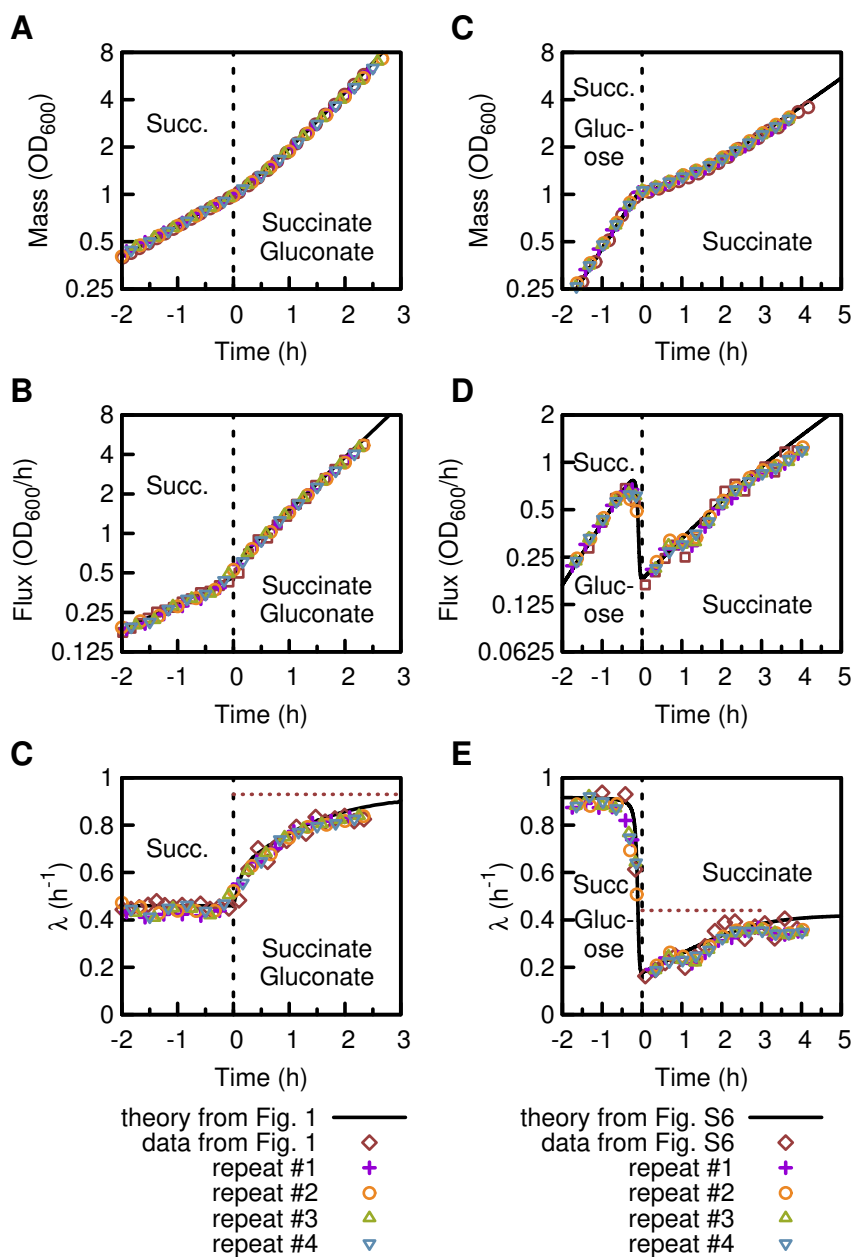


**Figure B.11:** Repeatability. Biomass, flux and growth rate for (A-C) the upshift from Fig. 3.1 and (D-F) for the diauxic shift shown in Fig. 3.2. Theory and red data is identical to Fig. 3.1 and Fig. 3.2, respectively. Four independent repeats (purple, orange green and blue) are plotted on top of the previously shown data.

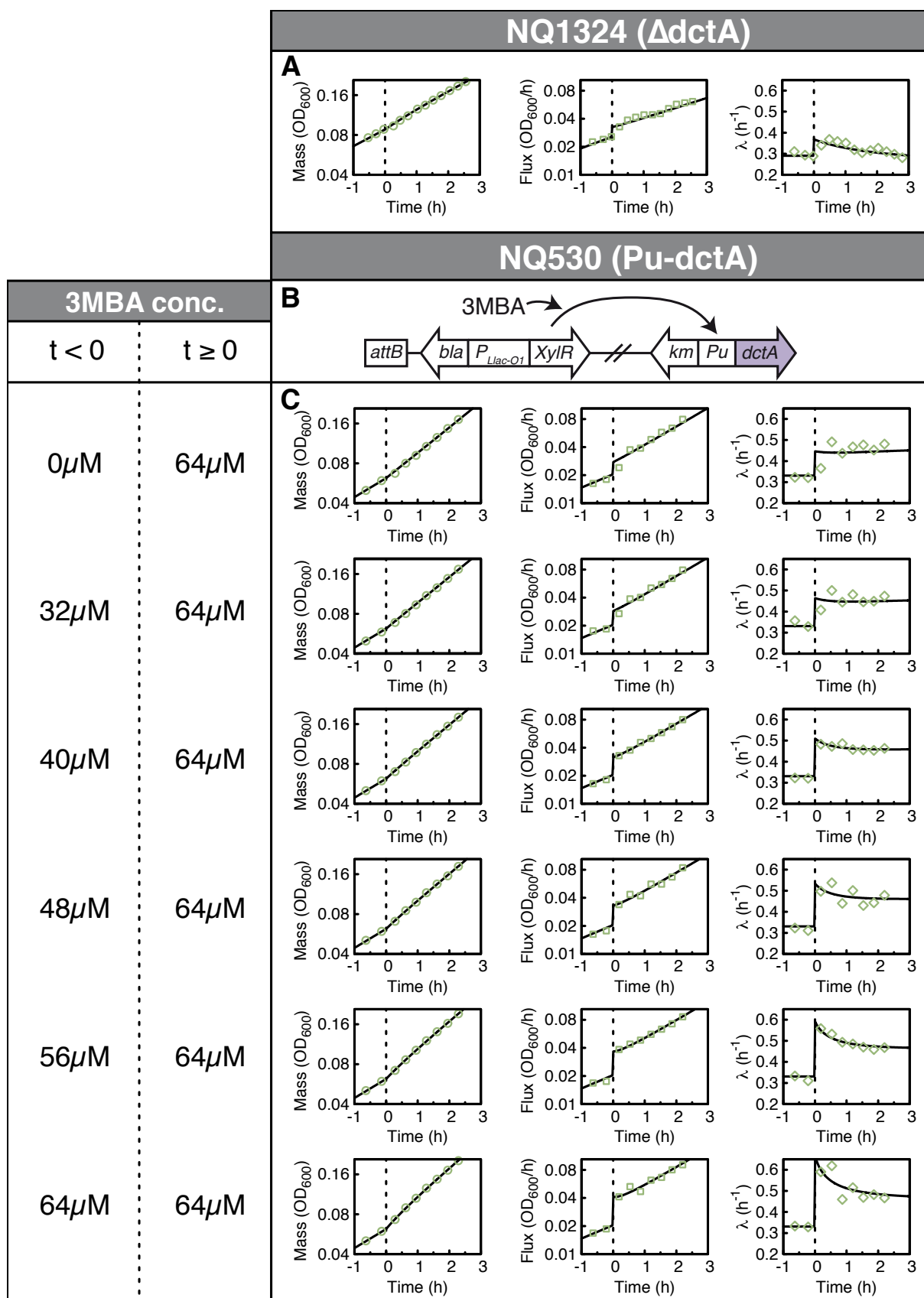


**Figure B.12:** Varying *dctA* pre-expression, extension of Figure 2 of the main text. Cells grown exponentially on N<sup>-</sup>C<sup>-</sup>, 20mM NH<sub>4</sub> and 0.1% mannose and supplemented with 20mM succinate at  $t = 0$ . Columns 1 to 3 show mass  $M$ , biomass flux  $J$  and growth rate  $\lambda$ . **(A)** NQ1324 ( $\Delta$ *dctA*) shows a small increase in growth rate upon upshift, despite the succinate transporter *dctA* being knocked-out. Final growth rate is not significantly increased over steady state growth on mannose alone. Steady state growth rate on Succinate alone was barely detectable for NQ1324 ( $\lambda \lesssim 0.02/\text{h}$ ). Fitting the theory yields  $\Delta\lambda = 0.078/\text{h}$ , as indicated with a triangle in Fig. 3.9E. **(B)** NQ530 (pu-*dctA*) titratable *dctA* expression strain. Promoter PLlac-O1 [209] (a promoter that is repressed by LacI but does not need CRP-cAMP for activation) drives *xylR* at the *attB* site. Pu promoter is activated by the regulator XylR upon induction by 3-methylbenzyl alcohol (3MBA). Different 3MBA concentrations are used to induce the Pu promoter, to control expression levels of *dctA*. **(C)** During pre-shift growth 3MBA concentration in the medium set from 0 to 64  $\mu\text{M}$  (from top to bottom), as indicated in the figure. 3MBA concentration is increased to 64  $\mu\text{M}$ , a common level for all upshifts, after the shift  $t \geq 0$ . The theory (black lines) is calculated using the initial and final growth rates  $\lambda_i^* = 0.33/\text{h}$  and  $\lambda_f^* = 0.46/\text{h}$  and fitting the initial condition  $\sigma(0)$ . This initial condition translates into  $\Delta\lambda$  shown in Fig. 3.9E via  $\Delta\lambda = \sigma(0)\phi_{\text{Rb}}(0) - \lambda_i^*$ , with the ribosome content  $\phi_{\text{Rb}}(0) = \phi_{\text{Rb},0} + \lambda_i^*/\gamma$ . The results of the fits are summarized in Table B.3 and shown in Fig. 3.9

## B.7 Supplementary Tables

**Table B.1:** Physiological parameters of wild type NCM3722 during steady state growth under carbon limitation. Ribosomal protein ( $M_{Rb}$ ) content is converted from RNA via a factor  $0.46 \mu\text{g R-protein}/\mu\text{g RNA}$  [34]. Data is visualized in Figs. 1.3 and 1.5.

Carbon substrate	IPTG (mM)	$\lambda$ (1/h)	Protein ( $\mu\text{g}/\text{mlOD}$ )	RNA ( $\mu\text{g}/\text{mlOD}$ )	<i>placZ</i> (MU)	$\phi_{Rb} = M_{Rb}/M_P$	Dry mass ( $\mu\text{g}/\text{mlOD}$ )
20mM Proline	1	0.13	345	46.9	-	0.103	-
0.1% Mannose	1	0.19	312	48.6	20177	0.118	416
0.2% Fructose	1	0.61	277	58.4	10756	0.160	423
20mM Gluconate	1	0.91	234	71.0	5772	0.230	400
0.2% Glucose	1	0.91	241	65.1	3636	0.205	403
0.2% Glycerol	1	0.62	271	56.5	11069	0.158	418
20mM Oxaloacetic acid (OAA)	1	0.79	244	70.3	7761	0.219	-
20mM OAA + 0.2% Glucose	1	1.04	232	71.3	2474	0.234	-
20mM OAA+ 0.2% Glycerol	1	0.93	235	70.5	4389	0.228	-
20mM Pyruvate	1	0.71	264	64.8	9364	0.187	-
20mM Succinate	1	0.45	294	56.8	14356	0.147	427
20mM Succ. + 20mM Gluconate	1	0.98	237	71.9	3790	0.230	-

**Table B.2:** Physiological parameters of titratable strains during steady state growth. Carbon uptake proteins *dctA* (Succinate, NQ530), *lacY* (Lactose, NQ381) and *glpFK* (Glycerol, NQ399) are under control of the *pu* promoter. Expression of the *pu* system is gradually induced by 3-methylbenzyl alcohol (3MBA). Ribosomal protein ( $M_{Rb}$ ) content is converted from RNA via a factor  $0.46 \mu\text{g R-protein}/\mu\text{g RNA}$  [34]. Data is visualized in Figs. 1.3 and 1.5.

Carbon substrate	Strain	IPTG (mM)	3MBA ( $\mu\text{M}$ )	$\lambda$ (1/h)	Protein ( $\mu\text{g}/\text{mlOD}$ )	RNA ( $\mu\text{g}/\text{mlOD}$ )	<i>placZ</i> (MU)	$\phi_{Rb} = M_{Rb}/M_P$
20mM Succinate	NQ530	1	25	0.06	348	45.3	19077	0.099
20mM Succinate	NQ530	1	50	0.16	317	44.7	18094	0.107
20mM Succinate	NQ530	1	100	0.25	309	49.4	17061	0.121
20mM Succinate	NQ530	1	500	0.40	290	52.9	12758	0.138
0.2% Lactose	NQ381	1	0	0.29	315	50.6	16093	0.122
0.2% Lactose	NQ381	1	25	0.43	293	54.9	12514	0.142
0.2% Lactose	NQ381	1	50	0.55	266	59.6	10194	0.170
0.2% Lactose	NQ381	1	100	0.61	283	61.6	9295	0.166
0.2% Lactose	NQ381	1	500	0.79	243	68.4	6399	0.213
0.2% Glycerol	NQ399	1	25	0.18	342	44.1	19499	0.098
0.2% Glycerol	NQ399	1	50	0.32	305	52.1	16688	0.130
0.2% Glycerol	NQ399	1	100	0.38	304	57.0	16468	0.143
0.2% Glycerol	NQ399	1	500	0.57	273	61.9	11308	0.173

**Table B.3:** Parameters defining Fig. 3.9. Upshifts were performed with NQ530 (pu-dctA), initial growth rate  $\lambda_i^* = 0.33/\text{h}$ , final growth rate  $\lambda_f^* = 0.45/\text{h}$ . 0.1mM was used to induce Plac driving *xylR*. The theory was fitted to the experimental data shown in Fig. 3.9 (from 0 3MBA and from 64  $\mu\text{M}$  3MBA) and intermediates shown in Fig. B.12, using the initial condition  $\lambda(0)$ , or equivalently  $\sigma(0) = \lambda(0)M(0)/M_{\text{RB}}(0)$ . Fitting results are summarized as  $\lambda = \lambda(0) - \lambda_i^*$  in the table and plotted in Fig. 3.9E versus the lacZ activity of strain NQ537 (pu-lacZ) at the corresponding pre-shift 3MBA levels (0 to 64  $\mu\text{M}$ ) and 0.1  $\mu\text{M}$  IPTG. Identical upshifts were performed with NQ1324 ( $\Delta$  dctA), yielding a non-zero  $\lambda$ .

Strain	Substrate 1	Substrate 2	IPTG (mM)	Pre-shift 3MBA( $\mu\text{M}$ )	Post-shift 3MBA ( $\mu\text{M}$ )	$\lambda$ (1/h)	Strain	<i>placZ</i> (MU)
NQ1324	0.1% Man.	20mM Succ.	0	0	0	0.078	-	-
NQ530	0.1% Man.	20mM Succ.	0.1	0	64	0.116	NQ537	292
NQ530	0.1% Man.	20mM Succ.	0.1	32	64	0.134	NQ537	2145
NQ530	0.1% Man.	20mM Succ.	0.1	40	64	0.180	NQ537	3396
NQ530	0.1% Man.	20mM Succ.	0.1	48	64	0.203	NQ537	5635
NQ530	0.1% Man.	20mM Succ.	0.1	56	64	0.261	NQ537	7816
NQ530	0.1% Man.	20mM Succ.	0.1	64	64	0.333	NQ537	12455

**Table B.4:** Parameters defining Fig. 3.11 of the main text. Strain NCM3722 grown exponentially on 0.2% Lactose and the combination 0.2% glucose and 0.2% lactose. Lac operon not artificially induced. For growth on glucose and lactose, lac expression is tightly repressed, yielding only 6% of the expression level on Lactose alone. Michaelis-Menten constant defining the uptake rate during glucose depletion according to Eq. (3.2) is shown in Table B.5.

Substrate	Strain	IPTG (mM)	Growth rate (1/h)	LacZ activity (MU)
0.2% Lactose	NCM3722	0	0.95	1557
0.2% Glucose + 0.2% Lactose	NCM3722	0	0.94	98

**Table B.5:** Michaelis-Menten constants of the substrates used in diauxic experiments in this paper. Data taken from the indicated references. These constants were used in Figs. 3.10 and 3.11

Substrate	Strain	$K_M$ ( $\mu\text{M}$ )	Ref
Gluconate	<i>E. coli</i>	212	[210]
Glycerol	<i>E. coli</i>	5.6	[211]
Glucose	<i>E. coli</i>	5	[131]

**Table B.6:** List of strains used in Chapter 3.

Name	Genotype	Ancestor	Function
NCM3722	-	-	Wild type K-12
NQ381	<i>attB::P<sub>Llac</sub>-O1-xylR, lacY::km-Pu-lacY</i>	NCM3722	Titratable <i>lacY</i>
NQ399	<i>attB::P<sub>Llac</sub>-O1-xylR, P<sub>glpFK</sub>::km-Pu</i>	NCM3722	Titratable <i>glpFK</i>
NQ530	<i>attB::P<sub>Llac</sub>-O1-xylR, PdctAK::km-Pu</i>	NCM3722	Titratable <i>dctA</i>
NQ537	<i>attB::P<sub>Llac</sub>-O1-xylR, PlacZ::km-Pu, lacY</i>	NCM3722	Titratable <i>lacZ</i>
NQ1324	<i>dctA</i>	NCM3722	<i>dctA</i> knockout

**Table B.7:** Growth rates of NCM3722 in N-C- medium supplemented with 20mM NH<sub>4</sub> and the carbon substrates S1 and S2 supporting growth rates  $\lambda_1$  and  $\lambda_2$  indicated in the first column. The combinations are co-utilized, with the co-utilization growth rate  $\lambda_{12}$  compared to predicted growth rates  $\lambda_{12}^{\text{th}}$  according to Eq. (B.6) and first calculated in Ref. [116]. A graphical comparison of the theoretical prediction and the data of this table are shown in Fig. B.2.

Substrate S1	Substrate S2	Strain	IPTG (mM)	$\lambda_1$ (1/h)	$\lambda_2$ (1/h)	$\lambda_{12}$ (1/h)	$\lambda_{12}^{\text{th}}$ (1/h)
20mM Succinate	0.2% Mannose	NCM3722	1	0.46	0.25	0.55	0.56
20mM Succinate	0.2% Arabinose	NCM3722	1	0.46	0.28	0.57	0.57
20mM Succinate	0.2% Xylose	NCM3722	1	0.46	0.58	0.75	0.73
20mM Succinate	0.2% Glycerol	NCM3722	1	0.46	0.62	0.78	0.75
20mM Succinate	0.2% Glucose	NCM3722	1	0.46	0.88	0.90	0.92
20mM Succinate	0.2% Gluconate	NCM3722	1	0.46	0.91	0.95	0.94
20mM Pyruvate	0.2% Arabinose	NCM3722	1	0.60	0.28	0.71	0.69
20mM Pyruvate	0.2% Xylose	NCM3722	1	0.60	0.58	0.78	0.79
20mM Pyruvate	0.2% Glycerol	NCM3722	1	0.60	0.62	0.86	0.81
20mM Pyruvate	0.2% Gluconate	NCM3722	1	0.60	0.91	0.97	0.97

**Table B.8: Proteome sectors during growth shifts.** Absolute expression of proteins classified by Hui et al [44] to the same proteome sector are summed into proteome sectors and the kinetics shown. Table shows proteome sectors (in %) during upshift (succinate add gluconate, Fig. 3.1) and downshift (succinate-gluconate downshift, Fig. 3.2) and various time points (second header; units in hours). Data shown in Fig. 3.13B-C.

Type of shift	Time (h)	$C \downarrow$	$C \uparrow$	$C -$
downshift	-0.25	60.14	26.68	13.17
downshift	0	60.63	26.34	13.03
downshift	0.33	58.26	28.58	13.16
downshift	1	51.86	34.76	13.38
downshift	2	45.95	41.04	13.01
downshift	3	44.94	42.45	12.61
downshift	3.5	43.83	43.42	12.75
downshift	4	43.65	43.7	12.65
upshift	-0.25	42.91	44.27	12.82
upshift	0	43.54	43.71	12.75
upshift	0.25	45.56	41.25	13.19
upshift	0.5	46.34	40.84	12.82
upshift	1	49.35	37.45	13.2
upshift	1.5	52.28	34.47	13.25
upshift	2	53.01	33.27	13.72
upshift	2.33	53.74	32.33	13.93

**Table B.9: Proteome groups during growth shifts.** Absolute expression of proteins classified to belong to the same protein group are summed and the kinetics shown. Table shows proteome groups (in %) during upshift (succinate add gluconate, Fig. 3.1) and downshift (succinate-glucose downshift, Fig. 3.2) and various time points (second header; units in hours). Data shown in Fig. 3.13D.

Type of shift	Time (h)	Translation aff. apparatus	Amino acid synthesis	Catabolic	Glycolysis	Motility	synthesis	Ribosomes	TCA	tRNA synthesis
downshift	-0.25	7.25	15.31	6.67	4.98	2.22	3.27	12.30	5.35	3.24
downshift	0	7.31	15.86	6.528	4.95	2.20	3.40	12.44	5.55	3.19
downshift	0.33	6.98	14.65	7.34	4.914	1.74	2.98	11.77	5.49	3.28
downshift	1	6.34	13.18	9.15	4.31	1.49	2.77	9.49	6.16	2.75
downshift	2	5.37	11.20	11.81	4.03	1.72	2.78	7.53	7.36	2.72
downshift	3	5.65	10.08	11.63	3.65	2.64	2.91	8.44	8.21	2.71
downshift	3.5	5.76	10.01	12.27	3.78	2.92	2.90	7.59	8.34	2.59
downshift	4	5.31	9.65	11.53	3.43	3.83	2.71	8.34	8.09	2.79
upshift	-0.25	5.71	9.20	10.19	3.35	4.55	2.68	8.71	9.76	2.61
upshift	0	5.71	9.08	10.02	3.44	4.87	2.68	9.12	9.38	2.52
upshift	0.25	5.98	9.94	9.26	3.56	3.87	2.94	9.6	9.56	2.62
upshift	0.5	6.12	9.89	9.10	3.71	3.56	2.87	10.36	9.41	2.75
upshift	1	6.47	11.36	8.57	3.70	3.56	3.12	10.29	8.21	2.97
upshift	1.5	6.53	12.01	7.54	3.96	3.56	3.01	11.95	7.33	2.94
upshift	2	6.69	12.61	7.51	4.33	3.38	3.1	11.11	6.65	3.06
upshift	2.33	6.96	12.65	7.10	4.15	3.48	3.20	10.84	6.45	3.13

# Appendix C

## Death during carbon starvation

### C.1 Supplementary Materials and Methods

#### C.1.1 Culture medium

The culture medium used in this study is based on  $\text{N}^- \text{C}^-$ . The medium was supplemented with 20mM  $\text{NH}_4\text{Cl}$  as nitrogen source, and 5 mM glycerol as the sole carbon source. In addition, in Fig. 4.12, glycerol was substituted with other carbon substrates (in ascending order of growth rate), which were removed by centrifugation (at 6000 RCF for 3 minutes): 20 mM glutamate, 0.1% mannose, 20 mM acetate, 0.2% fructose, 0.2% glycerol, 0.2% glucose, 0.2% lactose, 0.2% glycerol + 0.2% casamino acid, and 0.2% glucose + 0.2% casamino acid. 1 mM IPTG was added to media when necessary to fully induce the native lac operon. All chemicals were purchased from Carl Roth, Karlsruhe, Germany. Carbon free medium prepared in laboratories are prone carbon contamination and are known to support slow growth of a small population [106, 134, 212]. Carbon free medium of this work,  $\text{N}^- \text{C}^- + 20 \text{ mM } \text{NH}_4\text{Cl}$ , supported growth of about  $10^4$  CFU/ml.

#### C.1.2 Growth procedure

Growth was carried out as described in Section B.5. The limiting nutrient in the growth medium, 5 mM glycerol, is depleted at an optical density ( $\text{OD}_{600}$ ) of around 0.5, and a cell density of about  $5 \cdot 10^8$  CFU/ml. Due to the high affinity of about 5  $\mu\text{M}$  [211], glycerol is depleted fast. Due to the absence of acetate excretion, of this strain in this medium [82], no significant amount of metabolizable waste products remained in the medium. Alternative to inducing starvation by glycerol depletion, cells can be washed by centrifugation with no significant differences in the death rate.

For small culture volumes, 5 ml of experimental culture were grown in 20 mm  $\times$  150 mm glass test tubes (Fisher Scientific, Hampton, NH, USA) with disposable, polypropylene Kim-Kap closures (Kimble Chase, Vineland, NJ, USA). Larger volumes, 25, 50 and 100 ml were grown in 125, 250 and 500 ml baffled Erlenmeyer flasks (Carl Roth), respectively, and Kim-Kap closures. All cultures were grown in a shaking water bath (WSB-30, Witeg, Wertheim, Germany) with water bath preservative (Akasolv, Akadia, Mannheim, Germany).

To measure growth, at each time point a 200  $\mu\text{l}$  sample was extracted and optical density was measured using a 1 mm path length Sub-Micro Cuvette (Starna, Ilford, United Kingdom) at 600 nm in a Spectrophotometer (Genesys 20, ThermoScientific, Waltham, MA, USA).

### C.1.3 Starvation

Viability was measured by plating on LB agar and counting the colony forming units (CFU). Samples were diluted in fresh  $\text{N}^- \text{C}^-$  without carbon substrate and spread on LB agar using Rattler Plating Beads (Zymo Research, Irvine, CA, USA). LB agar was supplemented with 25  $\mu\text{g}/\text{ml}$  2,3,5-triphenyltetrazolium chloride to stain colonies and increase contrast for automated colony counting (Scan 1200, Interscience, Saint-Nom-la-Bretche, France) of 100-200 colonies per petri dish (92 x 16 mm, Sürstedt, Nambrecht, Germany). Staining or automation of counting had no significant effect on viability measurements or accuracy, compared to unstained, manually counted samples (<1% systematic error).

Starvation in the microfluidic chamber, Fig. 4.3A-C was performed in the absence of flow. Cells after entry to starvation were loaded into the device, in the presence of propidium iodide, which measures loss of membrane integrity.

### C.1.4 Staining

Established [213], commercial BacLight<sup>®</sup> LIVE/DEAD (Thermo Fisher Scientific Inc., Waltham, Massachusetts, USA) staining was used when cells were microscopically imaged, according to manufactures specifications.

### C.1.5 Strains

All strains used in this study are derived from wild type *E. coli* K-12 strain NCM3722 [29]. *rpoS* knockout was transferred from JW5437-1 to NCM3722 via P1 transduction to yield strain NQ1191.

## C.2 Supplementary Figures

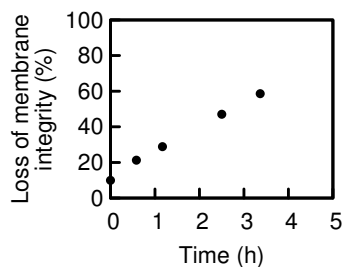


**Figure C.1: Loss of membrane integrity after UV-sterilization.** Cells shortly after entry to starvation were stained using Live/Dead stain, see Section C.1 and counted manually. After about 2-3 h half of the population has lost its membrane integrity.

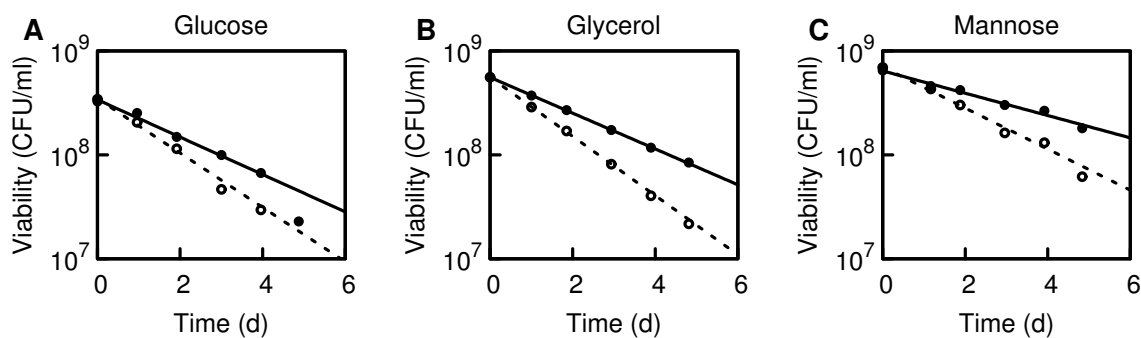


**Figure C.2: Exponential decay in other environments and strains.** Wild-type (closed symbols) and  $\Delta rpoS$  knock-out mutants (open symbols) were grown on different carbon substrates at different growth rates (A: glucose, 0.91/h, B: glycerol 0.70/h, and C: mannose 0.3/h). Viability was recorded by plating (CFU/ml). In all experiments cells follow an exponential decay (lines) with growths increasing with increasing growth rate, and under  $rpoS$  knock-out, see Fig. C.2. Data taken by Elena Biselli (TUM, Germany).



# Appendix D

## Preventing systemic spread of pathogens

### D.1 Supplementary Material and Methods

#### D.1.1 Animals

Male C57BL/6J mice were purchased from Charles River (Sulzfeld, Germany). All experiments were performed using mice at the age of 8 to 12 weeks. Animals were housed under conventional conditions with free access to food and water. The experiments were performed according to the German legislation for the protection of animals and approved by the local government authorities.

#### D.1.2 Reagents

Lipopolysaccharide (LPS, from *Escherichia coli* O111:B4; 10 ng intrascrotally (i.s.); Sigma-Aldrich, Schnellendorf, Germany) was used to induce inflammation of the cremaster muscle. Anti-GPIIb $\alpha$ /CD42b monoclonal antibodies (mAb; clone Xia.B2; 50  $\mu$ g i.v.; 48 h, 24 h, and 6 h prior to induction of inflammation; emfret Analytics, Eibelstadt, Germany) was used for the depletion of platelets. Anti-Ly-6G mAb (clone 1A8; 150  $\mu$ g intravenously (i.v.); 24 h and 6 h prior to induction of inflammation; BD Biosciences, San Jose, CA, USA) was used for the depletion of neutrophils. Microvascular thrombus formation was analyzed upon administration of heparin (500 IU intraarterially (i.a.); 10 min prior to induction of thrombosis; ratiopharm GmbH, Ulm, Germany), GPIIb $\alpha$  blocking antibody Fab' fragments (Xia.B2; 2.5 mg/kg, p0p/B, i.a.; 10 min prior to induction of thrombosis; emfret Analytics), a non-peptic GPIIb/IIIa inhibitor (GR144053 trihydrochloride; 10 mg/kg i.a.; 10 min prior to induction of thrombosis; R&D Systems, Lille, France), anti-vWF polyclonal Ab (100  $\mu$ g in 100  $\mu$ l PBS i.a.; 10 min prior to induction of thrombosis; Dako Deutschland GmbH, Hamburg, Germany), anti-CD40 mAb (clone 1C10; 50  $\mu$ g in 100  $\mu$ l PBS i. a.; 10 min prior to induction of thrombosis; eBiosciences, San Diego, CA, USA), anti-CD40L/CD154 mAb, anti-CD62P mAb (clone RB40.34; 50  $\mu$ g in 100  $\mu$ l PBS i.a.; 10 min prior to induction of thrombosis; BD Bioscience), anti-CD11b mAb (clone M1/70; 50  $\mu$ g in 150  $\mu$ l saline; BioLegend, San Diego, CA, USA), DNase I (RNase free; 100 U per mouse; i.a.; 4 h and 10 min prior to induction of thrombosis; Thermo Fisher Scientific, MA, USA), or appropriate vehicle/control antibodies. Neutrophils were visualized *in vivo* by an anti-Ly6G mAb (clone 1A8; PE-labeled; 5  $\mu$ g in 100  $\mu$ l PBS i. a.; BD Biosciences). Platelets were visualized *in vivo* by an anti-GPIIb $\beta$  derivat (X-649; DyLight 649-labeled; 5  $\mu$ g in 100  $\mu$ l PBS i. a.; emfret Analytics).

### D.1.3 In vivo microscopy on the mouse cremaster muscle

#### Surgical procedure

The surgical preparation of the mouse cremaster muscle was performed as originally described by Baez (31) with minor modifications. Mice were anesthetized using a ketamine/xylazine mixture (100 mg/kg ketamine and 10 mg/kg xylazine), administered by intraperitoneal (i.p.) injection. The left femoral artery was cannulated in a retrograde manner for administration of microspheres/bacteria, antibodies, or inhibitors. The right cremaster muscle was exposed through a ventral incision of the scrotum. The muscle was opened ventrally in a relatively avascular zone, using careful electrocautery to stop any bleeding, and spread over the pedestal of a custom-made microscopy stage. Epididymis and testicle were detached from the cremaster muscle and placed into the abdominal cavity. Throughout the procedure as well as after surgical preparation during in vivo microscopy, the muscle was superfused with warm buffered saline.

#### Phototoxic injury

Microvascular thrombus formation was induced by phototoxic injury as described before (32). For this purpose, animals received an i.a. injection of a FITC-dextran solution (150 kDa, 2,5 %, 6 ml/kg bodyweight, Sigma-Aldrich). 5 min later, the vessel of interest (300  $\mu\text{m}$  in length) was exposed to continuous epi-illumination using the FITC filter cube and appropriate illumination ( $\lambda=488$  nm). To assure intergroup comparability, the mean fluorescence intensity was determined in each of the analyzed vessels immediately after onset of light exposure.

#### In vivo microscopy

The setup for *in vivo* microscopy was centered around an Olympus BX 50 upright microscope (Olympus Microscopy, Hamburg, Germany), equipped for stroboscopic fluorescence epi-illumination microscopy. Light from a 75-W xenon source was narrowed to a near-monochromatic beam of a wavelength of 700 nm by a galvanometric scanner (Polychrome II, TILL Photonics, Graefelfing, Germany) and directed onto the specimen via a FITC filter cube equipped with dichroic and emission filters (DCLP 500, LP515, Olympus). Microscopy images were obtained with Olympus water immersion lenses [60x/numerical aperture (NA) 0.9, 20x/NA 0.5, and 10x/NA 0.3] and recorded with an analog black-and-white charge-coupled device (CCD) video camera (Cohu 4920, Cohu, San Diego, CA, USA) and an analog video recorder (AG-7350-E, Panasonic, Tokyo, Japan).

To visualize the behavior of leukocytes and platelets during microvascular thrombus formation, selected experiments were performed using an *in vivo* microscopy setup centered around an AxioTech-Vario 100 Microscope (Zeiss MicroImaging GmbH, Goettingen, Germany), equipped with a Colibri LED light source (Zeiss MicroImaging GmbH) for fluorescence epi-illumination microscopy. Light was directed onto the specimen via filter set 62 HE (Zeiss MicroImaging GmbH) fitted with dichroic and emission filters [TFT 495 + 610 (HE); TBP 527 + LP615 (HE)]. Microscopy images were obtained with an AxioCam Hsm digital camera using a 20x and 40x water immersion lenses (0.5 NA, Zeiss MicroImaging GmbH). The images were processed with AxioVision 4.6 software (Zeiss MicroImaging GmbH).

#### Quantification of leukocyte kinetics and microhemodynamic parameters

*In vivo* microscopy records were analyzed offline using ImageJ (National Institutes of Health, Bethesda, MD) and Cap-Image (Dr. Zeintl, Heidelberg, Germany) image analysis software. The onset of thrombus was defined as the first observation of endothelially adherent platelets during

thrombus formation. Cessation of thrombus formation was defined as the complete occlusion of the vessel segment with flow cessation for >60s. The cut off time for thrombus formation in venules was 1500s, in arterioles 2700s. Firmly adherent leukocytes were determined as those resting in the associated blood flow for 30s and related to the luminal surface per 100  $\mu\text{m}$  vessel length. Transmigrated leukocytes were counted in regions of interest (ROI), covering 75  $\mu\text{m}$  on both sides of a vessel over 100  $\mu\text{m}$  vessel length. By measuring the distance between several images of one fluorescent bead under stroboscopic illumination, centerline blood flow velocity was determined. From measured vessel diameters and centerline blood flow velocity, apparent wall shear rates were calculated, assuming a parabolic flow velocity profile over the vessel cross-section.

### Experimental protocols and groups

Three postcapillary venules (diameter: 30-50 $\mu\text{m}$ ) and one arteriole (diameter: 20-35  $\mu\text{m}$ ) were randomly chosen in a central area of the spread-out cremaster muscle. In a first set of experiments, thrombus formation in these microvessels was analyzed upon phototoxic injury 6 h after i.s. injection of PBS or LPS (n=9 per group). In separate experiments, the effect of heparin (administration 10 min prior to phototoxic injury), platelet depletion, or neutrophil depletion on microvascular thrombus formation was analyzed 6 h after i.s. injection of PBS or LPS (n=3-4 per group). In further experiments, the role of various adhesion/signaling molecules potentially mediating interactions of endothelial cells, leukocytes, and/or platelets for venular thrombus formation was analyzed upon application of blocking mAb or inhibitors (administration 10 min prior to phototoxic injury) 6 h after i.s. injection of LPS (n=4 per group). Finally, deposition of fluorescence-labeled micro-beads or non-pathogenic *E. coli* bacteria (K12 strain; stained with Hoechst (1:500);  $10^9$  in 100  $\mu\text{l}$  PBS i.a.) in venular thrombi was analyzed upon phototoxic injury 6 h after i.s. injection of PBS or LPS (n=3 per group).

After *in vivo* microscopy, blood samples were collected by puncturing the inferior *vena cava* for the determination of systemic leukocyte and platelet counts using a ProCyte Dx cell counter (IDEXX Laboratories, Westbrook, ME, USA). Anesthetized animals were then killed by bleeding to death.

#### D.1.4 Microfluidic device

##### Fabrication of microfluidic devices

Microfluidic devices were fabricated by molding silicone elastomer (PDMS Silygard 184, Dow Corning; Midland, MI, USA) to master molds constructed by photolithography on silicon wafers. The mold consisted of two layers of SU-8 photoresist (MicroChem Corp., Westborough, MA, USA), created by two superimposed patterns. A 32  $\mu\text{m}$  thick layer of the channel layout was superimposed with an 8 $\mu\text{m}$  thick layer of the channel layout with cut-outs of 'bump structures', yielding a negative mold with 40  $\mu\text{m}$  thick channels and 8  $\mu\text{m}$  thick bumps. The bump diameter was chosen to be 8  $\mu\text{m}$ , resulting in cylindrical bumps with blunt edges due to photolithography limitation. The channel width was chosen to be 40  $\mu\text{m}$ , resulting in a quadratic 40 x 40  $\mu\text{m}$  cross-section. The channel layout consisted of four channels of different bump densities (0, 10, 25, and 50 bumps per  $10^4 \mu\text{m}^2$ ), fed from the same source and leading into the same sink. Bumps were randomly placed at non-over-lapping positions throughout the channel using a standard MATLAB random number generator routine. A serpentine (40  $\mu\text{m}$  x 40  $\mu\text{m}$  x 16 mm) between channels and sink was designed as hydrodynamic resistance to reduce the flow rates to physiological conditions.

The PDMS was mixed according to the manufacturer's instructions, poured onto the wafer and cured for one hour at 80 °C. The cured PDMS was separated from the wafer and inlets and outlets were punched. The chip was then cleaned, exposed for 30s to oxygen plasma (Diener electronics GmbH+Co. KG, Ebhausen, Germany) and irreversibly bond to a microscope slide.

### D.1.5 Microfluidics experiments

#### Fluorescence microscopy

Microscopy was performed using a Nikon Ti-E inverted microscope system with automated stage and shutters controlled by NIS-Elements (Nikon, Tokyo, Japan). Five positions spanning a total of 40  $\mu\text{m}$  x 830  $\mu\text{m}$  were recorded in each of the four channels every minute using a CFI P-Apo DM 100x objective and a SCMOS camera (Zyla-5.5, Andor, Belfast, Northern Ireland). Platelets were labeled with anti-GPIIb $\beta$  derivate (X-649; emfret Analytics, Germany) and fluorescence emission was recorded.

#### Experimental protocol

Microfluidic chips were flooded and flushed with phosphate-buffered saline (PBS) before microfluidic flow experiments. A reservoir of heparinized diluted mouse whole blood was connected to the microfluidic chip by silicone tubing and directed into the inflow of the device. Four channels with different densities of bump structures (as described above) were simultaneously perfused with the diluted whole blood and the flow velocity was controlled by adjusting the hydrostatic pressure. Blood flow velocity was kept in range of physiological flow velocities in mouse venules. Blood was diluted 10-fold with PBS for time-lapse microscopy in order to avoid that the high density of cells obstructed the microscopy light passing through the cross-section of the channel. During perfusion, time-lapse microscopy was performed on the four channels to visualize capture, adhesion, and aggregation of platelets. After 10 minutes of perfusion, the number of adherent platelets was counted.

### D.1.6 Fluid dynamics simulation

The fluid was simulated in a 2D, 160  $\mu\text{m}$  x 40  $\mu\text{m}$ , geometry, using commercial finite element simulation tools (COMSOL Multiphysics, Stockholm, Sweden). Due to the low Reynolds numbers found in the microvasculature, we assumed laminar flow. The platelet was considered a discrete, inelastic object that due to its small size does not alter the fluid flow in its vicinity. This allows for calculation of the fluid flow first, and afterwards using the solution to solve the translational and rotational movement of the platelet. Translation was calculated assuming Stokes drag, using the fluid velocity at the center of mass of the platelet. Rotation was induced by choosing the rotational velocity such that the average torque along the surface of the platelet was zero. Both translational and rotational movements in this approximation do not alter the fluid flow, and were calculated using a custom-written MATLAB (Mathworks, Natick, MA, USA) script.

### D.1.7 Confocal microscopy

For the analysis of CD40, CD40L/CD154, or vWF expression in microvascular thrombi, mouse cremaster muscles were prepared (6 h after i.s. injection of 10 ng LPS diluted in 400  $\mu\text{l}$  PBS) and microvascular thrombus formation was induced by phototoxic injury as described above. Excised cremaster muscles were fixed in 4 % paraformaldehyde. Tissues were then blocked and permeabilized in PBS, supplemented with 10 % goat serum (Sigma Aldrich) and 0.5 % Triton X-100 (Sigma Aldrich). After incubation at 4C for 12 h with antibodies directed against GPIIb $\beta$

derivate (X-649; DyLight 488-labeled; emfret Analytics), Ly6G/C (GR-1; Alexa Fluor 647-labeled; Invitrogen), and CD40 (rat anti-mouse; eBiosciences), CD40L/CD154 (rat anti-mouse; BD Bioscience), or vWF (rabbit polyclonal; abcam), tissues were incubated were incubated with an Alexa Fluor 546-linked goat anti-rat antibody or an Alexa Fluor 546-linked goat anti-rabbit antibody for 180 min at room temperature. Immunostained tissues were mounted in PermaFluor (Beckmann Coulter, Fullerton, CA) on glass slides. Confocal z-stacks typically covering approximately 30  $\mu\text{m}$  (z-spacing 1.0  $\mu\text{m}$ ) were acquired using a Leica SP5 confocal laser-scanning microscopy (Leica Microsystems, Wetzlar, Germany) with an oil-immersion lens (Leica; 40x; NA 1.40).

### D.1.8 Statistics

Data analysis was performed with a statistical software package (SigmaStat for Windows; Jandel Scientific). The ‘t-test’ (two groups) or the ‘One-way ANOVA test’ followed by the ‘Dunnett test’ (> two groups) was used for the estimation of stochastic probability in intergroup comparisons. Mean values and SEM are given. P values < .05 were considered significant.

## D.2 Supplementary Figures

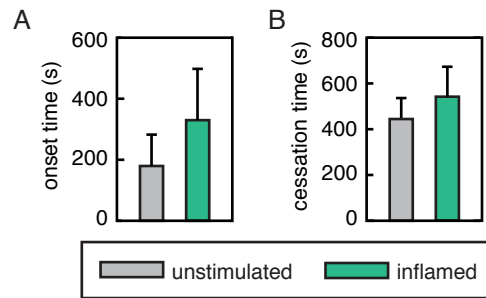


**Figure D.1: Thrombus formation in arterioles.** Thrombus formation in arterioles of the cremaster muscle of WT mice was induced by phototoxic injury as detailed in Section D.1.2. Panels show quantitative data for onset (A) and cessation (B) times in WT mice after intrascrotal injection of PBS or LPS (mean  $\pm$  SEM for n=4 per group). Data taken by Daniel Puhr-Westerheide (LMU, Germany).

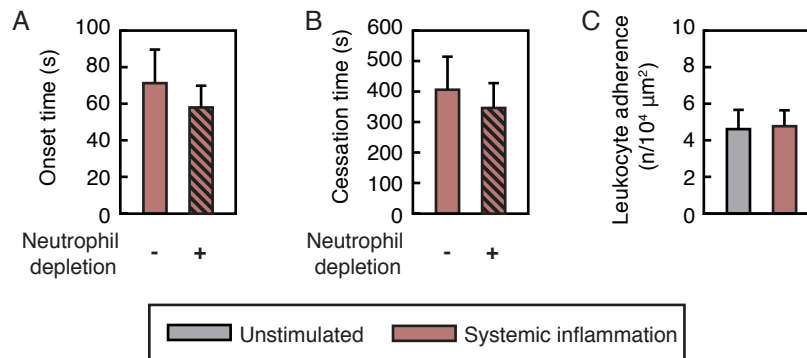


**Figure D.2: Microvascular thrombosis in early stages of endotoxemia.** Thrombus formation in venules of the cremaster muscle of WT mice was induced by phototoxic injury as detailed in Section D.1.3. Panels show quantitative data for onset (A) and cessation (B) times of thrombus formation 6 h after intra-peritoneal injection of LPS as well as the number of intravascularly adherent leukocytes 6 h after intra-peritoneal injection of PBS or LPS (meanSEM for n=4 per group). Data taken by Daniel Puhr-Westerheide (LMU, Germany).

# Bibliography

- [1] K. Gupta, T. M. Hooton, K. G. Naber, B. Wullt, R. Colgan, L. G. Miller, G. J. Moran, L. E. Nicolle, R. Raz, A. J. Schaeffer, *et al.*, “International clinical practice guidelines for the treatment of acute uncomplicated cystitis and pyelonephritis in women: a 2010 update by the infectious diseases society of america and the european society for microbiology and infectious diseases,” *Clinical infectious diseases*, vol. 52, no. 5, pp. e103–e120, 2011.
- [2] T. A. Russo and J. R. Johnson, “Medical and economic impact of extraintestinal infections due to escherichia coli: focus on an increasingly important endemic problem,” *Microbes and Infection*, vol. 5, no. 5, pp. 449–456, 2003.
- [3] J. B. Kaper, J. P. Nataro, and H. L. Mobley, “Pathogenic escherichia coli,” *Nature Reviews Microbiology*, vol. 2, no. 2, pp. 123–140, 2004.
- [4] J. D. van Elsas, A. V. Semenov, R. Costa, and J. T. Trevors, “Survival of escherichia coli in the environment: fundamental and public health aspects,” *The ISME journal*, vol. 5, no. 2, pp. 173–183, 2011.
- [5] G. T. Macfarlane and S. Macfarlane, “Human colonic microbiota: ecology, physiology and metabolic potential of intestinal bacteria,” *Scandinavian Journal of Gastroenterology*, vol. 32, no. sup222, pp. 3–9, 1997.
- [6] M. A. Savageau, vol. 122, p. 733. *The American Naturalist*, 1983.
- [7] S. Taheri-Araghi, S. D. Brown, J. T. Sauls, D. B. McIntosh, and S. Jun, “Single-cell physiology,” *Annual review of biophysics*, vol. 44, pp. 123–142, 2015.
- [8] L. K. Poulsen, F. Lan, C. S. Kristensen, P. Hobolth, S. Molin, and K. A. Krogh, “Spatial distribution of escherichia coli in the mouse large intestine inferred from rna in situ hybridization,” *Infection and immunity*, vol. 62, no. 11, pp. 5191–5194, 1994.
- [9] C. U. Rang, T. R. Licht, T. Midtvedt, P. L. Conway, L. Chao, K. A. Krogh, P. S. Cohen, and S. Molin, “Estimation of growth rates of escherichia coli bj4 in streptomycin-treated and previously germfree mice by in situ rna hybridization,” *Clinical and diagnostic laboratory immunology*, vol. 6, no. 3, pp. 434–436, 1999.
- [10] S. F. Phillips and J. Giller, “The contribution of the colon to electrolyte and water conservation in man,” *The Journal of laboratory and clinical medicine*, vol. 81, no. 5, pp. 733–746, 1973.
- [11] J. Cremer, I. Segota, C.-y. Yang, M. Arnoldini, J. T. Sauls, Z. Zhang, E. Gutierrez, A. Groisman, and T. Hwa, “Effect of flow and peristaltic mixing on bacterial growth in a gut-like channel,” *Proceedings of the National Academy of Sciences*, p. 201601306, 2016.

- [12] I. T. Kudva, K. Blanch, and C. J. Hovde, "Analysis of escherichia coli o157: H7 survival in ovine or bovine manure and manure slurry," *Applied and environmental microbiology*, vol. 64, no. 9, pp. 3166–3174, 1998.
- [13] H. Fukushima, K. Hoshina, and M. Gomyoda, "Long-term survival of shiga toxin-producing escherichia coli o26, o111, and o157 in bovine feces," *Applied and Environmental Microbiology*, vol. 65, no. 11, pp. 5177–5181, 1999.
- [14] S. E. Finkel, "Long-term survival during stationary phase: evolution and the gasp phenotype," *Nature Reviews Microbiology*, vol. 4, no. 2, pp. 113–120, 2006.
- [15] C. Zimmer, *Microcosm: E-coli and the New Science of Life*. Random House, 2012.
- [16] Z. D. Blount, "The unexhausted potential of e. coli," *Elife*, vol. 4, p. e05826, 2015.
- [17] B. S. Crick F.H., Barnett L. and W.-T. R.J., "General nature of the genetic code for proteins," *Nature*, vol. 192, pp. 1227 – 1232, 1961.
- [18] I. Lehman, M. J. Bessman, E. S. Simms, and A. Kornberg, "Enzymatic synthesis of deoxyribonucleic acid," *J. biol. Chem*, vol. 233, pp. 163–170, 1958.
- [19] A. Stevens, "Incorporation of the adenine ribonucleotide into rna by cell fractions from *E. coli* b," *Biochemical and biophysical research communications*, vol. 3, no. 1, pp. 92–96, 1960.
- [20] E. L. Ellis and M. Delbrück, "The growth of bacteriophage," *The Journal of general physiology*, vol. 22, no. 3, pp. 365–384, 1939.
- [21] A. Lwoff, "Lysogeny," *Bacteriological Reviews*, vol. 17, no. 4, p. 269, 1953.
- [22] F. Jacob, D. Perrin, C. Sánchez, and J. Monod, "L'opéron: groupe de gènes à expression coordonnée par un opérateur," *CR Acad. Sci. Paris*, vol. 250, pp. 1727–1729, 1960.
- [23] F. Jacob and J. Monod, "Genetic regulatory mechanisms in the synthesis of proteins," *Journal of molecular biology*, vol. 3, no. 3, pp. 318–356, 1961.
- [24] E. Englesberg, J. Irr, J. Power, and N. Lee, "Positive control of enzyme synthesis by gene c in the l-arabinose system," *Journal of Bacteriology*, vol. 90, no. 4, pp. 946–957, 1965.
- [25] S. Linn and W. Arber, "Host specificity of dna produced by escherichia coli, x. in vitro restriction of phage fd replicative form," *Proceedings of the National Academy of Sciences*, vol. 59, no. 4, pp. 1300–1306, 1968.
- [26] M. Meselson and R. Yuan, "Dna restriction enzyme from e. coli.," *Nature*, vol. 217, no. 5134, pp. 1110–1114, 1968.
- [27] B. J. Bachmann, "Derivations and genotypes of some mutant derivatives of escherichia coli k-12," *Escherichia coli and Salmonella: cellular and molecular biology*, 2nd ed. ASM Press, Washington, DC, pp. 2460–2488, 1996.
- [28] F. R. Blattner, G. Plunkett, C. A. Bloch, N. T. Perna, V. Burland, M. Riley, J. Collado-Vides, J. D. Glasner, C. K. Rode, and G. F. Mayhew, "The complete genome sequence of escherichia coli k-12," *science*, vol. 277, no. 5331, pp. 1453–1462, 1997.

- [29] E. Soupene, W. C. van Heeswijk, J. Plumbridge, V. Stewart, D. Bertenthal, H. Lee, G. Prasad, O. Paliy, P. Charernnoppakul, and S. Kustu, "Physiological studies of escherichia coli strain mg1655: Growth defects and apparent cross-regulation of gene expression," *Journal of Bacteriology*, vol. 185, no. 18, pp. 5611–5626, 2003.
- [30] J. Monod, "The growth of bacterial cultures," *Annual Review of Microbiology*, vol. 3, no. 1, pp. 371–394, 1949.
- [31] A. Campbell, "Synchronization of cell division," *Bacteriological Reviews*, vol. 21, no. 4, p. 263, 1957.
- [32] M. Schaechter, O. Maaløe, and N. O. Kjeldgaard, "Dependency on medium and temperature of cell size and chemical composition during balanced growth of salmonella typhimurium," *Microbiology*, vol. 19, no. 3, pp. 592–606, 1958.
- [33] S. Cooper, "The origins and meaning of the schaechter-maaloe-kjeldgaard experiments," *Journal of General Microbiology*, vol. 139, no. 6, pp. 1117–1124, 1993.
- [34] M. Scott, C. W. Gunderson, E. M. Mateescu, Z. Zhang, and T. Hwa, "Interdependence of cell growth and gene expression: Origins and consequences," *Science*, vol. 330, no. 6007, pp. 1099–1102, 2010.
- [35] F. C. Neidhardt and B. Magasanik, "Studies on the role of ribonucleic acid in the growth of bacteria," *Biochimica et Biophysica Acta*, vol. 42, pp. 99–116, 1960.
- [36] J. R. Warner, "The economics of ribosome biosynthesis in yeast," *Trends in Biochemical Sciences*, vol. 24, no. 11, pp. 437–440, 1999.
- [37] H. Bremer and P. P. Dennis, "Modulation of chemical composition and other parameters of the cell at different exponential growth rates," *EcoSal Plus*, vol. 1, no. 2, 2013.
- [38] J. Forchhammer and L. Lindahl, "Growth rate of polypeptide chains as a function of the cell growth rate in a mutant of escherichia coli 15," *Journal of Molecular Biology*, vol. 55, no. 3, pp. 563–568, 1971.
- [39] P. P. Dennis and H. Bremer, "Differential rate of ribosomal protein synthesis in escherichia coli b/r," *Journal of Molecular Biology*, vol. 84, no. 3, pp. 407–422, 1974.
- [40] S. Klumpp, M. Scott, S. Pedersen, and T. Hwa, "Molecular crowding limits translation and cell growth," *Proceedings of the National Academy of Sciences*, vol. 110, no. 42, pp. 16754–16759, 2013.
- [41] X. Dai, M. Zhu, M. Warren, R. Balakrishnan, V. Patsalo, H. Okano, J. R. Williamson, K. Fredrick, Y.-P. Wang, and T. Hwa, "Reduction of translating ribosomes enables escherichia coli to maintain elongation rates during slow growth," *Nature Microbiology*, vol. 2, p. 16231, 2016.
- [42] C. You, H. Okano, S. Hui, Z. Zhang, M. Kim, C. W. Gunderson, Y.-P. Wang, P. Lenz, D. Yan, and T. Hwa, "Coordination of bacterial proteome with metabolism by cyclic amp signalling," *Nature*, vol. 500, no. 7462, pp. 301–306, 2013.
- [43] M. Scott, S. Klumpp, E. M. Mateescu, and T. Hwa, "Emergence of robust growth laws from optimal regulation of ribosome synthesis," *Molecular Systems Biology*, vol. 10, no. 8, pp. 747–747, 2014.

- [44] S. Hui, J. M. Silverman, S. S. Chen, D. W. Erickson, M. Basan, J. Wang, T. Hwa, and J. R. Williamson, "Quantitative proteomic analysis reveals a simple strategy of global resource allocation in bacteria," *Molecular Systems Biology*, vol. 11, no. 2, pp. e784–e784, 2015.
- [45] F. J. Ryan, "Bacterial mutation in a stationary phase and the question of cell turnover," *Journal of General Microbiology*, vol. 21, no. 3, pp. 530–549, 1959.
- [46] A. Harrison, "The response of bacterium lactis aerogenes when held at growth temperature in the absence of nutriment: an analysis of survival curves," *Proceedings of the Royal Society of London B: Biological Sciences*, vol. 152, no. 948, pp. 418–428, 1960.
- [47] J. R. Postgate and J. R. Hunter, "The survival of starved bacteria," *Journal of General Microbiology*, vol. 29, no. 2, pp. 233–263, 1962.
- [48] A. Phaiboun, Y. Zhang, B. Park, and M. Kim, "Survival kinetics of starving bacteria is biphasic and density-dependent," *PLOS Computational Biology*, vol. 11, no. 4, p. e1004198, 2015.
- [49] M. Bergkessel, D. W. Basta, and D. K. Newman, "The physiology of growth arrest: uniting molecular and environmental microbiology," *Nature Reviews Microbiology*, vol. 14, no. 9, pp. 549–562, 2016.
- [50] R. Lange and R. Hengge-Aronis, "Identification of a central regulator of stationary-phase gene expression in escherichia coli," *Molecular microbiology*, vol. 5, no. 1, pp. 49–59, 1991.
- [51] A. Maciag, C. Peano, A. Pietrelli, T. Egli, G. De Bellis, and P. Landini, "In vitro transcription profiling of the  $\sigma_s$  subunit of bacterial rna polymerase: re-definition of the  $\sigma_s$  regulon and identification of  $\sigma_s$ -specific promoter sequence elements," *Nucleic acids research*, vol. 39, no. 13, pp. 5338–5355, 2011.
- [52] C. Peano, J. Wolf, J. Demol, E. Rossi, L. Petiti, G. De Bellis, J. Geiselmann, T. Egli, S. Lacour, and P. Landini, "Characterization of the escherichia coli  $\sigma_s$  core regulon by chromatin immunoprecipitation-sequencing (chip-seq) analysis," *Scientific reports*, vol. 5, p. 10469, 2015.
- [53] H. Merrikh, A. E. Ferrazzoli, A. Bougdour, A. Olivier-Mason, and S. T. Lovett, "A dna damage response in escherichia coli involving the alternative sigma factor, rpos," *Proceedings of the National Academy of Sciences*, vol. 106, no. 2, pp. 611–616, 2009.
- [54] H. E. Schellhorn and V. L. Stones, "Regulation of katf and kate in escherichia coli k-12 by weak acids," *Journal of bacteriology*, vol. 174, no. 14, pp. 4769–4776, 1992.
- [55] I. L. Jung and I. G. Kim, "Transcription of ahpc, katg, and kate genes in escherichia coli is regulated by polyamines: polyamine-deficient mutant sensitive to h<sub>2</sub>o<sub>2</sub>-induced oxidative damage," *Biochemical and biophysical research communications*, vol. 301, no. 4, pp. 915–922, 2003.
- [56] J. Jung, C. Gutierrez, and M. Villarejo, "Sequence of an osmotically inducible lipoprotein gene," *Journal of bacteriology*, vol. 171, no. 1, pp. 511–520, 1989.
- [57] R. Hengge-Aronis, "Signal transduction and regulatory mechanisms involved in control of the  $\sigma_s$  (rpos) subunit of rna polymerase," *Microbiology and Molecular Biology Reviews*, vol. 66, no. 3, pp. 373–395, 2002.

- [58] V. W. Soo and T. K. Wood, "Antitoxin *mqsA* represses curli formation through the master biofilm regulator *csgD*," *Scientific reports*, vol. 3, p. 3186, 2013.
- [59] R. E. Bishop, B. K. Leskiw, R. S. Hodges, C. M. Kay, and J. H. Weiner, "The entericidin locus of *Escherichia coli* and its implications for programmed bacterial cell death," *Journal of molecular biology*, vol. 280, no. 4, pp. 583–596, 1998.
- [60] S. E. Finkel and R. Kolter, "Evolution of microbial diversity during prolonged starvation," 1999.
- [61] Y. Rozen and S. Belkin, "Survival of enteric bacteria in seawater," *FEMS microbiology reviews*, vol. 25, no. 5, pp. 513–529, 2001.
- [62] C. A. Reeve, P. S. Amy, and A. Matin, "Role of protein synthesis in the survival of carbon-starved *Escherichia coli* K-12," *Journal of bacteriology*, vol. 160, no. 3, pp. 1041–1046, 1984.
- [63] P. M. Munro, M. J. Gauthier, V. Breittmayer, and J. Bongiovanni, "Influence of osmoregulation processes on starvation survival of *Escherichia coli* in seawater," *Applied and Environmental Microbiology*, vol. 55, no. 8, pp. 2017–2024, 1989.
- [64] E. A. Steinhaus and J. M. Birkeland, "Studies on the life and death of bacteria: I. the senescent phase in aging cultures and the probable mechanisms involved," *Journal of bacteriology*, vol. 38, no. 3, p. 249, 1939.
- [65] M. Zambrano, D. Siegele, M. Almiron, A. Tormo, and R. Kolter, "Microbial competition: *Escherichia coli* mutants that take over stationary phase cultures," *Science*, vol. 259, no. 5102, pp. 1757–1760, 1993.
- [66] O. Gefen, O. Fridman, I. Ronin, and N. Q. Balaban, "Direct observation of single stationary-phase bacteria reveals a surprisingly long period of constant protein production activity," *Proceedings of the National Academy of Sciences*, vol. 111, no. 1, pp. 556–561, 2014.
- [67] N. O. Kjeldgaard, O. Maaløe, and M. Schaechter, "The transition between different physiological states during balanced growth of *Salmonella typhimurium*," *Journal of General Microbiology*, vol. 19, no. 3, pp. 607–616, 1958.
- [68] O. Maaløe, "Regulation of the protein-synthesizing machinery—ribosomes, tRNA, factors, and so on," in *Biological regulation and development*, pp. 487–542, Springer, 1979.
- [69] M. Ehrenberg, H. Bremer, and P. P. Dennis, "Medium-dependent control of the bacterial growth rate," *Biochimie*, vol. 95, no. 4, pp. 643–658, 2013.
- [70] A. L. Koch, "Overall controls on the biosynthesis of ribosomes in growing bacteria," *Journal of theoretical biology*, vol. 28, no. 2, pp. 203–231, 1970.
- [71] P. P. Dennis and H. Bremer, "Macromolecular composition during steady-state growth of *Escherichia coli* B/r," *Journal of bacteriology*, vol. 119, no. 1, pp. 270–281, 1974.
- [72] R. Young and H. Bremer, "Polypeptide-chain-elongation rate in *Escherichia coli* B/r as a function of growth rate," *Biochem. J.*, vol. 160, no. 2, pp. 185–194, 1976.
- [73] S. Pedersen, "*Escherichia coli* ribosomes translate in vivo with variable rate," *The EMBO journal*, vol. 3, no. 12, p. 2895, 1984.

- [74] A. L. Koch, "The adaptive responses of *escherichia coli* to a feast and famine existence," *Advances in microbial physiology*, vol. 6, pp. 147–217, 1971.
- [75] H. Link, T. Fuhrer, L. Gerosa, N. Zamboni, and U. Sauer, "Real-time metabolome profiling of the metabolic switch between starvation and growth," *Nature Methods*, vol. 12, no. 11, pp. 1091–1097, 2015.
- [76] H. Taymaz-Nikerel, M. De Mey, G. Baart, J. Maertens, J. J. Heijnen, and W. van Gulik, "Changes in substrate availability in *escherichia coli* lead to rapid metabolite, flux and growth rate responses," *Metabolic engineering*, vol. 16, pp. 115–129, 2013.
- [77] A. L. Koch and C. S. Deppe, "In vivo assay of protein synthesizing capacity of *escherichia coli* from slowly growing chemostat cultures," *Journal of molecular biology*, vol. 55, no. 3, pp. 549–562, 1971.
- [78] H. Bremer and P. P. Dennis, "Transition period following a nutritional shift-up in the bacterium *escherichia coli* b/r : Stable rna and protein synthesis," *Journal of Theoretical Biology*, vol. 52, no. 2, pp. 365–382, 1975.
- [79] R. Schleif, "Control of production of ribosomal protein," *Journal of Molecular Biology*, vol. 27, no. 1, pp. 41–55, 1967.
- [80] D. Molenaar, R. van Berlo, D. de Ridder, and B. Teusink, "Shifts in growth strategies reflect tradeoffs in cellular economics," *Molecular systems biology*, vol. 5, no. 1, p. 323, 2009.
- [81] A. Y. Weiße, D. A. Oyarzún, V. Danos, and P. S. Swain, "Mechanistic links between cellular trade-offs, gene expression, and growth," *Proceedings of the National Academy of Sciences*, vol. 112, no. 9, pp. E1038–E1047, 2015.
- [82] M. Basan, S. Hui, H. Okano, Z. Zhang, Y. Shen, J. R. Williamson, and T. Hwa, "Overflow metabolism in *escherichia coli* results from efficient proteome allocation," *Nature*, vol. 528, no. 7580, pp. 99–104, 2015.
- [83] Q. K. Beg, A. Vazquez, J. Ernst, M. A. de Menezes, Z. Bar-Joseph, A.-L. Barabási, and Z. N. Oltvai, "Intracellular crowding defines the mode and sequence of substrate uptake by *escherichia coli* and constrains its metabolic activity," *Proceedings of the National Academy of Sciences*, vol. 104, no. 31, pp. 12663–12668, 2007.
- [84] A. Goelzer and V. Fromion, "Bacterial growth rate reflects a bottleneck in resource allocation," *Biochimica et Biophysica Acta (BBA)-General Subjects*, vol. 1810, no. 10, pp. 978–988, 2011.
- [85] K. Zhuang, G. N. Vemuri, and R. Mahadevan, "Economics of membrane occupancy and respiro-fermentation," *Molecular systems biology*, vol. 7, no. 1, p. 500, 2011.
- [86] R. Schuetz, N. Zamboni, M. Zampieri, M. Heinemann, and U. Sauer, "Multidimensional optimality of microbial metabolism," *Science*, vol. 336, no. 6081, pp. 601–604, 2012.
- [87] N. Tepper, E. Noor, D. Amador-Noguez, H. S. Haraldsdóttir, R. Milo, J. Rabinowitz, W. Liebermeister, and T. Shlomi, "Steady-state metabolite concentrations reflect a balance between maximizing enzyme efficiency and minimizing total metabolite load," *PloS one*, vol. 8, no. 9, p. e75370, 2013.

- [88] E. J. O'Brien, J. A. Lerman, R. L. Chang, D. R. Hyduke, and B. Ø. Palsson, "Genome-scale models of metabolism and gene expression extend and refine growth phenotype prediction," *Molecular systems biology*, vol. 9, no. 1, p. 693, 2013.
- [89] M. Mori, T. Hwa, O. C. Martin, A. De Martino, and E. Marinari, "Constrained allocation flux balance analysis," *PLoS Comput Biol*, vol. 12, no. 6, p. e1004913, 2016.
- [90] M. Nomura, R. Gourse, and G. Baughman, "Regulation of the synthesis of ribosomes and ribosomal components," *Annual review of biochemistry*, vol. 53, no. 1, pp. 75–117, 1984.
- [91] B. J. Paul, M. M. Barker, W. Ross, D. A. Schneider, C. Webb, J. W. Foster, and R. L. Gourse, "Dksa: a critical component of the transcription initiation machinery that potentiates the regulation of rna promoters by ppgpp and the initiating ntp," *Cell*, vol. 118, no. 3, pp. 311–322, 2004.
- [92] J. A. Klappenbach, J. M. Dunbar, and T. M. Schmidt, "rrna operon copy number reflects ecological strategies of bacteria," *Applied and environmental microbiology*, vol. 66, no. 4, pp. 1328–1333, 2000.
- [93] K. Peebo, K. Valgepea, A. Maser, R. Nahku, K. Adamberg, and R. Vilu, "Proteome reallocation in escherichia coli with increasing specific growth rate," *Molecular BioSystems*, vol. 11, no. 4, pp. 1184–1193, 2015.
- [94] A. Schmidt, K. Kochanowski, S. Vedelaar, E. Ahrné, B. Volkmer, L. Callipo, K. Knoops, M. Bauer, R. Aebersold, and M. Heinemann, "The quantitative and condition-dependent escherichia coli proteome," *Nature biotechnology*, vol. 34, no. 1, pp. 104–110, 2016.
- [95] V. S. Cooper, D. Schneider, M. Blot, and R. E. Lenski, "Mechanisms causing rapid and parallel losses of ribose catabolism in evolving populations of escherichia coli b," *Journal of Bacteriology*, vol. 183, no. 9, pp. 2834–2841, 2001.
- [96] T. F. Cooper, D. E. Rozen, and R. E. Lenski, "Parallel changes in gene expression after 20,000 generations of evolution in escherichia coli," *Proceedings of the National Academy of Sciences*, vol. 100, no. 3, pp. 1072–1077, 2003.
- [97] L. Pelosi, L. Kühn, D. Guetta, J. Garin, J. Geiselmann, R. E. Lenski, and D. Schneider, "Parallel changes in global protein profiles during long-term experimental evolution in escherichia coli," *Genetics*, vol. 173, no. 4, pp. 1851–1869, 2006.
- [98] M. Parter, N. Kashtan, and U. Alon, "Environmental variability and modularity of bacterial metabolic networks," *BMC evolutionary biology*, vol. 7, no. 1, p. 1, 2007.
- [99] A. Kreimer, E. Borenstein, U. Gophna, and E. Ruppín, "The evolution of modularity in bacterial metabolic networks," *Proceedings of the National Academy of Sciences*, vol. 105, no. 19, pp. 6976–6981, 2008.
- [100] A. Samal, A. Wagner, and O. C. Martin, "Environmental versatility promotes modularity in genome-scale metabolic networks," *BMC systems biology*, vol. 5, no. 1, p. 1, 2011.
- [101] J. Monod, "The phenomenon of enzymatic adaptation and its bearings on problems of genetics and cellular differentiation.," *Growth Symposium XI*, pp. 223–289, 1947.
- [102] P. P. Dennis and H. Bremer, "Regulation of ribonucleic acid synthesis in escherichia coli: An analysis of a shift-up," *Journal of Molecular Biology*, vol. 75, no. 1, pp. 145–159, 1973.

- [103] M. Thattai and B. I. Shraiman, “Metabolic switching in the sugar phosphotransferase system of *escherichia coli*,” *Biophysical Journal*, vol. 85, no. 2, pp. 744–754, 2003.
- [104] E. Kussell and S. Leibler, “Phenotypic diversity, population growth, and information in fluctuating environments,” *Science*, vol. 309, no. 5743, pp. 2075–2078, 2005.
- [105] M. Acar, J. T. Mettetal, and A. van Oudenaarden, “Stochastic switching as a survival strategy in fluctuating environments,” *Nature Genetics*, vol. 40, no. 4, pp. 471–475, 2008.
- [106] S. Boulineau, F. Tostevin, D. J. Kiviet, P. R. ten Wolde, P. Nghe, and S. J. Tans, “Single-cell dynamics reveals sustained growth during diauxic shifts,” *PLoS ONE*, vol. 8, no. 4, p. e61686, 2013.
- [107] O. Kotte, B. Volkmer, J. L. Radzikowski, and M. Heinemann, “Phenotypic bistability in *escherichia coli*’s central carbon metabolism,” *Molecular Systems Biology*, vol. 10, no. 7, pp. 736–736, 2014.
- [108] J. H. van Heerden, M. T. Wortel, F. J. Bruggeman, J. J. Heijnen, Y. J. M. Bollen, R. Planque, J. Hulshof, T. G. O’Toole, S. A. Wahl, and B. Teusink, “Lost in transition: Start-up of glycolysis yields subpopulations of nongrowing cells,” *Science*, vol. 343, no. 6174, pp. 1245114–1245114, 2014.
- [109] O. S. Venturelli, I. Zuleta, R. M. Murray, and H. El-Samad, “Population diversification in a yeast metabolic program promotes anticipation of environmental shifts,” *PLOS Biology*, vol. 13, no. 1, p. e1002042, 2015.
- [110] A. Kolb, S. Busby, I. I. Buc, S. Garges, and S. Adhya, “Transcriptional regulation by camp and its receptor protein,” *Annu. Rev. Biochem.*, vol. 62, no. 1, pp. 749–797, 1993.
- [111] J. Deutscher, C. Francke, and P. W. Postma, “How phosphotransferase system-related protein phosphorylation regulates carbohydrate metabolism in bacteria,” *Microbiology and Molecular Biology Reviews*, vol. 70, no. 4, pp. 939–1031, 2006.
- [112] K. Potrykus and M. Cashel, “(p)ppgpp: Still magical? \*,” *Annual Review of Microbiology*, vol. 62, no. 1, pp. 35–51, 2008.
- [113] J. J. Lemke, P. Sanchez-Vazquez, H. L. Burgos, G. Hedberg, W. Ross, and R. L. Gourse, “Direct regulation of *escherichia coli* ribosomal protein promoters by the transcription factors ppgpp and dkxa,” *Proceedings of the National Academy of Sciences*, vol. 108, no. 14, pp. 5712–5717, 2011.
- [114] V. Hauryliuk, G. C. Atkinson, K. S. Murakami, T. Tenson, and K. Gerdes, “Recent functional insights into the role of (p)ppgpp in bacterial physiology,” *Nature Reviews Microbiology*, vol. 13, no. 5, pp. 298–309, 2015.
- [115] M. Basan, M. Zhu, X. Dai, M. Warren, D. Sévin, Y.-P. Wang, and T. Hwa, “Inflating bacterial cells by increased protein synthesis,” *Molecular systems biology*, vol. 11, no. 10, p. 836, 2015.
- [116] R. Hermsen, H. Okano, C. You, N. Werner, and T. Hwa, “A growth-rate composition formula for the growth of *E. coli* on co-utilized carbon substrates,” *Molecular Systems Biology*, vol. 11, no. 4, pp. 801–801, 2015.

- [117] H. D. Murray, D. A. Schneider, and R. L. Gourse, "Control of rna expression by small molecules is dynamic and nonredundant," *Molecular Cell*, vol. 12, no. 1, pp. 125–134, 2003.
- [118] C. L. Lawson, D. Swigon, K. S. Murakami, S. A. Darst, H. M. Berman, and R. H. Ebright, "Catabolite activator protein: Dna binding and transcription activation," *Current Opinion in Structural Biology*, vol. 14, no. 1, pp. 10–20, 2004.
- [119] L. N. Csonka, T. P. Ikeda, S. A. Fletcher, and S. Kustu, "The accumulation of glutamate is necessary for optimal growth of salmonella typhimurium in media of high osmolality but not induction of the prou operon," *Journal of bacteriology*, vol. 176, no. 20, pp. 6324–6333, 1994.
- [120] L. Reitzer, "Nitrogen assimilation and global regulation in escherichia coli," *Annual Review of Microbiology*, vol. 57, no. 1, pp. 155–176, 2003.
- [121] V. Chubukov and U. Sauer, "Environmental dependence of stationary-phase metabolism in bacillus subtilis and escherichia coli," *Applied and Environmental Microbiology*, vol. 80, no. 9, pp. 2901–2909, 2014.
- [122] P. Milon, E. Tischenko, J. Tomsic, E. Caserta, G. Folkers, A. La Teana, M. V. Rodnina, C. L. Pon, R. Boelens, and C. O. Gualerzi, "The nucleotide-binding site of bacterial translation initiation factor 2 (if2) as a metabolic sensor," *Proceedings of the National Academy of Sciences*, vol. 103, no. 38, pp. 13962–13967, 2006.
- [123] K. Gausing, *Ribosomes: Structure, Function and Genetics*. Baltimore (Maryland): University Park Press, 1980.
- [124] D. J. Kiviet, P. Nghe, N. Walker, S. Boulineau, V. Sunderlikova, and S. J. Tans, "Stochasticity of metabolism and growth at the single-cell level," *Nature*, vol. 514, no. 7522, pp. 376–379, 2014.
- [125] S. Busby and R. H. Ebright, "Transcription activation by catabolite activator protein (cap)," *Journal of Molecular Biology*, vol. 293, no. 2, pp. 199–213, 1999.
- [126] C. Condon, C. Squires, and C. L. Squires, "Control of rna transcription in escherichia coli," *Microbiological reviews*, vol. 59, no. 4, pp. 623–645, 1995.
- [127] A. M. Fallon, C. S. Jinks, G. D. Strycharz, and M. Nomura, "Regulation of ribosomal protein synthesis in escherichia coli by selective mrna inactivation," *Proceedings of the National Academy of Sciences*, vol. 76, no. 7, pp. 3411–3415, 1979.
- [128] J. Stülke and W. Hillen, "Carbon catabolite repression in bacteria," *Current opinion in microbiology*, vol. 2, no. 2, pp. 195–201, 1999.
- [129] M. Y. Pavlov and M. Ehrenberg, "Optimal control of gene expression for fast proteome adaptation to environmental change," *Proceedings of the National Academy of Sciences*, vol. 110, no. 51, pp. 20527–20532, 2013.
- [130] N. Giordano, F. Mairet, J.-L. Gouzé, J. Geiselman, and H. De Jong, "Dynamical allocation of cellular resources as an optimal control problem: novel insights into microbial growth strategies," *PLoS Comput Biol*, vol. 12, no. 3, p. e1004802, 2016.

- [131] J. Lengeler, A. M. Auburger, R. Mayer, and A. Pecher, "The phosphoenolpyruvate-dependent carbohydrate: Phosphotransferase system enzymes ii as chemoreceptors in chemotaxis of escherichia coli k12," *MGG Molecular & General Genetics*, vol. 183, no. 1, pp. 163–170, 1981.
- [132] A. Battesti, N. Majdalani, and S. Gottesman, "The rpos-mediated general stress response in escherichia coli\*," *Annual review of microbiology*, vol. 65, pp. 189–213, 2011.
- [133] W. Kollath, "Vitaminähnliche substanzen in ihrer wirkung auf das wachstum der influen-zabazillen.," *Zentr. Bakt. Parasitenk., Abt.I., Orig.*, vol. 93, pp. 506–519, 1924.
- [134] E. I. Garvie, "The growth of escherichia coli in buffer substrate and distilled water," *Journal of bacteriology*, vol. 69, no. 4, p. 393, 1955.
- [135] A. L. Koch, "Death of bacteria in growing culture," *Journal of bacteriology*, vol. 77, no. 5, p. 623, 1959.
- [136] C. Mason, G. Hamer, and J. D. Bryers, "The death and lysis of microorganisms in envi-ronmental processes," *FEMS microbiology letters*, vol. 39, no. 4, pp. 373–401, 1986.
- [137] S. Dukan and T. Nyström, "Oxidative stress defense and deterioration of growth-arrested escherichia coli cells.," *The Journal of biological chemistry*, vol. 274, no. 37, pp. 26027–26032, 1999.
- [138] L. Wang and M. J. Wise, "Glycogen with short average chain length enhances bacterial durability," *Naturwissenschaften*, 2011.
- [139] F. C. Neidhardt, J. L. Ingraham, and M. Schaechter, "Physiology of the bacterial cell: a molecular approach," 1990.
- [140] A. J. Wolfe, "The acetate switch," *Microbiology and Molecular Biology Reviews*, vol. 69, no. 1, pp. 12–50, 2005.
- [141] M. De Mey, S. De Maeseneire, W. Soetaert, and E. Vandamme, "Minimizing acetate formation in *E. coli* fermentations," *Journal of industrial microbiology & biotechnology*, vol. 34, no. 11, pp. 689–700, 2007.
- [142] J. H. Miller, "Experiments in molecular genetics," 1972.
- [143] J. Mandelstam and H. Halvorson, "Turnover of protein and nucleic acid in soluble and ribosome fractions of non-growing escherichia coli," *Biochimica et biophysica acta*, vol. 40, pp. 43–49, 1960.
- [144] H. Bremer and P. P. Dennis, *Modulation of chemical composition and other parameters of the cell at different exponential growth rates.*, p. 15531569. Washington, DC: Am Soc Microbiol, 2nd ed., 1996.
- [145] A. L. Koch, "Microbial physiology and ecology of slow growth.," *Microbiology and Molecular Biology Reviews*, vol. 61, no. 3, pp. 305–318, 1997.
- [146] T. Nyström and N. Gustavsson, "Maintenance energy requirement: what is required for stasis survival of escherichia coli?," *Biochimica et Biophysica Acta (BBA)-Bioenergetics*, vol. 1365, no. 1-2, pp. 225–231, 1998.

- [147] M. Eames and T. Kortemme, “Cost-benefit tradeoffs in engineered lac operons,” *Science*, vol. 336, no. 6083, pp. 911–915, 2012.
- [148] R. Hengge-Aronis, “Survival of hunger and stress: The role of rpos in early stationary phase gene regulation in e. coli,” *Cell*, 1993.
- [149] C. A. Reeve, A. T. Bockman, and A. Matin, “Role of protein degradation in the survival of carbon-starved escherichia coli and salmonella typhimurium.,” *Journal of Bacteriology*, vol. 157, no. 3, pp. 758–763, 1984.
- [150] R. Medzhitov, “Recognition of microorganisms and activation of the immune response,” *Nature*, vol. 449, no. 7164, pp. 819–826, 2007.
- [151] R. Pfeiffer, “Untersuchungen über das cholera gift,” *Medical Microbiology and Immunology*, vol. 11, no. 1, pp. 393–412, 1892.
- [152] C. R. Raetz and C. Whitfield, “Lipopolysaccharide endotoxins,” *Annual review of biochemistry*, vol. 71, p. 635, 2002.
- [153] R. Ross, “Atherosclerosis – an inflammatory disease,” *New England journal of medicine*, vol. 340, no. 2, pp. 115–126, 1999.
- [154] H. K. Eltzschig and T. Eckle, “Ischemia and reperfusion [mdash] from mechanism to translation,” *Nature medicine*, vol. 17, no. 11, pp. 1391–1401, 2011.
- [155] D. C. Angus and T. Van der Poll, “Severe sepsis and septic shock,” *New England Journal of Medicine*, vol. 369, no. 9, pp. 840–851, 2013.
- [156] B. Engelmann and S. Massberg, “Thrombosis as an intravascular effector of innate immunity,” *Nature Reviews Immunology*, vol. 13, no. 1, pp. 34–45, 2013.
- [157] S. P. Jackson, “Arterial thrombosis – insidious, unpredictable and deadly,” *Nature medicine*, vol. 17, no. 11, pp. 1423–1436, 2011.
- [158] S. Pfeiler, S. Massberg, and B. Engelmann, “Biological basis and pathological relevance of microvascular thrombosis,” *Thrombosis research*, vol. 133, pp. S35–S37, 2014.
- [159] V. Brinkmann, U. Reichard, C. Goosmann, B. Fauler, Y. Uhlemann, D. S. Weiss, Y. Weinrauch, and A. Zychlinsky, “Neutrophil extracellular traps kill bacteria,” *science*, vol. 303, no. 5663, pp. 1532–1535, 2004.
- [160] T. A. Fuchs, A. Brill, D. Duerschmied, D. Schatzberg, M. Monestier, D. D. Myers, S. K. Wroblewski, T. W. Wakefield, J. H. Hartwig, and D. D. Wagner, “Extracellular dna traps promote thrombosis,” *Proceedings of the National Academy of Sciences*, vol. 107, no. 36, pp. 15880–15885, 2010.
- [161] S. Massberg, L. Grahl, M.-L. von Bruehl, D. Manukyan, S. Pfeiler, C. Goosmann, V. Brinkmann, M. Lorenz, K. Bidzhekov, A. B. Khandagale, *et al.*, “Reciprocal coupling of coagulation and innate immunity via neutrophil serine proteases,” *Nature medicine*, vol. 16, no. 8, pp. 887–896, 2010.
- [162] M.-L. von Brühl, K. Stark, A. Steinhart, S. Chandraratne, I. Konrad, M. Lorenz, A. Khandoga, A. Tirniceriu, R. Coletti, M. Köllnberger, *et al.*, “Monocytes, neutrophils, and platelets cooperate to initiate and propagate venous thrombosis in mice in vivo,” *The Journal of experimental medicine*, vol. 209, no. 4, pp. 819–835, 2012.

- [163] K. Martinod, M. Demers, T. A. Fuchs, S. L. Wong, A. Brill, M. Gallant, J. Hu, Y. Wang, and D. D. Wagner, "Neutrophil histone modification by peptidylarginine deiminase 4 is critical for deep vein thrombosis in mice," *Proceedings of the National Academy of Sciences*, vol. 110, no. 21, pp. 8674–8679, 2013.
- [164] S. Baez, "An open cremaster muscle preparation for the study of blood vessels by in vivo microscopy," *Microvascular research*, vol. 5, no. 3, pp. 384–394, 1973.
- [165] R. E. Rumbaut, R. V. Bellera, J. K. Randhawa, C. N. Shrimpton, S. K. Dasgupta, J.-F. Dong, and A. R. Burns, "Endotoxin enhances microvascular thrombosis in mouse cremaster venules via a tlr4-dependent, neutrophil-independent mechanism," *American Journal of Physiology-Heart and Circulatory Physiology*, vol. 290, no. 4, pp. H1671–H1679, 2006.
- [166] K. N. Patel, S. H. Soubra, R. V. Bellera, J.-F. Dong, C. A. McMullen, A. R. Burns, and R. E. Rumbaut, "Differential role of von willebrand factor and p-selectin on microvascular thrombosis in endotoxemia," *Arteriosclerosis, thrombosis, and vascular biology*, vol. 28, no. 12, pp. 2225–2230, 2008.
- [167] F. N. Gavins, J. Russell, E. L. Senchenkova, L. D. A. Paula, A. S. Damazo, C. T. Esmon, D. Kirchhofer, R. P. Hebbel, and D. N. Granger, "Mechanisms of enhanced thrombus formation in cerebral microvessels of mice expressing hemoglobin-s," *Blood*, vol. 117, no. 15, pp. 4125–4133, 2011.
- [168] W. S. Nesbitt, E. Westein, F. J. Tovar-Lopez, E. Tolouei, A. Mitchell, J. Fu, J. Carberry, A. Fouras, and S. P. Jackson, "A shear gradient-dependent platelet aggregation mechanism drives thrombus formation," *Nature medicine*, vol. 15, no. 6, pp. 665–673, 2009.
- [169] Y. Zheng, J. Chen, and J. A. López, "Flow-driven assembly of vwf fibres and webs in in vitro microvessels," *Nature communications*, vol. 6, 2015.
- [170] F. J. Tovar-Lopez, G. Rosengarten, M. Nasabi, V. Sivan, K. Khoshmanesh, S. P. Jackson, A. Mitchell, and W. S. Nesbitt, "An investigation on platelet transport during thrombus formation at micro-scale stenosis," *PloS one*, vol. 8, no. 10, p. e74123, 2013.
- [171] N. A. Mody and M. R. King, "Three-dimensional simulations of a platelet-shaped spheroid near a wall in shear flow," *Physics of Fluids (1994-present)*, vol. 17, no. 11, p. 113302, 2005.
- [172] N. A. Mody and M. R. King, "Platelet adhesive dynamics. part i: characterization of platelet hydrodynamic collisions and wall effects," *Biophysical journal*, vol. 95, no. 5, pp. 2539–2555, 2008.
- [173] N. A. Mody and M. R. King, "Influence of brownian motion on blood platelet flow behavior and adhesive dynamics near a planar wall," *Langmuir*, vol. 23, no. 11, pp. 6321–6328, 2007.
- [174] C. R. Sweet, S. Chatterjee, Z. Xu, K. Bisordi, E. D. Rosen, and M. Alber, "Modelling platelet–blood flow interaction using the subcellular element langevin method," *Journal of The Royal Society Interface*, vol. 8, no. 65, pp. 1760–1771, 2011.
- [175] E. N. Sorensen, G. W. Burgreen, W. R. Wagner, and J. F. Antaki, "Computational simulation of platelet deposition and activation: I. model development and properties," *Annals of biomedical engineering*, vol. 27, no. 4, pp. 436–448, 1999.

- [176] L. Crowl and A. L. Fogelson, “Analysis of mechanisms for platelet near-wall excess under arterial blood flow conditions,” *Journal of fluid mechanics*, vol. 676, pp. 348–375, 2011.
- [177] W. Wang, T. G. Diacovo, J. Chen, J. B. Freund, and M. R. King, “Simulation of platelet, thrombus and erythrocyte hydrodynamic interactions in a 3d arteriole with in vivo comparison,” *PloS one*, vol. 8, no. 10, p. e76949, 2013.
- [178] N. Jain, “A scanning electron microscopic study of platelets of certain animal species.,” *Thrombosis et diathesis haemorrhagica*, vol. 33, no. 3, pp. 501–507, 1975.
- [179] S. Lippok, T. Obser, J. P. Müller, V. K. Stierle, M. Benoit, U. Budde, R. Schneppenheim, and J. O. Rädler, “Exponential size distribution of von willebrand factor,” *Biophysical journal*, vol. 105, no. 5, pp. 1208–1216, 2013.
- [180] T. V. Colace and S. L. Diamond, “Direct observation of von willebrand factor elongation and fiber formation on collagen during acute whole blood exposure to pathological flow,” *Arteriosclerosis, thrombosis, and vascular biology*, vol. 33, no. 1, pp. 105–113, 2013.
- [181] B. Savage, F. Almus-Jacobs, and Z. M. Ruggeri, “Specific synergy of multiple substrate–receptor interactions in platelet thrombus formation under flow,” *Cell*, vol. 94, no. 5, pp. 657–666, 1998.
- [182] P. André, C. V. Denis, J. Ware, S. Saffaripour, R. O. Hynes, Z. M. Ruggeri, and D. D. Wagner, “Platelets adhere to and translocate on von willebrand factor presented by endothelium in stimulated veins,” *Blood*, vol. 96, no. 10, pp. 3322–3328, 2000.
- [183] H. Ni, C. V. Denis, S. Subbarao, J. L. Degen, T. N. Sato, R. O. Hynes, and D. D. Wagner, “Persistence of platelet thrombus formation in arterioles of mice lacking both von willebrand factor and fibrinogen,” *The Journal of clinical investigation*, vol. 106, no. 3, pp. 385–392, 2000.
- [184] C. Oury, K. Daenens, H. Hu, E. Toth-Zsamboki, M. Bryckaert, and M. F. Hoylaerts, “Erk2 activation in arteriolar and venular murine thrombosis: platelet receptor gpib vs. p2x1,” *Journal of Thrombosis and Haemostasis*, vol. 4, no. 2, pp. 443–452, 2006.
- [185] A. Zarbock, R. K. Polanowska-Grabowska, and K. Ley, “Platelet-neutrophil-interactions: linking hemostasis and inflammation,” *Blood reviews*, vol. 21, no. 2, pp. 99–111, 2007.
- [186] C. Kleinschnitz, M. Pozgajova, M. Pham, M. Bendszus, B. Nieswandt, and G. Stoll, “Targeting platelets in acute experimental stroke impact of glycoprotein ib, vi, and iib/iiia blockade on infarct size, functional outcome, and intracranial bleeding,” *Circulation*, vol. 115, no. 17, pp. 2323–2330, 2007.
- [187] C. Kleinschnitz, S. F. De Meyer, T. Schwarz, M. Austinat, K. Vanhoorelbeke, B. Nieswandt, H. Deckmyn, and G. Stoll, “Deficiency of von willebrand factor protects mice from ischemic stroke,” *Blood*, vol. 113, no. 15, pp. 3600–3603, 2009.
- [188] A. Brill, T. A. Fuchs, A. K. Chauhan, J. J. Yang, S. F. De Meyer, M. Köllnberger, T. W. Wakefield, B. Lämmle, S. Massberg, and D. D. Wagner, “von willebrand factor–mediated platelet adhesion is critical for deep vein thrombosis in mouse models,” *Blood*, vol. 117, no. 4, pp. 1400–1407, 2011.

- [189] S. Nishimura, I. Manabe, M. Nagasaki, S. Kakuta, Y. Iwakura, N. Takayama, J. Oeohara, M. Otsu, A. Kamiya, B. G. Petrich, *et al.*, “In vivo imaging visualizes discoid platelet aggregations without endothelium disruption and implicates contribution of inflammatory cytokine and integrin signaling,” *Blood*, vol. 119, no. 8, pp. e45–e56, 2012.
- [190] J. Rossaint and A. Zarbock, “Platelets in leukocyte recruitment and function,” *Cardiovascular research*, p. cvv048, 2015.
- [191] C. N. Jenne and P. Kubes, “Platelets in inflammation and infection,” *Platelets*, vol. 26, no. 4, pp. 286–292, 2015.
- [192] V. Evangelista, S. Manarini, R. Sideri, S. Rotondo, N. Martelli, A. Piccoli, L. Totani, P. Piccardoni, D. Vestweber, G. de Gaetano, *et al.*, “Platelet/polymorphonuclear leukocyte interaction: p-selectin triggers protein-tyrosine phosphorylation-dependent cd11b/cd18 adhesion: role of psgl-1 as a signaling molecule,” *Blood*, vol. 93, no. 3, pp. 876–885, 1999.
- [193] R. Polanowska-Grabowska, K. Wallace, J. J. Field, L. Chen, M. A. Marshall, R. Figler, A. R. Gear, and J. Linden, “P-selectin-mediated platelet-neutrophil aggregate formation activates neutrophils in mouse and human sickle cell disease,” *Arteriosclerosis, thrombosis, and vascular biology*, vol. 30, no. 12, pp. 2392–2399, 2010.
- [194] V. Sreeramkumar, J. M. Adrover, I. Ballesteros, M. I. Cuartero, J. Rossaint, I. Bilbao, M. Nácher, C. Pitaval, I. Radovanovic, Y. Fukui, *et al.*, “Neutrophils scan for activated platelets to initiate inflammation,” *Science*, vol. 346, no. 6214, pp. 1234–1238, 2014.
- [195] Z. Patko, A. Csaszar, G. Acsady, K. Peter, and M. Schwarz, “Roles of mac-1 and glycoprotein iib/iiia integrins in leukocyte-platelet aggregate formation: stabilization by mac-1 and inhibition by gpiib/iiia blockers,” *Platelets*, vol. 23, no. 5, pp. 368–375, 2012.
- [196] C. Longstaff, I. Varjú, P. Sótonyi, L. Szabó, M. Krumrey, A. Hoell, A. Bóta, Z. Varga, E. Komorowicz, and K. Kolev, “Mechanical stability and fibrinolytic resistance of clots containing fibrin, dna, and histones,” *Journal of Biological Chemistry*, vol. 288, no. 10, pp. 6946–6956, 2013.
- [197] A. H. Gershlick, A. P. Banning, A. Myat, F. W. Verheugt, and B. J. Gersh, “Reperfusion therapy for stemi: is there still a role for thrombolysis in the era of primary percutaneous coronary intervention?,” *The Lancet*, vol. 382, no. 9892, pp. 624–632, 2013.
- [198] B. C. Campbell, P. J. Mitchell, T. J. Kleinig, H. M. Dewey, L. Churilov, N. Yassi, B. Yan, R. J. Dowling, M. W. Parsons, T. J. Oxley, *et al.*, “Endovascular therapy for ischemic stroke with perfusion-imaging selection,” *New England Journal of Medicine*, vol. 372, no. 11, pp. 1009–1018, 2015.
- [199] M. Goyal, A. M. Demchuk, B. K. Menon, M. Eesa, J. L. Rempel, J. Thornton, D. Roy, T. G. Jovin, R. A. Willinsky, B. L. Sapkota, *et al.*, “Randomized assessment of rapid endovascular treatment of ischemic stroke,” *New England Journal of Medicine*, vol. 372, no. 11, pp. 1019–1030, 2015.
- [200] G. Churchward, H. Bremer, and R. Young, “Macromolecular composition of bacteria,” *Journal of theoretical biology*, vol. 94, no. 3, pp. 651–670, 1982.
- [201] K. M. Fagerbakke, M. Heldal, and S. Norland, “Content of carbon, nitrogen, oxygen, sulfur and phosphorus in native aquatic and cultured bacteria,” *Aquat. Microb. Ecol.*, vol. 10, pp. 15–27, 1996.

- [202] S. J. Pirt, "The maintenance energy of bacteria in growing cultures," *Proceedings of the Royal Society B: Biological Sciences*, vol. 163, no. 991, pp. 224–231, 1965.
- [203] K. A. Datsenko and B. L. Wanner, "One-step inactivation of chromosomal genes in escherichia coli k-12 using pcr products," *Proceedings of the National Academy of Sciences*, vol. 97, no. 12, pp. 6640–6645, 2000.
- [204] S. Benthin, J. Nielsen, and J. Villadsen, "A simple and reliable method for the determination of cellular rna content," *Biotechnol Tech*, vol. 5, no. 1, pp. 39–42, 1991.
- [205] E. W. Deutsch, L. Mendoza, D. Shteynberg, T. Farrah, H. Lam, N. Tasman, Z. Sun, E. Nilsson, B. Pratt, B. Prazen, *et al.*, "A guided tour of the trans-proteomic pipeline," *Proteomics*, vol. 10, no. 6, pp. 1150–1159, 2010.
- [206] R. Craig and R. C. Beavis, "Tandem: matching proteins with tandem mass spectra," *Bioinformatics*, vol. 20, no. 9, pp. 1466–1467, 2004.
- [207] E. Sperling, A. E. Bunner, M. T. Sykes, and J. R. Williamson, "Quantitative analysis of isotope distributions in proteomic mass spectrometry using least-squares fourier transform convolution," *Analytical chemistry*, vol. 80, no. 13, pp. 4906–4917, 2008.
- [208] M. T. Sykes, Z. Shajani, E. Sperling, A. H. Beck, and J. R. Williamson, "Quantitative proteomic analysis of ribosome assembly and turnover in vivo," *Journal of molecular biology*, vol. 403, no. 3, pp. 331–345, 2010.
- [209] R. Lutz and H. Bujard, "Independent and tight regulation of transcriptional units in escherichia coli via the lacr/o, the tetr/o and arac/i1-i2 regulatory elements," *Nucleic acids research*, vol. 25, no. 6, pp. 1203–1210, 1997.
- [210] S. Tong, A. Porco, T. Isturiz, and T. Conway, "Cloning and molecular genetic characterization of the escherichia coli gntR, gntK, and gntU genes of gntI, the main system for gluconate metabolism," *Journal of bacteriology*, vol. 178, no. 11, pp. 3260–3269, 1996.
- [211] R. T. Voegelé, G. D. Sweet, and W. Boos, "Glycerol kinase of escherichia coli is activated by interaction with the glycerol facilitator," *Journal of bacteriology*, vol. 175, no. 4, pp. 1087–1094, 1993.
- [212] S. A. Westermayer, G. Fritz, J. Gutiérrez, J. A. Megerle, M. P. Weißl, K. Schnetz, U. Gerland, and J. O. Rädler, "Single-cell characterization of metabolic switching in the sugar phosphotransferase system of escherichia coli," *Molecular microbiology*, 2016.
- [213] M. Berney, F. Hammes, F. Bosshard, H.-U. Weilenmann, and T. Egli, "Assessment and interpretation of bacterial viability by using the live/dead baclight kit in combination with flow cytometry," *Applied and environmental microbiology*, vol. 73, no. 10, pp. 3283–3290, 2007.



# Acknowledgements

Undertaking this PhD has been a truly life-changing experience for me and it would not have been possible without the support and guidance that I received from many special people. First and foremost I want to thank my advisor, Prof. Dr. Ulrich Gerland for the giving me the opportunity to do my thesis under his supervision. He gave me all the freedom and encouragement I could hope for, and had at the same time always an open ear for new ideas. Thank you for initiating my stay in San Diego, where I met my wonderful wife Annick. Thank you for entrusting me with setting up your freshly acquired lab at TUM. The experience of this responsibility has crucially advanced my personal and scientific development. I further want to thank Prof. Dr. Terence Hwa for inviting me to stay and work at his laboratory at UC San Diego for 1.5 years. This very fruitful time was crucial for me. Not only did I learn how to do quantitative biology experiments in your laboratory, but also a deep sense of critical thinking. Your meticulous comments were an enormous help to me. Thank you for being a mentor and taking the patience to teach me!

I am in debt to the people who trained me at wet lab work. Thank you Sabine Scheu for taking care of my infancy steps in a microbiology laboratory at the LMU in Prof. Dr. Kirsten Jung's lab and Prof. Dr. Minsu Kim who trained me at UC San Diego in both wet lab and microfluidic work.

I would like to express my gratitude to all of my collaborators and co-workers. I would like to thank David Erickson and Matteo Mori for fruitful discussions on growth shifts in San Diego. Thanks Vadim Patsalo for joining our growth shift project and contributing your immaculate mass spec data. I further like to thank the entire remaining Hwa lab, especially Jonas Cremer, Mya Warren and Tomoya Honda for their comments, discussions and for being nice people.

I would like to express the deepest appreciation to all the people who helped making the TUM lab a success. Thank you Elena Biselli for three years as a office and lab mate. Your pristine measurements were key to the success of our joint work. Without you this work would not have materialized. Thanks Constantin Ammar for pushing us forward with your hard work and smart ideas. Thanks Mariel Huiman-Garcia for being relentless. I am grateful to all the people from the Gerland lab who helped me get through this thesis. Special thanks to Patrick Hillenbrand and Giovanni Giunta for warm encouragement and constructive feedback. Florian Hinzpeter, Felipe Tostevin, Michael Wolff, Manon Wigbers, Johannes Nübler, Philipp Seifert and many more gave constructive comments that I am grateful for.

Special thanks to Daniel Pühr-Westerheide for introducing me to the medical scientific field and for leading the platelet project. Experiments and discussions with you were one of the most fun and rewarding during my entire PhD. I hope we will continue this string of research!

I would like to offer my special thanks to Dr. Zeynep Ökten and her lab, in particular Thi-Hieu Ho, for offering their help and resources for setting up our TUM lab. I have greatly benefited from the support of our secretary Laura Darabas, who helped me in understanding TUM bureaucracy, and who fixed all my mistakes. I owe a very important debt to Dr. Michael Erikstad, Prof. Dr. Alex Groisman, Andrea Mückl, Matthäus Schwarz-Schilling, Lukas Aufinger

and Prof. Dr. Fritz Simmel for assistance in microfluidic design and manufacturing.

I am very grateful to the German Fulbright Commission for funding my research at UC San Diego and to the American people for receiving me so kindly in their beautiful country.

I want to thank my family and friends for supporting me throughout this thesis. Thank you for encouraging me to sally forth, visiting me in San Diego and receiving me back in Munich.

Last, but most certainly not least, I am deeply in debt to my wonderful wife Annick. Thank you for supporting me every single minute of this PhD. Thank you for understanding and encouraging me. Thank you for being by my side. I love you dearly.